Polarization and gain phenomena in dye-doped polymer micro-lasers

Iryna Gozhyk

ENSC-2012 Nº 285

THESE DE DOCTORAT

DE L'ECOLE NORMALE SUPERIEURE DE CACHAN

Présentée par

Iryna GOZHYK

pour obtenir le grade de

DOCTEUR DE L'ECOLE NORMALE SUPERIEURE DE CACHAN

Domaine:

SCIENCES PHYSIQUES

Sujet de la thèse:

Polarization and gain phenomena in dye-doped polymer micro-lasers

Thèse présentée et soutenue à Cachan le 16/10/2012 devant le jury composé de:

FÉRON Patrice	Professeur (ENSSAT)	Président
BRETENAKER Fabien	Directeur de Recherches (Laboratoire Aimé Cotton)	Rapporteur
CHARRA Fabrice	Directeur de Recherches (CEA)	Rapporteur
PANSU Robert	Directeur de Recherches (ENSC)	Examinateur
SAMUEL Ifor	Professeur (University of St Andrews)	Examinateur
LEBENTAL Mélanie	Maître de Conférences (ENSC)	Directrice de these
FORGET Sébastien	Maître de Conférences (Université Paris 13)	Directeur de these
ZYSS Joseph	Professeur (ENSC)	Directeur de these

Laboratoire de Photonique Quantique et Moléculaire
ENS CACHAN/CNRS/UMR 8537
61, avenue du Président Wilson, 94235 CACHAN CEDEX (France)

Abstract

The demonstration of an electrically pumped organic laser remains a major issue of organic optoelectronics for several decades. This goal requires an improved device configuration so as to reduce losses which are intrinsically higher under electrical excitation compared to optical pumping. Moreover a systematic investigation of the material properties is still missing and should lead to a reliable estimate of the lasing threshold under optical pumping, and then to a lower limit for electrical pumping.

In this thesis we addressed the issue of gain and polarization properties of organic materials in the case of dye-doped polymer thin films. The originality of this work lies in the study of materials via the features of dielectric micro-lasers, allowing to investigate the issues of gain and mode coupling and the physics of open systems.

We propose a quantitative description of amplification in organic materials. The "gain-loss-threshold" relation was developed and demonstrated for a Fabry-Perot type cavity, opening the way to study both amplification in organic materials and light out-coupling in dielectric micro-cavities via the lasing threshold. Within this context, different cavity shapes were studied, for instance squares, where light out-coupling takes place by diffraction at dielectric corners.

We evidence that polarization properties of such lasing system originate from the intrinsic fluorescence anisotropy of dyes, which required to develop a specific anisotropic model going beyond the existing theory. We also investigated the role of the cavity geometry on the polarization states of the micro-lasers and proposed different ways to influence these features.

Résumé

La démonstration de la première diode laser organique reste un défi majeur en opto-électronique organique. Parmi les nombreuses problématiques à étudier, l'aspect « matériau » (gain et pertes) est capital. Par exemple, la limite théorique basse du seuil laser en pompage électrique pourrait être connue s'il existait une méthode d'estimation fiable du seuil laser en pompage optique.

Dans cette thèse nous avons étudié le gain et la polarisation de lasers basés sur des couches minces de polymère dopées par des colorants organiques. L'originalité de ce travail repose sur l'étude des propriétés du matériau organique à travers l'analyse des caractéristiques de microlasers. Cela permet aussi de s'intéresser aux problématiques de couplage gain-mode et aux systèmes ouverts.

Nous proposons une description quantitative du processus d'amplification dans les matériaux organiques. Une relation liant gain, pertes et seuil est établie dans le cas d'une cavité Fabry-Perot, ce qui permet par la suite l'étude de l'amplification optique et de l'extraction de la lumière dans les cavités diélectriques à travers la mesure précise du seuil laser. Nous avons exploré différentes formes de cavités, comme les carrés où la lumière est couplée vers l'extérieur par diffraction au niveau des coins.

Nous avons démontré que l'anisotropie de fluorescence intrinsèque des molécules de colorant gouverne la polarisation de tels systèmes lasers. Nous avons développé à cette occasion un modèle original incluant la distribution non-isotrope des molécules dans le polymère. Nous avons aussi étudié le rôle de la géométrie de la cavité sur l'état de polarisation du laser, et différents moyens de contrôler cet état.

Acknowledgments

I am infinitely grateful to Mélanie Lebental and Joseph Zyss at LPQM for giving me an opportunity to conduct this interesting multidisciplinary thesis research under their kind guidance. In particular, I thank Joseph Zyss for his vast capacity of generating amazing ideas, for his dedication and great efforts towards shaping self-consistent scientists from his students. I am indebted to Mélanie Lebental for a thoughtful guidance of my work, for organizing numerous interesting collaborations and providing me possibilities to develop working skills in several fields. I also thank her to teach me patience while overcoming routine difficulties of scientific work. I had the chance to be partially guided by two more advisers: Sébastien Forget and Sébastien Chenais at Paris 13 University. I am grateful to both of them for this enriching experience, their well-directed suggestions and fruitful discussions.

I would like to express my gratitude to the jury of my thesis defense: to Patrice Féron for chairing the jury, to Fabien Bretenaker and Fabrice Charra for accepting to be my referees, to read and evaluate my manuscript, to Ifor Samuel for making a long trip to participate at my defense and last but not least to Robert Pansu.

This thesis research was done in numerous collaborations. Although some projects met technological difficulties and were left for future studies, each and single one of them was a great experience and helped me to develop important skills, which will be undoubtedly useful in future. Consequently, I would like to express my gratitude to the collaborators and colleagues to whom I owe this wonderful experience. For their invaluable contribution I thank Christian Ulysse from LPN (for performing electron-beam lithography) and Joseph Lautru from IDA (for advices on technological aspects). I am grateful to all our collaborators from PPSM laboratory: Jean-Frederic Audibert, Arnaud Brosseau, Gilles Clavier, Rachel Meallet-Renault and Robert Pansu for the large amount of work we have done together, their commitment and availability, and fruitful discussions. I thank a lot Elena Smotrova and Alex Nosich from IRE, Ukraine for suggesting a new shape for our micro-lasers, which revealed interesting features of our system. It was a great pleasure to work with Bernard Geffroy, Denis Tondelier, Jean-Charles Vanel and Yvan Bonassieu from LPICM, Ecole Polytechnique on OLEDs and OLETs. I would also like to thank Emmanuelle Deleporte from LPQM and her PhD students Yi Wei and Gaetan Lanty for our work on hybrid materials. I am very grateful to the non-permanent members of Melanie and Joseph team I've been working with during these 3 years: Sergei Lozenko, Clement Lafargue, Salim Zerkani, Viktor Tsvirkun, Severin Charpignon, Maxime Boudreau, Stefan Bittner and especially Nadia Djellali.

I thank Isabelle Ledoux, director of LPQM lab for wonderful conversations and helpful advices, her concern about PhD students of the lab and efforts to provide a financial support for their scientific activities. I also thank administration of LPQM and IDA for their kind help, as well as École doctorale sciences pratiques of ENS de Cachan for financial support of my thesis work.

I would like to thank also Francois Treussard, Jean-Sebastien Lauret and Vasyl

Shynkar for enlightening discussions, and all the PhD and internship students at LPQM for the wonderful atmosphere, so important for an efficient work.

Finally I believe this thesis would have been impossible without the support of my loving family, friends in Ukraine and France; and also Volodymyr Bezrychko, Alexander Zinchenko, Volodymyr Stetsiyk and Valerii Grugoryk, who by their very example and passion to physics influenced my choice of profession and lead me within the very first but so important steps towards a PhD thesis.

Contents

Introduction

Among existing commercial light-emitting systems, two main groups can be distinguished on the basis of their purpose: incoherent light sources towards lightening and visualization, and coherent ones for the transmission and processing of information. The first group embodies a great variety of devices, starting from all sort of lamps to light emitting monitors and diodes, while the second deals with lasers of no less diversified types. To this day, the most efficient and stable devices of both families are based on semiconductor materials, mainly belonging to III-V compound semiconductors, in spite of a most serious drawback - their limited emission wavelengths. Much in contrast, tunability over a broad spectral range [1], and as result the possibility of generating ultrashort pulses (up to 6 fs [2]), and high output power are major advantages of organic materials such as laser dyes and organic semiconductors.

While undoubtedly a late-bloomer with respect to its semiconductor counterpart, polymer and more generally organic materials based photonic technology has continuously progressed over the last decades. The performance capabilities of organic light emitting diodes (OLED's)[3, 4] have evolved into an industrially viable domain and found numerous applications, such as displays for modern cell-phones. Meanwhile polymer based integrated optical devices, including electro-optic modulators, have matured into robust alternatives to inorganic semiconductor based devices, with specific assets of their own, among which the possibility of flexible substrates, and a more adequate starting point towards photonic chemical or biosensors [5]. Laser dyes have also been implemented into fiber technology, providing considerably better amplification of signal compared to conventional rare-earth elements [6] as well as more user-friendly potential for home appliances.

In the realm of lasing dye-based devices, various configurations of solid-state dye-doped systems have been developed over past decades, such as distributed feedback lasers (DFB), fiber lasers, planar micro-lasers and VECSOLs. This thesis is concentrating on the study of the last two types. The development of solid state dye-lasers is a highly needed spin-off in the wake of earlier liquid dye lasers, which are bulky, toxic and hard to in maintain. However, they have not challenged so far the success of compact inorganic semiconductor devices yet, due to the barrier of electrical pumping. These systems remain cumbersome, due to the demand of an additional pumping laser. It has however been somewhat simplified by the demonstration of hybrid integration whereby a semiconductor based pump is packaged with an organic laser [7].

The problem of electrical pumping of organic devices have been thoroughly examined during last two decades, where many clever configurations aiming to optimize the structure and reduce the losses were tried, albeit in vain. A firmly established conclusion is that the optical pumping threshold sets the lowest theoretical limit to the electrical pumping one. To our knowledge, there is no systematic approach towards a reliable estimate of the lasing threshold in dye-based systems.

Our present work is focusing on the impact of organic gain materials on the emission properties of dye-doped polymer micro-lasers. To address this topic, we use the advantage of a multidisciplinary approach to explore the amplification properties of gain medium in conjunction with physical features of dielectric resonators. This thesis follows three main but highly interconnected research lines. Firstly, we intend to make a contribution to the development of electrically-pumped organic laser by providing the tool for selecting the gain material based on its estimated

gain properties and optically pumped threshold. The polarization features of the emission of dye incorporated in thin films configuration have not been thoroughly studied to our knowledge. We address this second issue in order to get a better insight on the properties of dye-doped thin film micro-lasers. Lastly, this subject is of high interest towards OLEDs technology, which deals with organic materials in similar configurations, as one of its current issues is in the generation and control of a polarized emission. Dielectric micro-cavities, regardless of the nature of the lasing material they happen to be embedding, allow to address deep fundamental issues pertaining to the physics of open system, while appearing also as promising candidates towards engineering applications. In the present work, dielectric micro-cavities were used mainly as a bench-marking tool, so as to provide a comparative insight on the gain properties of amplification material, and more generally to study various light out-coupling mechanisms at stake.

We will start by presenting the state of art, and then provide the thesis outline.

State of the art

- Organic light-emitting diodes

Electroluminescence in organic materials was demonstrated in the fifties [8] starting with organic crystals, which allowed to study current injection mechanism and recombination processes as well as to engineer suitable materials for electrode contacts etc. However, the progress in the field was hampered by the low conductivity of organic materials at that time. The first efficient organic diode was reported only in 1987 [3]. In their work Ching W. Tang and Steven Van Slyke from Eastman Kodak proposed a novel two-layer structure with separate hole and electron transporting layers based on evaporated low molecular weight materials, that resulted in a charge recombination and light emission at their interface. Discovery of highly conductive polymers in the sixties(awarded the Nobel prize in Chemistry in 2000) resulted in the creation of polymer LED (PLED), first demonstrated in 1990 by Burroughes [4] with poly(p-phenylene vinylene) (PPV).

Further technology developments were subsequently developed along two directions: OLED's based on small molecules, allowing to create a multi-layer structure by thermal evaporation, and polymer-based OLED's, containing only two active layers which advantage of simple spin-coating or ink-jet printing fabrication technologies.

Since their inception, OLED's have focused the attention of researchers due to possible applications to large area full-color flat-panel flexible displays and new lightning technologies with similar assets. However OLED's emit non-polarized light, which is a serious drawback that prevents their implementation in optical communication and data storage, 3-D imaging systems, to say nothing about the improvement of OLED emission contrast. There were numerous works focused on the possibility to achieve linearly polarized emission from OLED's. Most of them make use of the alignment techniques (stretching of the film, thermal treatment [9], Langmuir-Blodgett technique [10], vapor phase epitaxy [11], precursor conversion on aligned substrates [12], orientation on pre-aligned substrates [13, 14] etc.) on oligomers or liquid crystalline polymers to favour a uniaxially oriented materials. Others proposed the incorporation of polarization elements, such as reflective polarizer with a quarter waveplate [15], into the OLED packaging structure. In spite of all those efforts, to the best of our knowledge, polarization properties of dye molecules in thin-film configuration were not addressed in these studies.

- Solid state dye lasers

The first solid-state dye lasers were reported in 1967, shortly after invention of their solution-based predecessors. The invention was made by Soffer and McFarland [1], who doped a poly(methylmetacrylate) (commonly referred as PMMA) with the Rhodamine 6G dye, and used a frequency doubled Nd laser for pumping. Then Snavely and Peterson [16] followed the same lines to fabricate PMMA rods, doped with different dyes of the Rhodamine family. For a long period, a rod structure of several cm's in size remained the standard for solid-state dye lasers. Such solid-state dye lasers provide the benefits of good quality output beams, relatively high output energies (of the order of 100mJ and higher [17, 18]) as well as excellent optical slope efficiencies up to 86% [17, 18]. Still their main drawback stems from their time-consuming fabrication, based on a sol-gel, co-polymerization or radical polarization techniques, up to several days or even weeks [18] to be further completed by delicate steps of surface processing, such as cutting an polishing.

The progress in the field of OLED's, namely the improvement in thin organic films fabrication techniques, led to the decrease in dimensions of solid-state lasers. The first optically pumped organic micro-cavity was reported by Tessler et al. in 1996 [19], based on a 100 nm thick film of PPV, fabricated by thermal evaporation. The possibility to create a thin polymer film with a good morphology, resorting to a wide class of techniques from spin-coating to thermal evaporation, pushed the development of a variety of organic thin film devices, such as distributed feedback resonators (DFB [20, 21, 22] and DBR [23]), vertical micro-cavities (VCSEL) [19], micro-lasers (micro-disk [24], micro-rings [25], micro-toroids [vahala] etc.). In-spite of their numerous advantages, the development of solid-state organic lasers suffers from a serious drawback: the current absence of viable electrical pumping schema remaining to be conceived and demonstrated. The race towards such a break-through has mobilized the best teams in the field throughout the world, leading to interesting propositions albeit disappointing at the end. It has nevertheless allowed to ripe some interesting scientific side benefits such as an evidence of very high threshold currents to be reached at the expense of the material stability. Therefore, current systems still demand the use of another laser to provide an optical pumping.

- Organic laser diode issue and hybrid pumping

The success of OLED and PLED technology on the one hand and unsuccessful attempts over twenty years t develop organic laser diode on the other, is a manifestation of the basic physical difference between spontaneous and stimulated emission processes, especially in the context of organic materials.

The excitation of stimulated emission is always characterized by a threshold, which suggests a balance between cavity losses and the gain in the amplification medium. The lowest theoretical limit J_{th} of the electrically-driven threshold in organic semiconductor material can be estimated from the value of its optically-pumped threshold I_{th} under assumption of maximum recombination rate and neglecting the current-induced losses and metal contact[26] (for electron charge q and energy of pumping photon $h\nu$):

$$J_{th} = \frac{q}{h\nu} I_{th}$$

The lowest reported threshold under optical pumping is of the order of 100 W/cm^2, reached in conjugated polymers [27]. This value suggests that without an improvement in gain properties of the implemented materials, organic diode laser can be achieved with current at densities no less then 100 A/cm^2(an estimate

of about 80 A/cm^2 is reported in the literature for small molecules blends of the Alq_3:DCM type [28]). Although PLED's are known to sustain current densities up to 1 kA/cm^2, highly efficient electroluminescence in organic materials is generally obtained at lower currents.

It appears, that electrically-pumped organic material have several losses mechanisms, which grow rapidly with the current. This creates a negative feedback loop, that results in material degradation at pumping currents still low compared to the threshold value [29].

The first problem is that electroluminescent efficiency in organic semiconductors is far below unity (for fluorescence-emitting OLED). Only one fourth of the excited molecules actually contribute to population inversion and hence gain, due to a 25% being the theoretical spin-degeneracy statistical limit. In reality the lower values down to about 20% were measured experimentally [30]. Indeed, recombination events produce light-emissive singlet excitons as well as triplet excitons. The latter do not emit light in fluorescent materials (while they do in phosphorescent ones) and are responsible for singlet-triplet annihilation losses. Moreover, single excitons can themselves be lost in annihilation processes, such as a singlet-singlet (mainly in crystalline materials [31]) or singlet-polaron, or singlet-triplet processes (dominant in amorphous materials [31, 32]). These effects are much less relevant in optically-pumped devices, due to the difference in features of photon absorption and charge recombination processes in organic semiconductors.

Current injection is also responsible for loss mechanisms absent in optically-excited system such as charge-induced absorption and losses on metal electrodes [26, 33, 34]. In the presence of a high density of charge carriers in the medium, a non-negligible number of molecular ions is created. In the case of organic semiconductors, strong absorption in the visible and up to the IR region [35, 28] will generally contribute to reabsorption of emitted photons.

Organic semiconductors exhibit low intrinsic mobility (10^{-2}-10^{-3} cm^2/Vs for holes, but up to 0.1 cm^2/Vs for electrons [36, 37]), which limits the useful thickness of organic layers ($\leq$ 200 nm) for laser diode applications [38]. High absorption of the metal contacts comes into play, at the expense of waveguide modes of such thin layer remain in contact with the closely adjacent metal contacts along the full length of the laser. In addition, the gain region volume is very small in such thin film configurations, thus the amplification may be always inferior to the above described cumulated losses.

Several configurations were proposed to reduce the impact of one or several losses mechanisms, as for instance to tune the waveguiding mode so as to decrease its overlap with electrodes [40, 41], or move the recombination region away from the electrodes (using light-emitting field-effect transistor coupled to distributed feedback resonator [42]). However, reproducible experiments [31] with reliable proof of lasing [43] in the electrically pumped organic devices remain to be done.

The only way to eliminate losses induced by electrical pumping is in separation of the electroluminescent pump from the optical gain region. This idea was proposed in the late nineties [31] and first realizations were demonstrated during last decade, by means of various pumping sources: micro-chip lasers [44], inorganic laser diodes [45, 46] (building upon the availability of new InGaN sources, emitting blue light up to the W power range) or even incoherent LED for pumping[7].

The selection of organic materials used for direct or indirect electrical pumping experiments is generally based on the previously acquired experience in the group or can be found in the literature from published gain or threshold values and electronic structure of species. We propose herein a tool, based on the analysis of photo-physical properties and amplified spontaneous emission features of gain

media, which can be useful for the preselection of the implemented materials.

- Dielectric micro-cavities

Micro-spheres played a foremost pioneering role in an exploration of the potential of dielectric micro-resonators.

The optical analog of acoustic whispering gallery modes in dielectric resonators was discovered in the sixties starting from mm-size spheres[47], and in the eighties extended to micro-meter dye-doped droplets [48]. A leap forward in the field started in the ninetees, when extremely high quality factors of $8{\cdot}10^9$ were reported for fused silica micro-sphere [49]. Numerous devices based on micro-sphere resonators were designed and the first steps towards their realization reported in the following years: tunable filters [50], low-threshold [51] and multi-mode [52] lasers on rare-earth elements, narrow-line laser diode with improved stability (by coupling to a micro-sphere [53]), cavity-QED experiments (radiative coupling of atoms in a dilute vapor to the external evanescent field of WGM [54]), bio-sensor for protein detection [55] etc. Several of the above mentioned prototype devices are nowadays successfully commercialized, others are still being improved in academic environment, for instance a single virus detection set-up [56].

Although the intrinsic properties of micro-sphere resonators are indeed outstanding and no passive other resonator shape has yet challenged to their characteristics, their applications stay limited by the difficulty of on-chip fabrication and integration. In this regard, other high-Q cavity shapes came into focus: toroids ($Q \propto 10^8$ [57]), micro-disks on a pillar ($Q \propto 10^4$ in semiconductor [58], $Q \propto 10^6$ in silica [59]), photonic crystals ($Q \propto 10^4$ [60]). The high quality factor of such resonators results from their circular symmetry (except for photonic crystals), which demands high fabrication precision and limits the contour flexibility. As the inhomogeneities in the cavity bulk generally cause a decrease in the quality factor, among various functionalization methods preference is generally given to the deposition of outer gain layers [61]. Thereby, the technology of on-chip fabrication for high-Q micro-cavities stays complex and involves many-steps.

Increased possibilities towards the control of the cavity contour have allowed to move forward to planar dye-doped polymer micro-cavities [62]. These are the targets of research lead by Melanie LEBENTAL and Joseph ZYSS in the micro-cavities group at LPQM, ENS de Cachan, where this thesis research was performed. The solid foundation for this thesis work was provided by the achievements of the previous PhD students in the group: Tahar BEN MESSAOUD [63], Melanie LEBENTAL [64], Nadia DJELLALI [65] and Sergey LOZENKO [66]. Although such micro-lasers exhibit a significantly lower quality factor ($Q \propto 10^3$), they are advantageous due to simple fabrication technique (detailed in Chapter 2 of this thesis) and the possibility to engineer at will any arbitrary 2-D shape. The latter is of a high interest, as it permits the experimental verification of theoretical predictions on open dielectric cavities [67, 68] which is a broad ongoing domain of fundamental physics. Moreover the low light confinement permits to study at the same time the gain properties of amplification medium and to address the fundamental problems of light diffraction on the dielectric corners. In-spite of moderate quality factor compared to toroid micro-cavities, planar dye-doped polymer micro-lasers are also suitable for sensing applications, for instance, a detection of the 10^{-6}M concentration of Hg^{2+} in liquid solution was reported by our group [66].

Now that the developments in the domains of interest are presented, we will continue with the thesis outline.

Thesis structure

This manuscript is organized in six parts as follows.

The first chapter details generic physical properties of laser dyes. The dynamics of absorption and emission processes are first introduced. We then focus on the universally used definitions of various quantitative figures of merit for these processes and we review the conditions and techniques necessary for their experimental assessment. Laser operation in planar dye-doped polymer micro-cavities is described based on rate-equations. Finally, as examined micro-lasers are made of thin polymer films light confinement in this configuration is considered, with the help of effective refractive index approximation.

The second chapter provides a description of the micro-laser fabrication processes as well as details all the experimental arrangements and techniques used in the experimental studies. As the thesis focuses on the lasing properties of dye-doped plastic micro-lasers, experimental set-up's used towards this end-goal are first specified. To achieve a deeper insight on the lasing properties, we also investigate the photo-physical properties of dyes, the dynamics of their spontaneous and stimulated emission, and the polarization effects as from spontaneous emission. Thus we proceed with a description of all the necessary equipment.

Laser dyes hold rather strong intrinsic polarization properties due to their structural electronic properties. The third chapter is devoted to the exploration of the consequences this effect in various dye-based laser configurations. At the molecular origin of the polarization effects, the phenomenon of fluorescence anisotropy, is first explained. As the existing phenomenological approach is inconsistent with our experimental configuration, a more general model is proposed and experimentally verified. Next, the change of pump polarization state now at the level of stimulated emission is discussed in the amplified spontaneous emission configuration and planar micro-lasers of various shapes. Finally, the polarization state of the full-pledged micro-laser emission is shown to be rooted in basic fluorescence features, except in the case of Whispering Gallery Modes.

For most examined micro-laser shapes, the output emission is mainly in-plane polarized, which is caused by the imbalance on the fluorescence level of the polarized components in favor of the in-plane one. The scope of the research presented in the fourth chapter is in the wake of the model provided in the third chapter, to attempt to influence and eventually the output polarization of micro-lasers. We evidenced the two basic mechanisms in this part: pumping via energy transfer, and pumping to a higher singlet state. The first method applies to the amplified spontaneous emission regime, but due to low gain the lasing threshold could not be reached. However the second method, resulted in a noteworthy influence on the output polarization in the case of VECSOL dye-doped lasers and shape-dependent effects in the case of planar micro-lasers.

As was mentioned in the introduction, the state-of-the-art in the research domain of the solid-state dye-containing optically-pumped amplification and lasing systems brings in a broad variety of experimental results albeit missing solid foundations for analysis and predictions. This issue is addressed in the fifth part of this thesis by the proposition of a model, based on photo-physical properties of the system, which can be useful to estimate gain and threshold values in dye-doped polymer films and lasers. First the commonly used gain definitions are critically discussed and an alternative method, that permits the comparison of gain properties in different systems, is proposed. A general relation between gain and threshold is then derived and experimentally verified on the example of a Fabry-Perot cavity.

The final chapter is devoted to the application of the previously predicted gain properties of dye-doped polymer layers to investigate the light out-coupling in dielectric resonators of specific shapes. More precisely, the thorough study of square-shaped micro-lasers allowed us to address the problem of light diffraction on dielectric corners and obtain experimental value for the light reflection on such corners. To conclude, attention is paid to the possible co-existence of different mode types that may jointly contribute to the lasing threshold, as discussed on the examples of rectangle and kite-shaped micro-cavities.

List of notations

α - angle between pump beam linear polarization and observation direction [degrees];

α_r - the linear propagation losses within the cavity [a.u.];

β - angle between absorption and emission dipoles [degrees];

γ - angle defined from normal to layer plane, describing emission inside a layer in non-vertical and non-edge direction [degrees];

γ_0 - angle γ after refraction at the layer surface [degrees];

$\gamma(\lambda)$ - normalized threshold function [a.u.];

$\triangle\lambda$ - spectral width at half maximum [nm];

$\triangle\lambda_{10\%}$ - spectral width at 10% maximum [nm];

$\triangle\lambda_{0.5\%}$ - spectral width at 0.5% maximum [nm];

ε_A - molar absorptivity [cm^2mol^{-1}];

η^* - relative population density of molecules in the excited state [a.u.];

θ_0 - characteristic angle in orientation distribution [degrees];

θ_a - angle describing the orientation of the absorption dipole of a dye in the polymer bulk with respect to the normal to the polymer layer plane [degrees];

θ_e - angle describing the orientation of the emission dipole of a dye in the polymer bulk with respect to the normal to the polymer layer plane [degrees];

κ - factor describing relative orientation of donor and acceptor molecules taking part in FRET [a.u.];

$\overrightarrow{\mu_s}$ - dipole moment of molecular surrounding species [D];

$\overrightarrow{\mu_g}$ - dipole moment of molecule in ground state [D];

$\overrightarrow{\mu_e}$ - dipole moment of molecule in first excited singlet state [D];

ν - photon frequency [Hz];

$\Pi_{e\,\gamma}$ - magnitude of Poynting vector of emission along $\boldsymbol{\gamma}$ axis;

ρ - density of the material [g cm^{-3}];

ρ - ratio of intensities emitted along edge direction under the pump beam polarization oriented respectively along over orthogonally to the emission direction [a.u.];

$\rho(\nu)$ - energy density per unit volume of radiation per unit frequency interval [J s m^{-3}];

σ_a - absorption cross-section [cm^2];

σ_e - emission cross-section [cm^2];

τ_{ASE} - amplified spontaneous emission lifetime [s];

τ_{cav} - photon lifetime in the cavity [s];

τ_f - fluorescence lifetime [s];

τ_r - characteristic time of matrix reorganization [s];

τ_T - triplet-state lifetime [s];

τ_p - pump pulse duration [s];

ϕ - luminescence quantum yield [a.u.];

ϕ_D - quantum yield of degradation [a.u.];

χ_c - critical angle of total internal reflection [degrees];

A - absorbance [a.u.];

$c(wt\%)$ - weight concentration [a.u.];

$\overrightarrow{d_a}$ - absorption transition dipole of the fluorophore;

$\overrightarrow{d_e}$ - emission transition dipole of the fluorophore;

d_H - ratio of I_H components of fluorescence emission, obtained under pump with the orthogonal polarization [a.u.];

d_{min} - cutoff thickness of plane polymer waveguide [cm];

E - efficiency of Förster resonance energy transfer (FRET) [a.u.];

$f(\Omega)$ - orientation distribution [a.u.];

$g(\nu)$ - transition line shape [Hz^{-1}];

g_m - net material gain [cm^{-1}];

g_{mod} - net modal gain [cm^{-1}];

G - set-up-induced depolarization [a.u.];

$G(\lambda)$ - actual gain, the difference between gain and losses [a.u.];

i_p - number of pump photons per unit pumped area per unit time [$cm^{-2}s^{-1}$];

i_e - number of emitted photons per unit pumped area per unit time [$cm^{-2}s^{-1}$];

I_{sat} - pump intensity, which reduces the absorption to half of its small-signal value [MW cm^{-2}];

I_{th} - pump intensity at threshold [MW cm^{-2}];

I_γ - fluorescence intensity along $\boldsymbol{\gamma}$ emission direction [W cm^{-2}];

$I_{||}$, $I_\perp$ - fluorescence intensity components emitted along vertical emission direction and polarized respectively parallel and orthogonal to pump beam polarization [W cm^{-2}];

I_P , I_H - fluorescence intensity components emitted along edge emission direction and polarized respectively in the layer plane or along its thickness [W cm^{-2}];

$I_{P'}$, $I_{H'}$ - fluorescence intensity components emitted along $\boldsymbol{\gamma}$-axis and polarized respectively in the layer plane and orthogonally to$\boldsymbol{\gamma}$ and $I_{P'}$ [W cm^{-2}];

$J(\lambda)$ - overlap integral [cm^2mol^{-1}];

k_{FRET} - FRET rate constant [s^{-1}];

ka - normalized frequency [a.u.];

K - slope of the the linear part of a modal gain change with the pump intensity [cm MW^{-1}];

L - length for a round-trip mode path [cm];

M_{dye} - molar mass of molecules [g mol^{-1}];

M_t - total number of dye molecules in the system [a.u.];

M_0, M_1 - number of dye molecules in the system, being respectively in ground or first excited energy state [a.u.];

n - refractive index [a.u.];

n_{eff} - effective refractive index [a.u.];

N - molecular density [cm^{-3}];

N^* - density of excited molecules [cm^{-3}];

P - polarization ratio [a.u.];

P_a - absorption probability [a.u.];

r - fluorescence anisotropy [a.u.];

$\bar{r}$ - the average distance between fluorophores in the medium [cm];

r_0 - fundamental anisotropy [a.u.];

r_{loss} - overall losses in the resonator cavity (involving both refraction and propagation losses) [a.u.];

P_E - polarization ratio along edge emission direction [a.u.];

P_V - polarization ratio along vertical emission direction [a.u.];

Q - quality factor [a.u.];

R - the Fresnel intensity reflection coefficient [a.u.];

R_0 - Förster radius [cm];

V_f - polymer free volume [a.u.];

w - width of the ribbon micro-cavity [cm].

Chapter 1

Generic properties of dye-doped polymer films

Laser dyes feature remarkable emission properties, such as a high quantum yield, wavelength tunability throughout the whole visible spectral range and the pulsed operation[1] with duration of down to several fs [2]. At the same time laser dyes are most complex light-emitting systems. There are many specific properties that may prove relevant in a specific configuration, and thus must be taken into account towards the a design of devices based on laser dyes.

The present thesis addresses some specific as well as fundamental properties of lasing in dye-doped polymer micro-cavities. This chapter reviews the generic properties of systems which served as basic templates in our work.

The description begins with the photo-physical properties of dyes, and a special place is given to the change of characteristics with their incorporation into polymer matrix.

In order to provide the analysis of stimulated emission, the rate equation of a lasing process will be addressed. A set of equations, describing lasing in dye-containing cavities of a generic configuration, will be derived and discussed in the second part of this chapter.

Finally, special attention is paid to the guiding properties of thin polymer layers.

1.1 Photo-physical properties of laser dyes

In order to provide efficient gain for a system to lase, dye molecules should possess sufficient absorption at the pumping wavelength as well as high stimulated emission rate. The absorption and emission properties of fluorophores are related to the possible electronic transitions in the molecule, their average duration (or lifetime) and probability. Last but not least, the surrounding medium can induce a significant variation on these properties.

The present work exploited several laser dyes and fluorophores. Full description of these dyes, including their chemical structures, usual names etc. are detailed in Appendix C, while in the full thesis text their abbreviations are being used. Naturally we start the description of our lasing system with the analysis of the photo-physical properties of dyes that are being used, as these are factors influence strongly the emission properties.

The photo-physical properties of the laser dyes are addressed in this part in the following order. An overview on the dynamics of excitation and de-excitation

[1] Liquid dye lasers may also operate in CW regime with the aid of specific elements, such as dye jet flow system.

processes in the molecule is given first. Then the absorptive properties are addressed separately through the modulus and the vector nature of transition dipole in relation with the molecular structure. The emission properties are discussed and finally the influence of surroundings (polymer and other dye molecules in the vicinity) is being highlighted.

1.1.1 Timescale of absorption and de-excitation processes

The ensemble of absorption and de-excitation processes (radiative and non-radiative) that may take place in a generic fluorescent molecule are usually visualized by the celebrated Perrin–Jablonski diagram (Figure 1.1)[69, 70]. The fundamental electronic state S_0 is a singlet state, but the excited states (denoted 1, 2 etc.) exist in both singlet (S) and triplet (T) form. An important property of dye molecules is that each energy state is assigned a set of vibrational levels. For instance, the statistical population of molecules at vibrational levels of the S_0 state is given by the Maxwell-Boltzmann distribution [69, 71].

The absorption of a photon can lead to molecular excitation to one of the singlet states (S_1, S_2 etc.), depending on the photon wavelength, polarization and molecular state prior to absorption. The absorption time-scale is assumed very short (1 fs) compared to the nuclei displacement time, and can be thus considered as instantaneous (Born-Oppenheimer approximation).

Table 1.1: *Characteristic times of the processes depicted on Fig.1.1 from [69].*

Process	*Value range*
Absorption	1 fs
Vibrational relaxation	1-100 ps
Fluorescence (τ_f)	0.1-100 ns
Internal conversion (IC)	10-1000 ps
Inter-system crossing (ISC)	0.1-10 ns
Triplet lifetime (τ_T)	1μs-1 s

De-excitation can take place via one of the following mechanisms: fluorescence, inter-system crossing, internal conversion and triplet de-excitation.

The term internal conversion (IC) stands for a non-radiative transition between two electronic states, that have the same ($S_1 \rightarrow S_0$ etc.) spin multiplicity. The efficiency of IC depends on the energy gap between the states involved in the process (a larger gap will decrease the probability, which accounts for the reason why the IC of a $S_2 \rightarrow S_1$ transition is much more efficient compared to the IC of $S_1 \rightarrow S_0$), as well as competition with other de-excitation processes that are possible from the excited level.

A non-radiative transition between two electronic states of different spin multiplicities but vibrational levels of the same energy is referred under inter-system crossing (ISC). This is strictly speaking a forbidden transition, that may however take place when the spin–orbit coupling term is large enough. ISC from the S_1 state results in transition of the dye molecule to the T_1 state. This creates in turn the possibility of photon absorption to a higher triplet state, thus reducing the fluorescence efficiency by decreasing the number of absorbed photons that may contribute to fluorescence. Moreover, a molecular population in the T_1 state can result in activation of photobleaching mechanisms [72], which are extremely detrimental to emission.

As for the emission properties, fluorescence takes place from the S_1 state, while for many fluorescent species de-excitation from the T_1 state is non-radiative (except for phosphorescent ones) and the T_1 state lifetime is very long compared to

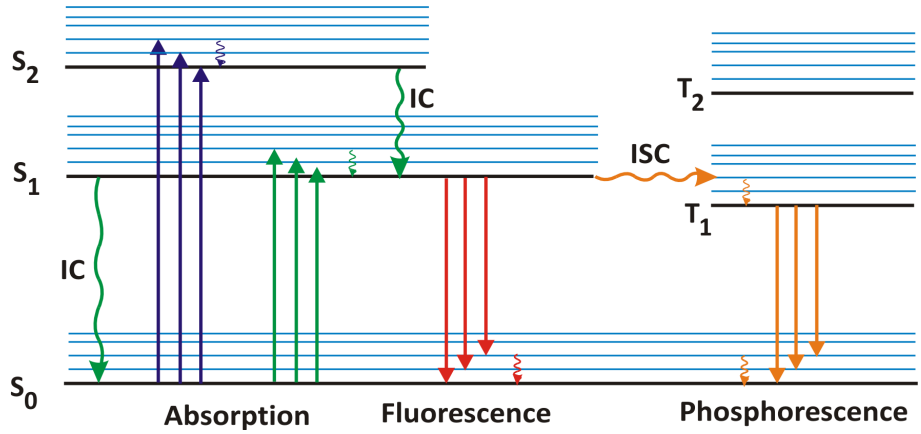

Figure 1.1: *Perrin–Jablonski diagram [69]. IC stands for internal conversion, and ISC - inter-system crossing.*

fluorescence (Tab.1.1). Taking into account the fact, that the population density of molecules in the T_1 state (ISC efficiency) depends on the population density in the S_1 state and is capable to quench the emission, the avalanche of molecular population in the T_1 state is highly undesirable in a lasing system.

For this reason, pulsed pumping is used in solid-state dye-based lasers. [2]Typically used value for pulse duration can reach 10 ns (lower than triplet lifetime) while repetition rate is generally not higher than 10 kHz (the deviations are related to specific properties of used dye). This way the small amount of molecules that have been excited to the T_1 state are given enough have enough time to relax before the onset of the next pumping pulse.

Now that the timescale and basic processes taking part in excitation and de-excitation have been presented, we proceed with the quantitative analysis of absorptive and emitting photo-physical properties.

1.1.2 Absorbance of the investigated dyes

Among the photo-physical properties of dyes, some can be readily defined from standard experiment (for example absorbance and emission spectra), whereas others are demanding rigorous study and detailed determination (absorption and emission cross-section). In fact, the definition of parameters in the second group is always based on those of the first one. For this reason, we start with the description of the basic photo-physical parameters.

This Sub-section recalls the conventional absorbance definitions in literature. Then the absorbance curves, obtained experimentally for dye-doped polymer combinations used in this work are presented and discussed.

All the processes considered herein in fact are non-linear in the dynamical sense. For instance, the absorption of a fluorophore exhibits a linear behavior with the incident power up to some threshold (Fig.1.2.a), and then depending on the molecular properties, saturable absorption (SA) or reverse saturable absorption (RSA) takes place [73].

The linear region of this curve follows the Beer–Lambert–Bouguer law, which states that the transmission of the light intensity (not its amplitude) through a medium (ratio of the output to the input intensity, Fig.1.2.a) can be represented by an exponential dependence on absorbance (the combination of absorption co-

[2]Pulsed pumping is not obligatory for liquid dye lasers, they may operate in CW regime due to addition of triplet state quencher into solution, or dye jet flow systems.

efficient and the length of the light path):

$$T = \frac{I_1}{I_0} = e^{-A} = e^{-\alpha d} \tag{1.1}$$

where d [cm] is either the sample thickness (for measurements in solid films) or the cuvette inner length (for a liquid solution).

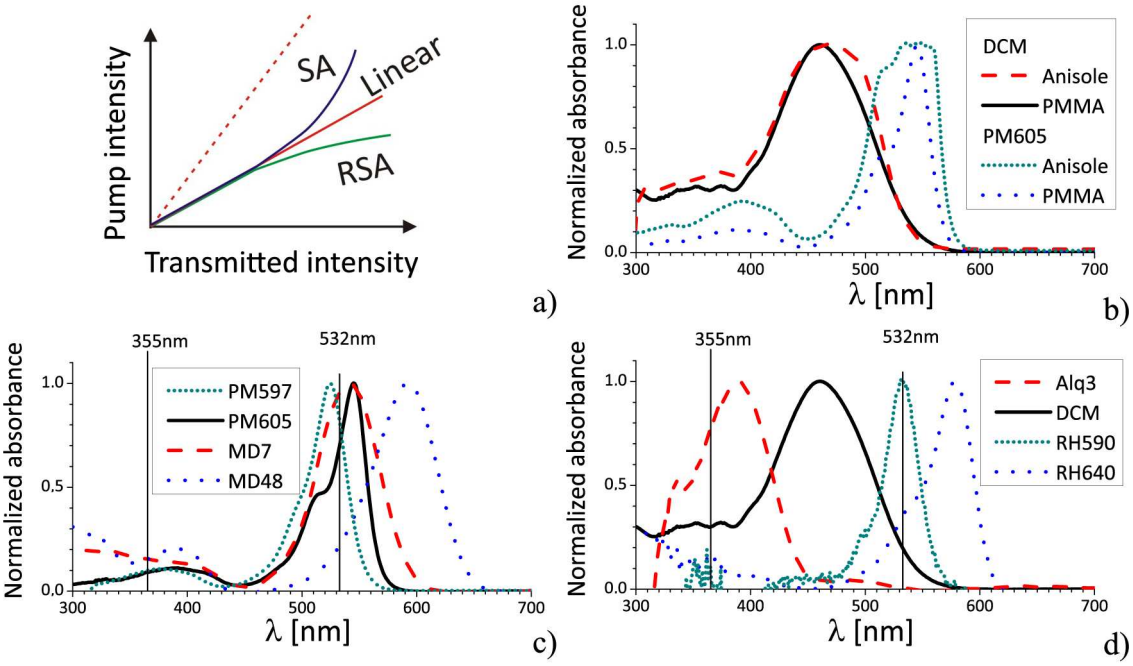

Figure 1.2: *Illustration on some absorption properties of dyes: a) linear and non-linear regimes of absorption (the dashed curve describes the non-absorbed pumping signal). Normalized absorbance of dyes in PMMA (5 wt%): b) DCM, PM605 (the dotted curves show the absorbance of dyes in anisole without PMMA, dye concentration about 1mM/L), c) Pyrromethene-family dyes (PM605, PM597, MD7, MD48); d) Rhodamine dyes (RH640, RH590), Alq_3 and DCM (shown for reference). The change in a concentration of the dye does not influence the normalized curves.*

Due to historical reasons the absorbance definition in chemistry is expressed in terms of $\log_{10}(\frac{I_1}{I_0})$ factor instead of natural logarithm. Attention should then be paid while using the spectrophotometer, as quite often the standard settings on software assume a $\log_{10}$ formula. Moreover the expressions frequently used by different communities, such as absorption cross-section (σ_a $[cm^2]$) in physics and molar absorptivity (ε_A $[mol^{-1}cm^2]$) in chemistry, are derived from absorption coefficients defined in different ways. To avoid the confusion, we will refer all these parameters to the absorbance, defined by Eq.(1.3):

$$\sigma_a = \frac{A}{dN} \tag{1.2}$$

$$\varepsilon_A = \frac{1}{\ln(10)} \frac{A}{dc} \tag{1.3}$$

Here N and c stand respectively for the molecular density $[cm^{-3}]$ and molar concentration $[mol\ cm^{-3}]$ of the absorbing species in the medium (see Appendix C.1.1 for details):

$$c = \frac{c(wt\%)}{c(wt\%)+1}\frac{\rho}{M_{dye}} \tag{1.4}$$

$$N = c(wt\%)\frac{N_A}{M_{dye}}\frac{1}{V_f} \tag{1.5}$$

that are defined from the molar mass of the dye or fluorophore M_{dye}, the polymer free volume V_f (Appendix C.1.1), the Avogadro constant $N_A = 6.022 \cdot 10^{23} mol^{-1}$, the density of the material ρ, which for small concentrations of dye can be assumed to be that of the polymer ($\rho(PMMA) = 1.19\, g\, cm^{-3}$), and the mass concentration of dye $c(wt\%)$ (the *wt%* stands stands for *weight %*).

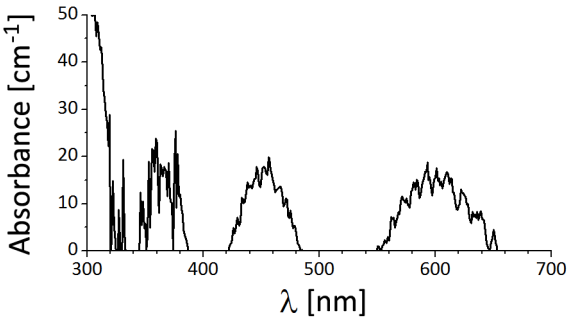

Figure 1.3: *Absorbance of non-doped PMMA (for reference, the peak absorbance of a 5 wt% dye-doped PMMA is of the order of 10^2-$10^4\, cm^{-1}$).*

Some absorption spectra are plotted on Fig.1.2. They were measured on a spectrophotometer from a 5 wt% dye-doped PMMA film deposited over a glass substrate. An identical glass substrate was used as the reference. The absorbency of the non-doped PMMA layer was measured separately (Fig.1.3), and then used for the correction of the dye-doped absorbance curves (although its influence is negligible). To facilitate the visualization, the experimental data are plotted in a normalized way, while the exact values (maximum and values at the pumping wavelengths) are refered to the Appendix C (Table C.2). A quick glance on the normalized absorbance curves (Fig. 1.2.c, d) makes it clear that for the optimal usage of dyes, the pumping wavelength should be adjusted so as to allow for the excitation of the dye at its absorption peak. In this respect, the standard 532 nm excitation that we use is close to optimal for such dyes as PM605, PM597, MD7 and RH590, but meets a red-absorption edge excitation for DCM, and a blue-edge one for RH640 and MD48.

As is well known, the shape and a spectral location of the dye absorption curve depends on its surroundings, such as the solvent nature and concentration [74] or the polymer matrix [77]. The effect is generally explained via the solvatochromic properties of the dye (Sub-section 1.1.7). Experimental graphs on the absorption of DCM and PM605 in anisole, plotted on Fig.1.2.b together with those in a PMMA matrix, confirm the relevance of this effect in our case. The absorption curve in the solvent is wider compared to the one in PMMA, and in the case of DCM, its maximum is clearly red-shifted. The analysis of the mechanisms that can lead to such effect is made in Sub-section 1.1.7. Such experimental results underline the importance of measuring precisely the absorption of the system that is going to be used for the study.

The concentration of the dye in the prepared polymer-solvent solution may not correspond to the one obtained in the polymer film, due to solution filtering and evaporation, in particular during spin-coating. We therefore assume the final

concentration to be a bit lower than the targeted one, and so the estimation of the absorption cross-section values may appear somewhat rough. The observed deviation of molar absorptivity in different samples made from the same solution is nevertheless less then 6%. Taking into account an inaccuracy in the definition of absorption cross-section from the absorption spectrum, it is advisable to operate with absorbance per unit film thickness. This parameter can be used for the inverse problem: estimation of the density of molecules in bulk. For reference, the values of absorbance per unit thickness are given in Tab.C.2 (in Appendix C).

The influence of pulse duration on the absorptive properties of the dyes was verified and no noticeable difference was seen between the cases of stationary and up to 500 ps pumping.

In summary, we determined the absorbance properties of all the dyes used in the thesis, and verified that a pumping source at 532 nm can be applied for the excitation of our system, however with an efficiency varying with the dye molecules.

1.1.3 Fluorescence spectra

The fluorescence spectra contain the information on several important properties of the dye emission: the exact spectral region of emission and the distance between peaks of absorption and fluorescence spectra, which underly the efficiency of radiative de-excitation, re-absorption and resonance energy transfer between molecules of the same type (Section 1.1.6). The experimental fluorescence spectra are discussed in this Sub-section.

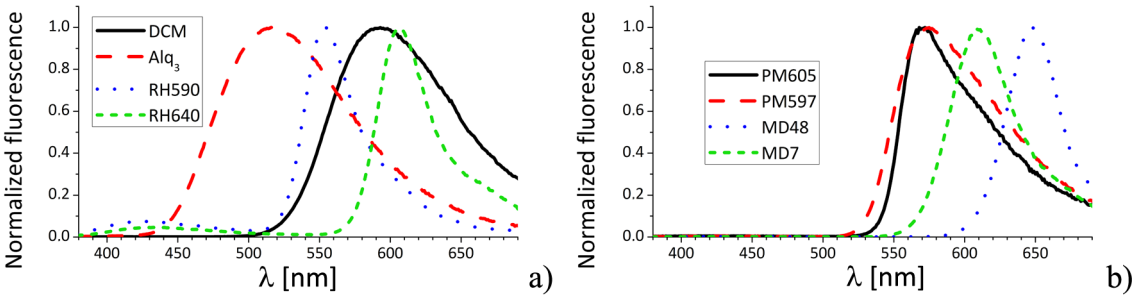

Figure 1.4: *Fluorescence spectra of thin PMMA layers (about 600nm), doped by various dyes: a) DCM, Alq_3, RH590, RH640; b) Bodipy-family dyes: PM597, PM605, MD7, MD48.*

The data presented here were obtained with a Fluorolog FL3-221 Horiba Jobin-Yvon spectrofluorimeter (Sub-section 2.3.3) on thin dye-doped polymer layers spin-coated on a glass substrate. The fluorescence spectra are plotted on Fig.1.4.

The distance between maximum wavelength of fluorescence and absorption spectra, known in the literature as the Stokes shift (generally given in cm^{-1}) is deduced for each dye and presented in Tab.1.2.

Table 1.2: *Comparison of the absorbing properties of the investigated dyes and Alq_3 (λ_F stands for the wavelength at the maximum of fluorescence spectrum and $\Delta\nu_{ST}$ for Stokes shift).*

Molecule	λ_F[nm]	$\Delta\nu_{ST}$ [cm^{-1}]	*Molecule*	λ_F[nm]	$\Delta\nu_{ST}$ [cm^{-1}]
DCM	592	$4.8{\cdot}10^3$	RH640	607	$8.26{\cdot}10^2$
PM605	570	$8.05{\cdot}10^2$	RH590	554	$7.8{\cdot}10^2$
PM597	574	$1.63{\cdot}10^3$	Alq_3	517	$6.36{\cdot}10^3$
MD7	610	$2.06{\cdot}10^3$	MD48	647	$1.41{\cdot}10^3$

Alq_3 molecule is a classical fluorophore, however unable to provide stimulated emission.

The efficiency of fluorescence emission is generally accounted for by its quantum yield. The Rhodamine family dyes are expected to be the most efficient among the laser dyes available in our study, as they are known to feature a high quantum yield (about 0.8, Tab.C.1 in Appendix C). However, these dyes exhibit the smallest Stokes-shift, as seen in Tab.1.2. In case of stimulated emission, a small Stokes-shift sets a serious re-absorption problem (will be discussed in Chapter 4), resulting in substantial decrease of the efficiency of the lasing system.

Thereby, the efficiency of the stimulated emission process depends both on quantum yield and Stokes-shift. These parameters also depend on the surroundings (as will be precised in Sub-section 1.1.7) and should be studied in a polymer matrix, in consistence with further studies of stimulated emission.

1.1.4 Absorption and emission cross-sections

The direct experimental definition of absorption and emission cross-sections are rather involved. An unknown number of doped dye molecules degrade over the polymerization process. Thereby the definition of the dye density per unit of sample volume, proposed in Exp.(1.5), is at best approximate. The proper determination of N is complex and delicate, demanding the dissolution of the dye-doped polymer after measurements to perform reference absorption measurements in a solvent [78]. Moreover, the estimation of absorption cross-section from spectrometer measurements in liquid solution is correct only for the region close to the maximum of absorption. The vibrational levels of the ground state are thermally populated in solution. And so thermally excited molecules contribute to the absorption in long-wavelength region, and spectrometer measurement is no more reliable [79].

We chose another way to define the absorption cross-section value, that is its derivation from the emission cross-section of dye. This latter value can be determined from the fluorescence spectrum, and other parameters such as the quantum yield and the fluorescence lifetime. Emission cross-section can be also measured directly with femtosecond UV-visible transient absorption spectroscopy [80]. In any case, a reliable expression should be used for the deduction of absorption cross-section.

There are different formulas cited in literature for the estimation of the absorption and emission cross-sections. Developed for an atomic oscillator to describe the processes of light-matter interaction in semiconductors and rare-earth elements, those are generally inconsistent with more complex emitters such as dye molecules.

To clear these issues, we derive the expressions from the equilibrium of absorption and emission events at thermal equilibrium.

The famous Einstein relations between spontaneous emission A_{21}, stimulated emission B_{21} and absorption rate B_{12} (all defined per unit frequency interval) are [81]:

$$\begin{aligned} g_1 B_{12} &= g_2 B_{21} \\ A_{21} &= 8\pi h\nu \frac{\nu^2}{(c/n)^3} B_{21} \end{aligned} \tag{1.6}$$

here n stands for the refractive index of the medium.

Equations (1.6) were derived for a 2-level atomic system from the steady-state condition of an equal number of absorption and emission events per unit of time

(g_i - is a degeneracy of E_i energy level, M_i is a number of atoms in the i energy state, with $i = 1, 2$) [82, 81]. Then, the total population $M_1 + M_2$ being constant over time:

$$\frac{\partial M_1}{\partial t} = -\frac{\partial M_2}{\partial t} = - M_2 A_{21} - M_2 \rho B_{21} + M_1 \rho B_{12} = 0 \tag{1.7}$$

Here $\rho(\nu)$ is the energy density per unit volume of radiation per unit frequency interval, defined at thermal equilibrium by the Plank black-body radiation law [82, 81]:

$$\rho(\nu) = \frac{8\pi h\nu^3}{(c/n)^3} \frac{1}{exp(h\nu/kT) - 1} \tag{1.8}$$

The relative populations of the two energy levels in a system with a large number of similar atoms, at thermal equilibrium at temperature T, are given by the Boltzmann ratio [82, 81]:

$$\frac{M_2}{M_1} = exp(-(E_2 - E_1)/kT) \tag{1.9}$$

The absorption and emission cross sections can then be expressed in terms of the Einstein coefficients in the following way:

$$\begin{aligned} \sigma_e &= \frac{A_{21}\lambda^2}{8\pi c n^2} \\ \sigma_a &= \sigma_E \frac{g_2}{g_1} \end{aligned} \tag{1.10}$$

For the reasons described just below, the validity of Eq.(1.10) for an assembly of dye molecules is questionable and so we will try to find a more adequate definition.

The Eq.(1.10) is valid for isolated atomic systems. The analysis, straightforward in the case of isolated two-level system, complicates dealing with condensed media with emitting impurities, such as rare-earth elements. One must consider two metastable energy levels, each of them consisting of a large manifold of sub-levels. This time, thermal occupancy of each sub-level then must be taken into account [83]. In first order approximation, this effect can be explained with the transition line-shape term $g(\nu)$, which describes the distribution of molecules on the vibrational manifold of excited state [82, 81]:

$$\begin{aligned} n_2(\nu) &= n_2 g(\nu) \\ \int g(\nu)\, d\nu &= 1 \end{aligned} \tag{1.11}$$

The absorption and emission cross sections in this case can be deduced from the Fuchtbauer-Ladenberg equations [84]:

$$\begin{aligned} \sigma_e &= \frac{A_{21}\lambda^2}{8\pi c n^2} g(\nu) \\ \sigma_a &= \sigma_E \frac{g_2}{g_1} \end{aligned} \tag{1.12}$$

Still, organic dye molecules are not amenable to equations (1.12), as absorption and emission take place at different wavelengths (absorption and emission spectra being Stokes-shifted). Two transition line-shapes should be considered: $g_a(\nu)$ and $g_e(\nu)$, which respectively describe absorption and emission. Then the population rate equation (1.7) changes into (inspired by [84, 81]):

$$\frac{\partial M_1}{\partial t} = B_{21}\rho(\nu_e)\, g_e(\nu_e)\, M_2 d\nu - B_{12}\rho(\nu_a)\, g_a(\nu_a)\, M_1 d\nu + A_{21} g_e(\nu_e)\, M_2 d\nu \quad (1.13)$$

It is convenient to work with entities like population densities N (cm^{-3}), which can be easily achieved by dividing both sides of the equation by the medium volume V. The net change of the density of molecules in the excited state corresponds to the $\rho(\nu)d\nu$ differential energy per photon. Thus Eq.(1.13) can be modified as follows:

$$\frac{\partial}{\partial t}\left(\frac{\rho(\nu)}{h\nu}d\nu\right) = B_{21}\rho(\nu_e)\, g_e(\nu_e)\, N_2 d\nu - B_{12}\rho(\nu_a)\, g_a(\nu_a)\, N_1 d\nu + A_{21} g_e(\nu_e)\, N_2 d\nu \quad (1.14)$$

As the absorption and emission takes place at different frequencies (or wavelengths), it is natural to consider separately the flux of absorbed and emitted photons:

$$\begin{aligned} \frac{\partial \rho(\nu_a)}{\partial t} &= -h\nu_a B_{12}\rho(\nu_a)\, g_a(\nu_a)\, N_1 \\ \frac{\partial \rho(\nu_e)}{\partial t} &= \phi h\nu_e B_{21}\rho(\nu_e)\, g_e(\nu_e)\, N_2 + \phi A_{21} g_e(\nu_e)\, N_2 \end{aligned} \quad (1.15)$$

The fluorescence quantum yield (ϕ) which appears in the second equation, specifies that the emission of the photon is not the only de-excitation process possible in the system. Indeed, for the sake of simplicity, spontaneous emission will be further neglected ($A_{21} = 0$).

The next step in the evaluation of σ_a and σ_e is the change of differentiation variable from time t to space x. The differential time dt characterizes the period during which the electromagnetic wave travels trough a differential material thickness dx with refractive index n, and so $dt = ndx/c$. Now straightforward integration of the equations (1.15) leads to the following expressions that can be described in terms of absorption and emission cross-sections:

$$\begin{aligned} \ln\left(\frac{\rho(\nu_a)}{\rho_0(\nu_a)}\right) &= -h\nu_a B_{12} g_a(\nu_a)\, N_1 n\frac{\mathrm{x}}{c} \equiv -\sigma_a \mathrm{N_1 x} \\ \ln\left(\frac{\rho(\nu_e)}{\rho_0(\nu_e)}\right) &= \phi h\nu_e B_{21} g_e(\nu_e)\, N_2 n\frac{\mathrm{x}}{c} \equiv \sigma_e \mathrm{N_2 x} \end{aligned} \quad (1.16)$$

The cross-sections can then be defined from:

$$\begin{aligned} \sigma_a &= h\nu_a B_{12} g_a(\nu_a)\frac{n}{c} \\ \sigma_e &= \phi h\nu_e B_{21} g_e(\nu_e)\frac{\mathrm{n}}{c} \end{aligned} \quad (1.17)$$

Then relation between the Einstein coefficients in Eq.(1.6) is only valid for a two-level system. More correct expressions, derived for an atomic system incorporated

in dielectric bulk [83, 85], are not applicable to laser dyes. In the present estimation we analyzed the ensemble of dye molecules as a two-level system, accounting for their breaking down into vibrational manifolds by the transition lineshapes $g_a(\nu)$ and $g_e(\nu)$. The Einstein coefficients can then be taken as the total probabilities of the transitions between two manifolds, which effectively amounts to a two-level system. This allows to use Eq.(1.6) to complete our calculations.

The absorption cross-section can be presented trough the emission cross-section, which in turn can be defined by some measurable parameters (taking into account the relation between A and B Eq.(1.6)):

$$\begin{aligned} \frac{\sigma_a}{\sigma_e} &= \frac{\nu_a}{\phi\nu_e}\frac{g_a(\nu_a)}{g_e(\nu_e)} \\ \sigma_e &= \frac{\lambda^2}{8\pi n^2 c}\phi A_{21} g_e(\nu) \end{aligned} \tag{1.18}$$

The first equation represents the relation between both coefficients. The comparison of the cross-sections at the wavelength of the maximum of each curve allows to define a scaling factor:

$$\frac{\sigma_a^{max}}{\sigma_e^{max}} = \frac{1}{\phi}\frac{\lambda_e}{\lambda_a} \tag{1.19}$$

This equation is identical to the one mentioned in the literature [86], except for the presence of the quantum yield ϕ. The physical meaning of the equal ratios of peak emission cross-sections and their peak frequencies is explained in Ref.[86] by the very close values of the transition matrix element for the absorption and emission. The important conclusion that comes from our expression (1.19) is that maximum of the absorption cross-section curve of an organic dye is *always higher* than its maximum emission cross-section.

As for the second equation in Eq.(1.18), it is similar (except for the quantum yield) to the definition of the emission cross-section used for rare-earth elements [87]. A_{21} is usually presented via the fluorescence lifetime as τ_f^{-1}. The emission line-shape $g_e(\nu)$ can be expressed in terms of wavelength: $g(\lambda) = g(\nu)\frac{c}{\lambda^2}$ (derived from the condition $\int g(\nu)d\nu = \int g(\lambda)d\lambda$). And the curve itself originates from the fluorescence spectrum: $g_e(\lambda) = \frac{f(\lambda)}{\int f(\lambda)d\lambda}$.

Finally the expression for the emission cross-section of dye molecules is:

$$\sigma_e = \frac{\phi\lambda^4}{8\pi n^2 c\tau}\frac{f(\lambda)}{\int f(\lambda)d\lambda} \tag{1.20}$$

It is identical to the expression for dyes reported in [86], and abides to a full quantum-mechanical derivation as in [88].

The estimation we provided in this Sub-section is rather approximate. Their scope was to provide the expression on absorption and emission cross-section that would contain measurable parameters. Still the results appear to be in good correspondence with those provided by quantum-mechanical considerations.

1.1.5 Vectorial nature of the absorption and emission properties of dye

The absorption and emission properties of a single dye molecule depend strongly on the orientation of the pumping beam polarization with respect to the molecular structure, thus exhibiting a vectorial nature. The theoretical basis of this issue

is addressed in this part. Its application to our used dyes is explained on the orientation of their absorption transition dipoles from quantum computations.

The fluorophores are generally represented by absorption and emission dipoles [89, 69, 70]. The efficiency of the absorption process thus depends on the respective orientation of the polarization of an incident photon with the absorption dipole of the molecule. The orientation of such an absorptive transition as well as its oscillator strength related magnitude depend strongly on the incident photon wavelength.

The absorption dipole is defined in quantum terms following vectorial matrix element (see p.434 of ref.[90]):

$$\vec{d_a}(f \to e) =< \psi_f \,|\, \hat{\vec{d}} \,|\, \psi_e > \tag{1.21}$$

where ψ_f and ψ_e are the stationary wavefunctions of the ground and excited states, and $\hat{\vec{d}}$ is a vector operator that is the sum of the position vectors of all charged particles weighted with their charge. Absorption is a fast process: the position of the nucleus are thus assumed to be fixed, and it is only the electronic part of the wavefunctions which changes between ψ_f and ψ_e. Laser dyes are often planar aromatic molecules and the $S_0 \rightarrow S_1$ transition corresponds to the transfer of a single electron from a π to a $\pi^\star$ orbital. These orbitals are both antisymmetrical with respect to the molecular plane, so that the integral (1.21) along the direction perpendicular to this plane is zero, since the global function to integrate is odd. Hence $\vec{d_a}(0 \to 1)$ lies in the plane of the molecule. If the dye is pumped onto its S_2 state, the excited wavefunction involves in general a $\pi^\star$ orbital as well, and $\vec{d_a}(0 \to 2)$ remains in the plane of the molecule. However the profile of the $\pi^\star$ orbitals in the plane are different, and thus their corresponding $\vec{d_a}$ are not parallel.

The definition of the emission dipole is similar to Eq.(1.21), except for ψ_e. Usually the upper state from which fluorescence starts being red-shifted with respect to ψ_e. Strictly speaking, the emission dipole is hence different from the absorption dipole of the same transition. However the rearrangement in the S_1 state is in general not very large and the angle β between the dipoles remains close to zero.

We used Gaussian From Gaussian© computations (conducted by Gilles Clavier, PPSM) to examine the above mentioned properties of the absorption dipoles of the dyes used in this study. Such a simulation allows to define the orientation of the absorption dipole with respect to the molecular skeleton (defined by Descartes coordinates), as shown on Fig.1.5. Details on the simulated dipoles (coordinates, oscillator strength and wavelength) are summarized in Tab.C.5 (Appendix C). The calculations are based on the assumption of an isolated molecule (in vacuum), which leaves to some discrepancy between the calculated wavelength and the real absorption spectrum.

When excited to a S_n state, the system first relaxes to S_1, from which emission can then take place. Thus the orientation of the emission dipole of a laser dye is fixed. In the general case, the absorption dipoles to the S_1 and S_2 states and the corresponding emission dipoles are not coplanar, as depicted on Fig.1.6, except for rather rare case of molecules with 2-D skeleton (such as DCM). So the angle between $\vec{d_a}(0 \to 1)$ and $\vec{d_a}(0 \to 2)$ is not equal to the difference $\beta_2 - \beta_1$.

The $S_0 \rightarrow S_1$ and $S_0 \rightarrow S_2$ absorption moments of the planar DCM molecule (Fig.1.5.a) are oriented at about 50° with respect to each other (Tab.C.5). Their value is comparable with that found in the literature, e.g. of the order of 65° [91] (obtained experimentally for pumping at 450 and 340 nm correspondingly).

The variation of the pumping wavelength can cause a drastic change on the orientation of the absorption dipole, and thus of the angle between absorption and

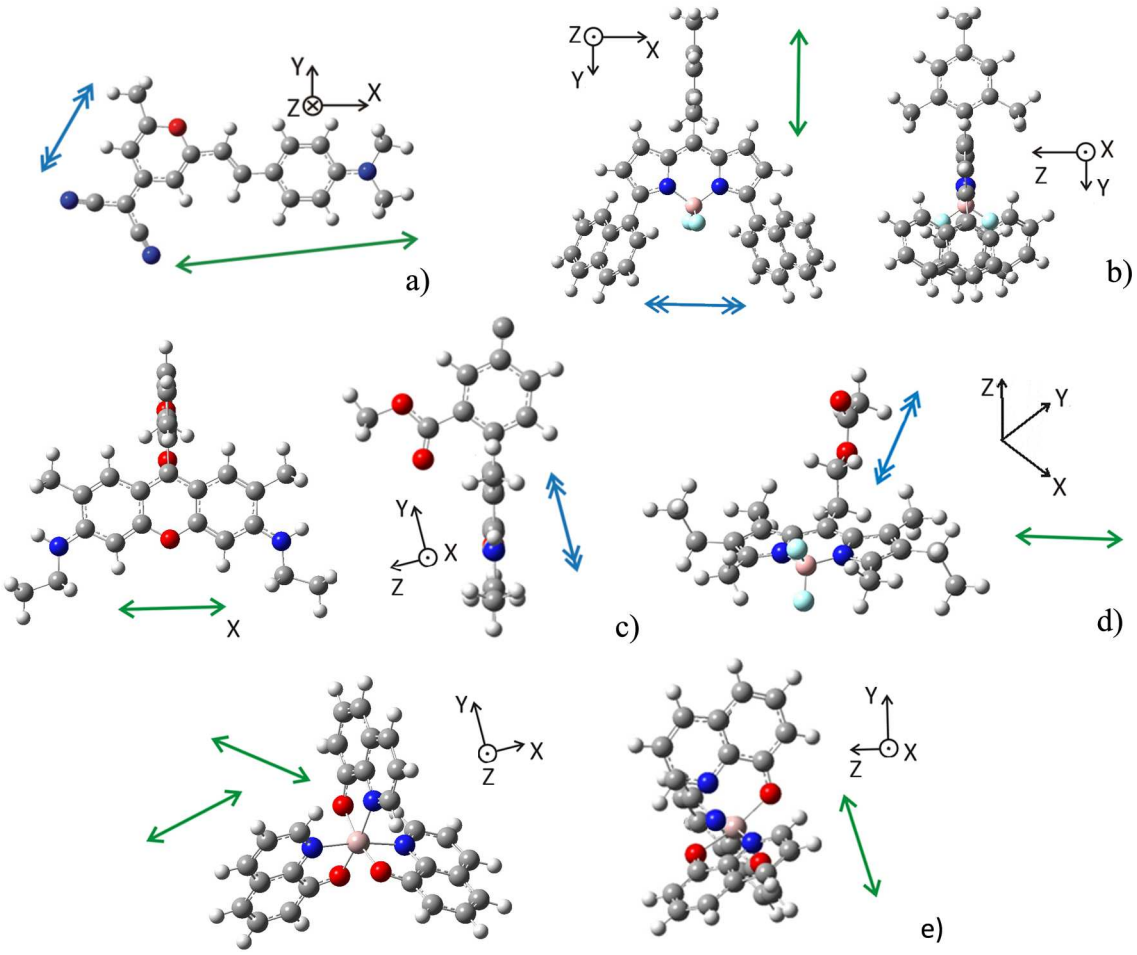

Figure 1.5: *Absorption dipoles within the coordinate system of a molecule(the absorption dipole moments are indicated with a single green arrow for the $S_0 \rightarrow S_1$ transition and with a double blue arrow for the $S_0 \rightarrow S_2$ transition): a) DCM, b) MD7; c) RH590; d) PM605; e) Alq_3.*

emission dipoles (Chapter 3).

The RH640 and RH590 (Fig.1.5.c) molecules display almost identical orientation of their absorption dipoles with respect to their molecular structure: $S_0 \rightarrow S_1$ absorption lays in the planar part of the molecule, while $S_0 \rightarrow S_2$ lays orthogonally to it along the tail.

Although the MD7 molecule has a clear 3-D skeleton, its absorption dipoles are oriented in its main plane (Fig.1.5.b). MD7 exhibited the highest photo-stability among other laser dyes in the present work (as detailed in Sub-section 4.2.5), and it is possible that orientations of absorption and emission dipoles contribute to this property.

The PM605 dye (Fig.1.5.d) has two $S_0 \rightarrow S_2$ dipoles, one of which is very close

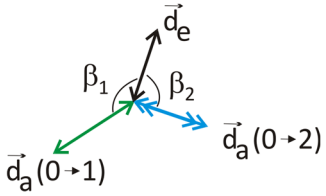

Figure 1.6: *Schema of the respective orientations of the absorption dipoles of $S_0 \rightarrow S_1$ transition and $S_0 \rightarrow S_2$ transition and the emission dipole of the laser dye molecule.*

to $S_0 \rightarrow S_1$ and lays within the planar part of the molecule, and another as in the case of RH590 - along the tail.

Alq_3 possesses 3 absorption moments (UV pumping, which correspond to $S_0 \rightarrow S_1$ for this fluorophore), and they are oriented at the angles 45, 90, 135° with respect to each other due to high symmetry.

The presented simulations aimed to predict the properties of fluorescence anisotropy (Chapter 3) in our used dyes, that will be addressed in Chapters 3 and 4. Although for the majority of dyes, the analysis is inconsistent without an evaluation of the emission dipole orientation, the obtained results still provided us with an insight on the molecular properties, and allowed a quantitative comparison with experiment in the case of the DCM molecule.

1.1.6 Förster resonance energy transfer

Among all the possible interactions between two fluorescent molecules, the non-radiative transfer of excitation energy plays an important role. The generic name for this effect is resonance energy transfer (RET) and there exists several mechanisms that can lead to it. In this part we make a short analysis of the RET process that can take place in the systems we study.

Förster resonance energy transfer (FRET), named after the German scientist Theodor Förster, stands for one of the RET types, when the excitation of the donor molecule is transferred to the acceptor molecule by means of a Coulombic interaction (long range dipole-dipole interaction). FRET's are known to work for energy transfer between singlet states only [69, 92].

FRET corresponds to a very weak coupling regime of the interaction between molecules, so that the donor-acceptor pair do not form a real exciton. As vibrational relaxation precedes energy transfer, the absorption spectra are not modified (in contrast to strongly coupled excitons). It appears impossible to detect the presence of FRET by direct spectroscopy studies. The emission dynamics and polarization should then be addressed.

The efficiency of the FRET process is defined as the fraction of photons which are transferred to the acceptor over all the photons absorbed by the donor:

$$E = \frac{k_{FRET}}{k_D + k_{FRET}} \tag{1.22}$$

where k_D is the rate of deactivation from the excited state (all the de-excitation processes) of donor alone in the absence of any energy transfer channels and k_{FRET} stands for the FRET rate constant.

We consider the field, which surrounds an classical oscillating electric dipole $\overrightarrow{p_D}$. It results from the emission dipole of the donor molecule and is given by [92]:

$$\overrightarrow{E_D}(\overrightarrow{r}) = \frac{1}{|\overrightarrow{r}|^3}\left(\frac{3(\overrightarrow{p_D}\cdot\overrightarrow{r})\overrightarrow{r}}{|\overrightarrow{r}|^2} - \overrightarrow{p_D}\right) \tag{1.23}$$

where $\overrightarrow{r}$ connects the dipole to the observation point.

FRET can be described in terms of dipole-dipole interaction between donor and acceptor, laying at a distance r from each other. The rate constant of FRET is proportional to the squared interaction energy between both dipoles [92]:

$$k_{FRET} \propto \left(\overrightarrow{E_D}(\overrightarrow{r})\cdot\overrightarrow{p_A}\right)^2 = \frac{|\overrightarrow{p_D}|^2\,|\overrightarrow{p_A}|^2}{r^6}\kappa^2 \tag{1.24}$$

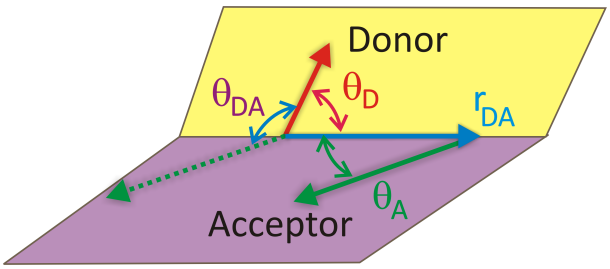

Figure 1.7: *On κ^2 calculations: θ_{DA} is the angle between the emission dipole of the donor and the absorption dipole of the acceptor, θ_D and θ_A are the angles between these moments and the vector r_{DA} joining the donor and the acceptor.*

The expression on the right hand side of Eq.(1.24) is nothing but compact representation of the scalar product on its left hand side, which allows to separate the magnitude (r, $|\overrightarrow{p_D}|$, $|\overrightarrow{p_A}|$) and angular properties (κ). Parameter κ is used for description of the relative orientation of donor and acceptor dipoles and is obtained by deriving Eq.(1.24) from Eq.(1.23) (the angles θ_{DA}, θ_D and θ_A are depicted on Fig.1.7):

$$\kappa = \cos\theta_{DA} - 3\cos\theta_D \cos\theta_A \tag{1.25}$$

So that κ^2 varies within range [0, 4]. In fact, this parameter depends not only on the respective orientation of the two dipoles involved, but on their positions in space as well. For instance if the two dipoles are collinear (angle between the two planes depicted on Fig.1.7 equals zero and $(\theta_D + \theta_A) = \pi$) and lay on the same line ($\theta_D = 0$; $\theta_A = \pi$) $\kappa^2 = 4$, but if they are next to each other ($\theta_D = \theta_A = \pi/2$) $\kappa^2 = 1$.

In reality different possible orientations of dipoles should be taken into account and thus the κ^2 parameter should be averaged over the ensemble of molecules. In the general case such integration should also account for the variation of the distance between the pair molecules Eq.(1.24), and so the factor $1/\left(r_{DA}/\overline{r}_{DA}\right)^6$ should appear in κ^2. However the latter complicates seriously the calculations, and the κ^2 values found in literature (for instance, values provided in a following paragraph) are generally obtained while neglecting the variation of the distance between molecules.

If during the excited state lifetime of the donor the orientations of the donor and acceptor randomize by rotational diffusion, then $\kappa^2 = 2/3$. Meanwhile, in the case of static but random donor–acceptor orientations during the lifetime of the excited state (as should be for solid state matrix) $\kappa^2 = 0.476$ [70].

The generally used expression for FRET rate constant is [69, 70, 92]:

$$k_{FRET} = k_D \left(\frac{R_0}{r}\right)^6 \tag{1.26}$$

$$E = \frac{1}{1 + \left(\frac{r}{R_0}\right)^6} \tag{1.27}$$

Here R_0, commonly referred as the Förster radius, is a distance at which the FRET fluorescence becomes equally probable to ordinary fluorescence by a donor molecule (R_0 values for studied dyes are reported in Appendix C). Its expression is given by:

$$R_0^6 = \frac{9000 \ln(10) \kappa^2 \phi_D}{128 \pi^5 N_A n^4} J(\lambda) \tag{1.28}$$

where the overlap integral J is:

$$J(\lambda) = \frac{\int_0^\infty F_D(\lambda) \varepsilon_A(\lambda) \lambda^4 d\lambda}{\int_0^\infty F_D(\lambda) d\lambda} \tag{1.29}$$

The Förster radius is seen to depend on the *photo-physical properties* of the donor-acceptor molecules as well as the *respective orientation* of their emission and absorption transition dipoles (κ). ϕ_D is the fluorescence quantum yield of the donor in the absence of energy transfer, n is an average refractive index of the medium in the wavelength region where the spectral overlap is significant, $F_D(\lambda)$ the fluorescence spectrum of donor (normalized to its integral in the overlap integral expression), the molar absorption coefficient of the acceptor $\varepsilon_A(\lambda)$ (in [cm^{-1} mol^{-1}]), N_A the Avogadro constant.

The name FRET is generally used to describe the energy transfer between different species. The term homo-FRET is used when the process takes place between molecules of the same type.

The r value can be estimated from the density of dyes in the polymer layer given in Eq.(1.5) as $\bar{r}^3 = N^{-1}$:

$$\bar{r} = \left(c(wt\%) \frac{N_A}{M_{dye}} \frac{1}{V_f} \right)^{-1/3} \tag{1.30}$$

It should be noticed, that small variations of the parameters ϕ_D, $J(\lambda)$ and κ do not introduce significant change of the Förster radius value, due to slow variation of the $x^{\frac{1}{6}}$ functional power law. For example, the increase of the quantum yield by a factor of 2 modifies R_0 by only about 12%.

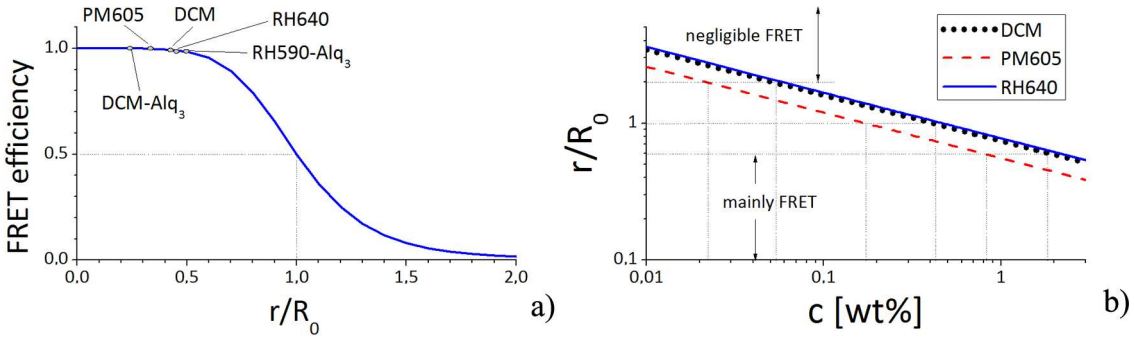

Figure 1.8: *FRET efficiency for examined dyes: a) FRET efficiency as function of distance between molecules (Eq.(1.27,1.28,1.30)), here points indicate the value of FRET for dyes taken at 5 wt% concentration in PMMA; b) normalized distance between molecules in the film as function of dye concentration. The homo-FRET (between molecules of the same type) are calculated for PM605, DCM and RH640, while in a case of the combination RH590-Alq3, the FRET takes place from Alq3 to RH590.*

FRETs calculated for the examined dyes The experimental study on photo-physical properties of used dyes, presented in the previous Sub-sections were used to estimate the Förster radius from Eq.(1.28) and the average distance between molecules from Eq.(1.30). Then the FRET efficiency was found from Eq.(1.27) and plotted on Fig.1.8.a. The influence of the dye mass concentration on the average distance between molecules is depicted on Fig.1.8.b.

For all used commercial dyes, a concentration of 5 wt% provides a FRET efficiency of the order of E = 1 (Tab.C.7, Fig.1.8.a), which means that FRETs play a very important role in the emission features.

The influence of the dye concentration can be estimated from the r/R_0 ratio, as depicted on Fig.1.8.b. If $r/R_0 = 1$, the FRET efficiency is 50% (as shown on Fig.1.8.a), and at a r/R_0ratio of 2, efficiency goes down to 1.5%. In fact even at dye concentration of about 0.5-1% FRET efficiency is still quite high: 50% at 0.41 wt% concentration of DCM or RH640, and at 0.3 wt% concentration of PM605. Further lowering of the dye concentration reduces FRET to 1.5% at 0.035 wt% of PM605 and 0.05 wt% of DCM or RH640. These estimations are in good agreement with experimental results on the DCM dye as reported in [93], where the influence of FRET was still noticeable at a concentration of 0.83 wt%, but vanished for 0.4%. We also performed an experimental study of the influence of dye concentration on FRET, which will be discussed in Chapter 3.

FRET plays a non-negligible role in the fluorescence emission of our examined systems. The standard dye mass concentration in polymer micro-lasers, examined in this work, was 5 wt% The FRET efficiency at this concentration level equals to 1 for all the dyes used in the study, accounting for the overall fluorescence emission. A more thorough analysis of the FRET process in dye-doped thin polymer films, as well as its experimental exploration are presented in Chapter 3.

1.1.7 Influence of the molecular environment

The surroundings can provide a non-negligible impact on the absorption and emission spectral properties of a fluorescing molecule [70, 69]. In case of fluorescence emission, three important processes can interfere: solvatochromism shifts, the red edge absorption effect and the Weber effect. All three processes are outlined in this Sub-section, followed by analysis of experimental absorption and emission spectra in this respect.

Solvatochromism A fluorescent molecule in the ground state displays in general a non-zero dipole moment ($\overrightarrow{\mu_g}$). In the absence of absorption and emission processes the dye molecule is in the equilibrium with its surroundings (characterized by a dipole moment $\overrightarrow{\mu_s}$, depending either on the solvent polarity or on its polarizability in the presence of the dye. For instance PMMA displays $\mu_s = 1.6$ D [77] and anisole $\mu_s = 1.25$ D [94]). The absorption of a photon is a very fast process (1 fs) compared to the nuclei motion, but entails the displacement of electrons, thus causing an almost instantaneous change of the dipole moment of the molecule to $\overrightarrow{\mu_e}$. For instance, the DCM molecule is known to have $\mu_g = 6.1$ D and $\mu_e = 26.3$ D [74]. Upon the excitation and quasi-immediate subsequent changes of the molecular dipole moment almost instantaneously, the surrounding reorganizes itself so as to relax to a state with a minimal free energy[3].

The presence of a possible solvatochromic shift of the fluorescence spectrum depends on the ratio of the characteristic time of reorganization (τ_r) over the fluorescence lifetime (τ_f) :

[3]The reorientation processes, discussed in literature, concerns the solvent only

- $\tau_r < \tau_f$: the reorganization process is then more rapid than the emission and the system has enough time to relax before the onset of the emission, the emitted photon has then a lower energy and thus a red shift is observed in the emission, as depicted on Fig.1.9.b;
- $\tau_r > \tau_f$: the emission starts in a non-relaxed surroundings, which is analogous to the non-polar solvent as depicted on Fig.1.9.a, and no spectral change is observed;
- $\tau_r \sim \tau_f$: the first emitted photons correspond to shorter wavelengths, while longer ones show-up latter. A spectral shift is observed but there is no direct relation to solvent polarity. Generally such spectrum is broader due to the spectral shift between the first and the last emitted photons.

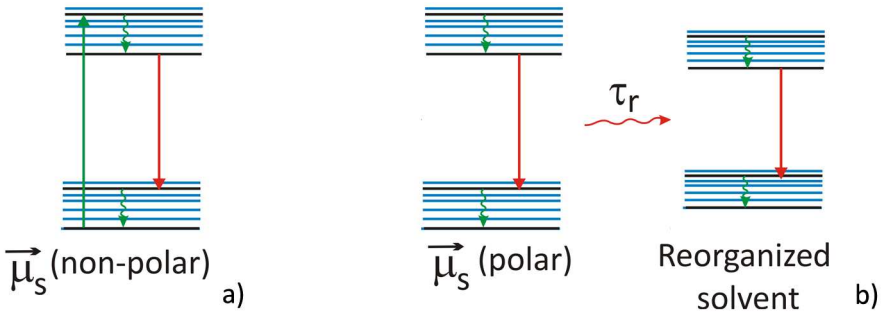

Figure 1.9: *Mechanism of the solvatochromic influence on the fluorescence properties of dyes: a) Perrin-Jablonski diagram for a dye in a solvent with low polarity, b) Perrin-Jablonski diagram for a dye in a polar solvent.*

In summary, the Stokes-shift increases in polar solvents, and both absorption and emission spectra should be performed.

Red edge absorption Another phenomenon capable for the shift in fluorescence spectrum is the red edge absorption. It appears when a polar dye in the *viscous* solution is excited at the the red edge of the absorption band of a dye (for example DCM under 532 nm pumping). Such excitation selects for dye molecules more bounded to surroundings. And thus the re-emitted photon has lower energy comparing to the case of pumping at the center of absorption band. Such fluorescence spectrum will be also red-shifted. However, in a fluid solution the reorientation of the solvent molecules is rapid enough to eliminate this effect [70].

The Weber effect As the Förster resonance energy transfer (FRET) normally occurs in a region where the absorption spectrum of the donor molecule and the fluorescence spectrum of the acceptor molecule overlap (Sub-section 1.1.6), homo-FRET (i. e. transfer between molecules of the same type) will take place at the red edge of the absorption band. It thus leads to the same red shift as described in previous Sub-section. Comparing the emission spectra of a sample with a lower dye concentration (where homo-FRET is less efficient) and a highly concentrated sample, one will observe a clear red shift of the latter. However a difference between spectra of two samples with unequal concentrations, but high enough for the FRET to appear, will not be significant.

Change in the quantum yield

The quantum yield ϕ represents the ratio of the number of photons emitted in the system to those absorbed. There exist two groups of measurement techniques

for definition of the photo-luminescence quantum yield: relative and absolute. Relative measurement is made under the controlled conditions (dye molar concentration and temperature) and compared to the reference, the error is generally more than 5%. The calorimetric methods [75] (asbolute) can be applied in solution as well (measurement of heat deposited by vibrational relaxation), and when $\phi > 0.9$ they provide low measurement error of about 1%. The mostly used and highly reliable[4] method for definition of quantum yield in a solid state is the usage of integration sphere [76] (hollow sphere, covered internally with Lambertian reflector).

We did not perform the measurement of the quantum yield during this thesis, but used the values found in the literature. However, the importance of the measurement conditions (exact solid state matrix) should be emphasized, especially due to the fact that the quantum yield varies with the surroundings.

The quantum yield for spontaneous emission of a laser dye in a liquid solution is known to depend on the nature of the solution polarity [70]. The change in quantum yield with the solvent is related to the change in non-radiative decay. Generally this results in the increase of quantum yield in polar solvents. However, if the growth of solvent polarity causes an internal charge transfer (ICT, typical for polar solvents), the quantum yield lowers. The absence of Brownian movement of dye molecules in the solid state matrix eliminates some non-radiative de-excitation ways, and the quantum yield in solid state is generally higher [70].

In summary, the quantum yield values published in literature should be used carefully and thorough attention should be payed on the conditions, at which the claimed value was measured.

Application to examined dyes

Here we provide the analysis of the spectral shifts of fluorescence emission in used species with change of concentration and environment.

The experimentally observed fluorescence spectra of various concentrations of DCM, RH640 and PM605 dyes in PMMA and also in liquid anisole are shown on Fig.1.10.

The shift between fluorescence spectrum of dye in anisole and in low-concentration PMMA film is remarkable Fig.1.10. Meaning that fluorescence spectrum of dye in solution may be used only for a rough spectral localization of the emission maximum, but not for the estimation of stimulated emission cross-section [5].

As for the fluorescence of a dye imbedded in the polymer matrix, it is highly concentration-dependent (Fig.1.10). Indeed, the increase of dye concentration induces a red-shift of the fluorescence spectrum. But the pattern of the change fits the Weber effect rather than the solvatochromism, as the emission spectrum stops shifting at a specific concentration (for example 2.3% for RH640 on Fig.1.10.b).

[4] As it eliminates the effects of emission anisotropy in a solid state.

[5] As the the dipole moment of anisole is lower compared to a PMMA ($\overrightarrow{\mu_s}$ =1.25D [94] against $\overrightarrow{\mu_s}$=1.6D [77]), we would expect the fluorescence spectrum of dye in anisole solution to be blue-shifted compared to PMMA-based one, which is not the case. In fact, a higher molar dye concentration was used to prepare the anisole solution.

The 5 wt% concentration of a dye in a polymer corresponds to about 10-100 μM/L. Due to much higher density in a polymer matrix as compared to an anisole solution, a negligibly small quantity of moles (about 0.2 μM versus 20-50 μM in polymer, for 10 ml of solution) had to be used to prepare the anisole solution. Finally, the dye quantities of about 0.1-1 mg, necessary to prepare the anisole solution, are generally below the uncertainty range of the microbalance (except for the DCM dye).

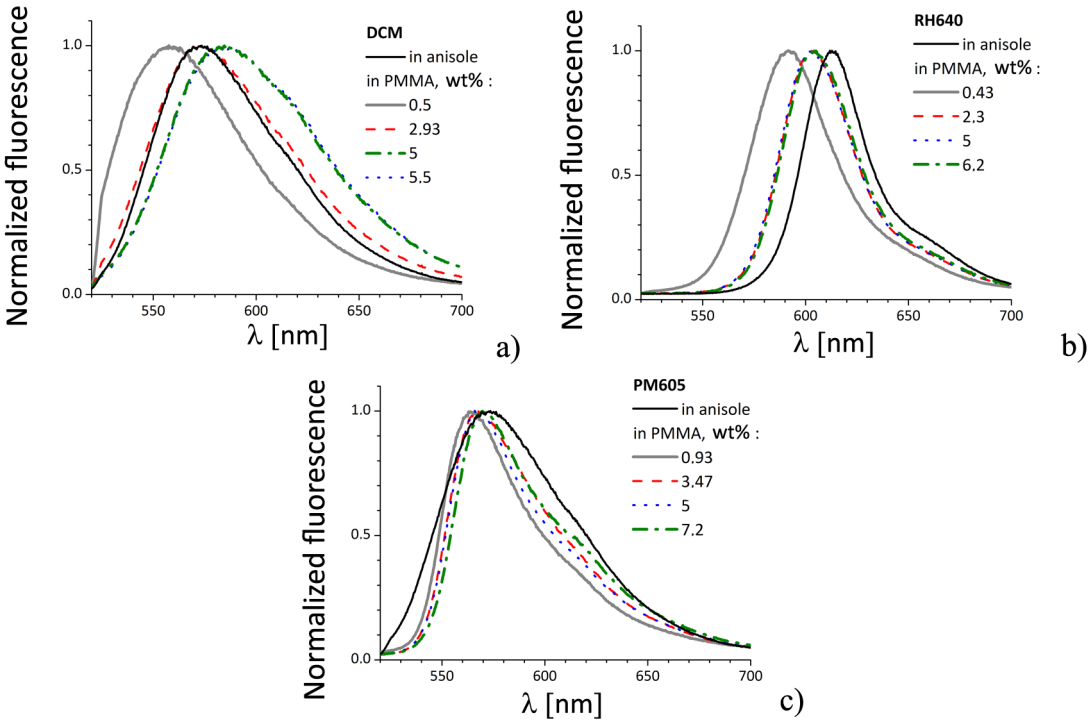

Figure 1.10: *Illustration on the influence of the molecular environment on the emission properties of dyes. Fluorescence spectra of various concentrations of the dye respectively in a thin PMMA film and in an anisole solution (without PMMA): a) DCM, b) RH640 and c) PM605.*

Although solvatochromism does not really play a role on the fluorescence spectrum of a dye in a PMMA matrix, it may be one of the reasons for the red shift of the ASE spectrum, as the duration of ASE is shorter than fluorescence and may be of the order of the reorganization time of PMMA.

The fluorescence spectrum of a dye molecule depends on its concentration and environment, and thus should be measured in the exact configuration. There exists several mechanisms, that can lead to a spectral shift of the fluorescence. The understanding of those mechanisms is important for the analysis of the stimulated emission process.

1.2 Laser system based on dye molecules

Complete description of lasing in a dye-based system demands to consider the population of all singlet and triplet energy levels involved in the process. This issue was addressed by researches [71] on the first stages of liquid dye lasers development, resulting in bulky expressions, demanding a deep knowledge of the exact dye structure.

In fact, the experimental arrangement can eliminate the participation of some levels to the lasing process, such as for instance triplet levels. The growth of population of such levels in ensemble of dye molecules is highly undesirable and results inevitably in emission quenching, as their de-excitation happens via radiation-less channels and thus does not contribute to lasing. Once excited to T_1, a state molecule stays there for a relatively long period of time (Tab.1.1), compared to absorption and other de-excitation processes. So the role of triplets is usually minimized in solution dye lasers by the addition of triplet-quenching agents or the implementation of a continuous recycling flow of the dye solution. In solid dye-doped media, the commonly used method to eliminate the triplets is pulsed

pumping [29, 127]. Indeed sub-microsecond pumping with sub-kHz repetition rate permits to minimize the amount of ISC events and ensures for molecules in triplet states a sufficient time-lapse for relaxation to the ground state before the onset of the next pulse.

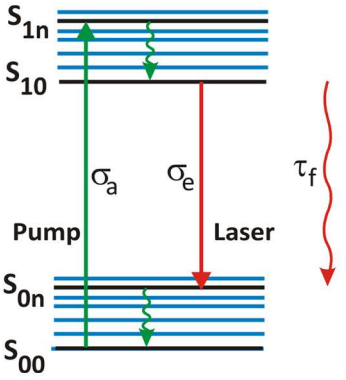

σ_a	Absorption cross-section [cm^2]
σ_e	Emission cross-section [cm^2]
τ_f	Fluorescence lifetime [ns]
i_p	Pumping intensity [$cm^{-2}s^{-1}$]
i_e	Emitted intensity [$cm^{-2}s^{-1}$]

Figure 1.11: *Dye molecule as a 4-level lasing system.*

Regarding absorption to higher excited states, $S_1 \rightarrow S_2$ transition is generally negligible unless the $S_0 \rightarrow S_1$ absorption is saturated by highly intense pumping.

In first approximation, we may consider only the S_0 and S_1 manifolds as those actually taking part in lasing. Moreover these two manifolds can be accounted for by an equivalent system made-up of only 4 energy levels. These are namley the lowest vibrational levels of S_0 and S_1 manifold S_{00} and S_{10}, and higher vibrational levels S_{0n} and S_{1n}, where $S_{00} \rightarrow S_{1n}$ corresponds to the energy of a single pumping photon and $S_{10} \rightarrow S_{0n}$ to the energy of the emitted photon.

The absorption of the pumping photon leads to the excitation of the molecule into the S_{1n} energy state, which is followed by rapid non-radiative vibrational relaxation that brings the molecule to the S_{10} state. In as much as the fluorescence lifetime is longer compared to the duration of the vibrational relaxation process, we can consider the population of S_{1n} as void. The same rational can be applied to S_{0n}.

Taking into account all mentioned simplifications and assumptions, the following set of equations can be derived:

$$\begin{aligned} M_t &= M_0 + M_1 \\ \frac{dM_0}{dt} &= -\sigma_a i_p M_0 + \sigma_e i_e M_1 + \frac{M_1}{\tau_f} \\ \frac{dM_1}{dt} &= \sigma_a i_p M_0 - \sigma_e i_e M_1 - \frac{M_1}{\tau_f} \end{aligned} \tag{1.31}$$

Here M_t stands for the total number of dye molecules in the system, M_0 - number of molecules in the ground state, M_1 - number of molecules in the excited state. τ_f is the fluorescence lifetime, σ_a is the absorption cross-section at the pumping wavelength, and σ_e - the emission cross-section at the emission wavelength of the dye within the polymer host. The photon flux for the pump and the emission are accounted for by i_p and i_e respectively (number of photons per unit pumped area per unit time [$cm^{-2}s^{-1}$]).

The number of molecules in the first excited and ground singlet states are related by Eq.1.31. It is then sufficient to explore the dynamics of one of them. We will focus on the first excited singlet state, and change the notation to the relative population density of molecules in the excited state: $\eta^* = N_1/N$ (the

population density of dye molecules in the sample being $N = M_t/V$ [cm^{-3}]). The rate equation for η^* alone can be obtained from the closure equation in the set (1.31) by substituting $M_0 = M_t(1 - \eta^* V)$:

$$\frac{d\eta^*}{dt} = \sigma_a i_p - \left(\sigma_e i_e + \sigma_a i_p + \frac{1}{\tau_f}\right)\eta^* \tag{1.32}$$

The pump that we use in our experiment is a pulsed source with sub-nanosecond pulse duration (approximately $\tau_p \sim 500$ps). Thus we estimate the signal as a Gaussian temporal function, with duration τ_p and average intensity i_{p0} :

$$i_p(t) = \frac{2}{\sqrt{\pi}} i_{p0} exp\left[-\left(\frac{t}{\tau_p/2}\right)^2\right] \tag{1.33}$$

The area of this function equals $i_{p0}\tau_p$, which is the total number of pumping photons per unit area of sample.

One more parameter needs to be further defined, that is the emitted intensity i_e. The flux of emitted photons encompasses the photons supplied by fluorescence (thus proportional to the number of excited molecules: N^*/τ_f), plus the photons created by stimulated emission (depending on the emitted flux and number of excited molecules at the same time $\sigma_e i_e N^*$). In the meantime the flux of emitted photons is decreased by the light out-coupling conditions, which is proportional to the flux.

The photon lifetime in the cavity τ_{cav} is a parameter introduced to describe the light out-coupling losses in the cavity. It can be estimated from the cavity losses (r_{loss} - involving both refraction and propagation losses) per unit time necessary for light to perform a round-trip passage at a given mode or a given orbit (e. g. nL=$2nw$ for a Fabry-Perot type mode, where w stands for the ribbon width):

$$\exp\left(-\frac{nL}{c\tau_{cav}}\right) = r_{loss} \tag{1.34}$$

The cavity loss τ_{cav} can then be expressed as:

$$\tau_{cav} = -\frac{nL}{c \ln r_{loss}} \tag{1.35}$$

For instance, in the case of a ribbon micro-cavity, losses are simply $r_{loss} = R^2(1-\alpha_r)^2$, where R is the Fresnel intensity reflection coefficient and α_r describes the linear propagation losses within the cavity (due to dominant refraction losses at normal incidence at the dielectric border, it can be estimated as $r_{loss} = R^2$).

Then the number of photons emitted in the unit length of the mode path is as follows:

$$\frac{di_e}{dx} = \left(\sigma_e i_e + \frac{1}{\tau_f}\right) N\eta^* - \frac{i_e}{\frac{c}{n}\tau_{cav}} \tag{1.36}$$

Introducing the variable change $dx = \frac{c}{n}dt$, the following expression for i_e can be derived:

$$\frac{di_e}{dt} = \frac{c}{n}\left(\sigma_e i_e + \frac{1}{\tau_f}\right) N\eta^* - \frac{i_e}{\tau_{cav}} \tag{1.37}$$

The photon flux entities i_e and i_p, introduced in this part, are purposely expressed in normalized units, to facilitate control on simulations. Still, simple multiplication by the photon energy ($h\nu$) allows to express the data within units more practical for experimental verification, namely intensity [$W\text{cm}^{-2}$].

Equations (1.32), (1.33) and (1.37) form the basis for the numerical simulations of the optically pumped thresholds and emission dynamics that will be further addressed in Chapter 5.

1.3 Resonators made of thin film

This Section is devoted to a short description of the light confinement in thin polymer films which is an important aspect of planar micro-lasers functionality. We first discuss general concepts of light confinement and explain the choice of the substrate, and then proceed with the effective refractive index concept, which simplifies the description and mode analysis of 3-D dielectric resonators.

We study micro-lasers, made of a thin dye-doped polymer film, with an in-plane shape patterned by lithography methods (Section 2.1, for the early wave-guiding theory of the organic laser see [20]). As the in-plane size ($\propto 100\,\mu m$) is much bigger compared to the wavelength of propagating light ($\propto 0.6\,\mu m$) as well as the cavity height ($\propto 0.6\,\mu m$), the system can be considered in terms of a slab waveguide, as shown on Fig.1.12.a: the bottom layer describes a substrate with refractive index n_1, the middle layer is a dye-doped polymer with refractive index n_2 and finally the top layer represents the surrounding (n_3= 1, as experiments described in this thesis were held in the air).

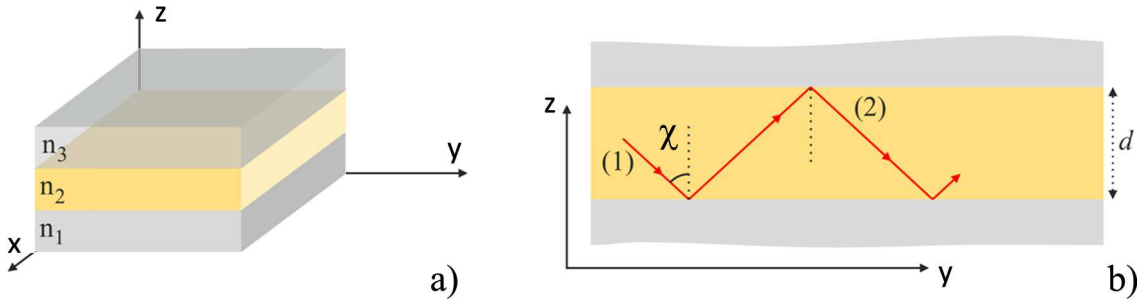

Figure 1.12: *Polymer layer viewed as a slab waveguide: a) schematic representation of our standard geometry as a 3-layer system (1 - substrate, 2 - guiding layer and 3 - surrounding) b) ray propagation inside the guiding layer.*

The basic principle of light confinement in a such polymer layer can be described in terms of geometrical optics: a ray, that meets the layer boundary at an angle smaller than χ_c (critical angle of total internal reflection, TIR), is refracted, while in the opposite case it is confined inside the layer, as depicted on Fig.1.12.b.

The critical angle is described by the following formula:

$$\chi_c = \arcsin\left(\frac{n_i}{n_2}\right) \tag{1.38}$$

where n_i stands for the refractive index of the adjacent medium (i = 3 for air, i = 1 for a silica substrate).

The refractive index of poly(methylmetacrylate) (PMMA, polymer used as a host matrix) in the visible range is about 1.49 [95]. Depending on the concentration and the nature of the dye molecule, the doping of a PMMA results in slight increase

of its refractive index value (up to $n_2 = 1.54$ for DCM at 600 nm). Accordingly, all rays arriving at the air boundary with an angle $\chi > \chi_c(n_2 = 1.54) = 41^o$ are reflected back to the polymer layer and continue to propagate.

As for the layer substrate, we will consider two examples frequently used in the present work: a bare silicon wafer and one covered with a 2 μm silica layer. In the first case the refractive index of Si is about 3.9 at 630 nm [96] and TIR cannot take place. Such a substrate cannot be used for a laser experiment, but it is still useful to study non-confined emission such as fluorescence. The refractive index of silica (the oxide material that tops a silicon wafer) is $n_1 = 1.46$ at 600 nm [97] and $\chi_c = 76.7^o$, thus allowing for moderate confinement.

The ray optics depiction of light guiding by multiple reflections is a good starting point for the qualitative understanding of the process, however falling short of providing a mode analysis. This question demands electrodynamic consideration.

The most general upstream to describe any electro-magnetic system is to find the solution of Maxwell's equations for the considered system abiding to specific boundary conditions. For the sake of simplicity we consider a simplified set of Maxwell's equation, that describe a system without free charge currents or magnetims [98, 99]:

$$\begin{aligned} \nabla \times \overrightarrow{H}(\overrightarrow{r}, t) &= \frac{\partial \overrightarrow{D}(\overrightarrow{r}, t)}{\partial t} \\ \nabla \times \overrightarrow{E}(\overrightarrow{r}, t) &= -\frac{\partial \overrightarrow{B}(\overrightarrow{r}, t)}{\partial t} \\ \nabla \cdot \overrightarrow{B}(\overrightarrow{r}, t) &= 0 \\ \nabla \cdot \overrightarrow{D}(\overrightarrow{r}, t) &= 0 \end{aligned} \tag{1.39}$$

Here the electric displacement field $\overrightarrow{D}$ is related to electric field $\overrightarrow{E}$ through a dielectric permittivity tensor $\hat{\varepsilon}$, and the magnetic induction $\overrightarrow{B}$ is related to the magnetic field $\overrightarrow{H}$ via the magnetic permeability tensor $\hat{\mu}$:

$$\begin{aligned} \overrightarrow{D} &= \hat{\varepsilon}\overrightarrow{E}(\overrightarrow{r}, t) \\ \overrightarrow{B} &= \hat{\mu}\overrightarrow{H}(\overrightarrow{r}, t) \end{aligned} \tag{1.40}$$

We will further consider isotropic media where tensors can be reduced to scalar coefficients. Taking separately the curl of the first and second equations in (1.39) and using $\nabla \times \nabla \times \overrightarrow{X} = \nabla\left(\nabla \cdot \overrightarrow{X}\right) - \triangle\overrightarrow{X}$ as well as equations (1.40), the well known relation can be obtained performing a temporal Fourier transform of Eq.(1.39), also known as the Helmholtz equation):

$$\left(\triangle + k^2 n^2(\omega)\right)\overrightarrow{\Phi} = 0 \tag{1.41}$$

where $\overrightarrow{\Phi}$ stands for $\overrightarrow{E}$ or $\overrightarrow{B}$ (and for a monochromatic plane wave $\overrightarrow{E} = E\exp\left(i\left(\overrightarrow{k}\overrightarrow{r} - \omega t\right)\right)$), ω is the frequency of the harmonic plane wave, k - its wave-vector in vacuum, both being related by $k = \omega/c$.

Equations (1.41) should be completed by the boundary conditions, that ensures continuity of tangential components of both $\overrightarrow{E}$, $\overrightarrow{B}$ fields and continuity of normal component of $\overrightarrow{B}$ and of $\overrightarrow{D} = n^2(\omega)\overrightarrow{E}$.

There are two known 3-D dielectric distributions, for which the Helmholtz equation with boundary conditions and conditions on the field in infinity can be solved analytically: namely the sphere and the disc.

For infinite planar multilayer systems the solution of equation (1.41) can be decomposed into two sets of orthogonally polarized waves TE (with *electric* field component laying in the layer plane) and TM (resp. *magnetic* field component laying in the system plane). This allows to separate variables: $\Phi(x,\, y,\, z) = \psi(x,\, y)\,\zeta(z)$, and obtain following equation for z:

$$\left(\frac{d^2}{dz^2} + q^2\right)\zeta(z) = 0 \tag{1.42}$$

where q is a propagating constant along the z direction. Equation (1.42) leads to obvious solutions $\zeta(z) = \zeta_{\pm}\exp(\pm iqz)$, which allows to present field distribution in x,y-plane in more readily solvable equation:

$$\left(\triangle_{xy} + k^2 n_{eff}^2\right)\psi(x,\, y) = 0 \tag{1.43}$$

and $n_{eff}^2 = n^2 - q^2/k^2$ - effective refractive index, introduced to keep the overall structure of Helmholtz equation.

Constructive interference conditions must be satisfied for a wave to be guided in the dielectric slab. This condition suggests that after a single reflection (from each of the two boundaries) the outgoing wave must be in phase with the initial one.

As for the in-plane distribution function, it is generally expressed as a solution of equation:

$$r_{21} r_{23}\exp(2iqd) = 1 \tag{1.44}$$

The reflection coefficients of the wave at the boundary between polymer and substrate (r_{21}) or surroundings (r_{23}) are complex dephasing entities with unit modulus and depend on the polarization of the incident wave (TE or TM). Their phase ($\varphi/2$) can be found from expression ($\eta_{TE} = 1$, $\eta_{TM} = n_2^2/n_i^2$ are used fro compactness):

$$\tan\varphi = \eta\frac{\sqrt{n_{eff}^2 - n_i^2}}{\sqrt{n_2^2 - n_{eff}^2}} \tag{1.45}$$

And the following equation for the effective refractive index can be written [100]:

$$2\pi\frac{d}{\lambda}\sqrt{n_2^2 - n_{eff}^2} = \tan^{-1}\left(\eta\frac{\sqrt{n_{eff}^2 - n_i^2}}{\sqrt{n_2^2 - n_{eff}^2}}\right) + \tan^{-1}\left(\eta\frac{\sqrt{n_{eff}^2 - n_i^2}}{\sqrt{n_2^2 - n_{eff}^2}}\right) + \pi l \tag{1.46}$$

The solutions for TE and TM modes in our system (refractive indexes $n_1 = 1.46$, $n_2 = 1.49$, $n_3 = 1$) are depicted on Fig.1.13.b as a function of d/λ, which is convenient for analysis. The emission of dyes takes place at about 600 nm, and the mode structure will result from the cavity thickness. For instance, there is a

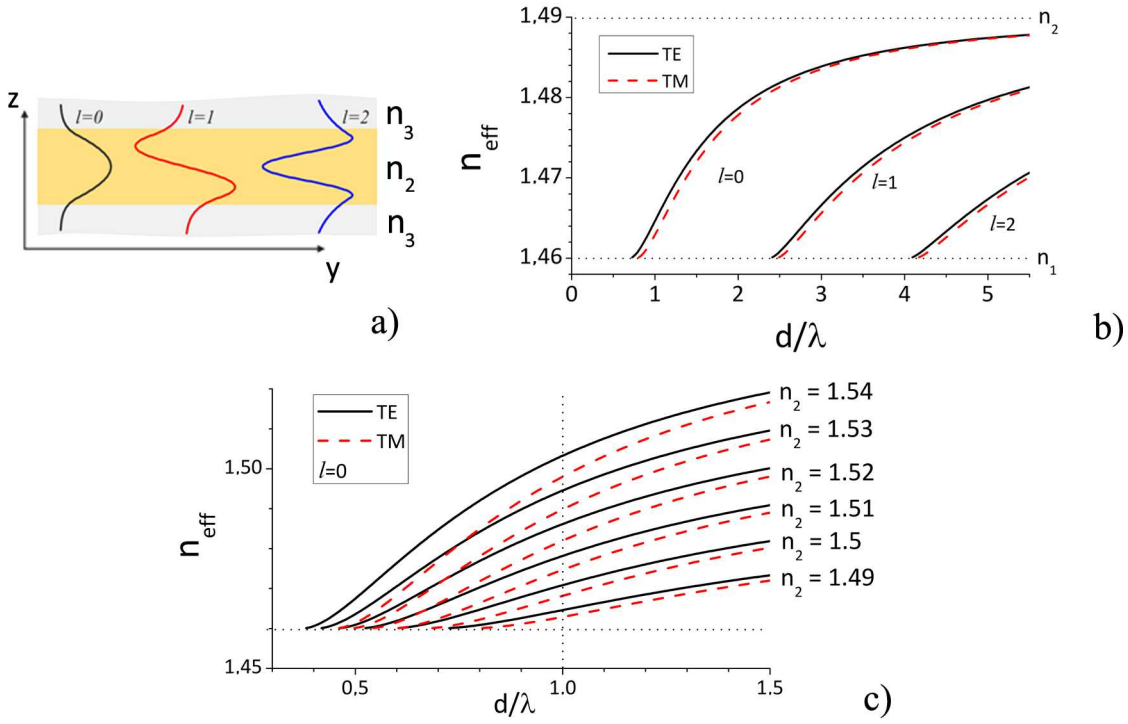

Figure 1.13: *Mode structure in traversal direction of a planar waveguide with symmetric environment (a), effective refractive index of a guiding layer as a function of d/λ for the non-doped PMMA (b) and for several values of refractive index slightly modified as result of doping the PMMA with a dye (c).*

cutoff thickness, under which no wave confinement is possible: $d_{min}^{TE} = 436\,nm$ and $d_{min}^{TM} = 484\,nm$ (note that such a cut-off does not exist for a symmetric environment, i.e. with $n_1 = n_3$). And if the cavity thickness comes close to the wavelength of the propagating light $d \approx \lambda$, there can only be one transverse mode in the cavity ($l = 0$, depicted on Fig.1.13.a and b) [101].

Doping with laser dyes increases the refractive index of PMMA (n_2). The value up to 1.54 was measured with the ellipsometry technique in DCM-doped PMMA films with doping rate about 5 wt% (performed by former PhD student [66]). The influence of the refractive index of the polymer on the wave-guiding properties of dye-doped PMMA slab is shown on Fig.1.13.c and calculations summarized in Tab.1.3. The increase of n_2 results in the lowering of the cutoff thickness and increase of the effective refractive index.

Table 1.3: *Wave-guiding properties of dye-doped PMMA slab: effective refractive index n_{eff} for a layer thickness equals λ, cutoff thickness d_{min}, cutoff thickness of second mode $d_{min}(l = 1)$, estimated by Eq.(1.46) for TE and TM modes in layer with $n_2 \epsilon [1.49; 1.54]$, $n_1 = 1.46$, $n_3 = 1$ and $\lambda = 600$ nm.*

n_2	d_{min}[nm]		n_{eff} $(d = \lambda)$		$d_{min}(l = 1)$ $[\mu m]$	
	TE	TM	TE	TM	TE	TM
1.49	435	485	1.465	1.463	1.45	1.49
1.5	360	410	1.471	1.468	1.24	1.3
1.51	315	360	1.478	1.475	1.09	1.15
1.52	280	325	1.486	1.481	0.99	1.04
1.53	250	300	1.495	1.489	0.91	0.95
1.54	230	275	1.503	1.498	0.84	0.89

In this regard, we took the condition of cavity height scaling $d \approx \lambda$ as a basic design rule for our planar micro-cavities. As a consequence, there is only one field

maximum along the cavity height and system can be considered as a quasi 2-D.

Chapter conclusion

The system that we study exhibits a stimulated emission of the laser dyes species, which posses rather specific photo-physical properties, embedded in the polymer matrix in the thin-film configuration. All three aspects: photo-physical properties, lasing mechanism and guiding effects; for the generic properties of our lasing system. They were discussed in this Chapter and provide a basis for the analysis held in all other Chapters of this thesis.

First we provided a thorough analysis of the photo-physical properties of the amplification medium used to obtain lasing in micro-cavities, considered in this work. Due to numerous effects , that can alter the measurable photo-physical properties, as explained in Sub-sections 1.1.7 and 1.1.6, due attention should be paid to properly define their experimental verification.

Then the possibility to analyze numerically the lasing process in our system was addressed and a set of rate equations (simplified version of the 4-level laser system) was developed for the exact system geometry. These equations will be used in Chapter 5.

Finally, the light confinement and the modal structure of a polymer thin-film-based resonator was discussed. We shown that following the condition $d \approx 600\,nm$ ($d \approx \lambda$) during cavity fabrication, the dimensionality of the resonator can be reduced to 2-D, as only one field maximum will be present along the cavity height.

Chapter 2

Fabrication process and experimental techniques

One of the key advantages of polymer-based micro-lasers is the simplicity of their fabrication technique. In contrast to semi-conductors, no high temperature process or toxic gases flow are needed. The basic layers are deposited simply by spin-coating without the need of more complex procedures such as sputtering, thermal evaporation or molecular beam epitaxy.

Moreover, the vast classes of existing polymers and laser dyes provide a large choice of potentially applicable materials and at the same time unique possibilities to tune the wavelength of the output emission throughout the visible region of the spectrum.

At the same time, such micro-lasers can be fabricated directly on a silicon wafer in contrast to conventional micro-spheres, which opens the possibility to a "on-chip" technology and the associated ease of integration with other "on-chip" elements.

The fabrication procedure consists of a the sequence of polymer layer spin-coating and a lithographic patterning. It is a quite powerful technique as it permits the creation of complex structures with several layers of resonators and waveguides [5].

The experimental study of dye-doped polymer micro-lasers aimed at reaching a general view on the emission features induced by the cavity shape and the gain medium. In order to distinguish between these two effects, the emission dynamics and polarization effects were examined in case of spontaneous and stimulated emission conditions. Also the gain behavior of dye molecules incorporated into a thin polymer film was addressed. All experimental set-up's used in the study are described in this chapter.

2.1 Fabrication

The solution of a polymer hosting a dye is obtained by mixing in the required proportions (Appendix A.1) the high purity dye powder and a commercial liquid mixture of the polymer with a proper solvent, then becoming a co-solvent of both the polymer and dye (which may not be straightforward and require an appropriate solvent search).

The sample preparation technique consists of either one or two principal steps: the fabrication of the dye-doped polymer layer, which, if necessary, is followed by lithographic shaping of the desired planar micro-laser cavity. A general overview of the process work-flow is presented here, while more the technical details are referred to Appendix A.

The first stage is identical for all samples used to study the photo-physical properties of dye molecules incorporated inside the polymer matrix as well as their stimulated emission properties (ASE and lasing). It includes the spin-coating of the dye polymer solution on a substrate (Fig.2.1) followed by low-temperature baking of the obtained layer (100-200 °C) in order to fully evaporate the solvent. At this point, the substrate type is the only difference between the samples prepared for different purposes: a glass slide is used to study the photo-physical properties and perform fluorescence measurements, and a silicon topped by a 2 μm thick layer of silica for ASE and lasing. The excess of polymer on the sample edge as depicted on Fig.2.1.c complicates the ASE measurement and requires the cleaving of the sample border as detailed in Appendix A.

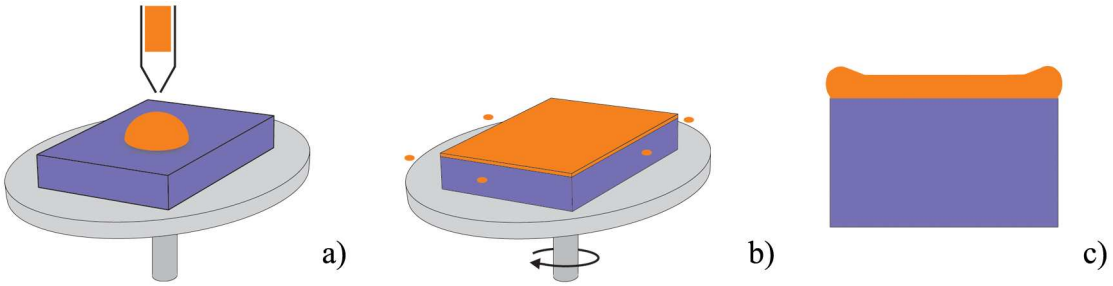

Figure 2.1: *Schematic depiction of the spin-coating process: a) deposition of a few droplets of the dye-polymer solution on a substrate; b) redistribution of the liquid during spinning; c) side view of the spin-coated layer (rounded parts show the accumulation of spun-coated material along the substrate border).*

The lithography process is based on the transfer of the desired geometrical pattern to the polymer layer by irradiation. Change in the chemical structure of the irradiated zone makes it soluble or insoluble (respectively corresponding to a positive or negative resist) to a specific basic or organic solution called "developer". Such patterning operation can be performed by electron-beam or photo-lithography, the exact fabrication sequence varying with the chosen method.

In the latter case, irradiation is provided by a UV source which is sufficient for a limited number of polymers (photo-resist). Thereby this type of lithography is rarely made directly on the given polymer layer, but on the photo-resist layer deposited on top of it. Even if the polymer can act as a photo-resist by itself (for instance PMMA), the additional photo-resist layer generally provides better fabrication quality of cavities.

Once the resist is deposed and prebaked (in order to get rid of solvent in the photo-resist layer and prevent its penetration inside the active polymer layer), the sample is covered by an optical mask and photo-lithography can then take place (Fig.2.2.a, b). All structures except the desired geometrical pattern vanishes after developing (Fig.2.2.c). Plasma etching finishes the patterning of the polymer layer (Fig.2.2.d) and numerous micro-lasers of various shapes (a top view of cavities made of different dye molecules is shown on Fig.2.2.e) are obtained on the same wafer.

The e-beam lithography process requires an expensive equipment and is time-demanding. Its advantage is in the high-resolution fabrication (20-30 nm) which is important for cavities of sophisticated shape, especially those containing corners. The e-beam lithography also provides sharp sidewalls (Fig.2.3.a). Moreover, the transferred pattern has only to be depicted on the electronic mask, which permits to try specific cavity shapes eventually unavailable on optical masks. The polymer layer itself acts as a positive (or negative) photo-resist, while the electron beam breaks the bonds in the irradiated regions of the polymer and thus tailors the

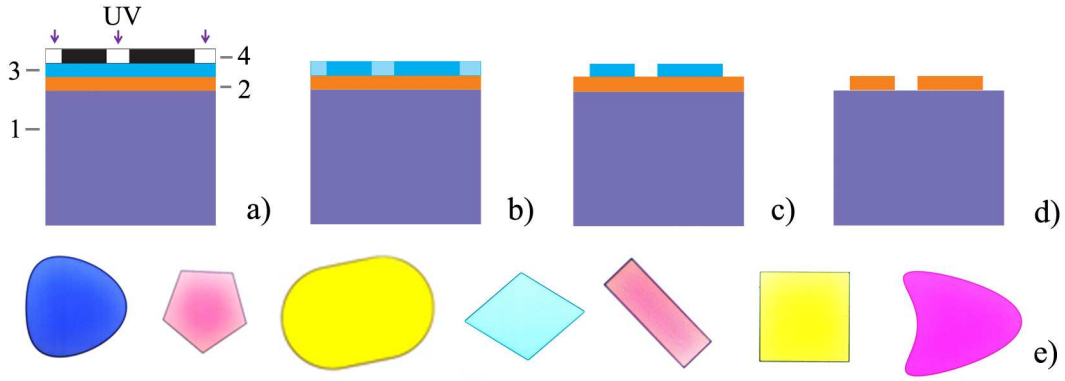

Figure 2.2: *Photo-lithographic fabrication scheme: 1 – wafer, 2 – dye-doped polymer layer, 3 – photo-resist layer, 4 – optical mask: a) irradiation by UV light; b) local changes in the chemical structure of the photo-resist; c) patterned photo-resist layer after developing; d) after plasma etching; e) optical microscope photos of the micro-lasers obtained by both methods (different dyes, top view).*

untouched areas (the effect is opposite in the case of a negative photo-resist, such as SU8).

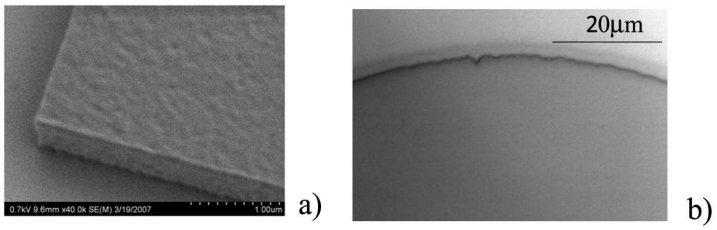

Figure 2.3: *E-beam lithography (a) versus photo-lithography (b).*

All the technological stages of fabrication were performed at the clean room of ENS de Cachan under the guidance of Joseph LAUTRU, except for the e-beam lithography, which was processed at the Laboratoire de Photonique et Nanostructures (LPN) by Christian ULYSSE.

The thickness value of planar micro-lasers presented in this thesis was ranging from 0.5-0.8 μm, chosen on purpose to get enough gain material for lasing and only one maximum of the electromagnetic field within the cavity thickness (Chapter 1.3). As far as the aim of this work was to study the influence of the gain medium on the emission properties of micro-laser, the study was performed on quasi 2-D (planar) micro-lasers and VECSOL's. Another PhD student in the group, Clement Lafargue, works currently in parallel on the fabrication and detection set-up for 3-D micro-lasers. In principle, the described fabrication method allows the production of cavities up to 10-20 μm thickness (this value varies with the spinning parameters and the polymer). It nevertheless limits cavity shape to cylindrical and parallelepiped-like resonator. Although quite demanding in the sense of piezo-controller accuracy, the two-photon polymerization technique permits the production of 3-D cavities of arbitrary shapes especially with recent commercial resists ([102], IP-photo-resist from Nanoscribe company).

2.2 Experimental set-up's for the study of micro-lasers

We focuses here on the study of the emission properties of dye-doped polymer micro-lasers of various shapes and content. The difference in a cavity configuration

between planar micro-lasers and VECSOL results in a variance of experimental arrangements and alignment techniques. This section contains the description of the equipment used for a study of lasing in dye-doped polymer micro-cavities, both quasi 2-D (Sub-sections 2.2.1 and 2.2.2) and VECSOLs (Sub-section 2.2.3).

The description starts with the set-up with which the major part of our experimental work on 2-D micro-lasers was performed (Sub-section 2.2.1). It was initially designed to perform only lateral emission detection. A possibility to conduct the measurements in directions departing from purely lateral observation was provided at the later stage of our work thanks to the contribution of Clement Lafargue. This 3-D-detection arrangement is addressed next (Sub-section 2.2.2). An explanation of the VECSOL experiment terminates this section.

2.2.1 Lateral emission detection

This Sub-section details the peculiarities of the experimental arrangement, which was most frequently used during our work. To start with, the basic principle of the experiment is explained, then the parameters of the pumping sources are described. The role of each optical element of the pumping branch of the set-up is subsequently discussed, then the detection arm is detailed.

A micro-laser is pumped from the top ("flood" configuration), while its lateral emission is detected. The sample positioning is done by the translation mount and controlled with an optical microscope. The detection system is fixed. The study of the directional emission properties of micro-lasers is done by sample rotation to the necessary angles by a rotating mount.

A scheme of the experimental set-up is depicted on Fig.2.4. Two pumping lasers were used in the study, namely a frequency doubled (532 nm) or tripled (355 nm) frequency Nd:YAG laser (Teem Photonics). The system of flip-flop mirrors allowed the rapid change from one pumping source to the other, sending the beam through a set of optical elements (wave-plates and polarizer) adapted for the corresponding wavelength. A thorough alignment procedure was regularly applied in order to maintain both beams centered at the same point on the cavity level. The normal incidence of the beam on the cavity surface was controlled as well.

The pulse duration of the pumping laser is about 500 ps (at 532 nm, and about 400 ps at 355 nm) and its repetition rate 10 Hz (optimal for long term use of dye-based micro-lasers [65], Sub-section 1.1.1).

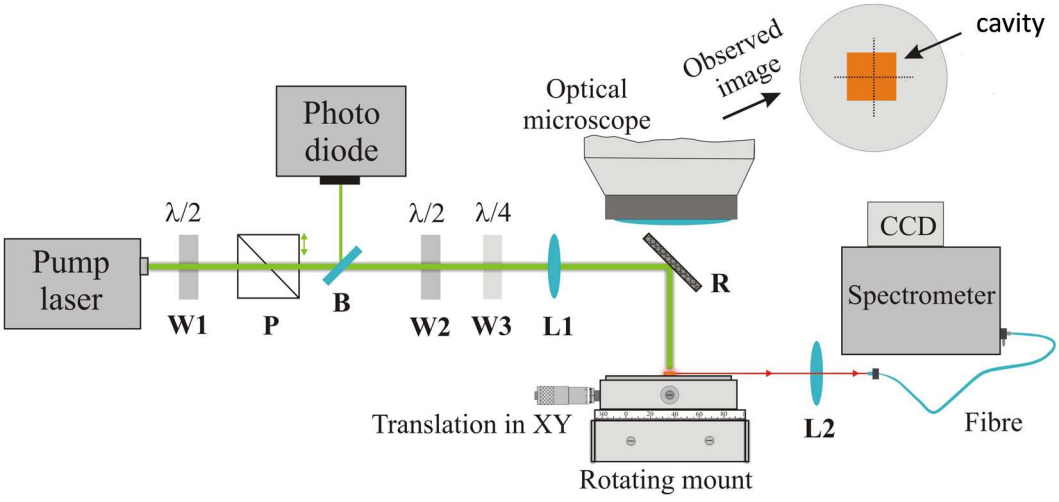

Figure 2.4: *Micro-lasers detection scheme in plane.*

We now detail the optical elements of the pumping branch of the set-up. The

polarization elements W1, P, W2 and W3 (Fig.2.4) are placed in standard sequence that allows the variation of pump beam intensity (half-wave plate W1 before the polarizer P) as well as the determination of pump beam polarization state (one more half-wave plate W2 after the polarizer is used to control the orientation of the linear pump beam polarization, if needed followed by a quarter wave plate W3 in order to provide a circular polarization for the pump beam). The ellipticity of the resulting linear polarization is negligibly small (Fig.2.5.a), while the circular polarization has about 10% irregular deviations from the theoretical expectation (Fig.2.5.b)

A beam-splitter (glass slide B), reflecting a small part of the pump power (15-20%) to the photo-diode, is placed after the polarizer before the second half-wave plate. A placement of a beam splitter after the second half-wave plate should be avoided, as in such case the measured power would then depend on the orientation of the linear polarization of the pump (as the ratio between s- and p-polarized components of the beam incident on the beam splitter varies with orientation of the second half-wave plate).

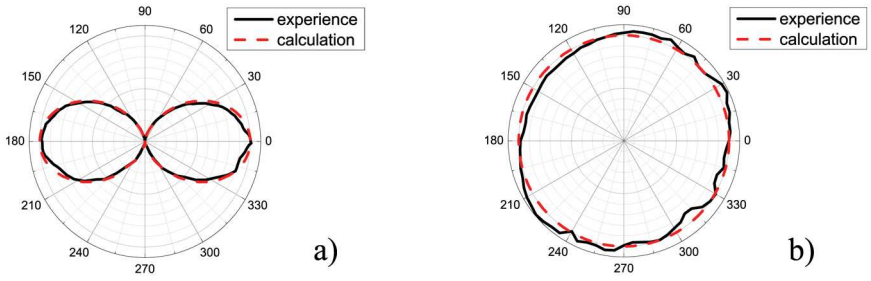

Figure 2.5: *Pump beam polarization state (a - linear, b - circular), presented as the normalized beam intensity just after W2 (a) or W3 (b) measured through a polariser (Polaroid film) by the photodiode (532nm pump wavelength). The angle plot on the diagrams corresponds to the angle between the polarizer and wave plate axes. The theoretical curves expected for polarizer transmission are shown by a red dashed line.*

The final step in a tailoring the pumping beam properties consists in the reduction of the beam size. This allows to achieve higher intensity values at the same power level. If the sample is fabricated by electron-beam lithography, the cavity is surrounded by the polymer matrix. For the sake of experimental accuracy, the size of the beam must be inferior to the size of the etched region (about 1mm). This condition is satisfied by lens L1 (f = 100 mm, Fig.2.4), that reduces the beam spot on the micro-laser level down to about 200 μm in diameter. The measurements of the beam size and profile (depicted on Fig.2.6) were performed with an uEye CCD camera for digital visualization and measuring (IDS imaging, the sensing region contains 1024*768 pixels of 6.6 μm side). The pumping beam has a circular shape (Fig.2.6.a) and a Gaussian intensity profile (Fig.2.6.b). The beam diameter in number of pixels (generally about 30) is inferred from the full width at half maximum (FWHM) of the intensity profile depicted on Fig.2.6.b. Then the beam diameter is found to be 198 $\pm$ 3.3 μm.

The cavity emission in the lateral direction is collected in the far-field with a lens L2 (f=100mm, collection angle about 5°) and then focused on the edge of an optical fiber, connected to an Acton SpectraPro 2500i spectrometer equipped with a Princeton Instruments PIXIS 100 cooled CCD camera (resolution: 1340 x 100; pixel size: 20 μm x 20 μm). The spectral resolution of the ensemble is 0.029 nm per pixel. The spectra of the micro-lasers are generally registered with an integration time of 3 s, which corresponds to 30 pump pulses (CCD camera

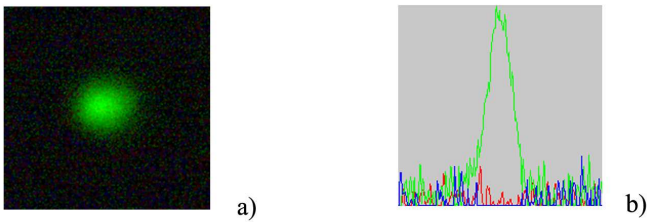

Figure 2.6: *Pump beam profile at the sample level, obtained with uEye CCD camera: a) beam shape; b) intensity profile.*

shutter is synchronized with the repetition sequence of the pumping laser pulses). This is done mainly to improve the signal to noise ratio at a reasonable level without bleaching effects.

2.2.2 3-D detection

We now provide the description of the 3-D detection set-up, that was used at the later stages of the thesis for experiments with pumping at varied incidence and non-lateral emission detection.

The micrometer precision positioning of a sample in 3-D space is commercially available, but is quite expensive. Another option to provide the 3-D measurements consists in variation of the detector position with respect to the fixed sample position.

The set-up conceived and mounted by Clement LAFARGUE also uses pumping of the cavity from the top and, in contrast to the previous lateral version, allows for the 3-D rotation of the detection system around a fixed cavity. In order to do this, the fiber is fixed to one of two rotating mounts oriented perpendicularly with respect to each other (Fig.2.7.a).

The crucial point is in the micrometer-precise positioning of the detector on the sphere around the sample, which is provided by rotating mounts. The minimum possible rotation step is 0.01°, but experiment is generally made with the step equal or higher to 1°, as bigger measurement precision is hindered by the collecting lens, used to focus light on the fiber entrance. There is also a region inaccessible to the detector due to its physical dimensions (as it would then block the pumping beam). This "blind zone" is situated around the pump beam and delineates a cone of angular width $\Delta = 7.5°$ (Fig.2.7.b).

A prism set on a flip-flop mount, placed after the polarizer depicted on Fig.2.4, allows to switch from a 2-D detection set-up to a 3-D one. So both arrangements use the same polarization control elements. The same Acton SpectraPro 2500i spectrometer is used for spectra detection.

The visualization of sample positioning is made by the uEye CCD camera for digital visualization and measuring (IDS imaging).

Apart from the possibility of non-lateral detection, this set-up has one more important advantage compared to the 2-D detection system: the possibility of controlled variation of the incidence of the pumping beam. This possibility proved very useful for several important experiments in this thesis.

2.2.3 VECSOL configuration

Another interesting configuration of dye-doped polymer lasers is the "Vertical External Cavity Surface Emitting Organic Laser" (VECSOL, Fig.2.8) [103, 104]. This Sub-section is devoted to the comparison of the VECSOL configuration with planar micro-lasers.

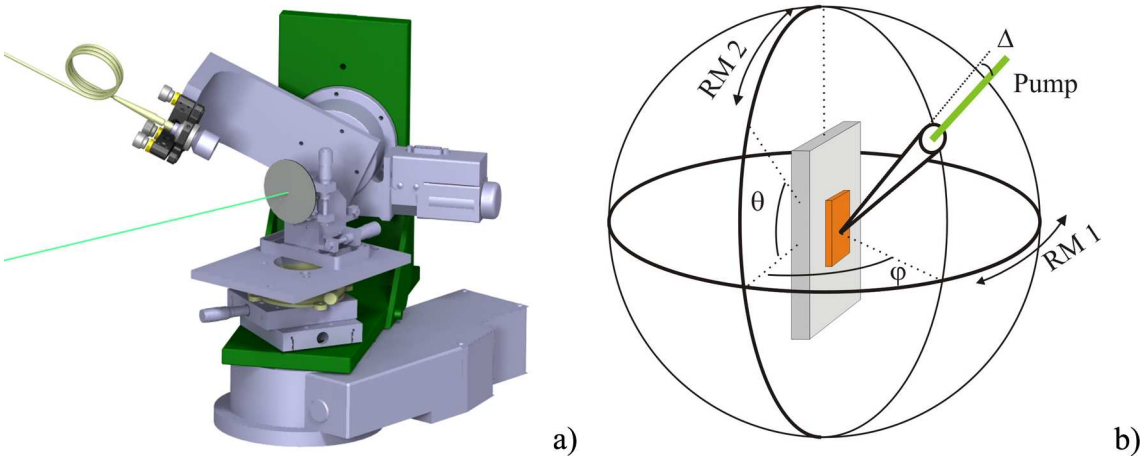

Figure 2.7: *3-D detection set-up a) overall scheme; b) detection geometry (the rotating mounts motion directions are shown by arrows RM 1, 2, the angle Δ shows a dark region due to the finite physical dimensions of the system).*

The gain medium in VECSOL cavities is also a dye-doped polymer layer, but this time directly deposited on a plane dielectric mirror by a spin-coating. The resonator is completed by a spherical dielectric mirror placed away from the polymer layer along the optical axis, leaving an air-gap of variable size. Such a straightforward technique supplies an inexpensive and simple geometry device with a good-quality easily detectable TEM_{00} laser beam, moreover with an improved lifetime (in the case of considerable bleaching the pump beam can be simply displaced to an undamaged part of the polymer layer).

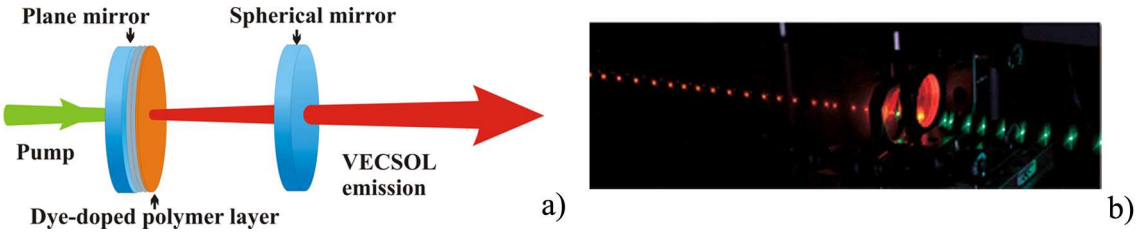

Figure 2.8: *Schema (a) and photo (b) on a vertical external cavity surface emitting organic laser (VECSOL).*

Therefore this architecture provides a good starting point to investigate the emission properties of the gain medium. Interestingly, the respective orientation of the pump beam and micro-laser emission (vertical or through emission) is not the same as for planar micro-lasers (edge emission), which is bound to influence the properties of the micro-laser emission (as will be shown in Chapter 3).

VECSOL's are one of the research subjects of the Organic Photonics group at Paris 13 University, in the team of Sebastien FORGET and Sebastien CHENAIS. The layer fabrication took place at Paris 13 University and followed the basis lines reported in Section 2.1 and Appendix A (except for a dye concentration of 1 wt% and a different type of PMMA matrix, allowing for the fabrication of 10 μm thick layers). The experimental study was conducted as well at Paris 13 University.

VECSOL experiments provided important information on the stimulated emission properties of dye-doped polymer layers in a simpler configuration. Parallel and complementary studies on dye-doped polymer lasers pumped in different configurations provide a useful insight on the nonlinear properties of the gain medium [105] as well as on the role of a system geometry regarding its emission dynamics

[106].

2.3 Set-up for the study of the emission dynamics and photo-physical properties of dyes

This section is devoted to a detailed description of the equipment used to study the photo-physical properties of our used dyes, as well as polarization and temporal aspects of their spontaneous and stimulated emission.

The absorption in dye-doped polymer layers was monitored by means of a spectrophotometer (Sub-section 2.3.1). The dynamics and anisotropy of fluorescence emission along vertical emission direction (through the sample) was examined by a FLIM set-up (Sub-section 2.3.2). As for the study of the polarization ratio in non-vertical emission direction as well as the assessment of the fluorescence emission efficiency under different pumping wavelengths, it was also addressed by a spectrophotometer (Sub-section 2.3.1).

Gain measurements in thin dye-doped polymer films were made by the "Variable Stripe Length" technique (VSL) described in Sub-section 2.3.4. Finally, the temporal behavior of the fluorescence and ASE emission was studied with the help of a streak-camera (Sub-section 2.3.5).

2.3.1 Spectrophotometer

The spectrophotometer utilized for the measurements of absorption spectra was a Lambda 950 from Perkin Elmer. Its spectral range is 175-3300 nm and its resolution is down to 0.05 nm in the UV and visible part of the spectrum.

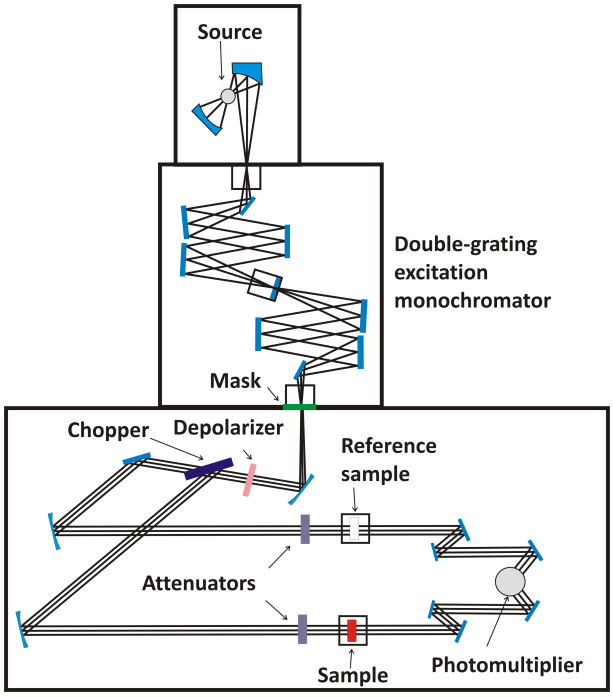

Figure 2.9: *Scheme of the Lambda 950 spectrometer.*

The light source (see Fig.2.9) is a pre-aligned tungsten-halogen and deuterium lamp. The pumping wavelength is varied by way of a double holographic grating monochromator (1440 lines/mm UV/Vis, blazed at 240 nm). After the wavelength is chosen, the beam passes through a beam mask, used to adjust the beam height to match samples of different dimensions. In order to correct the instrumental

polarization a beam depolarizer is used. The switch between sample and reference beam is done by a chopper, and the beam is attenuated before reaching the sample. The sample compartment contains the holders (adapted for glass slides and cuvettes holding liquid solutions) for a reference sample and the investigated sample itself. The detector used in the UV and visible range is a R6872 Photomultiplier.

Attention should be paid at the stage of data analysis, as the absorbance plot obtained as a result of this study is defined by a standard $\log_{10}(\frac{I_1}{I_0})$ formula (Chapter.1.1.2). In all absorption curves present in this thesis, the absorption of the polymer layer of a thickness equal to that of the sample is taken into account.

2.3.2 The FLIM set-up

Study of the fluorescence anisotropy (detailed in Chapter 3) was undertaken at the Laboratoire de Photophysique et Photochimie Supramoléculaires et Macromoléculaires (PPSM lab) of ENS de Cachan on the set-up shown in Fig.2.10 under the guidance of Jean-Frederic AUDIBERT and Robert PANSU. This is a "Fluorescence-Lifetime Imaging Microscopy" (FLIM) experiment, working in the regime of wide-field sample excitation.

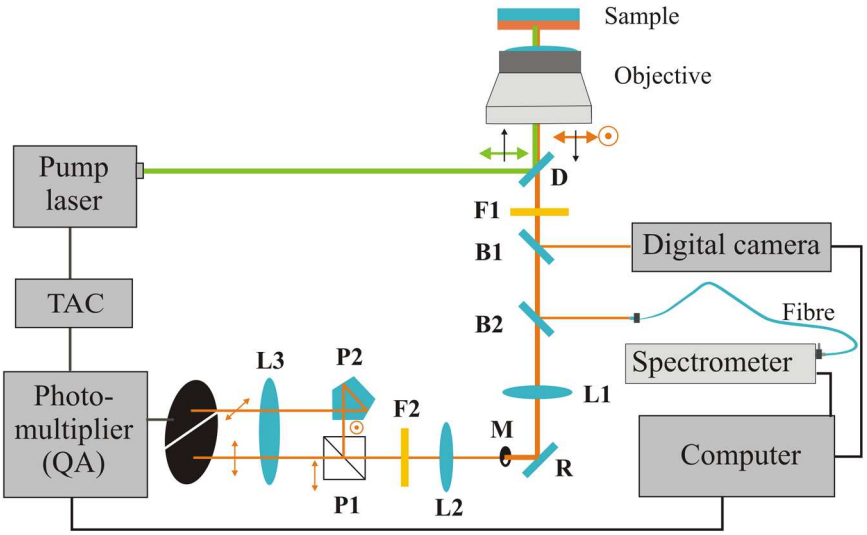

Figure 2.10: *Scheme of the set-up used to study the fluorescence lifetime and polarization properties. Here F1,2 - filters for pumping wavelength, D - dichroic mirror, B1,2 - beam-splitters, R - mirror, L1,2,3 - lenses, P1 - Glan prism, P2 - pentaprism, M - mask, TAC - time-to-amplitude converter. The acousto-optical element and nonlinear optical crystal are included into the block of the pump laser.*

This equipment permits the study of fluorescence emission properties in the vertical emission configuration (through the sample) for either an active thin polymer film deposed on a transparent substrate or a liquid sample in a transparent cuve [107]. The important advantage of this set-up is the simultaneous detection of two orthogonally polarized emission components (parallel and perpendicular to that of the pump), which is crucial for our purpose and is not available for the majority of current techniques in fluorescence emission analysis (where the polarized components, if registered at all, are detected in successive experiments [108]).

The sample excitation is made by Yb:KGW (SESAM mode-locked oscillator) laser at 1030 nm (Amplitude Systemes®, Bordeaux, France) with repetition rate 10MHz and pulse duration 400 fs. The passage through the extra-cavity external module, based on β-BaB_2O_4 (or β-BaB_2O_4 and β-BBO) crystal, provides frequency doubling and signal wavelength of 515 nm (or doubling and mixing resulting into

the frequency tripling and signal wavelength at 343 nm). Reflected towards the sample by the dichroic mirror (D), the laser beam enters the a Nikon Eclipse TE2000 inverted microscope. Finally to provide a wide-field excitation of the sample, the pumping beam is focused on the back focal point of the objective.

The principal element of the detection line is a time-resolved single-photon-counting photo-multiplier (QA, Europhoton Gmbh). This is a multi-channel plate photo-multiplier (PM) working in the single-photon counting mode. The anode contains five conductive parts, and the impact of a photo-electron causes the avalanche in two subsequent multi-channel plates, spreading over all five parts of the anode. The position of the photon on the photo-cathode is inferred from the values of the five charges collected by the anodes. The whole photo-cathode area (2.5 cm large) is then numerically divided in 256*256 pixels (100 μm side size) within which the photons are sorted by coordinate rounding. Five parameters are measured for each photon reaching the camera: the delay between the beginning of the laser pulse and the photon arrival on the camera, the photon arrival time with respect to the onset of the measurement, the avalanche amplitude and pixel coordinates (x,y). The synchronization of the pump pulses with the photo-multiplier is made by a TAC/SCA 567 module (time to amplitude converter from ORTEC®).

Before the start of the experiment, careful choice of the examined region of the sample is performed by means of both lateral sample positioning with the digital camera (Fig.2.10) to avoid visible inhomogeneities. Emission spectra are checked with the spectrometer (SD2000 Ocean Optics®, Fig.2.10) to ensure a significant fluorescence value.

An optical filter is placed after the sample (F1) to cut-off the transmitted part of the pump signal before the spectrometer. The fluorescence emission itself is then spatially cut by the mask (M) in the form of semi-circle, followed by splitting by the Glan prism (P1) in two polarizations namely parallel and perpendicular with respect to the polarization of the pump (respectively transmitted and reflected). The beam with perpendicular polarization is then turned around the propagation direction by passage though the pentaprism (P2). This prism is used to replace that half of the circular image, which had been initially cut by the mask, and thus reconstruct an image made of both polarizations separately on the photo-cathode. Due to the high sensitivity of the photo-cathode with respect to the spectrometer, one more filter (F2) is necessary to suppress completely the pumping signal before sending the image onto the detector.

The system of L1, 2, 3 lenses is used to prevent diffraction effects during the fluorescence beam propagation through the mask (M) and to enlarge the size of the beam arriving on the photo-cathode in order to cover all its sensitive surface.

The net measured values are corrected by the software before the start of data analysis to eliminate artifacts related to:

- the difference in fluorescence lifetime between parts of the photo-cathode due to artificial delays caused by the electronics;
- the fluorescence time dispersion due to the photon statistics (related to the averaging of number of photons collected by different pixels);
- the inhomogeneous gain map of the photo-cathode surface.

Finally the temporal evolution of the fluorescence intensity is deduced for parallel $I_{||}(t)$ and perpendicular $I_{\perp}(t)$ emission components by averaging the intensity over the corresponding half of the photo-cathode surface at a given moment in time.

Generally the fluorescence lifetime can be inferred directly from the intensity decay curve. The fluorescence emission possesses a mono-exponential temporal

decay in absence of fluorescence quenching factors as in the case of Förster resonant energy transfer (FRET) from an excited species to another dye or aggregate (Subsection 3.1.3).

However calculation of the anisotropy (Chapter 3) parameter demands additional data treatment and reference experiments. There is an imbalance in propagation time for both polarizations after the Glan prism, namely the perpendicular polarization is delayed for 150 ps while turning within the pentaprism. Moreover there is a wavelength-dependent difference in propagation losses for both polarizations.

The fluorescence emission of a dye mixed at low concentration with a solvent provides equal polarization components $I_{||}$ and $I_{\perp}$ due to the rotation of dye molecules (at the timescale bigger than the rotation time of the molecule in solution). Thus the detection-induced depolarization G and delay between polarization components can be measured within the reference experiment in solution of the same dye as used in the actual polymer sample. These parameters are then taken into account for the determination of the fluorescence anisotropy in the thin film:

$$r(t) = \frac{I_{||} - GI_{\perp}}{I_{||} + 2GI_{\perp}} \tag{2.1}$$

The system is capable to measure a signal of duration superior to 180 ps. The origin of such limitation is in the detection system, this boundary being determined from the direct measurement of a 1.2 ps pulse duration.

2.3.3 Spectrofluorimeter

The spectrofluorimeter Fluorolog FL3-221 Horiba Jobin-Yvon depicted on Fig.2.11 was used to study the efficiency and anisotropy of the fluorescence at different wavelengths for various dyes. All measurements were conducted on thin dye-doped polymer films deposed on a glass slide.

The sample excitation is performed by cw light from a broad spectrum source. The power of the excitation beam is monitored by the opening of the entrance slit (the overall lamp power is 450 W), and the wavelength is chosen by means of double-grating excitation monochromator. The detection is made also by a double-grating monochromator. The angular position of the sample can be varied, however there is an optimal angular range, where the parasite reflection of the excitation light to the sensitive element can be minimized (60-75^o of incidence from the normal of the sample).

The set-up permits the detection of polarized components (switch into position 2 in such case). The polarization ratio can be defined by the expression:

$$P = \frac{I_{VV} - GI_{VH}}{I_{VV} + GI_{VH}} \tag{2.2}$$

where

$$G = \frac{I_{HV}}{I_{HH}} \tag{2.3}$$

The grating factor G is included to correct for the polarization dispersion of the emission optics and detectors. The first letter in abbreviation VH (VV etc. in Eq. (2.2, 2.3)) stands for the polarization of the excitation beam $\alpha = 90^o$ or 0^o (respectively V or H), and the second - polarization of detected light P or H

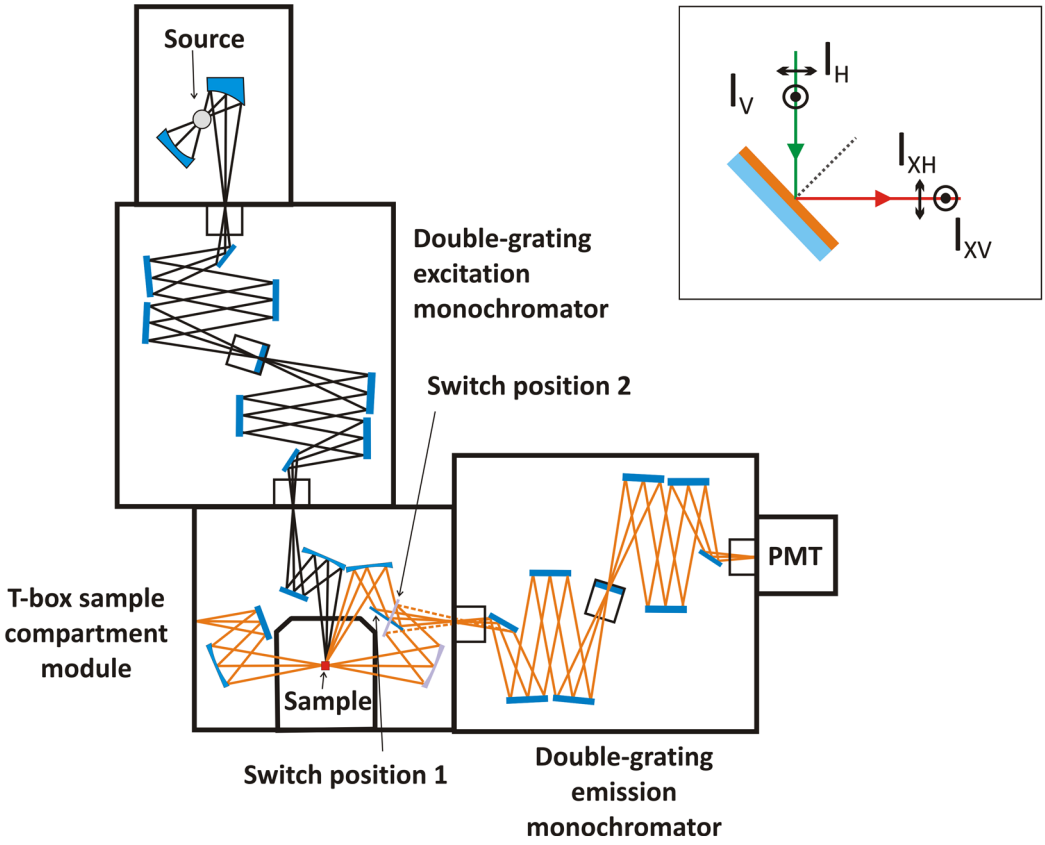

Figure 2.11: *Scheme of the spectrofluorimeter used in the study. PMT stands for Photomultimlier tube detector. The inset explaines the abbreviations used for the pump and detected beam polarizations.*

(respectively V or H). The definition of the grating factor G in (2.2) is taken from the device manual. It is based on the assumption that the intensities of the I_{HV} and I_{HH} components are equal, and the registered values thus differ only as a result of unequal responses from the detecting part. All measurements of the G factor were performed in liquid solutions of the dye in anisole. As G values a priori depend on the emission wavelength, they were recorded for all used dyes in order to cover their fluorescence emission band (Fig.D.2 in Appendix D).

2.3.4 Gain measurement technique in thin films

The principal gain measurement method used in literature is called the "Variable Stripe Length" (VSL) which had been proposed back in the early seventies [109] for semiconductors. However a proper study of gain in an active thin polymer film is a complex task, and attention should be payed to numerous potential experimental artifacts, as for instance diffraction problems and coupling effects [110]. In this Sub-section, the methodological overview is provided together with a description of the experimental arrangement used in the study.

The VSL is based on a 1-dimensional amplification model: if the pump cross-section is patterned in the form of a narrow stripe of variable extension, the photons propagating along the stripe will be the main contribution to the output emission. In the case where the gain can be considered homogeneous within the stripe axis, its value can be inferred from the output intensity dependence on the stripe length.

The emission within the infinitesimal stripe extension dz situated at a distance z from the edge is imposed by a couple of factors: the fraction of total number of photons spontaneously emitted in the solid angle $\Omega(z)$ propagating along the

stripe and those created as a result of the modal gain[1] amplification:

$$\frac{dI}{dz} = (A_{sp}N^* \times h\nu)\left[\frac{\Omega(z)}{4\pi}\right] + g_{mod}I \tag{2.4}$$

here A_{sp} is the spontaneous emission rate, N^* - the excited state population density, $h\nu$ - the energy of a single emitted photon. The net modal gain $g_{mod} = \Gamma g_m - \alpha_r$ contains the net material g_m gain taken with a waveguide confinement factor Γ, and the propagation loss coefficient α_r.

This general equation is integrable under few working hypothesis (constant collection efficiency, homogeneity of gain and pump intensity along the pumped stripe z) and reduces to:

$$I_{ASE}(z) = \frac{\left(A_{sp}N^*h\nu\frac{\Omega}{4\pi}\right)}{g_{mod}}(e^{g_{mod}z} - 1) \tag{2.5}$$

The gain value can be deduced from the experimental data by fitting them with equation (2.5), as was actually done for results presented in Sub-section 5.1.3.

The elegance of this method can be further taken advantage of the introducing gain saturation effects (via an intensity dependent factor for g_{mod} and N^*).

The VSL experimental study of optical gain measurements in active thin polymer films was performed at the Organic Photonics group (Paris 13 University) by Hadi RABBANI-HAGHIGHI, and the scheme exploited for the experiment is shown in Fig.2.12.

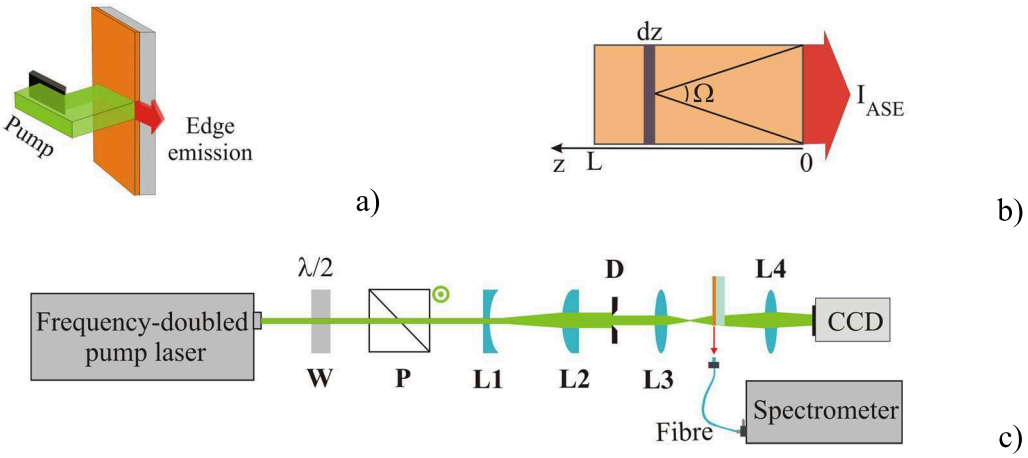

Figure 2.12: *Variable Stripe Length (VSL) technique: a) pumping and emission configuration, the length of the pumping region is controlled with a blade; b) scheme for ASE calculation; c) experimental set-up. Here W is a half-wave plate, P - polarizor, L1-4 stand for optical lenses and D for adjustable blades.*

The laser source was identical to the one we used for our micro-laser experiments: namely a Q-switched Nd:YAG laser at 1064nm (PowerChip, Teem Photonics; 700 ps pulse duration, 10 Hz repetition rate); more specific to this experiment is the use of external frequency-doubling Lithium triborate crystal (resulting in 532 nm pumping beam wavelength and about 500 ps duration). The standard combination of half-wave plate and polarizer (W, P Fig.2.12) is placed to vary the pump beam intensity (Sub-section 2.2.1).

[1]Modal gain is the result of a coupling of the material gain with the pump distribution and propagating mode profile inside the layer, is being discussed in details in Sub-section 5.1.2.

The laser beam was then focused through the cylindrical lens L2 into a thin stripe on the sample surface perpendicularly to the edge. The length of the stripe was controlled by a pair of adjustable blades D, where the central part of the stripe was selected to ensure a uniform intensity along the pump zone. Since the initial laser beam diameter was insufficient (1 mm) to perform an accurate study, the diverging lens L1 was introduced prior to the cylindrical one so as to enlarge the beam and obtain a final stripe width of 320 μm (measured at $1/e^2$ by a beam analyzer - Spiricon SCOR 20 CCD camera, 1600*1200 pixels with the 4.4 μm pixel side) [111].

In order to avoid diffraction effects of the pump stripe onto the blades, the optical conjugation of sample and blades was performed by an imaging system with one-time magnification (L3). ASE spectra were registered by the spectrometer, while the stripe shape and intensity distribution were controlled by CCD camera (Spiricon SCOR 20). The latter is optically conjugated to the sample by a L4 lens to eliminate diffraction effects on the image.

2.3.5 Streak-camera

Among various properties, we addressed experimentally the temporal characteristics of the fluorescence and ASE (results being discussed in Sub-sections 3.2.1 and 4.2.2).

Response time of the fast photo-diode is typically of the order of 1ns, which hinders the usage of such devices for the study of the processes of ns and sub-nanosecond duration. Optoelectronic streak-cameras are known to be optimal measurement tools for the direct monitoring of ultra-fast phenomena. This device serves to transform the temporal features of light pulses into spatial ones.

The accurate study of spontaneous and stimulated emission dynamics was performed with the available streak-camera set-up (OPTOSCOPE by ARP, Fig.2.13) of the Laboratoire de Photophysique et Photochimie Supramoléculaires et Macromoléculaires (PPSM lab) of ENS de Cachan under the guidance of Arnaud BROSSEAU. The set-up was designed to measure the optical pulses with durations of the order of ms down to ps.

The primary pump source is a Nd:YAG laser generating pulses with a duration of about 10 ns at 1064 nm. Some modification steps explained below provide 35 ps pumping pulses at either 532 or 355 nm. The initial pulse duration is first reduced by passage through the in-cavity volume with a laser dye solution with reverse saturated absorption property (Kodak 7834 dye in 1,2 dichloroethan). The next step consists in extracting a single pulse from the generated sequence by a Pockels cell. After several amplification stages the signal frequency is modified by a frequency doubling crystal (or doubling and mixing crystals) allowing to generate a pumping wavelength of 532 nm (or 355 nm).

The set-up is shown on Fig.2.13.a, where the above described part is depicted together with the pump laser. At its beginning, the pump beam is directed by beam-splitter (B) onto a fast photo-diode. Its output acts as a trigger for the analysis of the temporal characteristics by the streak camera. There is a necessity to introduce an artificial delay for the signal analyzed by the streak camera, in order to access the linear part of the sweep circuit curve. A 13m delay line is used to provide such delay (set of mirrors R1-R4).

The sample emission (fluorescence or ASE) under the pump beam excitation is directed to the entry slit of the monochromator (F1) and simultaneously enlarged with the system of lenses L1,2 (to cover all the sensitive region). After the intensity of the examined wavelength has been selected by the monochromator, light enters the streak-camera (Fig.2.13.b).

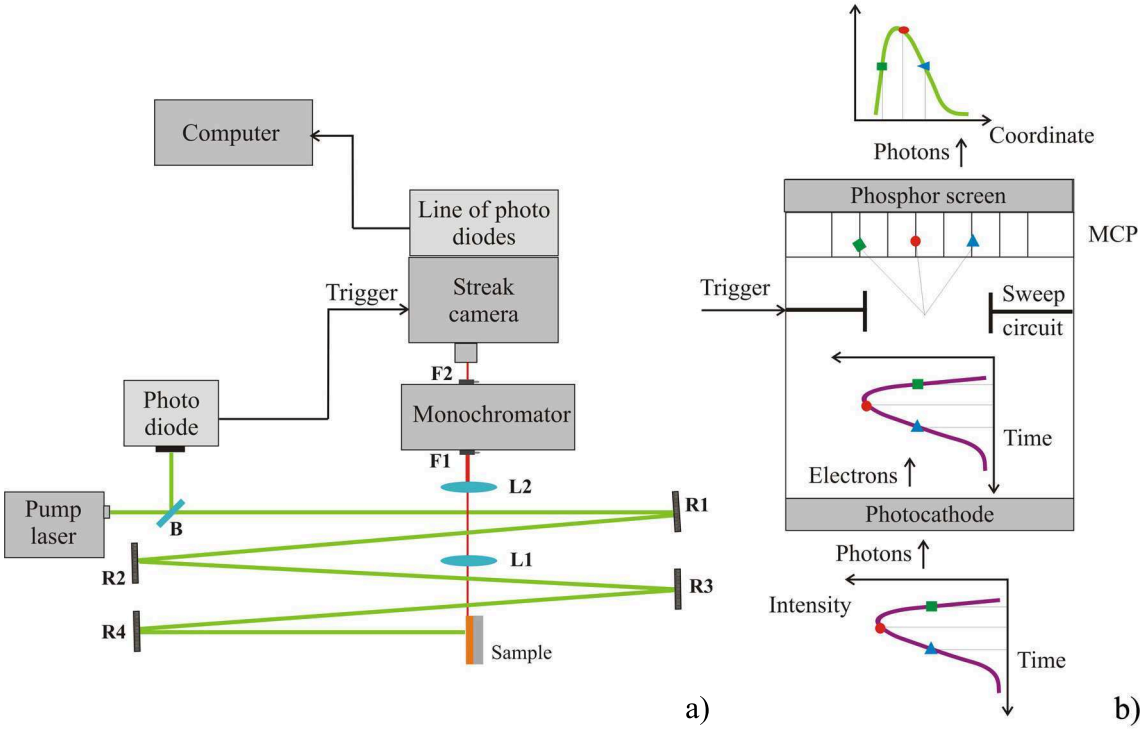

Figure 2.13: *Description of the streak-camera set-up: a) overall functional map of the system, b) streak-camera part. The elements given by acronyms are respectivelly a beamsplitter (B), mirrors (R1-4), lenses (L1,2), slits (F1,2) and multi channel plates(MCP).*

The arrival of photon on the photo-cathode surface causes the electron emission. While propagating through the vacuum tube towards the anode, the electrons are redirected by the sweep circuit (guided by the trigger) according to the moment of passage with the respect to the start of the acquisition (Fig.2.13.b). Thus the temporal character of the light pulse is transformed into a lateral position of the electrons on upon entering the multi-channel plate (MPC). The latter is used to amplify all the electrons before they impact the phosphor screen. The emission by the phosphor screen is read-out by a set of 512 photo-diodes (2.5 μm * 2.5 mm) and their output processed numerically.

Chapter 3

Emission anisotropy in thin film

Many powerful techniques in fluorescent detection are based on the effect of fluorescence anisotropy. Indeed, the emission properties of a laser based on fluorescing dye molecules are obviously affected by the eventual anisotropy of the gain medium. This was indeed demonstrated from the start of liquid dye lasers, and well into the eighties, numerous publications were devoted to this phenomenon. However the influence of such process on the emission properties of solid state lasers with the gain medium made of fluorescent molecules has, to our knowledge, not been systematically investigated to this day.

The aim of this chapter is therefore to prove that the intrinsic fluorescence anisotropy of specific dye molecules together with the polarization state of the pump beam are the two main factors that define the basic emission properties of dye-doped polymer systems. This Chapter starts with the reminder on the basics of fluorescence anisotropy theory, from the motivations that lead us to expand it all the way to details of the calculations for a micro-laser geometry so as to allow for comparison with experimental results.

The second part then focuses on the anisotropy of stimulated emission. The nonlinear enhancement of amplified spontaneous emission (ASE) and lasing result in the forcing of the emission properties and particularly of their polarization features as will be shown in the second part of the chapter.

3.1 Fluorescence anisotropy

The effect of fluorescence polarization in small fluorescent molecules was first described by Jean Perrin back in 1926. B the end of the 20th century, this issue had matured into powerful models and techniques for studying molecular interactions, as the latter strongly influences the emission properties of fluorophores (as present in the examined solution).

The emitting fluorophores are known to behave like radiating dipoles [89]. When a single fluorescent molecule is pumped by a linearly polarized light, it absorbs according to the projection of the polarization of incident light filed polarization on the absorption dipole[1] (Fig.3.1.a) and a photon polarized along the emission dipole is subsequently emitted (Fig.3.1.c). In most cases, for $S_0 \rightarrow S_1$ pumping, absorption and emission dipoles are close to collinear ($\beta \rightarrow 0$, where β is the angle between absorption and emission moments, Fig.3.1.b,c). An isotropic assembly of such molecules provides emission in all directions. The emission intensity along each propagation direction can be decomposed into two orthogonally polarized components.

[1] Is also know in literature as a "transition moment".

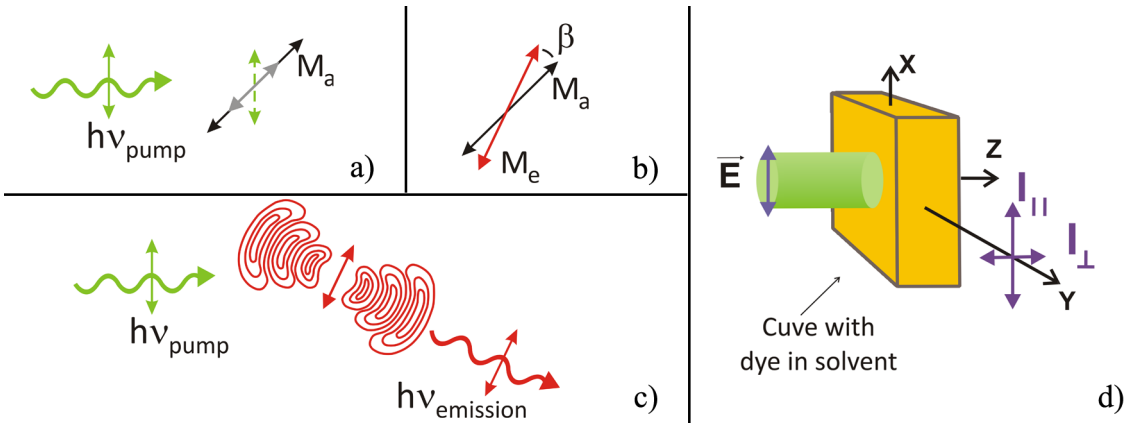

Figure 3.1: *Pictorial definitions of the various entities to the theory of fluorescence anisotropy: a) absorption of the incident photons by a dye molecule; b) emission and absorption dipoles of dye molecules; c) relative orientation of directions of propagation and polarization of the in- and outgoing photons; d) composition of the fluorescence emission - components polarized along (intensity $I_{||}$) and perpendicularly (intensity $I_{\perp}$) with respect to the pump polarization.*

The scheme on Fig.3.1.d depicts a classic experiment on fluorescence anisotropy [70, 69]. A small amount of the examined fluorophore is mixed with a solvent and put in the transparant flat bottom container, then pumped by a linearly polarized light propagating along the z direction. The detection of the fluorescence emission takes place along the y direction. If the pump is polarized along the x-axis, the emission along y has two polarized components respectively: along the pump ($I_{||}$) and orthogonal to it ($I_{\perp}$); the same two components will be observed when the detection takes place along the z direction. However the detection along the x direction will provide two $I_{\perp}$components, polarized orthogonally with respect to each other.

The ratio between the $I_{||}$ and $I_{\perp}$ intensity components accounts for polarization state of the fluorescence and is an intrinsic property of a given material. It can be described by either the anisotropy parameter (r) or the degree of polarization (or polarization ratio, P):

$$r = \frac{I_{||} - I_{\perp}}{I_{||} + 2I_{\perp}}$$
$$P = \frac{I_{||} - I_{\perp}}{I_{||} + I_{\perp}} = \frac{3r}{2 + r} \tag{3.1}$$

The magnitude of each parameter holds information as to the ratio of the $I_{||}$ over $I_{\perp}$ component, while its sign indicates which one is dominant over the other (for example r, $P > 0$ when $I_{||}$ is larger). Preference is given to one or the other of these parameters by different communities merely due to historical reasons [70, 69]. The physical difference between them lies in their respective normalization convention - either by the total emitted intensity along the observed direction for the P or the total emitted intensity along three axes for r, the latter being quite useful to analyze measurements in many-component liquid solutions. However the second normalization method is non-trivial in the general case of random emission directions with respect to the pump beam propagation and polarization orientation. Bearing this in mind, we prefer to focus hereafter on the polarization degree (P).

From its definition in (3.1), one may infer that the P parameter can hold any

possible value between -1 (for $I_{||} = 0$) and 1 (for $I_{\perp} = 0$). However the actual range is known to be different, as some values of P can not be reached due to molecular properties of molecular species. A textbook formula (to be proved later in the section devoted to calculation) for fluorescence detection technique describes the relation between the anisotropy parameter and the molecular properties (β being the angle between absorption and emission dipoles):

$$r_0 = \frac{3\cos^2\beta - 1}{5} \tag{3.2}$$

Known as the fundamental anisotropy, r_0 is the standard theoretical value for the r fluorescence anisotropy parameter and an isotropic distribution of dyes (as in the liquid phase) in the absence of any motion or depolarization processes [69, 70]. Thereby, in case of an isotropic distribution of fluorophores and in the absence of resonance energy transfer (RET), formula (3.2) must be valid as well for solid state media. In terms of *P,* the corresponding expression is as follows:

$$P_0 = \frac{3\cos^2\beta - 1}{\cos^2\beta + 3} \tag{3.3}$$

and shows that the actual excursion range for an isotropic distribution of dyes is [-1/3; 1/2], and not [-1; 1].

Nevertheless, some P values that we obtained experimentally in ASE and planar micro-laser configurations appeared to be beyond such a prescribed interval. We focus hereafter our attention on the fluorescence anisotropy theory in view of its application to our case, so as to try and account for the observed phenomena and learn to use them on purpose in the spirit of molecular and device engineering.

3.1.1 Motivations

The above described effect of fluorescence anisotropy might influence the emission properties of polymer-based dye-doped micro-lasers, where the gain medium is provided by dye molecules. The first research issue that needs to be addressed in this perspective are the possible limitations due to the fluorescence anisotropy in thin (0.5-20 μm) spin-coated polymer films, doped by a laser dye:

- The existing phenomenological approach does not account for a varying linear polarization orientation of the pump beam (Fig.3.2.a).

Decomposition of the emitted intensity into two orthogonal transverse components $I_{||}$ and $I_{\perp}$ is advantageous only if the pump beam is polarized orthogonally with the respect to the emission direction, as for instance in a vertical emission configuration (occurring along the z-axis while the pump is polarized within x-y-plane). However, an arbitrary pump polarization in the edge emission configuration (along the y-axis) is not orthogonal to observation direction. It is therefore convenient to operate with expressions containing measurable parameters. Thus to characterize the emission along y-axis, two polarizations (both orthogonal to the y-axis and with respect to each other) should be considered: along the layer height (I_H) and within the plane (I_P).

- Non-isotropic distribution of dye molecules in thin spin-coated films.

The fluorescence anisotropy theory was initially developed for fluorescent molecules in liquid solutions. The rotation of molecules leads to the random orientation of

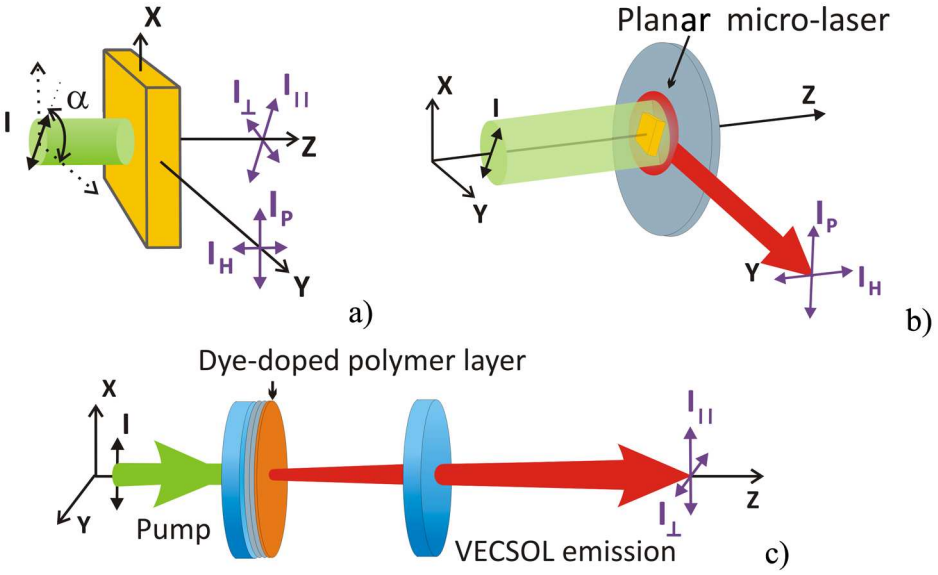

Figure 3.2: *Description of different lasers emission configurations with respect to the pump beam polarization: a) general scheme for an arbitrary orientation (angle α, defined with respect to the y-direction) of the linear polarization of the pump beam; b) planar micro-laser; c) VECSOL.*

the absorption dipoles of 3-D molecules. In the case of spin-coated polymer thin films doped by a laser dye, the fluorophores are more tightly encapsulated by the rigid matrix (a typical reorientation time in polymers is of the order of 5 ns as compared to 0.2-0.5 ns in liquid solutions [112]). An isotropic distribution of molecular dipoles must then be ensured by the fabrication process so as to simplify interpretations. Some publications state that spin-coating itself does not lead to radial alignment of molecules in PMMA polymer (although the alignment phenomenon is known for various other polymers). However there exists a possibility that in a thin polymer film the molecules are mainly oriented within the film plane [113]. Which brings in the need for an improvement of the fluorescence anisotropy theory in the case of a non-isotropic distribution of fluorophores.

- Anisotropy in the case of stimulated emission

The stimulated emission process, be it a lasing regime or amplified spontaneous emission (ASE), may lead to emission anisotropy features completely different from that in the fluorescence case, due to the nonlinear regime involved therein. But a deeper upstream understanding of the peculiarities of fluorescence anisotropy provides a better insight onto the description of stimulated anisotropy. This question is addressed in the second part of this chapter (Section 3.2).

In conclusion, the classic fluorescence anisotropy theory is inconsistent with our experiment. In order to conduct a proper study on polarization effects in our configuration a more general model should be developed, that takes into account all above mentioned issues (Sub-section 3.1.2).

An apparently natural way to proceed with the analysis would be in determination of the P parameter from such a general model, followed by a comparison of our experimental results with available literature on the one hand, and our model on the other. However the latter is rather difficult. Even in a typical fluorescence anisotropy set-up and in the simpler case of an isotropic distribution of molecules, the measured r_0 value is not constant for some molecules. It varies with the change of excitation wavelength even within one singlet band [70] due to the dispersion

of the absorption anisotropy. Moreover, their value is modified in the presence of the resonance energy transfer.

We are interested in the proper values of fluorescence anisotropy in thin dye-doped polymer film in the edge and vertical emission directions. However, the experimental verification on anisotropy in these directions may be challenging. In this regard, any model should provide the basis for an analysis of the emission in an arbitrary direction suitable for measurements. Thus, it should be able to infer the fluorescence polarization ratio along edge emission direction from the molecular structure and orientation in a film so as to compare it with the lasing regime.

Although the aim of our study is the stimulated emission of micro-lasers, attention is paid also to the analysis of spontaneous emission. Indeed, as will be shown in this and following chapters, some of the lasing features of our system evidence the distinctive impact of the fluorescence anisotropy of thin dye-doped polymer films on spontaneous and stimulated phenomena.

3.1.2 Model

This part is devoted to calculations of anisotropy properties of the edge emission (the field is denoted as E, along the y-axis direction on Fig.3.2.a-b, which corresponds to the propagation direction of a 2-D micro-laser emission) and vertical emission (denoted as V, along the z-axis direction on Fig.3.2.a,c , VECSOL configuration).

We start with the explanation of the calculation basis and critical issues. Then the polarized emission components of interest are calculated and analyzed. Finally the polarization ratio in various configurations is deduced and explored.

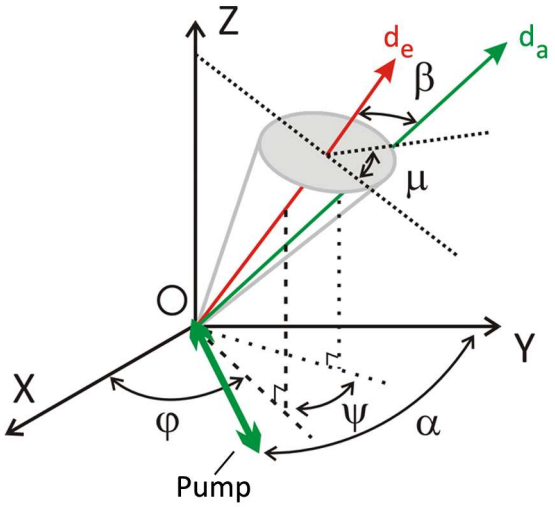

Figure 3.3: *Orientation of dipoles: absorption (d_a) and emission (d_e) moments are oriented at the angles θ_a and θ_e with respect to the z-axis, β - angle between moments, ψ - between their projections on the xy plane, φ - angle between the x-axis and projection of d_e on the xy-plane, α - angle between the y-axis and the pump beam polarization, the angle μ denotes the position of d_a on the cone around d_e (z-axis and vectors d_e and d_a are coplanar when μ=0 or π, with d_e in between z-axis and d_a when μ=0).*

Calculation model

First of all, some new parameters must be introduced to extend the terminology of fluorescence anisotropy in order to account for polarization effects in polymer-based planar micro-lasers:

• the angle α between the pump polarization and the y-axis (Fig.3.2.a),

• the intensity components polarized within the micro-laser plane (I_P) and orthogonally to it (I_H - along the cavity height) for the emission along y-axis (analog to $I_{||}$ and $I_\perp$ characterizing the emission along the z-axis, Fig.3.2.b, c).

The introduction of I_P and I_H instead of the more widely-used TE and TM specification is justified just as follows. Indeed the approximation of the effective refractive index applies to an in-plane configuration with infinite layers. The electromagnetic field can then be split into two sets of modes with independent polarizations, traditionally labeled as TE (and TM) if there is no electric (resp. magnetic) component along the z direction (see Fig.3.2.a for notations).

It must be pointed-out that, as the detection is only sensitive to the electric field, a measure of I_H involves only TM modes, while I_P should a priori gather both TE and TM modes (the polarizer influences only the electric field component).

In the case of ASE experiments with infinite layers, the electric components of the TM mode are measured in the far-field and are thus polarized purely orthogonally to the y direction (i.e. no E_x component). The strict equivalence TE-I_P and TM-I_H is then valid.

As the thickness of dye-doped polymer layer, spin-coated on a commercial wafer (thickness and refractive indexes of all layers being detailed in Chapter 2.1), was chosen on purpose so as to sustain a single maximum of the electric field, there exists only one mode for each polarization (e.g. one TE and one TM mode). These two modes have very close effective refractive index (1.50). However, tiny differences are enhanced by the non-linearity of stimulated emission. Firstly, the effective index of TE is slightly higher than that of TM ($\Delta n \simeq 5.10^{-3}$, Section 1.3), which means that the TE mode is more localized inside the gain layer [114] and thus more amplified. Secondly, the silica layer is finite. Losses through the silicon layer are then altering mostly the TM mode, which is less confined into the PMMA propagating layer. These arguments show that mode considerations (without molecular influence) can explain the discrepancy between both components.

In the general case of an arbitrary shape for the resonator, the validity of the effective index approximation fails at the boundary (since the layers are not infinite) [115], and the measure of P gives an insight onto the electromagnetic modes which co-exist within the cavity. So the I_P and I_H components are introduced in order to facilitate the comparison in different configurations of experimental results with theoretical predictions.

In order to proceed with calculations, the orientation of dipoles and the pump polarization should be defined. The unit vector of the excitation electric field is defined as $\mathbf{e} = \{\sin\alpha,\, \cos\alpha,\, 0\}$ (as referred previously, α is the angle between the pump beam polarization and the y axis). Considering the general case of a non-collinear orientation of the absorption and emission dipoles, we correspondingly introduce the unit vectors along dipole absorption and dipole emission (Fig.3.3) as:

$$\begin{aligned} \mathbf{u_a} &= \{\sin\theta_a \cos(\varphi+\psi)\,,\ \sin\theta_a \sin(\varphi+\psi)\,,\ \cos\theta_a\} \\ \mathbf{u_e} &= \{\sin\theta_e \cos\varphi,\ \sin\theta_e \sin\varphi,\ \cos\theta_e\} \end{aligned} \tag{3.4}$$

Orientations are given here in Cartesian coordinates referring to the spherical angular variable $\Omega = (\theta, \varphi)$. For the sake of simplicity, θ_e will be referred hereafter as θ.

The intensity emitted along a given axis (namely the γ-axis) in the far-field approximation can be presented as the following 3-D integral embedding the product

of the following ingredients: the absorption probability P_a; the emission probability described by the magnitude of Poynting vector $\Pi_{e\gamma}$ ($\Pi_{e\gamma}(\Omega) = \Pi_{ej}(\theta,\varphi) \propto \|\boldsymbol{\gamma} \times \mathbf{u}_e\|^2$) of emission along this axis and the orientation distribution $f(\Omega)$ of the fluorophore in the polymer film (Appendix B):

$$I_\gamma = I_{\gamma 0} \int_\Omega P_a(\Omega) \, \|\boldsymbol{\Pi}_{e\gamma}(\Omega)\| \, f(\Omega) d\Omega \tag{3.5}$$

The $I_{\gamma 0}$ constant (general name for I_{E0} or I_{V0}) contains the information on the absorption and emission properties of the dye and the pumping beam intensity, and its exact value is addressed in Chapter 5.

The absorption probability of a dye molecule is proportional to the scalar product of the pump excitation ($\mathbf{e}$) and the absorption moment of the molecule proportional to $\mathbf{u}_a$ (Appendix B.2):

$$P_a(\Omega,\mu,\psi) \propto \|\mathbf{e}\cdot\mathbf{u}_a\|^2 = \frac{1}{4}\left(A - B\sin^2\theta\,(1-\cos(2\alpha+2\varphi))\right) \tag{3.6}$$

where coefficients A and B are functions of β defines as $A(\beta) = 2 - 2\cos^2\beta$ and $B(\beta) = 1 - 3\cos^2\beta$.

The component of the Poynting vector along the axis of interest (y-axis and z-axis respectively for edge or vertical emission) can be decomposed in a combination of two orthogonal terms:

$$\begin{aligned} \Pi_{e\,y}(\Omega) &\propto \underbrace{\sin^2\theta\cos^2\varphi}_{I_P} + \underbrace{\cos^2\theta}_{I_H} \\ \Pi_{e\,z}(\Omega) &\propto \underbrace{\sin^2\theta\sin^2(\varphi+\alpha)}_{I_{||}} + \underbrace{\sin^2\theta\cos^2(\varphi+\alpha)}_{I_\perp} \end{aligned} \tag{3.7}$$

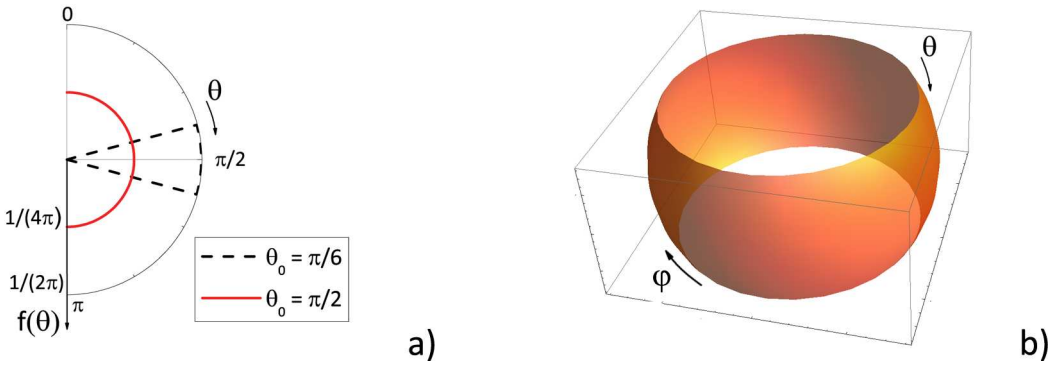

Figure 3.4: *Distribution function $f(\Omega)$: a) projection of the distribution in polar system of coordinates; b) same distribution on full spherical coordinates.*

In the absence of radial alignment during spin-coating, which we verified experimentally (see Sub-section 3.1.3) for the dye-doped films used in study, the dye distribution must be invariant with respect to rotation around the z-axis [113]. Furthermore, if a structural fluorophore distribution anisotropy takes place at the level of spin-coated thin films, in first approximation it should decrease the number of molecules with an emission dipole oriented orthogonally to the film plane. For an unique model to account for various fluorophore distributions (from in-plane (2-D) to an isotropic one (3-D)), a relevant parametrization of the distribution

function $f(\Omega)$ must be introduced. For the sake of simplicity we parametrize by way of an angular variable θ_0, defined in a range from 0 (pure 2-D) to $\pi/2$ (pure 3-D), and may be specific to each type of dye:

$$f(\Omega) = f(\theta, \varphi) = \begin{cases} \frac{1}{4\pi \sin\theta_0}, \ \theta \in \left[\frac{\pi}{2} - \theta_0; \frac{\pi}{2} + \theta_0\right]; \\ 0, \ \theta \in \left[0; \frac{\pi}{2} - \theta_0\right] \cup \left[\frac{\pi}{2} + \theta_0; \pi\right] \end{cases} \tag{3.8}$$

This distribution function accounts for a uniform orientation within a ring-like portion of the unit sphere, symmetrical with the respect to the equatorial x-y plane.

Intensity components

After subsequent integration over φ and θ, the following expressions can be obtained for the intensity components of emission along edge (I_P, I_H) and vertical ($I_{||}$, $I_\perp$) directions (Appendix B.2):

$$\begin{aligned} I_P &= I_{E0}\frac{1}{240}(10A(3 - \sin^2\theta_0) - \\ &\quad - B(2 - \cos 2\alpha)(15 - 10\sin^2\theta_0 + 3\sin^4\theta_0)) \\ I_H &= I_{E0}\frac{\sin^2\theta_0}{60}\left(5(A - B) + 3B\sin^2\theta_0\right) \\ I_{||} &= I_P\left(\alpha = \frac{\pi}{2}\right) \\ I_\perp &= I_P(\alpha = 0) \end{aligned} \tag{3.9}$$

Visualization of these expressions is plotted on Fig.3.5 which helps to reach some important conclusions. Some of these consequences can be actually foreseen without calculations just from symmetry considerations and the emission properties of single dipoles, thus confirming the validity of the model:

- The role of the pump beam polarization (angle α) is of great importance for the emitted intensity polarized within the layer plane (I_P-polarized component), no matter if the fluorophores distribution model is 3-D ($\theta_0 = \pi/2$, Fig.3.5.a) or 2-D ($\theta_0 = 0$, Fig.3.5.b). In fact, by setting any β value on the graph, one can see that the variation of the pump beam polarization introduces significant change to the I_P value. Moreover, in some limit case ($\beta \to \pi/2$), it becomes advantageous to apply the pumping beam polarized along ($\alpha = 0$) the emission direction, but not orthogonally to it ($\alpha = \pi/2$), which may seem counter-intuitive. Such variation is arising from the very nature of the molecules and is not at all influenced by the orientation of dyes, as it works theoretically for both 2-D ($\theta_0 = 0$) and 3-D ($\theta_0 = \pi/2$) models (Fig.3.5.a,b for $\beta \to \pi/2$).
- At the same time the component polarized orthogonally to the layer plane (I_H) does not depend at all on the orientation of the linear pump beam polarization (indeed $I_H(\alpha = 90) = I_H(\alpha = 0)$). Such conclusion can be also made from symmetry considerations taking into account, that the dye distribution used for the calculation is invariant with respect to rotation around the z-axis.

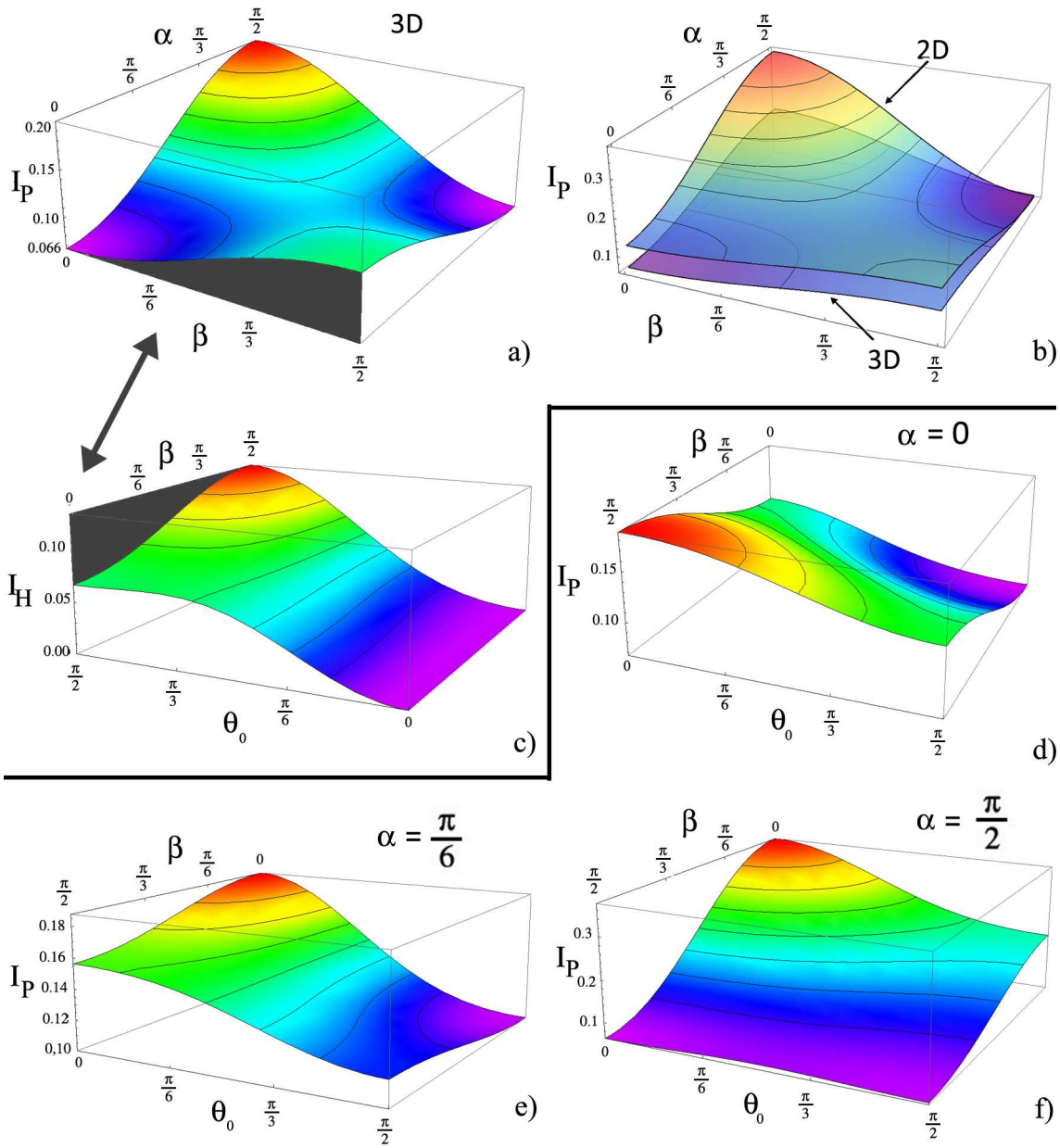

Figure 3.5: *Representations of I_P (polarized in plane) and I_H (polarized orthogonally to the sample plane) as functions of angles α (orientation of the pumping beam polarization), β (angle between absorption and emission dipoles) and θ_0 (angle describing the angular spread of the dye emission moment distribution around the x-y plane). $I_P(\alpha, \beta)$ for fixed value of θ_0: a) 3-D (i.e. $\theta_0 = \pi/2$); b) comparison of 3-D and 2-D (i.e. $\theta_0 = 0$); c) $I_H(\beta, \theta_0)$ component (I_H is independent of α). $I_P(\beta, \theta_0)$ for fixed values of α: d) $\alpha = 0$ ($I_P = I_\perp$), e) $\alpha = \pi/6$, f) $\alpha = \pi/2$ ($I_P = I_{||}$). All plotted intensity components are normalized by I_{E0}.*

- According to the model, when the orientation of the emission moments of the dye molecules is predominantly within the layer plane (2-D model, $\theta_0 = 0$), there is no emission polarized orthogonally to this plane. In other words the I_H component is canceling (Fig.3.5.c with $\theta_0 \to 0$). This is consistent with the well known property of radiating dipoles to display no emission in the direction orthogonal to the the dipole axis.

- The maximum of the I_H component in the 3-D ($\theta_0 = \pi/2$) case is achieved only for a configuration with orthogonal absorption and emission moments ($\beta \to \pi/2$, Fig.3.5.c).

- The I_P and I_H components are not equal in the general case, except for an isotropic distribution (3-D, $\theta_0 = \pi/2$) at $\alpha = 0$ (Fig.3.5.a,c, $\theta_0 = \pi/2$).

The aim of this study is in prediction of the fluorescence anisotropy, however a separate analysis of the polarized intensity components can appear useful for the experimental verification on the validity of a model. For instance, the fact that the I_H component is independent from the pumping beam polarization was proved experimentally (although for guided fluorescence, Fig. 3.15).

Polarization ratio

In order to describe the emission anisotropy one of the two parameters P or r should be evaluated (3.1). Considering the degree of polarization (P) for the emission from the edge and vertical configuration (Appendix B.2), the following expressions can be derived (Fig.3.6):

$$\begin{aligned} P_E &= \frac{C_1 + C_2 \cos^2\beta + \cos 2\alpha \,(3\cos^2\beta - 1)}{C_3 + C_1 \cos^2\beta + \cos 2\alpha \,(3\cos^2\beta - 1)} \\ P_V &= \frac{3\cos^2\beta - 1}{2} \frac{1}{C_4 + C_5 \cos^2\beta} \end{aligned} \tag{3.10}$$

Here the expression of $C_i = C_i(\theta_0)$ is detailed in Appendix B.3. It becomes obvious from these expressions, that in the general case the anisotropy of edge and vertical emission are strongly differing.

The presence of non-linearities in stimulated emission must influence its anisotropy, resulting in a value different from that in thespontaneous emission case. Indeed, the experimentally obtained P_E in the case of stimulated emission (will be discussed in Section 3.2) are shown to lay beyond the predictions from the theory of fluorescence anisotropy. But the comparison of both anisotropies is very important for the understanding of the peculiarities of lasing.

However, as was mentioned in the introduction, there is a possibility of non-isotropic distribution of dye molecules in spin-coated films. The model, developed in this Sub-section, aims at giving the theoretical basis for fluorescence anisotropy in the most general case including orientation effects in thin polymer films. Still, measurement of fluorescence anisotropy in the edge configuration in a thin polymer film remains rather involved (addressed in Section 3.2). Thereby, thorough analysis of the results, provided by our model, should help the interpretation of experimental results.

Exp.(3.10) describes the degree of polarization in the general case of a non-isotropic dye distribution. Now we address the limit cases of isotropic (3-D, $\theta_0 = \pi/2$) and in-plane (2-D, $\theta_0 = 0$) orientation of dye molecules, and examine each of them carefully, starting from 3-D orientation ($\theta_0 = \pi/2$):

$$\begin{aligned} P_E &= \frac{(3\cos^2\beta - 1)(1 - \cos 2\alpha)}{7 - \cos^2\beta - \cos 2\alpha \,(3\cos^2\beta - 1)}, \\ P_V &= \frac{3\cos^2\beta - 1}{3 + \cos^2\beta}, \end{aligned} \tag{3.11}$$

The formula for P_V is identical to Exp.(3.3), known from fluorescence detection and already mentioned in the introduction to this Chapter. Meanwhile P_E varies between 0 and P_V following the change of pump beam polarization from $\alpha = 0$ to $\alpha = \pi/2$ (see Fig.3.6.e).

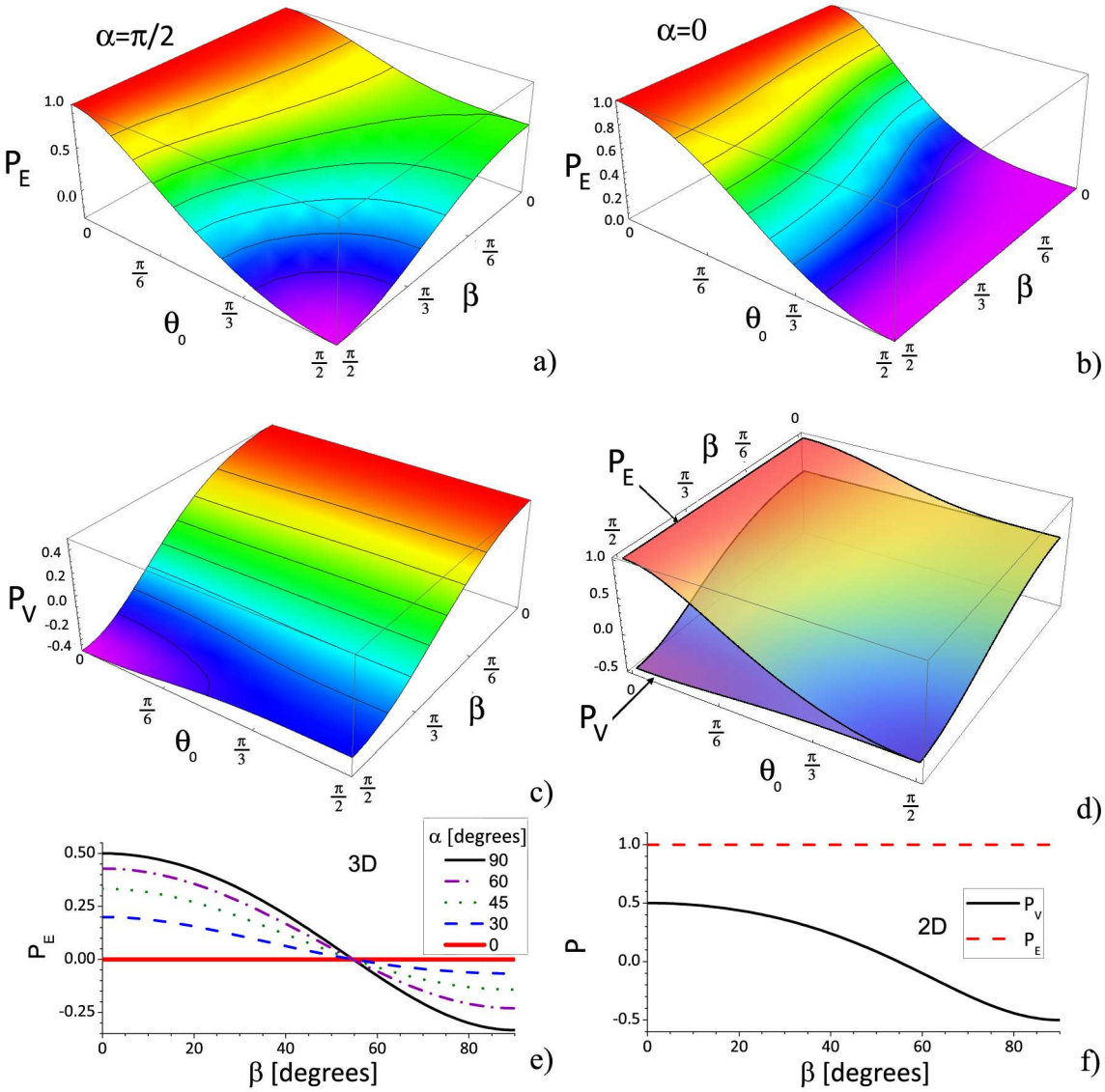

Figure 3.6: *Depiction of the polarization degree P for the edge (a-b) and the vertical emission (c), as well as their comparison at $\alpha = \pi/2$ (d), in the 3-D (e) and 2-D cases (f).*

In the 2-D case, the formulas (3.10) reduce to:

$$\begin{aligned} P_E &= 1 \\ P_V &= \frac{3\cos^2\beta - 1}{2 + 2\cos^2\beta} \end{aligned} \tag{3.12}$$

and are plotted on Fig.3.6.f.

The value of P_E, is valid, as the I_H component is canceling in the 2-D ($\theta_0 = 0$) case (there is no dipole emission in the direction orthogonal to its axis). The P_V value is also not identical to that in the 3-D case, and its range is broadened to the [-0.5; 0.5] interval.

Comparing the intermediate case between 3-D ($\theta_0 = \pi/2$) and 2-D ($\theta_0 = 0$) distributions of dyes (3.6.d), it becomes clear that $P_E \geq P_V$, leading to *higher anisotropy values,* other conditions being equal. In the stimulated emission regime, this should lead to significant difference in emission anisotropy between these two directions of observation (Section 3.2).

Also if the β angle lays somewhere in the range [45, 55°] interval P_V tends to zero regardless of the dye distribution, leading to a sort of "magic" angle for the dye in the polymer with respect to vertical emission direction.

The range of values for P_E and P_V parameters are both obviously influenced by two parameters: the dye distribution as defined by θ_0 and the molecular properties (β angle) (see Fig.3.6.a-f), while the pump beam polarization (α) affects only P_E.

The dipole distribution law influences slightly P_V, which means that an experimental analysis of the anisotropy along vertical direction is *insufficient* to get a full insight on the system, *and* θ_0 *remains undefined* (3.6.c). The lower limit for P_V is obtained at $\beta = \pi/2$ and varies from -1/2 to -1/3 respectively in the 2-D ($\theta_0 = 0$) and 3-D ($\theta_0 = \pi/2$) cases (Tab.3.1). Its upper limit is constant (equal to 1/2) for all distribution types, and is being reached at $\beta = 0$ (Fig.3.6.c,e,f).

Table 3.1: *The values of existence of P for various models*

	P_V	P_E
2-D	$\left[-\frac{1}{2};\ \frac{1}{2}\right]$	1
3-D	$\left[-\frac{1}{3};\ \frac{1}{2}\right]$	$\left[-\frac{1}{3};\ \frac{1}{2}\right]$
other case ($0 < \theta_0 < \pi/2$)	$\left[-\frac{1}{2C_4};\ \frac{1}{C_4+C_5}\right]$	$\left[\frac{C_1-\cos 2\alpha}{C_3-\cos 2\alpha};\ 1-\frac{C_3-C_2}{C_1+C_3+2\cos 2\alpha}\right]$

The situation is completely different for the P_E parameter (Tab.3.1): both the lower and upper limits grow with the change of dipoles distribution from 3-D ($\theta_0 = \pi/2$) to 2-D ($\theta_0 = 0$) models. Moreover, the range of P_E parameter can be varied with the pumping beam polarization: the lower limit (obtained as for P_V when $\beta \to \pi/2$) increases in a 3-D ($\theta_0 = \pi/2$) model from -1/3 at $\alpha = \pi/2$ to 0 at $\alpha = 0$. If we consider the P_E range at fixed θ_0 angle, its width increases when pumped with a polarization orthogonal with respect to the observation direction ($\alpha = \pi/2$). Still, the main conclusion is that a slight deviation from the isotropic model suggests an increase in the possible upper value of P_E, as shown on Fig.3.6.a. The fluorescence anisotropy along edge emission direction *may then be higher than* 0.5, which is the case for the amplified spontaneous emission in the examined thin films.

In conclusion, the provided calculations showed that $P_E > 0.5$ is possible for fluorescence emission in thin-film configuration, when the distribution of emission dipoles of dye is non-isotropic. In order to engineer a prevailing I_H polarization along the edge emission direction (3.6.a, $P_E < 0$) one should use molecules with almost orthogonal absorption and emission dipoles ($\beta \to \pi/2$) and a distribution close to isotropic (3-D, $\theta_0 = \pi/2$). Possibilities to reach such a regime are discussed in details in Chapter 4.

3.1.3 Comparison with experimental results

The experimental verification of fluorescence anisotropy aimed to investigate the following issues:

- checking the assumption of a non-isotropic distribution for the dye dipoles;
- assessing the reliability of our proposed model;
- further comparison with the stimulated emission case.

In this regard several series of measurements were performed with different equipment. Such approach allowed to explore various properties at the time and perform the cross-check on the experimental results. This section contains description of

the experiments held in the various configurations in order to explore the fluorescence anisotropy properties in the dye-doped thin polymer films. The results obtained with each technique are discussed as well.

We use the FLIM set-up, described in Sub-section 2.3.1, to conduct the experimental study on the dynamics of fluorescence anisotropy and the anisotropy itself along vertical emission direction (P_V). The 3-D detection set-up (Sub-section 2.2.2) and spectrophotometer (Sub-section 2.3.1) serve to examine the properties of the emission along other directions. In all cases, a polymer layer deposited on a suitable substrate, without a laser cavity, was used for the study.

3.1.3.1 FLIM

As already explained in Sub-section 2.3.1, the FLIM set-up provides the possibility to study simultaneously (with sub-micron spatial resolution) different properties of two orthogonally polarized components of the fluorescence [2]: namely the intensity value and the fluorescence lifetime (Fig.3.7). However the experimental arrangement itself causes a significant modification of the detected fluorescence signal. Such an influence must be identified and subtracted from the rough data (detailed in Appendix D.1).

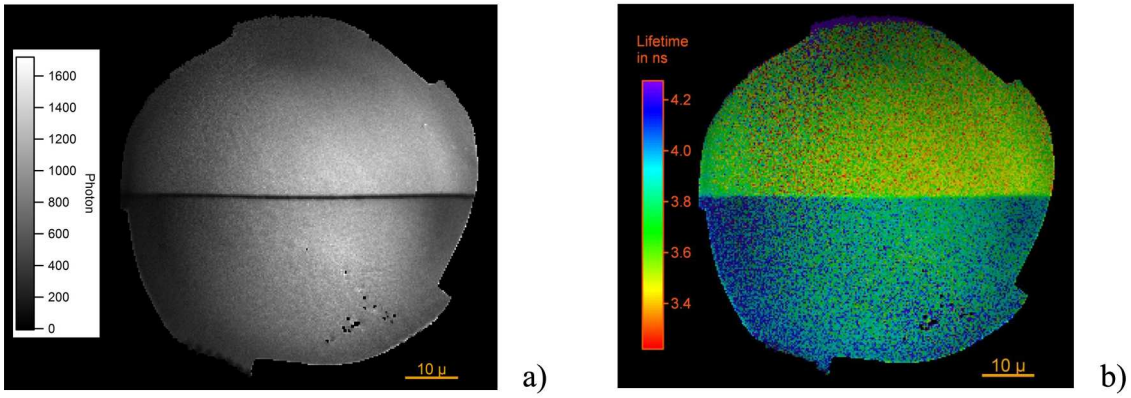

Figure 3.7: *Typical intensity (a) and fluorescence lifetime map (b) for $I_{||}$ (upper part) and $I_{\perp}$ (lower part) obtained from the FLIM imaging set-up.*

Calculations outlined in the previous sections were made for emission along some arbitrary direction, without taking into account the wide-field integration by the objective of the FLIM set-up (NA=0.75) [107]. Considering the possibility of the influence of such an effect on the deduced data, theoretical predictions were obtained by integration of the intensity values in a cone at a given direction, followed by renormalization of all parameters. It appears that for the vertical emission configuration, changes are negligibly small.

The FLIM set-up is traditionally used in the PPSM laboratory for fluorescence study in terms of fluorescence anisotropy (r). For the sake of the experimental soundness and in order to compare the obtained values with the ones published in literature, all data treatments reffered to r-terms (existence range [-0.2;0.4] for an isotropic distribution of dyes). At the end all calculated data were expressed back in terms of P.

Various concentrations of DCM, PM605 and RH640 dyes in a PMMA A6 polymer matrix were examined this set-up.

The analysis of the FRET influence on the anisotropy, provided in the previous section, makes it clear that in order to get the proper value of r for the dye-polymer

[2]The data treatment in our case implied spatial averaging of the sample map

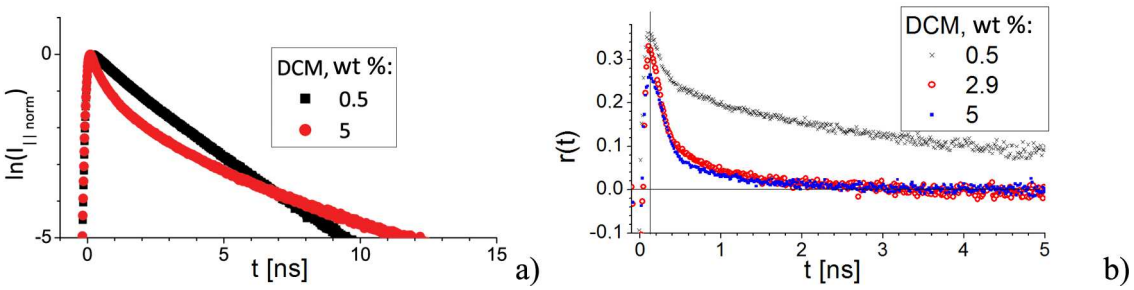

Figure 3.8: *Influence of FRETs on the fluorescence emission on the example of DCM in PMMA: a) mono- and bi-exponential decays of the $I_{||}$ intensity component respectively for 0.5 and 5 wt% concentration , b) reduction of anisotropy with the concentration increase.*

combination of interest, a very small concentration of dye must be used (usually less than 1 wt% [93]). Although the FLIM set-up allows to study the temporal evolution of the fluorescence as well as an eventual anisotropy parameter, the deduced r values vary with the dye concentration due to FRET that appears during the build-up time of the detected signal. The presence of FRET can be detected from the bi-exponential decay of the fluorescence [3] with the increase of dye concentration (Fig.3.8.a).

Table 3.2: *Fluorescence anisotropy (at $t = 0$) of the emission in vertical configuration for several dyes at different concentration levels (at 515nm pumping wavelength). Measurement error is estimated to be about ± 0.02.*

DCM, %	r	P_V	RH640, %	r	P_V	PM605, %	r	P_V
0.5	0.36	0.46	0.4	0.31	0.40	0.9	0.32	0.41
2.9	0.33	0.43	2.3	0.28	0.37	3.5	0.20	0.28
5	0.26	0.35	5	0.25	0.33	5	0.18	0.24
						7.3	0.15	0.21
Deduced β [degrees]								
15			25			25		

The results for three tested dyes are summarized in Tab.3.2. The anisotropy value indeed reduces with the increase of the concentration for those three dyes (Fig.3.8.b). Nevertheless, the fluorescence anisotropy exhibits a quite complex temporal behavior. For a DCM, with fluorescence lifetime of about 2 ns (Subsection 3.2.1), the anisotropy decays rapidly during the first 400 ps (Fig.3.8.b) regardless of dye concentration, followed by a slow exponential decay. Molecules that contribute to a highly anisotropic emission are preferentially oriented with their absorption dipoles along the pumping beam polarization. Such a rapid decrease of anisotropy at the very onset of emission might be caused by the bleaching of those molecules.

It is most noteworthy that anisotropy decays almost to zero during the first nanosecond of emission in samples with a dye concentration above 1% (thus with an important FRET contribution), contrary to samples with relatively small concentrations of dye (Fig.3.8.b).

Fitting these P_V values at lowest measured concentrations with the formula on polarization ratio (Eq.(3.10) from the previous Sub-section) β values are obtained and listed in Tab.3.2. However the dependance of P_V on the distribution type is

[3] A bi-exponential behavior does not provide full evidence on FRET, as it is also possible in case of aggregate formation or inhomogeneous incorporation of dyes in a polymer matrix [91]

weak within this β range, and no conclusion can be drawn from θ_0 values.

The β angle is expected to depend strongly on the pumping wavelength, such as in the case of pumping at the center of the absorption band of DCM with a β value of 25°[93] (at 450 nm) whereas $\beta = 15°$ for pumping at the red edge of the absorption band (at 515 nm). The 532 nm pump used in our micro-laser set-up is even more red-shifted with respect to absorption spectrum. Therefore, the values of P_V and β measured by FLIM may be quite different from values expected at 532 nm pumping.

3.1.3.2 Fluorescence anisotropy measurements on the 2-D set-up

The aim of a study presented in this Sub-section 3.1.3 was to examine experimental anisotropy values of the fluorescence emitted along the vertical and the edge emission directions, in order to check the validity of the proposed model and inferring a basis for the comparison with stimulated emission case.

Unfortunately the anisotropy along the vertical emission configuration does not allow for evetial validation or rejection of the proposed theoretical model. The study of edge emission gives an insight onto the fluorophore distribution. Moreover, it may be used as a cross-check of obtained results, as accordingly to the calculations discussed in the previous Sub-section (3.1.2), the P_E and P_V parameters may be deduced simultaneously from the measurements in the edge emission configuration, by simply varying the pump beam polarization (from $I_\perp = I_P(\alpha = 0)$ to $I_{||} = I_P(\alpha = \pi/2)$).

However it appeared impossible to conduct the proper experience on the fluorescence emission from a polymer slab along edge direction. This Sub-sub-section details all the experimental complications we faced in attempt to measure the edge fluorescence.

First of all, the choice of the sample substrate is crucial if the fluorescence is examined in non-vertical emission direction. In the layers deposited on a silicon wafer covered by 2 μm of silica (used for planar micro-lasers fabrication) the propagation of light becomes possible (even under CW pumping) inside the polymer layer then acting as a planar waveguide (Section 1.3). Most importantly, the created guided mode (Section 1.3) is bound to modify the fluorescence emission, as evidenced on Fig.3.9.a.

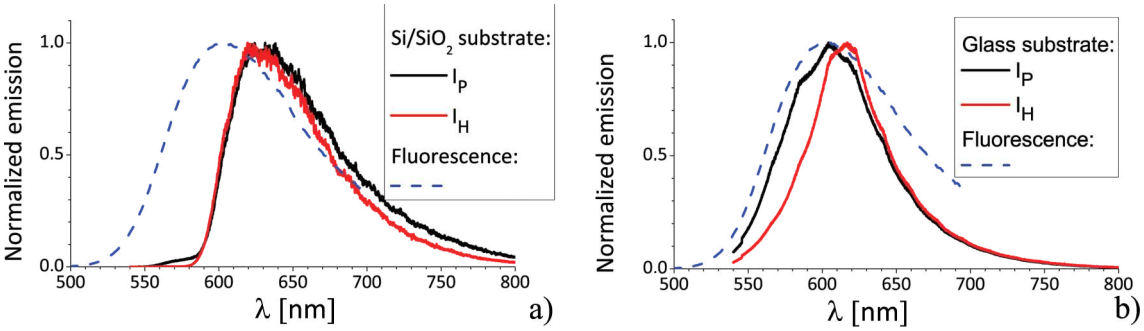

Figure 3.9: *Guided wave fluorescence spectra, measured in the edge emission configuration in a thin PMMA film doped by 5% of the PM605 dye deposited on: a) a Si wafer covered by 2 μm of silica, b) a glass slide. Comparison is made with the fluorescence spectrum measured in an oblique (e. g. "non-edge") emission direction in a film deposed on a Si wafer, whereby guiding is not possible. The excitation wavelength is 532 nm.*

The same problem exists in the case of a polymer layer deposited on a glass substrate (Fig.3.9.b). Such a system possesses an additional drawback: the excess

of polymer along the border due to the spin-coating centrifugation process (Section 2.1) that cannot be easily removed by cleaving as in the silicon-based wafer. Moreover, there are also manufacture defects of the glass slides border shape. Thus the emitted intensity varies strongly with the pump position and lacks reproducibility. The obtained results are shown in Appendix C.3.1. The P_{E} and P_{V} values are generally very close. This is in fact due to better guiding of TE-mode comparing to TM [114]. Taking into account the absence of the overlap with P_{V} values obtained by FLIM, the conclusion is that the wave-guiding influences strongly the emission anisotropy and measured values do not represent the emission anisotropy.

Finally, a sample made on a silicon substrate (without silica layer) is the best candidate towards an unambiguous experiment. In this case there should be no light propagation within the polymer layer (Section 1.3) and thus no risk of exciting ASE or coupling light into guided modes. However, the output intensity along the edge emission direction obtained from such a sample is extremely weak. It is further decreased by a polarizer placed just before the detector, so as to distinguish between the two orthogonally polarized components. The output intensity is then down to a level comparable with measurement error.

The problem arises from the absence of guiding properties in such a sample, so that photons propagating along the edge direction will be strongly attenuated by the absorption by the silicon substrate. Only a small fraction of emitted photons reach the sample edge. As far as the size of pumping region remains much larger than the layer thickness (200 μm diameter versus 0.6 μm height), a much greater amount of photons are refracted through the layer surface rather then at its edge.

In summary, emission along edge direction is either modified with guided effects or is of unacceptably low intensity, to be measured correctly with our equipment. This suggests that the fluorescence should be measured in some direction between vertical and edge, which is addressed in next two sub-sub-sections.

3.1.3.3 Fluorescence anisotropy measurements with the 3-D set-up

The experimental study was pursued with silicon wafer-based samples. The examined emission direction was tilted from layer plane and also non-vertical. At first the 3-D detection set-up (described in details in Sub-section 2.2.2) was used for this purpose. The experiment routine and obtained results are discussed in this sub-sub-section.

To start with, direction of the emission maximum was investigated, as depicted on Fig.3.10.b, and found at an angle $\gamma_0 = 45°$ (Fig.3.10.a). This refracted emission corresponds to internal light propagation at an angle $\gamma = 28.1°$ inside the slab (Fig.3.10.c). In fact, only emitted photons, that propagate within an interval $\gamma\,\epsilon[0; 40°]$ (Fig.3.10.c) can be refracted through the layer surface and thus detected. The difference between the shape of curves on Fig.3.10.b, d evidences that the fluorescence emitted inside the film is not completely uniform.

As the detection direction is different from vertical to edge configuration, the emission components polarized within the layer plane ($I_{P'}$) and orthogonally to it ($I_{H'}$) are calculated (following the same rational as for I_P and I_H, Appendix B.2). Then the polarization ratio $P_\gamma(\alpha, \beta, \theta_0)$ of the emission at $\gamma = 28.1°$ can be examined at two different pumping beam polarizations $\alpha = 90°$ and $\alpha = 0°$. In order to decrease the inaccuracy of the definition of the β and θ_0 angles, one more $d_H = I_{H'}(\alpha = 90)/I_{H'}(\alpha = 0)$ parameter is introduced. It can be easily deduced from the same data set and equals to 1 in the edge emission, but for an arbitrary emission direction it is also a function of β and θ_0.

The calculated curves for these three parameters $P_{\gamma=28}(\alpha = 90°)$, $P_{\gamma=28}(\alpha = 0°)$ and d_H are shown in the next sub-sub-section on Fig.3.12.a-c as function of θ_0 for

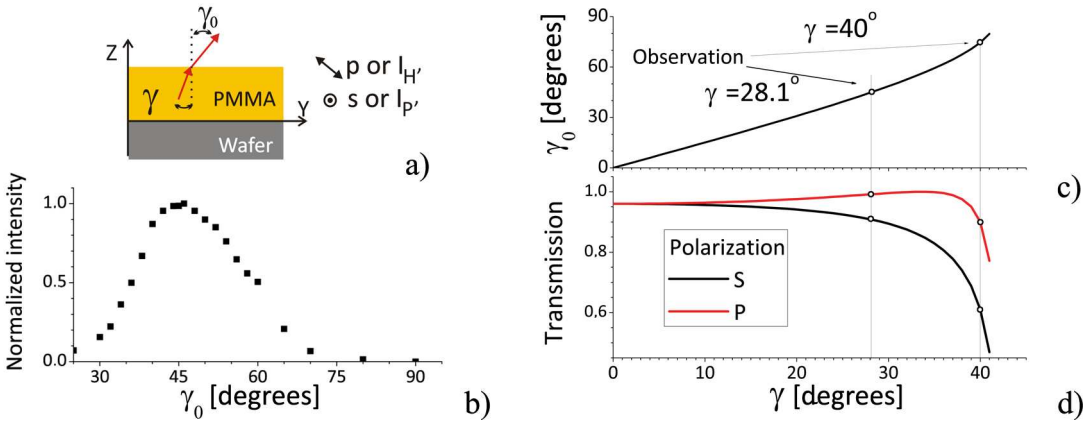

Figure 3.10: *Refraction of fluorescence emission through a sample surface: a) scheme indicating the orientation of incident (γ) and refracted (γ_0) rays in the coordinate system of the set-up (z - vertical emission, y - edge emission); b) experimental distribution of the intensity of the refracted fluorescence versus γ_0; c) visualization of the relation between γ_0 and γ from Snell's law (n(PMMA)=1.5); d) transmission coefficients on the PMMA-air border for s- ($I_{P'}$ polarized in the sample plane) and p- polarizations ($I_{H'}$ - polarized orthogonally to $I_{P'}$ and the emission direction).*

several values of β. The refraction of light at the non-orthogonal incidence of the polymer film boundary alters not only the emission direction, but the intensity of polarized components. So priory to data processing, the transmission coefficients for different polarizations should be taken into account (Fig.3.10.d).

The dye concentration in a sample defines the FRET efficiency (Sub-section 1.1.6), and at concentrations higher 1 wt% the emission anisotropy is significantly altered by FRET. We started with a sample of 5 wt% concentration of DCM in PMMA, to check the polarization ratio in this non-vertical emission direction and compare with results obtained with the FLIM set-up.

First attempt of experimental verification was made with the stable cw laser at 532 nm pumping wavelength (varied intensity up to 50 kW cm^{-2}). However a very rapid degradation of the signal was observed, which seriously affected the deduced parameters and made them unreliable. The values averaged within first measured 2-3 points are given in Tab.C.9 (Appendix C). The clear degradation was then witnessed by a decrease of registered intensity of differently polarized components with increase of pumping intensity. The polarization ratio and d_H parameter also changed with degradation: we stated the increase of $P_{\gamma=28}(\alpha = 90°)$ and decay of $P_{\gamma=28}(\alpha = 0°)$ and d_H.

For this reason we switched to the pulsed pumping regime (Sub-section 2.2.2), and obtained rather different result (Tab.3.3). The absence of notable degradation was evidenced by a stable deduced value of the P and d_H in a large region of the pumping intensities, as it is plotted on Fig.3.12.d.

On the beginning of this chapter one important assumption was made: namely absence of the radial alignment of molecules due to spin-coating. The whole developed model was based on this statement, so it appeared natural to verify it experimentally. The obtained values of polarization ratios in 5 wt% DCM in PMMA for the spin-coated film and dried droplet (apart from spin-coating fabrication following a standard protocol) were indistinguishable within the accuracy range (Tab.3.3).

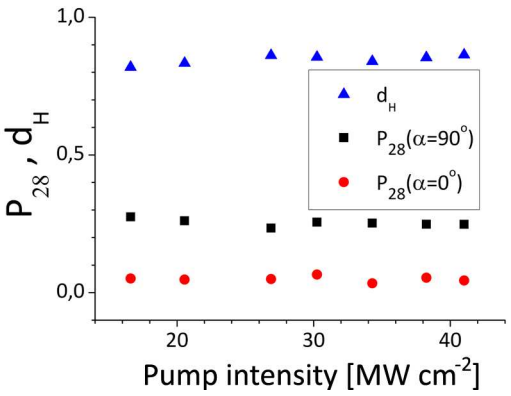

Figure 3.11: *Experimental plots for the polarization degree (P) and d_H parameter, obtained with 3-D detection set-up for the emission at $\gamma = 28.1°$ ($\gamma_0 = 45°$, Fig.3.10.a) with 5 wt% DCM in PMMA (spin-coated layer) under pulsed pumping. Deduced averaged values are provided in Tab.3.3.*

Table 3.3: *Fluorescence anisotropy of the emission at $\gamma = 28.1°$ of PMMA doped with 5 wt% of DCM, obtained with the 3-D set-up under pulsed pumping at 532 nm pumping wavelength.*

Sample	$P_\gamma(90)$	$P_\gamma(0)$	d_H
Spin-coated layer	0.25 ± 0.03	0.04 ± 0.03	0.85 ± 0.04
Droplet	0.25 ± 0.03	0.05 ± 0.03	0.87 ± 0.04

These results are surely insufficient to make proper conclusions. However, the polarization ratio for 5 wt% DCM obtained with 3-D set-up in non-vertical emission direction ($P_\gamma(90) = 0.25 \pm 0.03$) does not exactly match the one provided by FLIM set-up along vertical emission direction ($P_V = 0.38 \pm 0.02$). This may suggest that polarization ratio varies with emission direction.

3.1.3.4 Fluorescence anisotropy measurements on the spectrofluorimeter

The usage of the Fluorolog (Sub-section 2.3.3) set-up appeared to be the simplest way to conduct the anisotropy measurements along a non-vertical emission direction (very important, as emission along the vertical direction does not allow to verify the theoretical model, developed in Sub-section 3.1.2).

The monochromator placed just after the lamp source allows to choose any wavelength for excitation, the source signal being stable in time and allowing to excite the fluorescence emission at a relatively low power levels (43-96 μW depending on the wavelength, the beam size being about 1-2 cm^2). Vertical ($\alpha = 90°$) and horizontal ($\alpha = 0°$) polarizations can be used for fluorescence excitation. Both orthogonally polarized components $I_{P'}$ and $I_{H'}$ can be separately measured via the output polarizer.

The recorded polarized fluorescence component is influenced by the device, which should be taken into account priory to the data treatment. The depolarization effect of the set-up (G factor) and the variation of the excitation power with the position of entrance polarizer (G_H) were deduced from reference measurement in a low-concentration liquid solution of dye and anisole solvent, described in details in Appendix D.2.

The refraction of light at the polymer film boundary also alters the polarized components. The transmission coefficients for different polarizations should be taken into account (Fig. 3.10.d).

The sample was positioned so that emission at 75^o with respect to the normal was collected by the detector ($\gamma_0 = 75°$ on Fig.3.10). This corresponds to a light

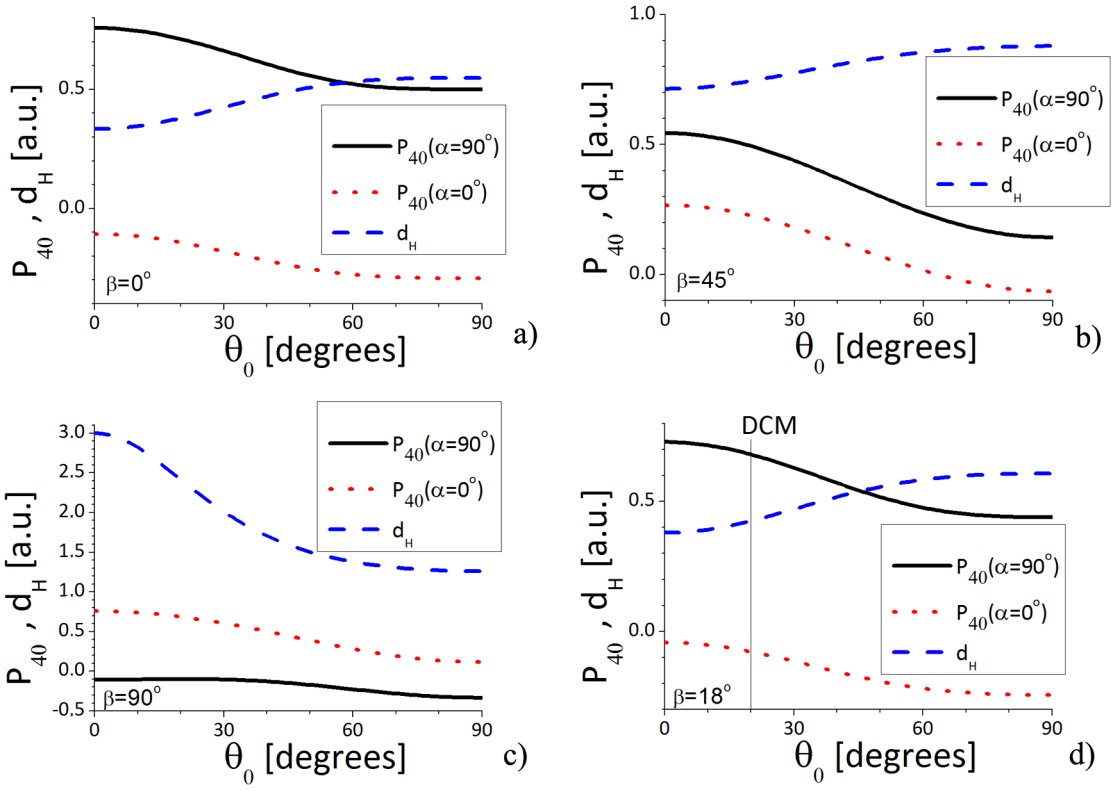

Figure 3.12: *Polarization degree and d_H parameter for the emission at $\gamma = 40°$, calculated from the model described in the previous section for a β angle of: a) 0°; b) 45°; c) 90°; d) 18°. Experimental values on P_{40} and d_H parameters for DCM dye are depicted on (d) (expreimental values differ from those given in Tab.3.5, as they already account for the refraction coefficients for different polarizations).*

propagating at $\gamma = 40°$ inside the polymer layer. The polarization ratio for DCM, RH640 and PM605 dyes is given in Tab.3.4 for different concentrations, and the data for other species as well as under excitation by UV are given in Appendix C.3.2.

Table 3.4: *Fluorescence anisotropy of the emission at $\gamma = 40°$ (at 532nm pumping wavelength) obtained with the spectrofluorimeter. $\alpha = 90°$ corresponds to the pumping polarization parallel to the sample plane. Measurement error is estimated to be about ± 0.03.*

DCM, %	$P_\gamma(\alpha = 90°)$	RH640, %	$P_\gamma(\alpha = 90°)$	PM605, %	$P_\gamma(\alpha = 90°)$
0.5	0.59	0.9	0.36	1.3	0.25
2.9	0.36	5	0.28	4.3	0.25
5	0.34	10	0.23	5	0.24

The anisotropy values (in case of $\alpha = 90°$) decay with an increase of dye concentration (Tab.3.4), and the absolute difference between anisotropy of low and high-concentrated samples is a measure of the important role played by FRET in the emission from low-concentration sample. For instance 1.3% of PM605 seems to be influenced strongly by FRET.

As we know from the measurements on the FLIM set-up, FRET does not play a significant role in the fluorescence emission at low dye concentration (at about 0.5%). Thus, anisotropy values obtained with the spectrofluorimeter from this sample were used to find which set of $\{\beta; \theta_0\}$ values match with all curves $P_\gamma(90)$, $P_\gamma(0)$ and d_H both for 532 nm and 355 nm pumping. The result is given in Tab. 3.6 and Tab.4.3. As DCM is a planar molecule, the absorption and emission dipoles

lie in the molecular plane, and the difference of β values obtained under pumping at various wavelength correspond to the angular distance between these two absorption moments. The $\triangle\beta$ inferred from analysis of fluorescence emission is 34^o and shows good agreement with the 38.4^o value obtained from quantum chemical calculations of the absorption transition dipoles from the molecular structure (Sub-section 1.1.5, Tab.C.5).

Table 3.5: *Parameters of the fluorescence anisotropy in the absence of FRET and for emission at $\gamma = 40°$ (at 532 nm pumping wavelength).*

	$P_\gamma(90)$	$P_\gamma(0)$	d_H
DCM	0.59	-0.12	0.46
RH640 (deduced)	0.54	-0.18	0.46
PM605 (deduced)	0.27	0.02	0.78

Knowledge of β and θ_0 allows to reach the polarization ratio along any emission direction, showing good correlation with FLIM values.

Considering the total intensity emitted at the edge mission direction, it is also possible to deduce the ratio under pumping of two linear orthogonal polarizations $\rho = I(0^o)/I(90^o)$ (Sub-section 5.2.4). And for the DCM molecule a match was found between the ρ value from fluorescence emission value of ρ and that obtained experimentally for ASE and lasing.

The lowest examined concentrations of PM605 and RH640 did not match all curves simultaneously, presumably due to FRET influence. In such cases, the experimental ρ values and P_V values obtained at the 343 nm pumping wavelength of the FLIM set-up were used to infer $\{\beta; \theta_0\}$ as well as $P_\gamma(90)$, $P_\gamma(0)$ and d_H values (Tab.3.5).

Table 3.6: *Fluorescence anisotropy of the emission at $\gamma = 40°$ degrees (at 532 nm pumping wavelength) obtained with the spectrofluorimeter. [1]Measurements could be altered by FRET due to relatively high dye mass concentration.*

Dye	DCM	RH640	PM605
β [degrees]	18 ± 4([93] measured 25° while pumping at 450 nm)	25 ± 4	51 ± 4
β [degrees] (515nm)	15 ± 4	25 ± 4[1]	25 ± 4[1]
θ_0 [degrees]	20 ± 4	27 ± 4	45 ± 4
Inferred P_E ± 0.03	0.9 ± 0.03	0.8 ± 0.03	0.5 ± 0.03
Inferred P_V ± 0.03	0.45 ± 0.03	0.39 ± 0.03	0.15 ± 0.03
P_V (by FLIM)	0.46 ± 0.02	0.39 ± 0.02	0.39 ± 0.02

In conclusions, measurement of the fluorescence anisotropy along various emission directions was a demanding issue.

The fluorescence anisotropy inferred from the FLIM experiment along vertical emission direction allowed for the detection of FRET presence by influences on the anisotropy at the dye doping rates higher of about 1 wt%. These experiments also proved consistent with the developed general model and provided the β value of 15 ± 4° for DCM dye under 515 nm pumping. However, anisotropy along vertical emission direction exhibits low variation with the change of θ_0 dye orientation parameter.

Therefore, verification of general anisotropy model demand the the anisotropy measurements to be performed along other emission directions. The edge emission direction is proved unsuitable for a proper experiment on the fluorescence anisotropy due to respectively guiding effects or very low output intensity value depending on the used substrate. We then adapted the general theory on arbitrary

emission direction and proved it consistent with spectrofluorimeter experiments at two different wavelength. According to these latter results, the dye distribution law depends on the molecular properties, while the angle between absorption and emission moments at 532 nm pumping is non-collinear. A low concentration (<0.5 wt%) RH640 and PM605-based samples should be further verified with spectrofluorimeter in order to confirm the obtained results.

3.2 Emission anisotropy in ASE and laser regime

In fact, the anisotropy value defined from a fluorescence process in the previous Section represents the anisotropy at the very onset of emission, before stimulated emission occurs. However, the stimulated emission process itself, be it a lasing regime or ASE, leads to emission anisotropy features completely different from that of fluorescence, due to the influence of nonlinearities. For instance, the drastic change in the polarization ratio upon the lasing threshold was reported in liquid dye lasers [116].

This problem is addressed here by the analysis of the temporal behavior of emission as well as the dynamics of its intensity components with respect to the change of the pump intensity.

3.2.1 Difference in dynamics

In order to provide a consistent study of the difference between the emission properties of spontaneous and stimulated emission, the dynamics of these processes should be addressed at first.

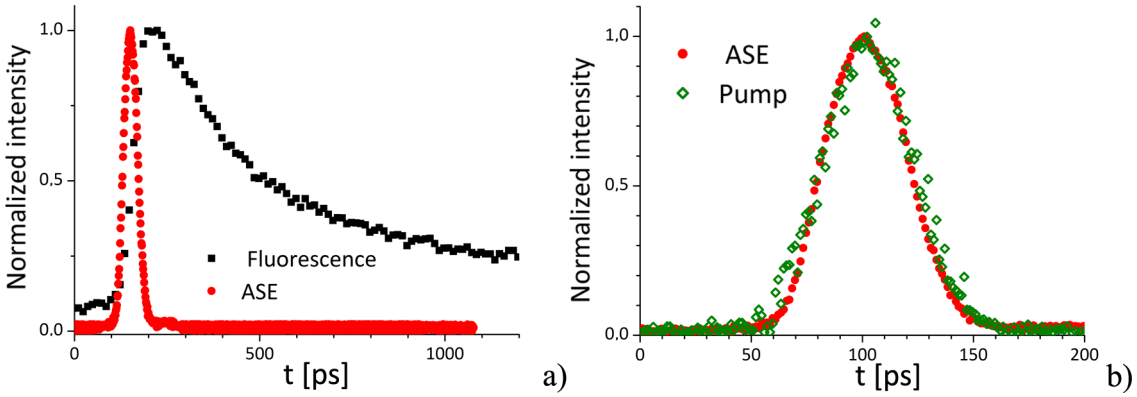

Figure 3.13: *Dynamics of the spontaneous and the stimulated emission in a layer of PMMA polymer doped with 5 wt% of DCM: a) fluorescence and ASE (error ± 60 ps), b) pump signal and ASE (error ± 1.3 ps).*

Results detailed in this section were obtained with the streak-camera (Subsection 2.3.1) on the dye-doped layer of PMMA. The polymer layer was deposited on an adequate substrate towards to the experiment, namely a silicon wafer for fluorescence measurement (except for RH640, where a glass slide was used) and silicon wafer covered by 2 μm silica for ASE.

The main result is that the duration of ASE appears to be much shorter than that of fluorescence: in the case of 5 wt% of DCM dye in PMMA the lifetime decreases to 43 ± 1.3 ps (from 1.8 ns typical for the fluorescence, Fig.3.13.a). In fact the temporal behavior of the ASE signal replicates that of the pumping (duration 44ps, Fig.3.13.b except for RH640, which exhibit a small exponential relaxation for ASE). Apparently in the case of a sub-nanosecond pump duration

or smaller, ASE is faster than fluorescence and thus should not be influenced by FRET.

Comparison of spontaneous and stimulated emission durations for RH640 and PM605 dyes is given in Tab.3.7.

Table 3.7: *Duration of fluorescence (τ_f) and ASE (τ_{ASE}) in PMMA layers doped by various dyes excited at 532 nm (DCM, PM605 and RH640).*

Dye	%	τ_f [ns]		τ_{ASE} [ps]
		Experimental	Literature	Experimental
DCM	0.5	2.0 ± 0.06	2.0 [91]	not measured
	5	1.8 ± 0.06		43 ± 1.3
PM605	5	1.5 ± 0.06	-	43 ± 1.3
RH640	5	2.56 ± 0.06	7.5 [117](λ_p=550nm)	38 ± 1.3

Finally, a more detailed study on the dynamics of both processes was made by repeating the measurements at various emission wavelengths (Fig.3.14). For all three dyes the ASE (Fig.3.14.a) and fluorescence (Fig.3.14.b) duration are shorter when pumped at the edges of the spectrum than at the maximum emission wavelength.

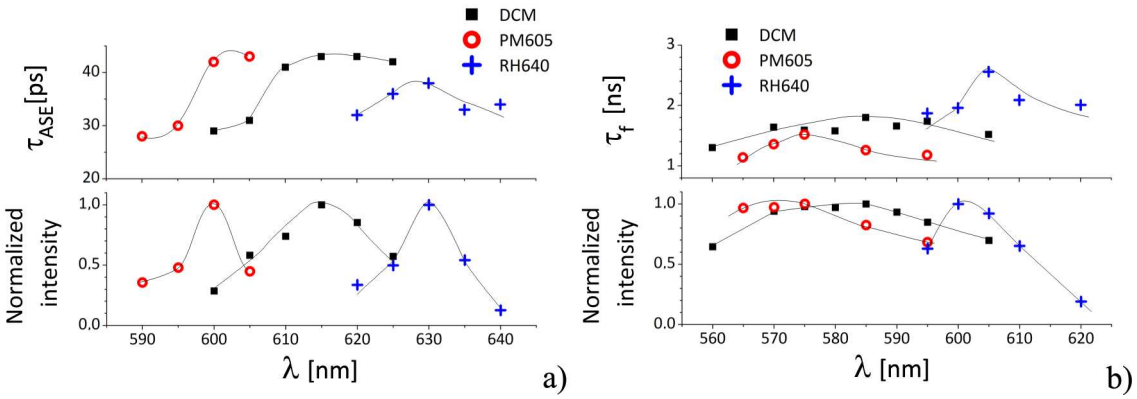

Figure 3.14: *Dynamics of stimulated (a) and spontaneous (b) emission in a layer of PMMA polymer doped with 5 wt% of DCM, RH640 or PM605. The upper frames show the process duration (error ± 1.3 ps for the ASE and ± 60 ps for the fluorescence), and the lower ones - the emission intensity for a series of wavelengths, normalized by the maximum intensity in the spectrum.*

3.2.2 Influence of nonlinearities in the ASE regime

Experiments to evidence edge and vertical emission anisotropy were performed respectively with an in-plane detection set-up at the LPQM (on a polymer layer deposited on a Si/SiO_2 wafer for ASE, as well as for planar micro-lasers) and in a VECSOL configuration at Paris 13 University.

The P plots describing the edge emission configuration in Fig. 3.15.a for ASE and fluorescence emission of various dyes show that the anisotropy of these two processes are quite different. Moreover the anisotropy of ASE appears to be far beyond the limit predicted by the fluorescence anisotropy model (Section 3.1).

The reason, behind such a striking difference was in the stimulated emission nature of ASE. The presence from the start of photons polarized in a given way induces molecules in the excited state to generate a larger amount of photons along this predominant polarization. Thus avalanche effect amplifies the difference between the polarized components (Fig.3.15.a). As the pump polarization lies

within the plane, dyes which are oriented with an absorption dipole in-plane are predominantly excited. Moreover, if β is small, they predominantly emit in-plane. Hence I_P is intensified and then P_E increases with the pump intensity (Fig. 3.15.a).

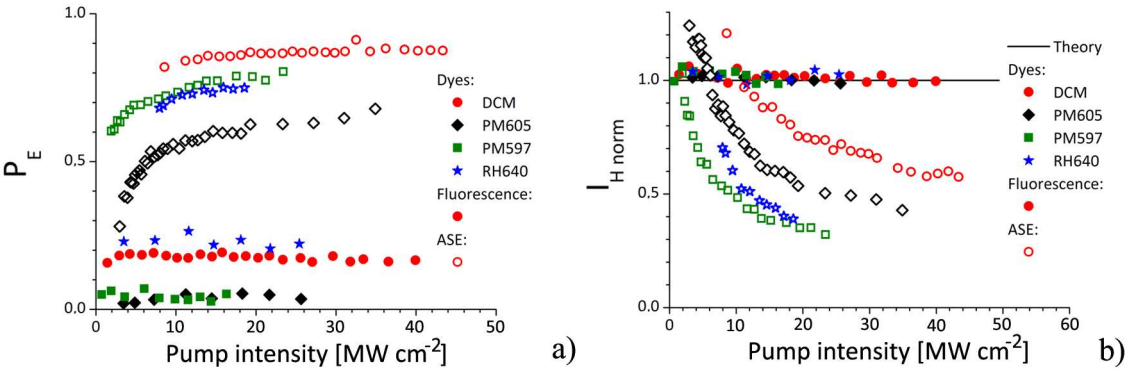

Figure 3.15: *Change of the anisotropy when going from guided fluorescence to ASE (fluorescence generated by CW pumping on a PMMA-doped layer deposited on a Si/SiO_2 wafer): a) P_E , b) I_H .*

One more proof in favor of such an explanation can be found in the behavior of the emitted intensity component that is polarized along the layer thickness (I_H). According to the fluorescence calculations presented in the previous section, I_H does not depend on the pump beam polarization, and thus the two orthogonal pump beam polarization $I_H(\alpha = \pi/2)$ and $I_H(\alpha = 0)$ are equal. This result applies perfectly in the case of fluorescence emission (Fig. 3.15.b), but fails for ASE.

To explain this discrepancy one needs to consider photon fluxes along different directions caused by a linear pump beam polarization. For the sake of simplicity only the in-plane propagation is considered. As far as the photon polarization is always orthogonal to the corresponding propagation direction, two photons with orthogonal polarizations will propagate in perpendicular directions. The linearly polarized pump beam causes photon emission in all directions (Section 3.1), however the emission probability is generally higher (for S_1 pumping) for photons polarized along the pump. Performing the measurement of the intensity component for two orthogonal polarizations $\alpha = \pi/2$ and $\alpha = 0$ is equivalent to measurements along two orthogonal emission directions (respectively standard y and x axis). Considering the photon fluxes in these two directions, it is obvious that the one which is polarized along the pump ($I(\alpha = \pi/2)$), shows higher intensity than the other ($I(\alpha = 0)$). As we deal with stimulated emission, the avalanche effect amplifies the difference between the in-plane emission components propagating in different directions which accounts for the inequality of the I_H components emitted in different directions (Fig. 3.15.b).

3.2.3 Emission anisotropy in micro-lasers

Laser feedback is bound to influence the ratio of these orthogonally polarized emission components with a crucial role played by the resonator shape. The subsequent analysis proceeds on the example of micro-lasers based on the DCM dye, followed by comparison with other molecules.

Generally P depends neither on α (orientation of the pump beam polarization), nor on the pump intensity, if recorded high enough above threshold (typically 20% higher). The results are quite reproducible, with error bars of about 0.05, which means that the differences between shapes in Fig.3.18 are relevant, and hence

relate to specific features of the resulting lasing modes.

The most straightforward shape for a resonator is a Fabry-Perot like cavity with the parallel edges defining the gain medium in-between. In a VECSOL [103], which is a vertical Fabry-Perot like cavity (with the gain layer spin-coated on one of the two mirrors, Sub-section 2.2.3), P was measured to be 0.84 and independent on the pump intensity up to 5 times the threshold value.

For a Fabry-Perot in the in-plane configuration, $P = 0.96$ (Tab.3.8) and also does not depend on the pump intensity (Fig.3.17.a). It should be mentioned, that we purposely designed and fabricated the in-plane Fabry-Perot not in the shape of a long rectangle, but in a way to have only two in-plane borders so as to avoid the possibility of a bi-modal regime (two Fabry-Perot type modes along and across the rectangle, Section 5.2).

Table 3.8: *Anisotropy values P_E measured by the in-plane detection set-up for various dyes for fluorescence, ASE and a ribbon micro-laser (error ± 0.03).*

Dye	DCM	PM605	RH640	MD7
Fluorescence	0.89	0.5	0.8	-
ASE	0.85	0.52	0.69	-
Laser	0.96	0.95	0.93	0.95

However, there is an important difference between the emission polarization of a planar Fabry-Perot and VECSOL: in the latter case, an intra-cavity Brewster plate is used in order to increase the losses and thus to cut off all the emission except the one with the desired polarization. In this case the P parameter was defined by the rotation of the polarizer axis with respect to the pump polarization position above the lasing threshold. The P parameter has another meaning here, namely the ratio of orthogonally polarized output intensity components in the absence of mode competition and at the same pump power value. The continuous lines on Fig.3.16 represent theoretical curves for fluorescence emission $I_X(\alpha)/I_X(\alpha = 0°)$ (formula (B.21), Appendix B.4) following a P_{V} value obtained experimentally for VECSOL emission (Tab.4.5). These theoretical curves were deduced for fluorescence intensity component $I_X(\alpha)$ emitted along vertical direction and polarized at the angle α with respect to the pump beam polarization. Then $I_X(\alpha' = 90°)/I_X(\alpha' = 0°)$ was deduced from VECSOL experiment and used to plot the theoretical curves for fluorescence. A surprising outcome is that the output intensity follows the distribution law of fluorescence anisotropy (Fig.3.16.b), which suggests that the fluorescence anisotropy may influence the threshold value in dye-doped polymer lasers (Subsection 5.2.4 is devoted to this question).

The polarization properties of planar micro-lasers vary significantly with the cavity contour.The non-orthogonal incidence at the dielectric border may induce a significant difference in reflection for the TE and TM polarized waves, which may cause a slight redistribution between the polarized components (Tab.3.9). In square and pentagon micro-lasers, P is greater than zero, so that the I_{p} component dominates. However P is significantly smaller than in a Fabry-Perot cavity, which evidences a redistribution of the light due to reflections at the borders. The difference between P_{square} (0.74) and $P_{\mathrm{pentagon}}(0.9)$ could arise from the periodic orbits sustaining the lasing modes, namely diamond orbit for the square (Section 6.1) and inscribed pentagonal orbit for the pentagon [101].

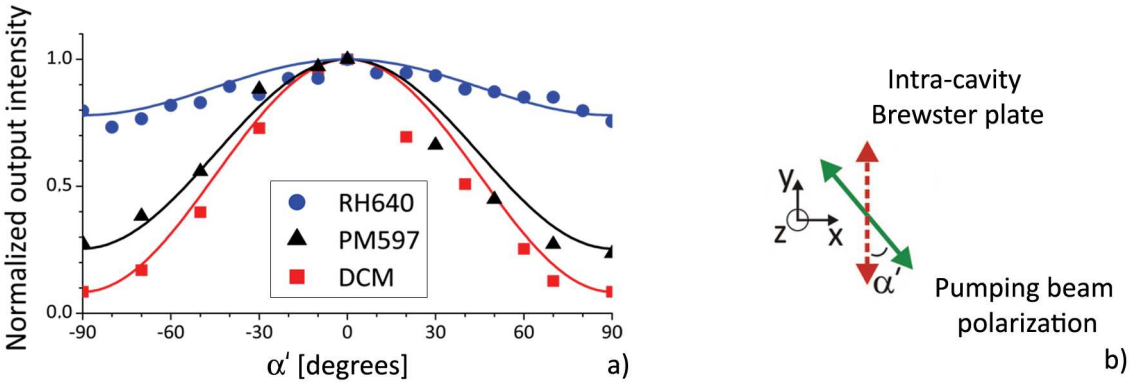

Figure 3.16: *Polarization properties of the VECSOL: a) output intensity of VECSOL lasers under a fixed pumping power at varying angles for pumping beam polarization with respect to the orientation of an intra-cavity Brewster plate; b) scheme on respective orientation of the pumping beam polarization and the orientation of an intra-cavity Brewster plate.*

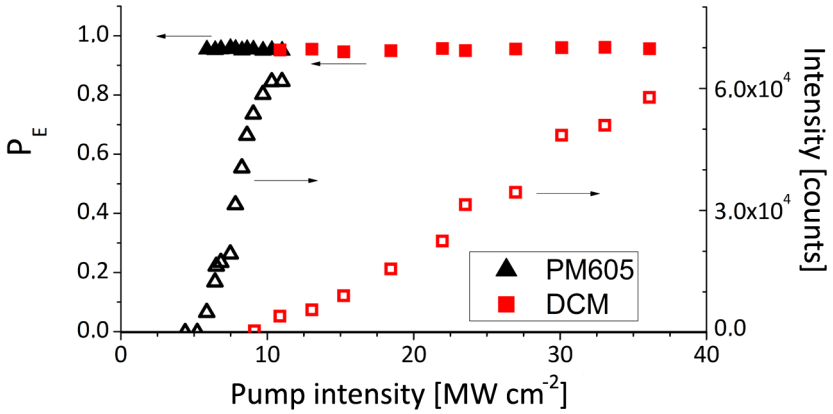

Figure 3.17: *Polarization ratio of a ribbon micro-laser. Empty and filled figures describe respectively the micro-laser output intensity and polarization ratio.*

Eventually, the limit case of whispering gallery modes (WGM) should be considered. In stadium cavities [118], P is close to 1, as in Fabry-Perot lasers, whereas spectral analysis confirm that the lasing modes are indeed WGM [68]. Actually the stadium shape leads to chaotic dynamical systems, which could result in a short photon lifetime and then to a lasing behavior close to that of a Fabry-Perot cavity. For stadiums, we did not notice any influence on P neither of the pump polarization α, nor of the cavity aspect ratio (ratio between length and radius, see [68] for instance). Disks should be the archetypal shape for WGM. But the presence of the substrate hinders their observation [119]. P values reported here were then measured from disks lying on a pedestal. As reported in [119], these cavities present two kinds of lasing mode families: WGM and Fabry-Perot like modes. The later behave like real Fabry-Perot modes, in particular regarding their P value. On the contrary, WGM are insensitive to the pump polarization α and their P value is close to zero, probably thanks to a long photon lifetime, which allows for efficient mixing of the polarized components at the boundary [120]. Finally we considered kite-shaped micro-lasers (Section 6.3), which are defined by a slight deformation from a disk [121] and present the crucial advantage to emit WGM without having to resort to a pedestal technology. In that case, P should tend to zero. The structure of the electromagnetic modes is then allowing by itself to flip the ratio between the polarized components, which was forced by gain properties for the

other shapes. However, experimental P value is negative, which may be caused by the co-existence of two modes (Fabry-Perot orbit and WGM) [122, 123].

Table 3.9: *Comparison of P obtained from ASE and laser above the threshold for several dyes. Measurement error is estimated to be about ± 0.03.*

P	DCM	PM605	MD7	P	DCM	PM605	MD7
Fluorescence	0.9	0.5	-	Stadium	0.95	0.87	0.1
ASE	0.85	0.52	-	Disk (WGM)	0	-	-
Fabry-Perot	0.96	0.95	0.9	Kite (FP mode)	0.8	0.7	0.9
Pentagon	0.9	0.95	-	Kite (WGM)	-0.2	-0.85	-0.7
Square	0.75	0.85	0.7	VECSOL(P_V)	0.84	-	-

These results obtained with different gain layers are gathered in Tab.3.9 and plotted for the DCM and PM605 on Fig.3.18. In fact, a nature of the dye also influences the P parameter, as evidenced for instance by the Whispering Gallery mode of a kite micro-laser, which exhibits slightly negative P for DCM-based cavity and highly $P <$ -0.5 for Bodipy dyes.

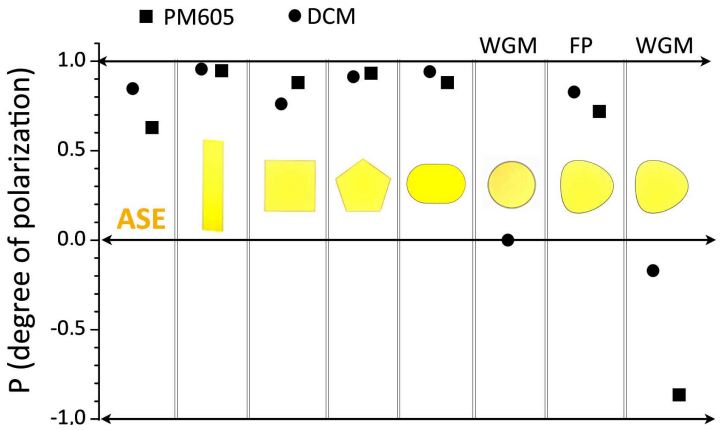

Figure 3.18: *Comparison of the emission anisotropy in micro-lasers of various shapes, based on DCM (circles) or PM605 (squares). FP stands for the Fabry-Perot periodic orbit of kite micro-laser, WGM - for its whispering gallery mode (Section 6.3).*

Meanwhile, the polarization ratio of ribbon micro-laser is $P > 0.9$ for all tested dyes. This results is inconsistent with published in the literature values. Indeed even the Fabry-Perot based on the liquid dye solution, where molecules can easily reorient, exhibit polarization ratio higher 0.5 [124]: $P = 0.7$ for solution of Coumarin 154 in methanol and $P = 0.9$ for PPV-derivative polymer in chlorobenzene (P value of dye is lower due to faster reorientation time).

Chapter conclusion

In this Chapter we provided a theoretical and experimental analysis of emission anisotropy in the dye-doped polymer layers and in the lasers based on them.

The existing fluorescence anisotropy model failed to explain our experimental results on emission anisotropy of a dye embedded in the polymer matrix. Thus we extended this model for a general case of non-collinear absorption and emission

dipoles of the dye, and when distribution in the medium is non-isotropic, allowing as well to account for random orientation in the layer plane of the linear pump polarization.

According to this general model, the emission anisotropy is not only defined by the molecular properties but varies also with observation direction, being higher in the layer plane (edge) than in emission direction orthogonal to it (vertical). Moreover, the obtained theoretical expressions for the emission along vertical direction suggest an impossibility to infer dye distribution parameter from measurements in this direction. However, the experimental verification of fluorescence anisotropy in the non-vertical direction posed many difficulties, such as modifications of the fluorescence emission influenced by substrate type or induced by energy transfer. In this regard, the emission anisotropy must be examined in lowest possible dye mass concentration, that still allows for a measurable output signal.

We performed an experimental study on fluorescence anisotropy, along vertical emission direction with the FLIM set-up, and in non-vertical direction with spectrofluorimeter. Contrary to general earlier assumption in liquid dye lasers, the absorption and emission dipoles of examined dyes under 532 nm pump were proved to be non-collinear. Moreover, the inferred dyes distribution is non-isotropic, with emission dipoles oriented mostly in the layer plane (in the cone around the plane, with the dye-dependent cone angle). This effect demands further exploration, especially because the expected distribution of the absorption dipoles stay close to isotropic and thus can not be easily detected with ellipsometry techniques.

Difference in the dynamics between fluorescence and amplified spontaneous emission, which we explored with the aid of a streak-camera for several dyes, suggests that stimulated emission alters the polarization properties. Indeed, the anisotropy features of planar micro-lasers depend strongly on the resonator shape, exhibiting a predominant in-plane polarization for all resonances except those with long photon lifetime, like Whispering Gallery Modes. However, we expect the predominant in-plane polarization of the fluorescence to play an important role in the polarization state of the stimulated emission. The following Chapter is devoted to the analysis of different approaches to influence the fluorescence and thus stimulated emission anisotropy in thin dye-doped polymer films, and their experimental verifications.

Some of these results were presented on the 492 WE-Heraeus-Seminar “Micro & macro-cavities in classical and non-classical light” (Physikzentrum Bad Honnef, Germany, 2011) and on the Matériaux et Nanostructures pi-Conjugués (MNPC) conference (Obernai, France, 2011), and published in Phys. Rev. A, 86, 043817 (2012).

Chapter 4

Shaping the emission polarization

In the previous Chapter, a detailed analysis of the emission anisotropy was presented. The nonlinearities of the lasing regime were proved to influence significantly the stimulated emission properties, in such a way that slight initial advantage of one polarized component over the other suffices to cause a difference in the laser emission properties (for a majority of cavities shapes).

Pumping to the S_1 level for a majority of fluorophores relies on a small value of the angle β. In order to change the prevalent emission polarization of planar microlasers from the in-plane (I_P) to orthogonal emission (I_H), one needs to somehow influence their balance at the fluorescence level, which in its turn can be made by-passing the relation between the orientation of the pumping beam polarization and that of emission dipole.

To reach this goal, we propose two different ways: pumping the laser dye by energy transfer via another species (on the example of the organo-metallic Alq_3 molecule) and also pumping to the second or higher singlet state of the dye molecule (pumping to S_n instead of S_1).

4.1 Pumping via energy transfer

The pumping mechanism of the dye molecule in this case is indirect (Fig.4.1.a): another substance is excited by the pumping and the excitation is subsequently passed to the dye molecule by resonant energy transfer (Sub-section 1.1.6). The influence on the output polarization in such a case is provided by two factors: the dye is no-more excited by an in-plane polarized field, and secondly if the absorbing molecule has several absorption dipoles, this can randomize still more the polarization of resulting excitation field.

The choice of the pumped molecule is constrained by the absorption band of the laser dye: the energy of the excited state of the molecule must overlap with the absorption band of the laser dye. This is indeed the case for all the dyes used in our study including Alq_3 pumped at 355nm (Fig.4.1.b). Alq_3 is a small fluorescing organo-metallic molecule, widely used in OLED technology and reported for its very efficient energy transfer when blend with DCM [38]. Unfortunately Alq_3 does not provide stimulated emission by itself, as otherwise it could have been a good candidate for lasing under UV pumping, especially taking into account its specific 3-D structure and presence of three non-collinear and symmetric absorption dipole moments attached to ligands as well as the robustness due to the Al metallic center. The lasing action by FRET from Alq_3 to DCM was already demonstrated in the cavity based on the co-evaporated Alq_3-DCM thin film (3 wt% of DCM) [39].

On the other hand, in the polymer-doped thin film configuration the mass concentration of doping compounds is limited (as explained lower in this Sub-

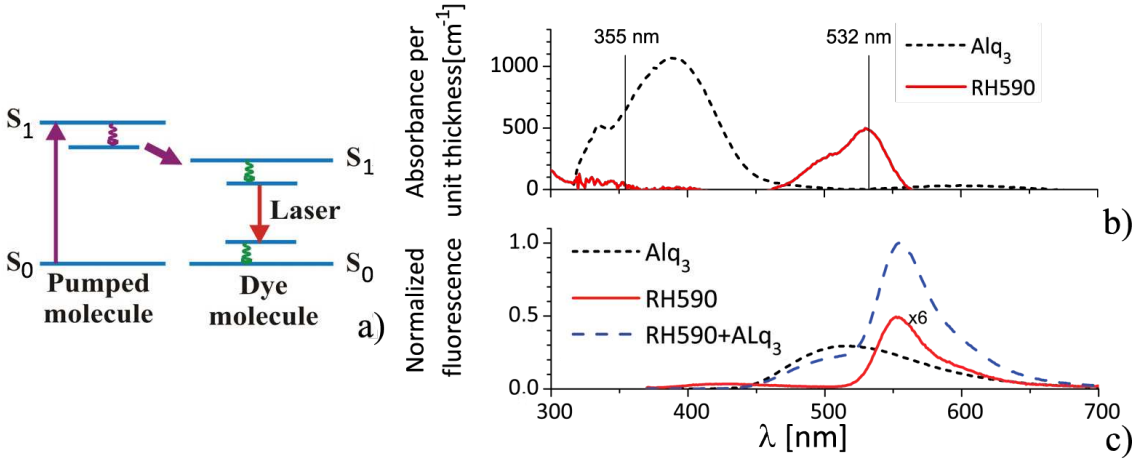

Figure 4.1: *Excitation of a dye via energy transfer: a) excitation scheme; b) absorbance of RH590, Alq_3 (measured with spectrophotometer, Sub-section 2.3.1), c) fluorescence of RH590, Alq_3 and RH590-Alq_3 mixture taken at equal molar quantities (measured with spectrofluorimeter, Sub-section 2.3.3). The absorption and fluorescence measurements were performed with dye-doped thin polymer films deposited on glass slide.*

section). Thus the amount of the Alq_3 cannot be several times exceeding the amount of a dye as was used in [39], and dye molecule in our application should have low absorbance at the pumped wavelength. Otherwise, there would be significant absorption by the dye itself which would decrease the energy transfer effect. The study of the absorption properties of dyes (Tab.C.2) shows that the Rhodamine family dyes exhibit at least 10 times lower absorbance at 355 nm compared to other available dyes.

The RH590 dye displays a very low absorbance in the UV (Fig.4.1.b) down to 8 times lower then RH640 (Tab.C.2). However, calculations on FRET efficiency (Sub-section 1.1.6) proved that the RH590 dye is not the best candidate for the experimental verification among those available in our study (as it exhibits the smallest Förster radius).

The presence of FRET in the fluorescence case for both combinations RH640-Alq_3 and RH590-Alq_3 was proved experimentally (for the UV pump, Tab.4.1, the variation of thickness between samples and difference in pumping power were taken into account), indeed the fluorescence intensity increases by 1/3 for RH640-Alq_3 in contrast to RH640 alone (comparing to only 10% for DCM molecule). As for RH590-Alq_3 it demonstrates remarkable growth in the fluorescence intensity up to 12 times, compared to RH590 (Fig.4.1.c).

Table 4.1: *Comparison of the fluorescence intensity of dyes pumped at 532 and 355 nm wavelength (at the same intensity level, thus 1.5 times less photons at 355 nm with respect to 532 nm), scaled to emission of 5 wt% DCM under 532 nm pumping (the difference in absorbance is not taken into account).*

Dye	Fluorescence	
	532 nm	355 nm
RH640	0.94	0.16
RH640-Alq_3	0.57	0.24
RH590	1.09	0.06
RH590-Alq_3	0.99	0.71
DCM	1	0.88
DCM-Alq_3	0.93	0.96

The species were taken in the mass proportion that allows to keep the stochiometric ratio at 1:1 molecule (for example RH590 to Alq_3). The mass concentration of dye in the polymer is supposed to be the highest possible in order to provide sufficient gain, but still limited by the possibility of quenching. As Alq_3 is taken at the same molar quantity as the dye, the mass concentration of both is also limited by homogeneity of a final multi-component polymer-based thin film, since this factor may decrease significantly the efficiency of the process. A 5 wt% mass concentration of dye in PMMA was used in this experiment. The first column of Tab.4.1 suggests that such concentration already induces some inhomogeneities in the layers, sufficient to decrease the fluorescence emission in dye-Alq_3 doped PMMA layer under 532 nm pump by up to 10-20% compared to PMMA layer of doped only with dye (as Alq_3 exhibits negligibly low absorption at 532 nm).

The fluorescence intensity of RH590-Alq_3 under 355 nm pumping is slightly lower then in case of DCM (Tab.4.1). But the ASE intensity of RH590-Alq_3 appeared to be quite low. However, it is still sufficient to study the polarization properties and show the imbalance in favor of the TM-polarized component: about 10% over the TE-polarized one ($P \approx 0$, not plotted).

The verification in a micro-laser configuration however failed due to a presumably too low gain value (that is insufficient to overcome the losses of the open dielectric resonator, Chapter 5). Indeed, the small Stokes shift of RH590 should lead to a high re-absorption rate, thereby decreasing the stimulated emission flux and quenching the lasing. In fact, lasing was never achieved even at 532 nm pumping in the RH590 based cavities (without Alq_3).

4.2 Pumping to S_n

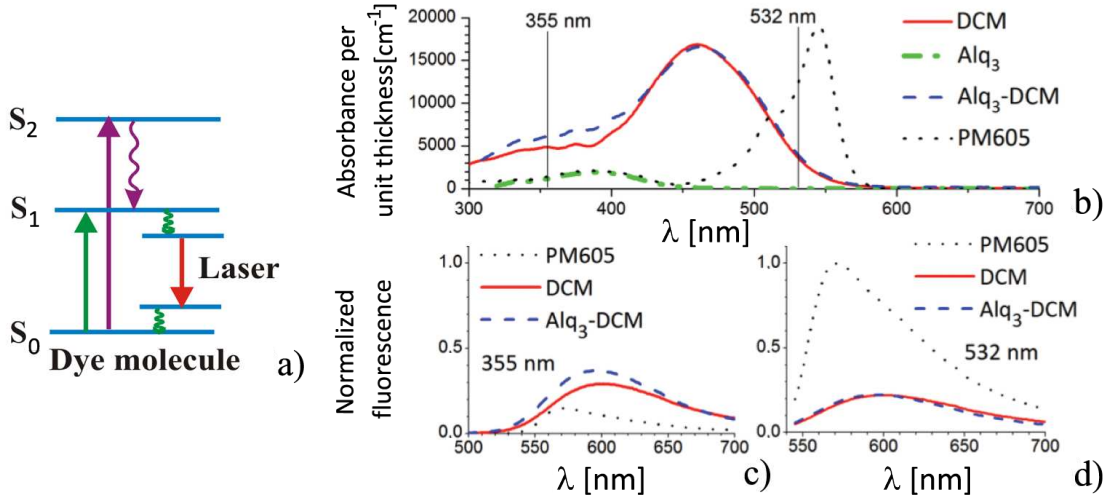

Figure 4.2: *Excitation of a dye via pumping to the S_2: a) excitation scheme; b) absorbance of DCM, PM605, Alq_3 and DCM-Alq_3 (measured with spectrophotometer, Sub-section 2.3.1); c), d) fluorescence of DCM, PM605 and DCM-Alq_3 (measured with spectrofluorimeter, Sub-section 2.3.3) at 355 nm (c) and 532 nm (d). The absorption and fluorescence measurements were performed with dye-doped thin polymer films deposited on glass slide. DCM-Alq_3 mixture prepared of equal molar quantities of DCM and Alq_3.*

According to the analysis presented in Sub-section 3.1.2, the polarization degree P may reach negative values, while the absorption and emission moments are orthogonal or close to orthogonal ($\beta \to \pi/2$). On the other hand, it is known, that for a majority of fluorophores the absorption moment of the second excited

singlet state is orthogonal to its first excited state absorption moment [70, 69]. For instance, the P_E value measured by [91] for DCM in n-hexane (% not mentioned) is changing from 0.38 (at 450 nm) to -0.04 (340 nm). It is additionally mentioned that the absorption moment of the $S_0 \rightarrow S_2$ transition is tilted at 65° with the respect to the $S_0 \rightarrow S_1$. Thereby the first way to influence the emission anisotropy is to pump the dye molecules in the UV (at 355 nm) where the 2nd excited singlet state is generally located (Fig.4.2.a, with a one-step transition in purple reaching S_2).

This does not influence the position of the dye emission band, as the molecules relax to the first singlet state in a non-radiative manner and it is only then that the emission takes place therefrom (as in the standard pumping scheme shown by a green arrow to S_1 on Fig.4.2.a).[1]

An important working condition on the proposed model is that the dye should posses sufficient absorbance at the new pumping wavelength region. This is not the kind of information reported in the literature especially for a dye incorporated into a polymer matrix. The absorbance had thus to be experimentally verified for all available dyes (leading for example to the normalized absorbance curves of DCM and PM605 on Fig.4.2.b).

The Rhodamine-family dyes exhibit quite low absorbance in the UV part of their spectrum, however the situation is more favorable with Pyrromethene-family dyes and even far above for DCM molecule.

This section is organized as follows. First we present the study on the fluorescence anisotropy under the UV pump, followed by the investigation of the emission dynamics in the respective cases of spontaneous and stimulated emission. The analysis of the polarization state of dye-doped lasers under UV pump will be started with the VECSOL and continued with the planar micro-lasers of various shapes. Finally, we will discuss the mechanisms of a degradation in the dye-doped polymer layers and compare the experimental degradation rates of the used dyes under our standard (532 nm) and UV (355 nm) pump.

4.2.1 Anisotropy of fluorescence for S_2 pumping

Before studying the influence of the pump wavelength on output polarization of dye-doped solid state lasers we address its impact on the spontaneous emission. This allows to perform an additional check on the calculations presented in Chapter 3 and to compare the experimental emission anisotropy under UV pump respectively for the spontaneous and stimulated processes. The fluorescence anisotropy was examined respectively along vertical (FLIM set-up) and tilted from vertical (spectrofluorimeter) emission directions.

The FLIM set-up (Sub-section 2.3.1) was used to conduct the fluorescence experiments in UV (at the 343 nm pumping wavelength) in vertical emission configuration on PMMA films doped with one of the following dyes: DCM, PM605 or RH640, all spin-coated on a glass slide (the absorption of latter was experimentally proved to be negligible at 343 nm wavelength compared to the one of dyes).

First measurements were performed on samples with a dye mass concentration of about 5%, as the absorbance and thus the emitted fluorescence is lower in UV pumping for PM605 and RH640. The inferred anisotropy values (and thus

[1] A slight difference was observed in the shape of the fluorescence curves comparing pumping conditions to S_1 versus S_2: the spectrum appears to be broader under UV pumping (Fig.4.3.b). This effect was noticed for the following dyes and their combinations with fluorophores incorporated into a PMMA matrix: DCM, PM605, PM597, DCM-Alq_3, RH590-Alq_3; while in case of Rhodamines and non-commercial Bodipy, no clear significant difference between fluorescence curves showed up.

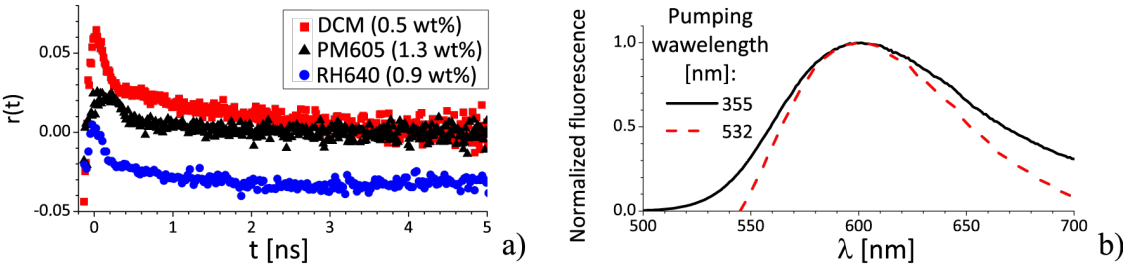

Figure 4.3: *a) Dynamics of the dye anisotropy under* S_2 *pumping (obtained from FLIM measurements); b) spectral enlargement of the fluorescence under* S_2 *pumping on the example of DCM.*

polarization ratios) were all found close to zero. Then films with lower dye concentrations (0.5 wt% DCM, 1.32 wt% PM605, 0.9 wt% RH640) were examined (Fig.4.3.a) and similar values of anisotropy evidenced (Tab.4.2).

Table 4.2: *Fluorescence anisotropy of the emission in vertical configuration for several dyes (at 343 nm pumping wavelength). Measurement error is estimated to be about ± 0.02.*

	DCM (0.5 wt%)	RH640 (0.9 wt%)	PM605 (1.32 wt%)
r	0.07	0.00	0.03
P_V	0.09	0.01	0.04

Further experiments were undertaken with the spectrofluorimeter (Sub-section 2.3.3) on the same samples (Tab.4.3) and very similar P_V values obtained in both cases. However P_E values inferred from spectrofluorimeter measurements are all higher than zero, which reduces the possibility to achieve the expected effect of polarization turning.

Table 4.3: *Fluorescence anisotropy of the emission at* $\gamma = 40°$ *degrees (at 355nm pumping wavelength) obtained with a spectrofluorimeter.*

Dye	DCM	RH640	PM605
β [degrees]	52 ± 4	54 ± 4	52 ± 4
$P_{\gamma_0}(90)$	0.27 ± 0.03	0.22 ± 0.03	0.19 ± 0.03
$P_{\gamma_0}(0)$	0.17 ± 0.03	0.2 ± 0.03	0.1 ± 0.03
d_H	0.91 ± 0.03	0.99 ± 0.03	0.93 ± 0.03
θ_0 [degrees]	20 ± 4	27 ± 4	45 ± 4
Inferred P_E	0.86 ± 0.03	0.75 ± 0.03	0.45 ± 0.03
Inferred P_V	0.05 ± 0.03	0.007 ± 0.03	0.04 ± 0.03

Contrary to our expectations, measured fluorescence anisotropy of our used dyes along the vertical emission direction does not exhibit a clear negative value, but rather tends to zero. Naturally the anisotropy values may be influenced by FRET. Subsequent study of fluorescence anisotropy performed with spectrofluorimeter in the observation direction tilted with respect to layer plane allowed for the deduction of all parameters of our model presented in Sub-section 3.1.2. The inferred P_V values tend to zero for all dyes, while P_E values, which we expected to achieve negative values under 355 nm pumping, in fact just slightly decreased compared to the case of to 532 nm pumping. This originates from the supposed non-isotropic orientation of the emission dipoles of dyes inside the polymer layer and non-orthogonal absorption and emission dipoles under 355 nm pumping. Therefore, 355 nm pumping is not likely to result in the attempted negative value of emission polarization ratio of the planar micro-lasers, based on our used dyes.

4.2.2 Dynamics of the emission process

The experimental study on the dynamics of fluorescence and ASE under UV pumping was performed with a streak-camera (Sub-section 2.3.1) on a layer of PMMA doped with a dye. The polymer layer was deposited on the adequate substrate: *a Si* wafer for fluorescence measurement and Si/SiO_2 wafer for ASE.

The dynamics of ASE obtained by way of S_2 pumping is quite similar to the standard S_1 pumping case: ASE replicates the pumping signal (duration 35 ps, Fig.4.4.b). And again the ASE of the RH640 dye relaxes close to exponentially although here the effect is more prominent than for the S_1 pumping (inset on Fig.4.4.b compared to the analogous graph for S_1 pumping on Fig.3.13.b).

However the fluorescence behavior of all three tested dyes changes drastically with the respect to S_1 pumping (Fig.4.4.a). Now there is a significant build-up time of about 300 ps (constant value for all three tested dyes) and it is only after that the fluorescence decay is observed. This delay may correspond to the characteristic time of the internal conversion from S_2 to S_1 level of the molecule.

The duration of the fluorescence emission under S_2 pumping (deduced from exponential fit of the decaying part of the curve shown on Fig.4.4.a, with the build-up time taken into account) appears to be about twice shorter than for S_1 pumping (a difference much larger than the new build-up time), except for the PM605 dye, where it is hard to make a clear statement due to quick degradation (Sub-section 4.2.5).

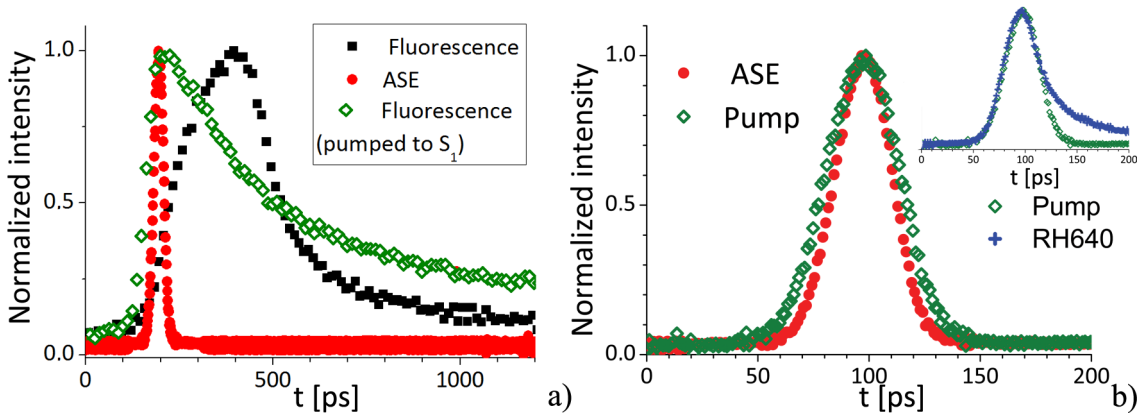

Figure 4.4: *Dynamics of the spontaneous and the stimulated emission in a layer of PMMA polymer doped with 5 wt% of DCM dye: a) fluorescence and ASE (error ± 60 ps, solid squares and circles represent respectively fluorescence and ASE under S_2 pumping), b) pump signal and ASE (error ± 1.3 ps, ASE of RH640 in the inset for comparison).*

The comparison of spontaneous and stimulated emission durations for DCM, RH640 and PM605 is given in Tab.4.4.

Table 4.4: *The fluorescence lifetime (τ_f) and ASE (τ_{ASE}) in a PMMA layer doped by various dyes (DCM, PM605 and RH640).*

Dye	%	τ_f [ns]	τ_{ASE} [ps]
DCM	5	0.86 ± 0.06	31 ± 1.3
PM605	5	0.82(at max)± 0.06	36 ± 1.3
RH640	10	1.33 ± 0.06	-
	5	-	42 ± 1.3

Checking for the fluorescence lifetime at a wavelength around the maximum of fluorescence spectrum (Fig.4.5.b) we observed a behavior analogous to the S_1

pumping case: duration on the sides of the spectrum is shorter than at the maximum emission wavelength.

Such a verification was difficult to perform in the ASE regime due to fast degradation of the material or low gain (Sub-section 4.2.5). For instance, the single point for ASE curves of RH640 on Fig.4.5.a corresponds to a single wavelength where ASE was actually observed using the streak-camera set-up (only fluorescence was present at other wavelengths). Nevertheless, the ASE spectra of DCM and PM605 (Fig.4.5.a) exhibit comparable emission durations at the spectral edges compared to their centers. Meanwhile, under pumping to the S_1 level the shorter wavelength of ASE spectra exhibited shorter duration, the effect we related to solvatochromic shift (Sub-section 1.1.7).

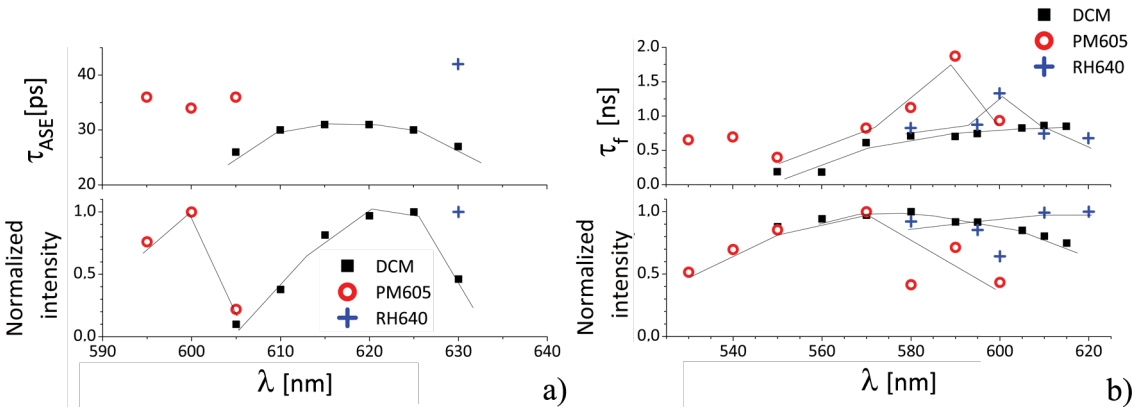

Figure 4.5: *Dynamics of stimulated (a) and spontaneous (b) emission in a layer of PMMA polymer doped with 5 wt% of DCM or PM605 dye or 10% of RH640 dye. The upper frame describes the process lifetime (error ± 1.3 ps for the ASE and ± 60 ps for the fluorescence), and the lower one - the emission intensity for an examined wavelength, normalized by the maximum intensity in the spectrum.*

Indeed, if the dipolar moment of the S_2 level of the molecule is lower then the one of the S_1 state, polymer relaxation is less relevant in the ASE emission and there is no solvatochromic shift.

4.2.3 VECSOL

The influence of the pumping wavelength on the VECSOL emission (Sub-section 2.2.3) was examined for a VECSOL made of a 20 μm thick PMMA film doped by 1 wt% of DCM or PM597. The pumping wavelength used in the study were 532 nm and 355 nm respectively for S_1 and S_n pumping.

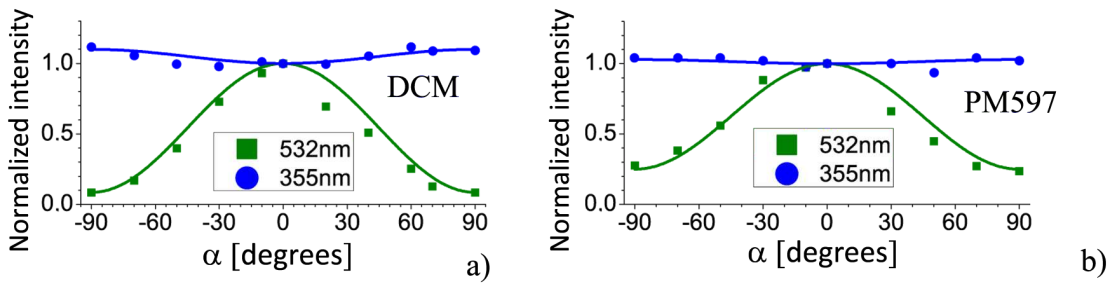

Figure 4.6: *Influence of the linear pumping beam polarization on the output emission (with polarization state fixed by the Brewster plate) of a VECSOL cavity with the gain medium provided by dye molecules: a) DCM, b) PM597; pumped at 532nm (square) or 355nm (circle). The laser emission is normalized by its value at* $\alpha' = 0$.

The experiment was carried-out by inserting a glass plate inside the VECSOL cavity at the Brewster angle to force the emission polarization, and then turning the polarization of the pump beam to an angle α'.

As predicted in Sub-section 3.1.2, the role of the pump beam polarization in the case of S_2 pumping is practically negligible compared to the S_1 pumping case (Fig.4.6).

The continuous lines on Fig.4.6 represent theoretical curves for fluorescence emission $I_X(\alpha)/I_X(\alpha = 0°)$ (formula (B.21), Appendix B.4) following a P_V value obtained experimentally for VECSOL emission (Tab.4.5). These theoretical curves were deduced for fluorescence intensity component $I_X(\alpha)$ emitted along vertical direction and polarized at the angle α with respect to the pump beam polarization. Then $I_X(\alpha' = 90°)/I_X(\alpha' = 0°)$ was deduced from VECSOL experiment and used to plot the theoretical curves for fluorescence.

Actually the orthogonally polarized components do not co-exist in VECSOL, as intracavity losses are strong to sustain all the components except the ones privileged by the Brewster plate. In fact the deduced P_V values characterizes the ratio of the output intensities of the two lasers, pumped by a linearly polarized beam, orthogonal and parallel to the laser polarization.

Agreement between experimental results for micro-laser emission and theoretical expressions for the fluorescence intensity, suggests that fluorescence anisotropy is one of the factors influencing the threshold value in dye-doped polymer lasers. This question is addressed in more details in Sub-section 5.2.4.

Table 4.5: *Anisotropy of the emission of a VECSOL laser at different pumping wavelength.*

P_V	DCM	PM 597
532 nm	0.85 ± 0.03	0.6± 0.03
355 nm	-0.05 ± 0.004	-0.02 ± 0.004

Moreover, the P_V obtained under UV pumping in VECSOL configuration is tends to zero, thus reproducing the results obtained with FLIM set-up.

Finally, we proposed and proved experimentally the possibility to abate the influence of the pump beam polarization on the emission properties of the VECSOLs.

4.2.4 Planar micro-lasers

Our experimental study was performed with the 2-D detection set-up (Sub-section 2.2.1) on planar micro-lasers of various shapes and with different dye molecules inside. Our study focused on the Pyrromethene-family and DCM, as they exhibit relatively high absorption in the UV. Also an attempt of hybrid pumping was made with the DCM-Alq_3 mixture.

First of all, serious degradation problems should be mentioned (Sub-section 4.2.5), which hindered the study of most of shapes of PM605-based cavities and some DCM-based ones. The cavities with higher threshold demanded an increase of pumping intensity to achieve lasing, and for some of them, full degradation appeared during the measurement of several emitted spectra. In contrast, cavities based on the MD7 dye demonstrated only slow degradation, comparable to that normally observed within S_1 pumping (Sub-section 4.2.5).

The emission anisotropy under UV pumping yielded surprising results: in general it is lower than the one for S_1 pumping, but except for the MD7-based square there was no inversion of the sign of polarization ratio observed under UV pumping (Fig.4.7, Tab.4.6). Only WGM-type modes (with stadium and kite contours)

exhibit a marked difference between polarization ratios under S_1 and S_2 pumping. It should be mentioned however that the polarization degree in the ASE case was slightly higher than zero, but still in favor of an in-plane polarized component. In these experiments, laser feedback does increase the difference between these two orthogonally polarized components.

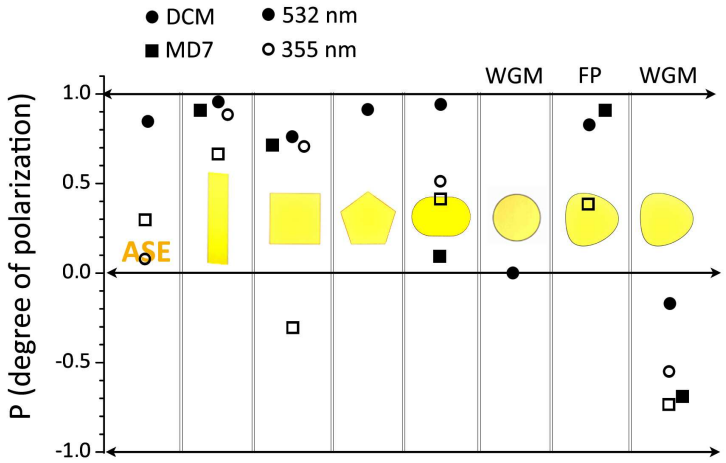

Figure 4.7: *Comparison of the emission anisotropy in micro-lasers of various shapes, based on DCM (circles) or MD7(squares) pumped to the* S_1 *(solid icon) and* S_2 *(empty icon) energy levels of the dyes.*

Table 4.6: *Comparison of P obtained from ASE and laser above the threshold at 355 nm pumping (error ± 0.03).*

	355nm			
P	DCM	PM605	DCM-Alq3	MD7
ASE	0.09	-0.3	-	0.3
Fabry-Perot	0.89	0.94	0.93	0.65
Square	0.7	-	0.55	-0.3
Stadium	0.5	0.35÷0.55	0.4	0.4
Kite (FP mode)	-	-	-	0.35
Kite (WGM)	-0.54	-	-0.53	-0.75

Hybrid pumping does not provide much change either, apart from a slightly slower degradation. Micro-lasers based on DCM-Alq_3 showed lower anisotropy, compared to pure DCM pumped to S_2 in square and stadium-shaped micro-lasers. The slight difference for Fabry-Perot resonator is close to being within the inaccuracy range.

On the other hand, if Alq_3 acted indeed as a source of FRET in relation with DCM molecules, but not just slightly changed the dye distribution model, it should have been used in higher concentration in order to compete with S_2 pumping. However, such an increase of Alq_3 concentration is not advisable, because of strong influence on the layer homogeneity. Moreover, even relatively small amount of Alq_3 used in present study caused sufficient fabrication problems during the electron-beam lithography. The resulting cavities had slightly rounded corners and non-vertical sidewalls (Fig.A.2.b,c, Appendix A).

In conclusion, we did not manage to influence significantly the polarization states of planar micro-lasers by exciting a dye to higher energy levels. On our opinion, this was caused by two following factors. Firstly, the material choice

was not optimal, as in spite of common belief, the examined dyes exhibit non-orthogonal transition dipoles of respectively absorption to S_n level (under 355 nm pump) and emission, which hinders the expected effect. Secondly, the polarization state of micro-laser emission is strongly influenced by the resonance type. For Fabry-Perot cavities, thanks to the feedback, there is an enhancement of the dominant polarization compared to ASE. On the contrary, for resonances with long photon lifetimes, like WGMs, the polarization states can be strongly modified by coupling of the electro-magnetic component at the cavity boundary.

4.2.5 The problem of degradation

The dye-degradation problem has been known since the inception of liquid dye lasers, whereby continuous recycling of the liquid was necessary to maintain the laser effect. In the field of solid-state lasers and amplifiers, polymer optical fibers are known for their very low degradation, which is normally explained by much lower dye concentrations (10 ppm) comparing to lasers and thus efficient heat evacuation in polymer matrix [78].

Apparently, enhanced photo-bleaching in the dye-doped polymer matrix under a high pumping intensity is caused by chemical interactions between the bleachable dye molecules and the polymer molecules, as well as lower solubility of dyes in polymers [125]. The associations of the dye molecules is problematic, sometimes giving rise to dimers, trimers, and other aggregates, which increase the bleaching efficiency and may also initiate laser-induced damages in the matrix. Concerning eventual chemical reactions with the polymer matrix, they may occur between the dye and the products of peroxide decomposition (if not present in the initial monomer composition, they may appear during the polymerization process due to contact with oxygen). Thus the long-term storage of dye-doped porous polymers is not advisable in ambient atmosphere.

At low pumping intensities (below value of the order of 100 MW cm^{-2} , Section 5.1) the absorption to S_1 (or T_1 via S_1) dominates and the photo-bleaching rate is linear with pumping intensity (I_P). The following increase in pump power causes saturation of the first excited state absorption, and excitation to a higher excited state may then proceed fast.

Moreover, two-photon absorption can result in electron energy transfer from the dye molecule to the polymer macromolecules. The subsequent vibrational relaxation of the first excited state of the polymer molecule leads to radical formation (also possible under simple UV irradiation of polymers). Radicals cause in turn the destruction of dye molecules in the excited S_n states when interacting with them. In order to prevent this effect, the modifying additives can be incorporated onto the polymer bulk (to provide cross relaxation from the vibrational levels of the polymer macromolecules).

Quantum yield of degradation, which basically defines the number of excitation cycles before molecular degradation is defined by:

$$\phi_D = \frac{\triangle N_D}{\triangle n_{phabs}} \tag{4.1}$$

is the number of degraded molecules ($\triangle N_D$) per absorbed photons ($\triangle n_{phabs}$).

Table 4.7: *Quantum yield of degradation for some of our dyes, found in the literature.*

dye	ϕ_D 532nm	ϕ_D 355nm	Source	Environment
RH590	1.2E-7	9.5E-3	[126]	HEMA-MMA
PM597	1.2E-7	-	[112]	COP(MMA-TMSPMA)

There exists a serious constraint against the use of UV light for pumping of a dye-based emitting medium. Indeed, a drastic and irreversible degradation of the dye (bleaching, Fig.4.8.a) takes place followed at times by the massive destruction of polymer bounds in the pumping region and even melting of the whole area (Fig.4.8.b, c).

The effect was not observed in traditional S_1 pumping scheme and the polymer itself does not exhibit significant absorption at 355 nm wavelength. In this regard, the possible strong degradation at 355 nm pump was not foreseen as potential problem.

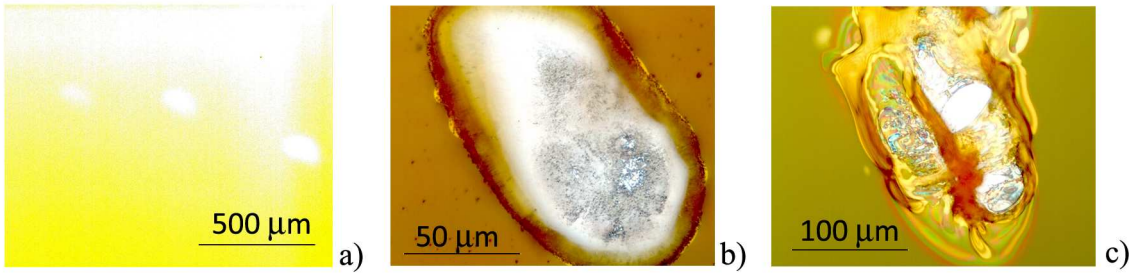

Figure 4.8: *Degradation process during ASE measurements on the PMMA layer doped with 5 wt% of DCM: a) bleaching, b) beginning of polymer melting, c) propagation of polymer melting. Pump intensity about 150 MW cm^{-2}.*

Dyes were illuminated during different periods of time and by various pump power values, but in each case the pumping was switched off whenever emission started to vanish. Defects in the layer thickness due to the melting of the polymer were noticed for both PM605 and DCM dyes in the ASE regime. However, depletion of the emission of planar micro-lasers was generally followed by bleaching only (Fig.4.9.a,b) except for DCM (Fig.4.9.c). All the white regions were checked with a profilometer and it is only in the case of DCM-based cavities that a change in layer thickness could be noted.

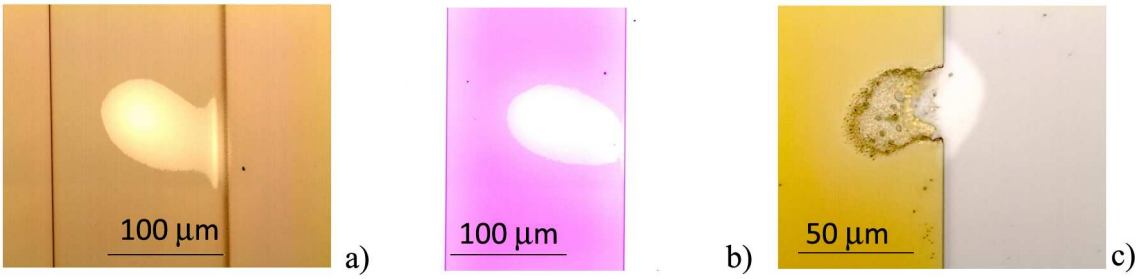

Figure 4.9: *Degradation of dye and polymer in ASE and lasing regimes on the example of a ribbon Fabry-Perot micro-laser made of 5 wt% of: a) RH590-Alq$_3$, b) PM605, c) DCM. Pump intensity about 70 MW cm^{-2})*

Such a fast degradation mechanism is caused by the interactions between dyes excited to S_2 and radicals in the polymer, both created by the same UV pumping.

Only MD7 dye did not seem to suffer from this problem.

Comparison of the ASE degradation rate for cases of $S_0 \rightarrow S_1$ and $S_0 \rightarrow S_2$ pumping was done in 5 wt% dye-doped PMMA layers and shown on Fig.4.10. The experiment could not have been done at the same pumping level at a given pump wavelength, due to the difference in absorbance and gain values. Indeed, a weak and noisy output intensity for Rhodamine occurs at the pumping intensity which the random lasing (see Appendix H) in Pyrromethene dyes. To avoid such complications, plots were made at the intensity values giving just the essential emission level. The curves presented on Fig.4.10.a were measured at pump intensities varying from 2 (for PM597) to 17 MW cm^{-2} (for RH640) during 10 minutes each. We also performed degradation studies with variation of pump intensity (in the above mentioned intensity range) and exposure duration, which showed that the increase in one of the two parameters equivalent to decrease in another by the same factor. For this reason, duration of exposure in curves plotted on Fig.4.10.a was normalized in order to present the degradation as if it was measured under the same pump intensity.

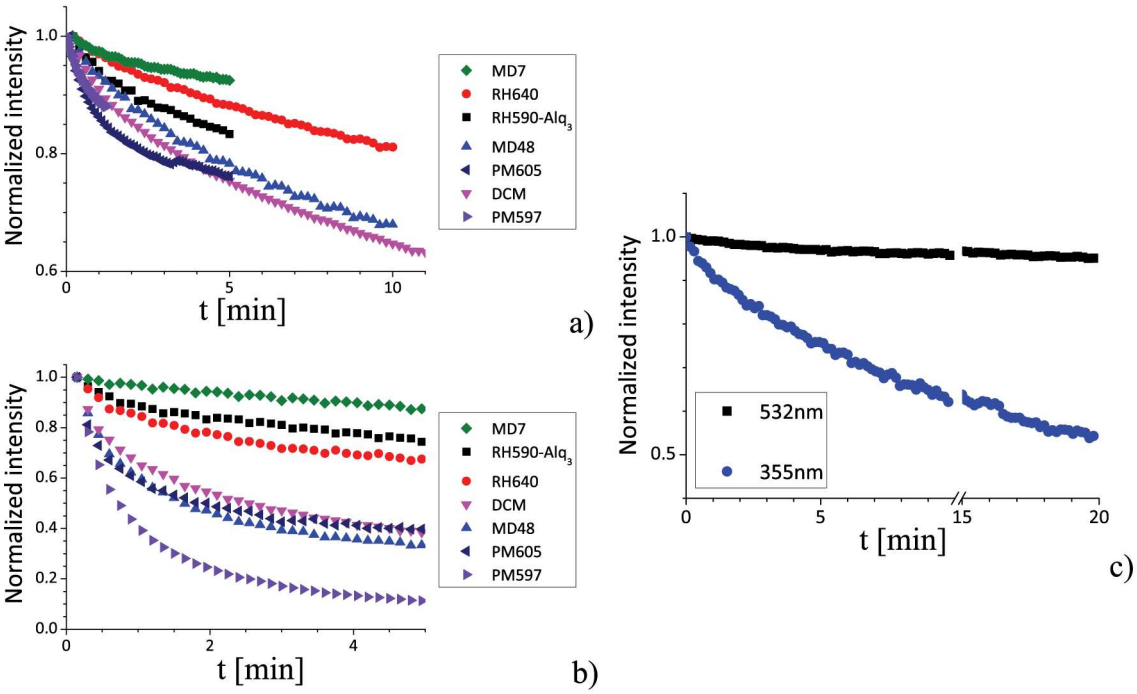

Figure 4.10: *Intensity decay of ASE emission of dye-doped polymer layers under pulsed pumping (500 ps, 10 Hz) at wavelength of: a) 532 nm (17 MW cm^{-2} for RH640 and MD48); b) 355 nm (pump intensity about 50 MW cm^{-2}); c) comparison of MD7 dye degradation under pumping at 532 (50 MW cm^{-2}) and 355 nm (about 50 MW cm^{-2}).*

Chapter conclusion

According to the general fluorescence anisotropy model developed in Chapter 3, the fluorescence emitted within the sample plane is mainly in-plane polarized under 532 nm pumping due to two factors, precisely the molecular properties of the dye and the in-plane polarization of the pump beam. In order to influence the predominant polarization of the stimulated emission, the polarization ratio of fluorescence emission must be altered. We proposed two ways to influence the emission anisotropy: by pumping via energy transfer or to higher energy states of

the dye.

To experimentally verify the first method, we chose the RH590 dye, as it exhibits the lowest among our used dyes absorption at the new pump wavelength. But the energy transfer between pumped organo-metallic molecule Alq_3 and RH590 appeared to be rather weak. Still we managed to obtain the imbalance in the ASE in favor of the intensity component polarized orthogonally to the layer plane. However, lasing via energy transfer pump was not witnessed, presumably due to weak transfer and high re-absorption losses in the RH590 dye, which exhibits relatively low Stokes shift.

Pumping to the higher excited states gave satisfactory results in the VECSOL configuration, where the output intensity under 355 nm pump was just slightly influenced by the pump beam polarization. As for the planar micro-lasers, they exhibited lower polarization ratio compared to the case of 532 nm pumping, but the change in the sign of polarization ratio was not achieved. The reason for this is in non-orthogonal ($\beta \neq \pi/2$) orientation of the molecular dipoles of respectively absorption to the S_n energy level and emission, what we proved via spectrofluorimeter anisotropy measurements. Still we do not exclude the possibility to change the polarization ratio of planar micro-lasers, when the dye molecule exhibits $\beta \to \pi/2$.

During the experimental study presented in this Chapter, we faced serious degradation problems in the majority of our dyes under 355 nm pumping. One of the secondary results of this study was in the revelation of the remarkable photostability under 532 as well as 355 nm pumping of non-commercial MD7 dye from Bodipy family, which outline a bright future in phonics for this molecule.

Some of these results were presented on Photonics West conference (San-Francisco, USA, 2012) and published in Phys. Rev. A, 86, 043817 (2012).

Chapter 5

Threshold estimation of dye-doped polymer lasers

For the last 20 years the top subjects in the fields of solid state dye lasers and amplifiers have remained the highest possible gain and the lowest optically pumping threshold values, especially as the latter defines a lower theoretical limit of the electrically pumped threshold [43]. A vast majority of such publications feature experimental study on either one or several dyes taken in a small concentration range, or organic semiconductors, both within specific resonator or amplifier configurations. No systematic comparison and assessment has been, to the best of our knowledge, proposed to this day, hence our motivation.

Moreover, there is no existing method, at least to our knowledge, that allows downstream the prediction of threshold or amplification values for a given dye-doped material from its reported usual photo-physical properties.

The purpose of this Chapter is thus to establish such a relation and prove its applicability to ribbon-shaped planar micro-lasers with a micro-laser engineering ambition in the wake of this study.

First, we analyze the gain properties of solid-state dye-based amplifiers. Then the relation between gain, losses and thresholds is established on the example of planar Fabry-Perot micro-laser. Finally, polarization effects on the threshold are discussed.

5.1 Gain in thin polymer films

The ability of dye molecules to amplify light incident on the sample is described in the literature by the material gain. This Sub-section starts with a review of gain definitions used in various contexts. Then we compare the gain values of different species from the literature and propose alternative ways to describe the gain. Experimental data on the gain values of thin dye-doped PMMA layers conclude the Sub-section.

5.1.1 Gain definition

The gain is basically an average growth rate of electro-magnetic flux per unit medium length. Both in optics with conjugated polymers and chemistry, the gain is usually given in dB (and the typical value in visible region is about 20-40 dB[1])[2].

[1]For a given gain in dB, its value in cm^{-1}can be found from $10^{g[dB]/10}/l[cm]$.

[2]In the case of plastic optical fibers (POF) there are few transparency windows in the visible region (namely around 520, 580 and 650 nm). Organic dyes were studied for signal amplification in local networks [133].

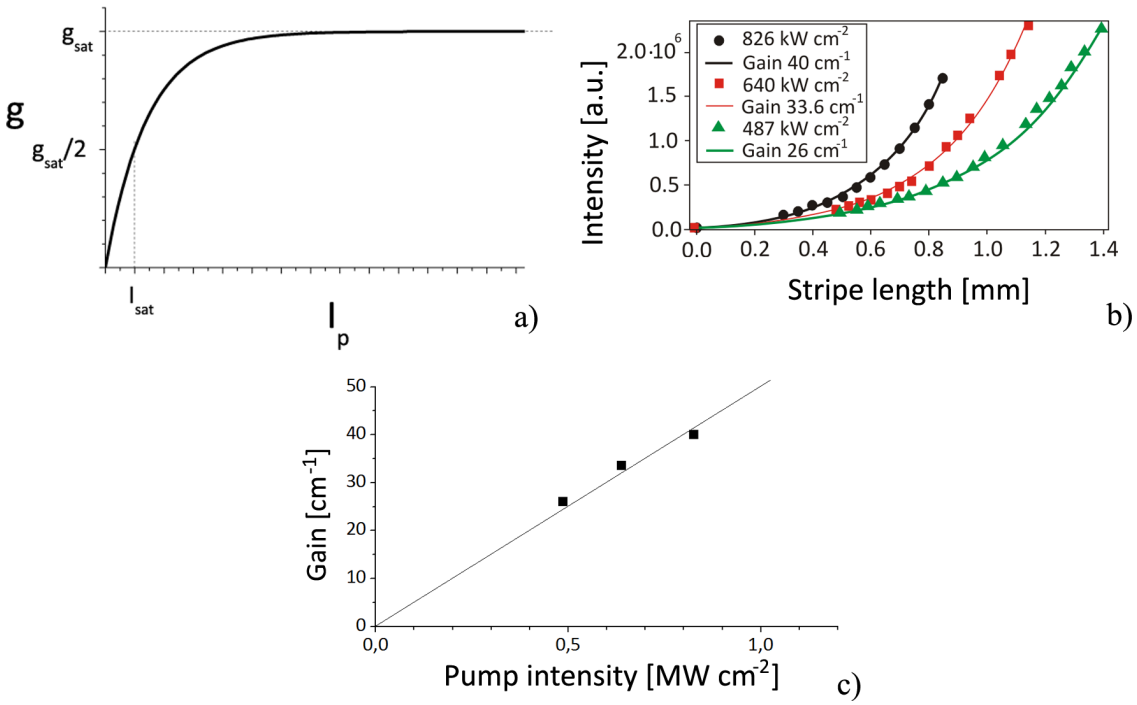

Figure 5.1: *Optical gain a) typical gain curve; b) gain inferred from a fit with Eq.(2.5) of the ASE curves, obtained by the VSL technique; c) experimentally obtained (deduced from curve in (b)) gain values for a 600 nm thick PMMA layer doped with 5 wt% DCM on a Si/SiO_2 substrate.*

The following general expression is used in literature to describe the relation between the gain and emitted intensity (in the case of homogeneously broadened amplifier) [110, 82, 127]:

$$g = \frac{g_{sat}}{1 + \frac{I_{out}}{I_{sat}}} \tag{5.1}$$

The expected gain curve as a function of the pump intensity is depicted on Fig.5.1.a. It exhibits a linear behavior until some threshold in the pump intensity, beyond which saturation occurs, leading as well to the decrease in the emitted intensity, as explained by Exp.(5.1).

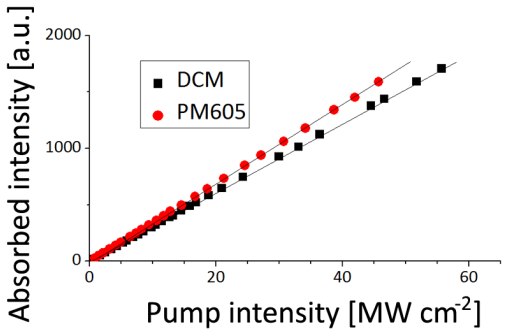

Figure 5.2: *Absorbed intensity under pulsed pumping (532 nm, 500 ps, 10 Hz) in a 600 nm thick PMMA layer doped with 5 wt% DCM (squares) or PM605 (circles) on a Si substrate, measured on the 3-D detection set-up (at 7° pump incidence) as a difference between signal reflected respectively from the reference substrate without polymer and from the sample. Present graph confirms the absence of absorption saturation effect in our system in the range < 50 MW cm^{-2}.*

In the linear regime the number of absorbed photons (e.g. the number of excited molecules) cannot be larger than the number of absorbers in the pumped volume. Thereby, the upper limit of the linear regime is caused by saturation of the S_1 absorption. Other absorption processes that become relevant at high pumping intensity are multi-photon absorption and absorption to higher excited singlet states. However quite often they are prone to fasten dye degradation (Sub-section 4.2.5). In many reports, the saturation intensity is determined as a pump intensity value, which reduces the absorption to half of its small-signal value and defined by the following expression [82]:

$$I_{sat} = \frac{h\nu}{\sigma_a \tau_{eff}} \tag{5.2}$$

where $h\nu$ is the energy of a pumping photon, σ_a the absorption cross-section and τ_{eff} the recovery time. According to this formula, typical saturation value range from 0.1 to 10 MW cm^{-2} when the fluorescence lifetime values are used under a recovery time. However, the assumption $\tau_{eff} = \tau_f$ can be used for description of the spontaneous but not the stimulated emission, which exhibits much higher time rate of excitation/de-excitation processes. In fact, the recovery time of dye within the ASE should be compared to the characteristic time of propagation of the photon flux in an amplifying medium. For instance, ASE flux in the stripe of 1 mm length has can be characterized by $\tau_{eff} = 5$ ps, resulting in the saturation intensity of about 350 MW cm^{-2}. In confirmation, no absorption saturation was observed in our standard thin dye-doped polymer layer pumped with intensities up to 50 MW cm^{-2}, as shown on Fig.5.2.

5.1.2 Gain in dye-doped systems

A rather misunderstanding and naive delusion is spread by the articles on gain values in thin films or fiber configurations stems from the more or less explicit assumption that the absolute value of gain can and therefore must be *as high as possible* (the highest values given in literature are respectively 50 cm^{-1} for dyes and around 300 cm^{-1} for conjugated polymers in thin film configuration or 30 dB in the field of optical fibers). Nevertheless, accurate confrontation with other experimental parameters (dye concentration, pump intensity level[3]) tend to show that high gain is not the best criterion for analysis.

Gain is measured at some intensity level. The comparison of absolute gain values makes no sense, as they could correspond to different intensities. So we propose to consider the slope $K = g/I_P$ [cm MW^{-1}]. Indeed the data presented in Tab.5.1 show that high gain values may be related to lower slopes (e.g. lines 1-3, Tab.5.1).

[3]Often pump intensity is not given and needs to be inferred somehow. A low power value for a small-sized beam actually means quite a high intensity value.

Table 5.1: *Gain values reported in the literature for different dyes, light-emitting polymers, rare-earth elements and semiconductors (S[cm^2] stands for the beam transverse cross-section if not mentioned in the article). Dye-doped matrices are described by numbers: 1 - PMMA, 2 - polystyrene, 3 - porous silicon, 4 - hybrid matrix (hybrid organic/inorganic sol-gel).*

Species	λ_{pump}, nm	λ_{em}, nm	g, dB	g, cm^{-1}	I_P, MW cm^{-2}	K=g/I_P, cm MW^{-1}	Reference
Dye pumped in visible and infrared							
IR1051 (4)	1064	1270	-	11	$3 \cdot 10^{-4}$	$37 \cdot 10^4$	[128]
RH640 (1)	575	632	-	54	$8 \cdot 10^{-2}$	680	[117]
PM650	532	616	25	486	23	21	[77]
DCJTB (2)	532	630	-	40.7	$16.3 \cdot 10^{-3}$	$2.5 \cdot 10^3$	[129]
PM567 (1)	532	575	-	20	2-3.4	5-10	[130]
DCM (2)	532	630	-	11.95	$75 \cdot 10^{-3}$	160	[129]
PDI-N (2)	533	580	-	10	$74 \cdot 10^{-3}$	135	[131]
Nile blue (3)	532	700	-	8.7	5.4	1.6	[132]
RH590(1)	532	580	26	3.32	$4 \cdot 10^{-3}$ /S	829*S	[78, 133]
RH B	532	633	23	2.9	$9.5 \cdot 10^{-4}$ /S	$3.03 \cdot 10^3$ *S	[134]
DO11 (1)	532	649	-	0.26	207	$1.27 \cdot 10^{-3}$	[135]
DCM(1)	532	560	3.5	2.24E-2	$2.5 \cdot 10^{-3}$ /S	9*S	[78, 133]
UV-pumped dye							
DCJTB[4] (2)	355	640	-	52.71	0.4/S	130*S	[136]
B2080 (2)	355	501	-	84	0.37	227	[137]
SP35 (2)	355	487	-	19.8	0.87	23	[138]
DW (4)	355	412	-	14	5	2.8	[139]
Light-emitting polymer and dendrimer							
BuEH-PPV	435	562	-	62	$4.1 \cdot 10^{-3}$	$15 \cdot 10^3$	[140]
MEH-PPV	532	660	-	71	0.74	96	[141]
G1 dendrimer	337	425	-	79	30	2.6	[142]
M-PPV	355	571	-	273	$88 \cdot 10^{-3}$	$3.1 \cdot 10^3$	[141]
Oligofluorene truxene T4	375	440	-	23	$16.3 \cdot 10^{-3}$	$1.41 \cdot 10^3$	[143]
Other species							
Er^{3+}-Yb^{3+}	980	1533	13	11.1	$2.2 \cdot 10^{-2}$	50	[144]
Nd^{3+}	488	1060	8	1.26	$3.14 \cdot 10^{-2}$	40	[145]
GaAs	337.1	820	-	$2 \cdot 10^3$	10	200	[146]
GaN	337.1	359	-	$1 \cdot 10^4$	10	$1 \cdot 10^3$	[146]

Instead of presenting the material gain by a number at some intensity, it could be more useful to provide the ratio of gain over the corresponding pump intensity, mentioning the saturation intensity value as well. The higher the K value, the more efficient emission at a given wavelength, and the lower pumping intensity is necessary. In fact, the advantage of such an approach is that K does not depend on the pumping beam polarization state (as will be established later, Sub-section 5.2.4).

Gain values presented in Tab.5.1, in case of thin polymer films, were mainly measured by the "Variable Stripe Length" technique (VSL, Sub-section 2.3.4). Strictly speaking, they do not correspond to the actual material gain. These are modal gain values, that is a result of a transverse overlap between the material gain (g) with the product of pump ($p(x, y)$) and propagating mode profiles ($f(x, y)$) inside the layer:

$$g_{mod} = \iint g\, p(x,y)\, f(x,y)\, dxdy \tag{5.3}$$

Variation of the film thickness results in the change of this value: for example the PMMA films doped with 50 mM of PM 567 [130] are characterized by gain values of 18.8 cm^{-1} for a 15 thick μm film and 20.6 cm^{-1} for a 5 μm one.

In summary, the gain values of some materials given in dB or cm^{-1} is inconsistent to predict the amplification in such material are due to at least two reasons:

- the gain varies with the pumping intensity and the knowledge of the slope between them as well as the intensity saturation are necessary to define a working region
- the gain for an optical mode depends on the pumping profile and distribution of the propagating mode inside the medium, and thus varies strongly with system geometry.

5.1.3 Gain in a PMMA-DCM layer

As explained above, the gain value in a wave-guiding structure is not to be confused with the basic gain material property, since it strongly depends on the geometry of the wave-guiding structure. Thus in order to estimate the K value in quasi 2-D micro-lasers,the gain must be measured in exactly the same layer configuration, namely a thin dye-doped PMMA layer fabricated following the protocol in Appendix A without lithography step.

Measurements were performed by Hadi RABBANI-HAGHIGHI from Paris 13 University at different pump fluencies by the VSL technique (Sub-section 2.3.4) in a 600 nm-thick layer with 5 wt% DCM-doped PMMA. The experimentally obtained curves of ASE intensity with respect to the change of the length of the pumping region are plotted on Fig.5.1.b. Then data are fitted by Eq.(*2.5*), under the following assumptions:

- an almost 1-D pump with an homogeneous pump intensity profile along the excited region;
- an absence of gain saturation;

The result of the fit is shown on Fig.5.1.c. the gain coefficient g increases indeed linearly with the pump intensity, leading to K = 50 $\pm$ 3 cm MW^{-1}, indicating efficient overlap between the gain and the mode profile along the layer cross-section. One more important property of the gain in our thin film configuration be in its dominant in-plane polarization (TE gain). Values published in the literature for PMMA-based structures are generally lower:

- DO11 - $1.27 \cdot 10^{-3}$ [cm MW^{-1}],
- DCM $<$ 2 [cm MW^{-1}],
- PM597- 5-10 [cm MW^{-1}],
- PM650 - 21 [cm MW^{-1}];

in contrast with 680 [cm MW^{-1}] for RH640 (Tab.5.1).

At this point, we compared the gain values found in articles and found out that the standard way of presenting the gain by its sole value is not appropriate. We propose an alternative way to better account for the gain value - by means of the slope coefficient $K = g/I_P$ [cm MW^{-1}] and pump saturation value I_{sat} [MW cm^{-2}] (Eq.(5.2)). Moreover, the gain of a given dye should be defined by measurement in the exact wave-guiding configuration it is going to be used. Also, the experiment should be held at several pumping power fluencies, in order to make

sure that the related gain values lie in the linear part of the gain curve. Following these guidelines, we proceed with measurement of the gain in our standard 5 wt% PMMA-DCM thin layer: K = 50 cm MW^{-1}.

5.1.4 Influence of the dye concentration on the emission properties

In this part we discuss the problem of concentration quenching [147] in dye-doped polymer and estimate experimentally the optimal dye concentration for use in 600 nm films.

The material gain depends on the concentration of fluorophore. A limited number of fluorophores will exhibit efficient emission when used at high concentration. But generally there exists an optimal concentration, beyond which the average distance between molecules becomes sufficient for energy transfer to take place and subsequent decrease of the emission.

Such optimal concentration will depend strongly on the polymer host, precisely on the free volume in the polymer bulk [148]. It must therefore be defined for the actual matrix used.

The main part of experimental results presented in this thesis was obtained on samples with dye concentration of 5 wt% (the standard used in the group over years). However it appeared interesting to verify how close this concentration is from the optimal one for the same dye. Such knowledge will prove for future research in our group.

A correct way to conduct this study would be to perform gain measurements by the VSL technique at different concentrations, as it demonstrated by Lu and colleagues in [129] (data from Table 1 in this article are presented on Fig.5.3.a).

We performed the preliminary experiment with a dye-doped polymer layer on our 2-D detection set-up (Sub-section 2.2.1). We examined the ASE (emitted intensity as a function of pump intensity) provided by Gaussian beam pumping at fixed distance from the sample side. Each curve was linearized and the slope values averaged for 3-5 measurements and then compared (Fig.5.3.b). The optimal concentration estimated in such a way is 2% for RH640, 4.5% for DCM and 5% for PM605.

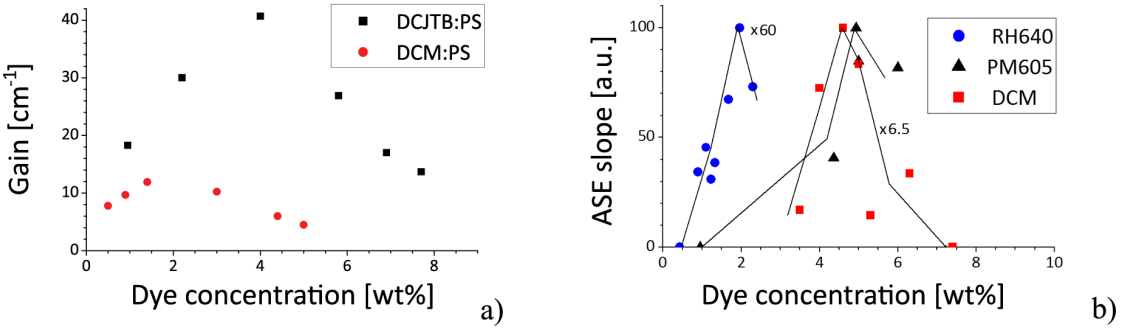

Figure 5.3: *Amplification in PMMA-doped layer for the varied dye concentration: a) gain values from Ref. [129]; b) slope of ASE curves measured by the 2-D set-up for PMMA doped with RH640, PM605 or DCM.*

One interesting effect was noticed during the experiment, namely a blue shift of the ASE peak with the increase of pumping power (Fig.5.4). This later effect is explained in Sub-section 5.2.3.

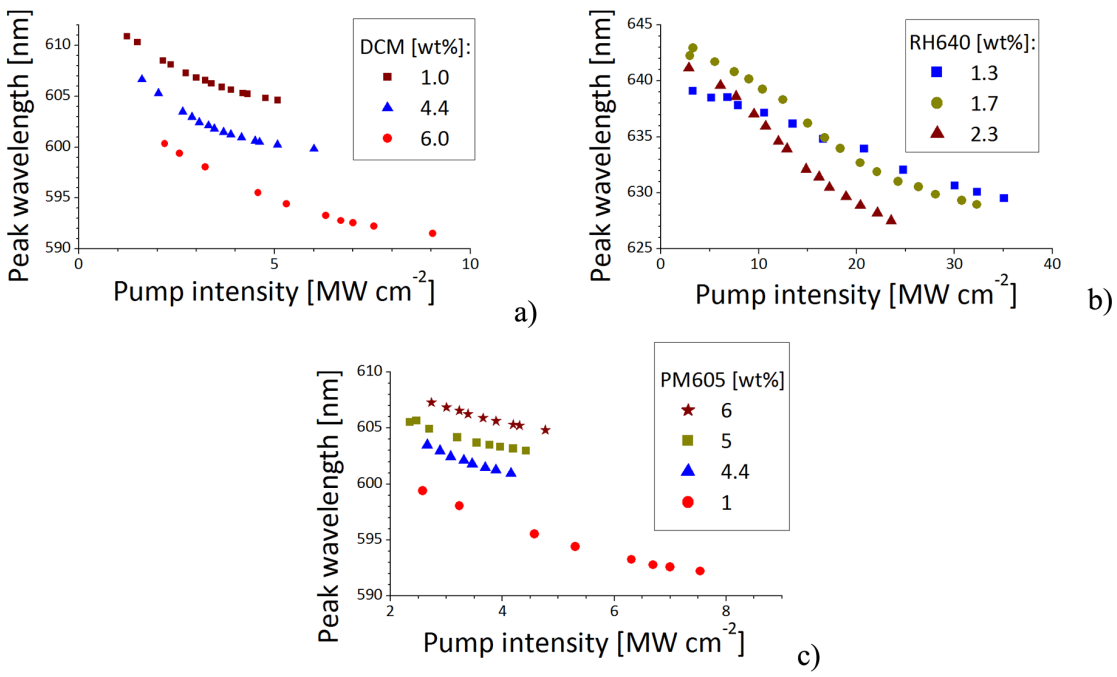

Figure 5.4: *Spectral shift of the ASE peak with the increase of pump power at various concentrations of: a) DCM, b) RH640, c) PM605.*

5.2 Ribbon-shaped micro-cavities

The aim of this Section of Chapter 5 is now to develop a tool to predict the threshold of 2-D micro-lasers from their known gain value or from the photo-physical properties of the dye. Among all micro-lasers in our study, we chose the simplest case of a ribbon-shaped Fabry-Perot micro-laser to model the experiment, for the following reasons:

- Fabry-Perot type modes are almost one-dimensional orbits;
- cavity losses are easily predictable (refraction prevails largely over all other types of losses, and may be considered as main source of losses)

It seems that the simplest shape of 2-D micro-resonators, that sustain Fabry-Perot type modes is the rectangle. However, as was already mentioned previously, the two Fabry-Perot type modes, propagating respectively along the short and long axes of the rectangle can then coexist. In order to prevent this effect, the Fabry-Perot resonator is purposely made of only 2 in-plane borders parallel, two other sides being left "fuzzy" (un-patterned, Fig.5.5.b). There exist other ways to eliminate undesirable Fabry-Perot modes: for instance to fabricate the shorter sides of the rectangle with irregular and non-symmetric borders (Fig.5.5.c). This method works well even with photo-lithography protocol, but the quality of the cavity sidewalls remains limited as compared to electron-beam lithography. To eliminate the possibility of misinterpretation, Fabry-Perot cavities made by electron-beam lithography were used in the present study. A fabrication by electron-beam lithography of ribbon-shaped Fabry-Perot resonators, depicted schematically on Fig.5.5.a, as less time demanding and sensitive to fabrication problems (comparing with cavities shown on Fig.5.5.c), we set our choice on this resonator shape.

The outline of this section is the following. At first the relation between modal gain and threshold of Fabry-Perot micro-laser is discussed. Then we propose a way to estimate the threshold from the basic photo-physical properties of the dye.

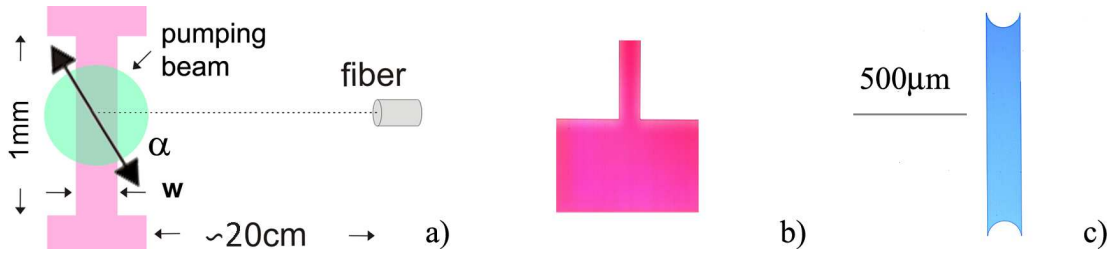

Figure 5.5: *Experimental study of Fabry-Perot resonators: (a) pumping configuration (α stands for the angular orientation of the linear pumping beam polarization with respect to the observation direction); optical microscope photos of 165µm PMMA-PM605 ribbon micro-laser made by e-beam (part of it only, as the overall cavity size is too big to enter the frame), another Fabry-Perot type cavity made from PMMA-MD48 by photo-lithography (c).*

Some peculiar effects of cavity size on the threshold value and the shift of emission spectrum are then discussed. The influence of the pumping beam polarization is subsequently addressed after that. The section is concluded by a confrontation of the experimental results with rate-equations numerical simulations.

5.2.1 Relation between gain and threshold

This part is focusing on the estimation of the laser threshold for micro-lasers when the modal gain value and losses are known. First, we need to establish the relation between these parameters.

In the absence of gain saturation, the linear gain coefficient g is expected to be proportional to the pump intensity I_P via the following expression:

$$g = KI_P \tag{5.4}$$

In spite of its apparent simplicity, this equation will play a central role in the subsequent analysis.

The K coefficient (already introduced in Sub-section 5.1.3) measured for standard DCM-doped PMMA films is about 50 cm MW^{-1} . We will use this value to predict the laser threshold of Fabry-Perot resonators.

Light propagates over a 200 μm distance over 1 ps in a medium with refractive index n=1.5. The fluorescence lifetime of dyes is of the order of few ns. Thus, with a 500 ps pulse pumping, we expect the micro-lasers to reach a stationary regime (for example corresponding to 250 round-trips in a Fabry-Perot ribbon microcavity of 200 μm width). However, the situation is completely different in presence of external resonator, for instance in a VECSOL configuration, where stationary state cannot be reached with sub-nanosecond pumping due to the system geometry [106]. In the stationary regime, the threshold is determined by the gain (and then the pump intensity) necessary to compensate the losses:

$$re^{g_{th}L} = 1 \tag{5.5}$$

Here $r = R^2$ with $R = \left(\frac{n-1}{n+1}\right)^2 \simeq 0.04$ standing for the Fresnel reflection coefficient at normal incidence at the boundary ($n \simeq 1.5$). The length L for a round-trip mode path in a ribbon cavity is $L = 2w$, where w stand for the width of the ribbon (Fig.5.5.a). Injecting Eq.(5.4) into Eq.(5.5) the pump intensity at threshold is then expected to be inversely proportional to w:

$$I_{th} = -\frac{\ln r}{KL} = -\frac{\ln R}{Kw} \tag{5.6}$$

Threshold measurements were carried out for three dyes DCM, PM605 and RH640 and reported in Fig.5.6. The values for RH640 are significantly higher compared to DCM and PM605, so it was plotted on a separate graph for better visualization. The intensity at threshold shows indeed a linear behavior with $1/w$, except for small cavities. This later effect is explained in Sub-section 5.2.3.

If we now calculate the threshold values for DCM with Eq.(5.6) using the previously defined parameters, we obtain a satisfactory quantitative agreement with the experimental values (see Fig.5.6.a).

This agreement implies several consequences.

Firstly the assumption of a stationary regime can be accepted in as much as Eq.(5.5) is valid.

Secondly spatial hole-burning does not influence the thresholds, whereas dye molecules lead to an homogeneous gain and the spectra are multi-modal, even at threshold .

Thirdly only the losses due to refraction are taken into account in Eq.(5.6).

Hence the quantitative agreement means that the losses due to the diffraction at the cavity edges do not modify the thresholds, as evidenced in [119], and that the Fresnel coefficient for an infinite wall R suffice to reproduce correctly the refraction at the boundary, even if the cavity thickness scales with the wavelength.

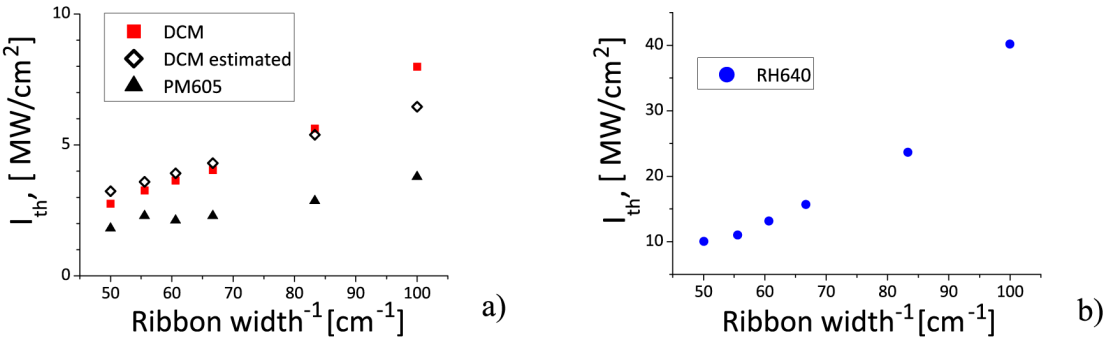

Figure 5.6: *Experimental threshold as a function of the ribbon width for different dyes: a) DCM and PM605, b) RH640. Graph (a) contains also an estimate of the thresholds for DCM-based lasers from Eq.(5.6). No adjusted parameter.*

This agreement opens a possibility to infer unknown gain values for other dyes, based on our reference measurement of DCM. The slope of linear part of the graph in Fig.5.6 is inversely proportional to K, and so tat the unknown K for a dye can be easily inferred. The calculated values are *K(RH640) = 15* and *K(PM605) = 82* cm MW^{-1} (both dyes were taken at a 5 wt% concentration in PMMA, which is not necessarily the optimal concentration, see Sub-section 5.1.4). Few more deduced values of K for tested dyes are presented in Tab.5.2.

Table 5.2: *Comparison of K values for all examined dyes obtained experimentally from the threshold values of ribbon micro-lasers.*

Dye	K [cm MW^{-1}]
DCM	48 ± 4
RH640	15 ± 1
PM605	82 ± 2
MD7	106 ± 2

In this part we established a relation between threshold, gain, losses and cavity size and proved its validity on the prototypical case of ribbon-shaped micro-lasers.

Due to huge refraction losses in ribbon micro-cavities any other type of losses does not contribute significantly and can then be ignored. Measurement of the Fabry-Perot threshold provides a way to readily define the unknown modal gain of the dye in thin polymer films by reference to measurement with DCM (within the assumption of equal refractive index of the two films).

5.2.2 Threshold estimation

The relation between gain and threshold established in previous part proved to be a nice operational tool towards the analysis of gain properties of dyes. However it is not going to work for low gain values, as cavities based on such material will simply not lase. For instance, the maximum pumping intensity of our set-up is about 190 MW cm^{-2}, thus material with $K < 1$ cm MW^{-1} will not achieve lasing even in a 200 μm wide ribbon configuration. To determine whether a given material has a high enough K coefficient gain measurements should be conducted in the precise matrix and layer configuration of interest, which in many cases available in the literature.

It is thus of ultimate interest to build a model for threshold prediction, based on the main photo-physical properties of dyes. In this part we focus on *quantitative* estimates of the gain, and on K in particular.

The density of excited molecules in the medium (N^*) can be estimated as the quantity of incident photons per unit of pumping area ($I_P\tau_p/h\nu$, where ν is the frequency of the pump photon and h - Planck constant) that are absorbed by the bulk material ($N\sigma_{ab}$, where σ_{ab} is the absorption cross-section, see Sub-section 1.1.4, and N - density of molecules in the sample) during the pumping pulse duration τ_p:

$$N^* = N\sigma_{ab}\frac{I_P}{h\nu}\tau_p \tag{5.7}$$

The actual gain at some pumping power is merely the difference between modal gain and losses. And if in the first order approximation we neglect, as in the previous part, triplet losses, absorption to higher excited singlet states and re-absorption, we obtain[88]:

$$G(\lambda) = \sigma_{em}N^* - r_{loss} = g - r_{loss} \tag{5.8}$$

where σ_{em} is the emission cross-section (Sub-section 1.1.4) and r_{loss} are cavity losses, involving both refraction and propagation losses.

Below threshold this difference is obviously negative. But at threshold the modal gain value is high enough to compensate the losses and thus combination of equations (5.4), (5.7) and (5.8) provides:

$$I_{th} = \frac{\sigma_{em}N^*_{th}}{K} = \frac{h\nu}{\tau_p}\frac{N^*_{th}}{N\sigma_{ab}} \tag{5.9}$$

From where we can infer the main formula of this Sub-section, that is the expression for K:

$$K = \frac{N\sigma_{ab}\sigma_{em}\tau_p}{h\nu} \tag{5.10}$$

It contains the absorption (σ_{ab}) and emission (σ_{em}) cross-sections, the density of dye molecules in a unit of polymer volume (N, cm^{-3}), energy of the pumping photons ($h\nu$, which in our case at 532 nm pumping is $3.53 \cdot 10^{-19} J$) and the duration of pumping pulse (τ_p = 500 ps). The beauty of this formula is that N and σ_{ab} figure as a product, marking their separate deduction unnecessary so that the absorbance value can be directly exploited as such. Actually as explained in Sub-section 1.1.4, the estimation of the molecular density is always rough, as an unknown percentage is filtered or degrades during polymerization.

Table 5.3: *Estimation of K values for various dyes by Eq.(5.10) at the central wave-length (λ_{em}) in a spectrum of 150μm width for a ribbon micro-laser. Given absorbance values ($\sigma_{ab}N$) were inferred from measured absorption spectra, while emission cross-sections σ_{em} were calculated by formula (1.20) from measured fluorescence spectrum and τ_f cited in literature.*

Dye, 5 wt%	DCM	RH640	PM605
τ_f [ns]	2	7,5	5
$\sigma_{ab}N$ [cm^{-1}]	$3.29 \cdot 10^3$	$6.45 \cdot 10^2$	$1.3 \cdot 10^4$
λ_{em}[nm]	606	607	594
σ_{em} [10^{-16} cm^2]	2.47	1.39	0.91
K [cm MW^{-1}] (estimated from Eq.5.10)	1150	127	1680
K [cm MW^{-1}] (from Tab.5.2)	48	15	82

However the result of calculation is rather disappointing (Tab.5.3), as all estimated values are 10-20 times higher than the experimentally obtained ones.

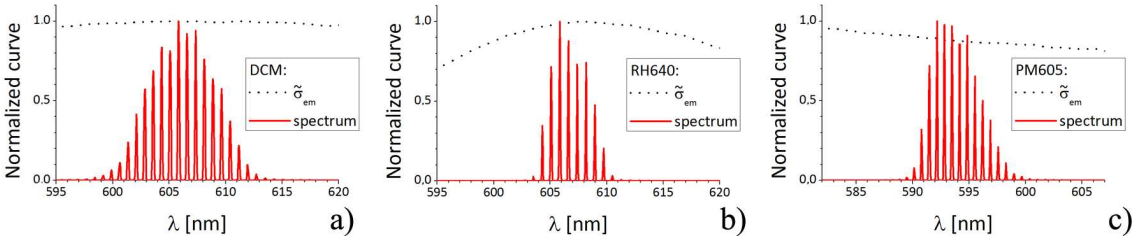

Figure 5.7: *Normalized spectra of 150μm width ribbon micro-lasers and normalized emission cross-section (deduced from Eq.(1.20) in Sub-section 1.1.4) for the given spectral region of the emission of dyes: a) DCM, b) RH640, c) PM605.*

The reason for this mismatch is that we estimated K based on an ideal one-peak emission. But the emission spectra exhibit several lasing peaks, as shown on Fig.5.7. And as will be showed later, in case of a multi-mode emission (m being the number of peaks in the spectrum) K should be estimated by the following expression:

$$K = \left(\sum_{i=1}^{m} K_i^{-1} \right)^{-1} \tag{5.11}$$

To explain this effect we first consider a system with two lasing wavelengths, shifted with respect to each other by a very small spectral interval, so that the gain value can be considered constant from peak to peak. The threshold is proportional to the number of excited molecules necessary to overcome the losses (N_c^*). If we deal with a bi-modal laser, this critical number of molecules corresponds to the sum for both wavelengths: $N_c^* = N_c^*(\lambda_1) + N_c^*(\lambda_2)$. And so the threshold of such system equals to the sum of thresholds allowing each peak to lase independently:

$$I_{th}^{/} = I_{th\,1} + I_{th\,2} \tag{5.12}$$

The number of peaks in our experimental spectra for ribbon micro-laser does not change after the threshold, so we are allowed to assume that all modes have the same threshold ($I_{th\,1} = I_{th\,2}$). Still we prefer to consider a more general case whereby the threshold of peaks can be different. Coexistence of several families of modes (corresponding to different orbits) is an example where such a precaution must be taken.

Each threshold can is inferred from the gain value via the K coefficient:

$$\begin{aligned} I_{th\,i} &= g/K_i \\ I_{th}^{/} &= g/K \end{aligned} \tag{5.13}$$

The first equation in Eq.(5.13) describes the case of single mode whereas the second equation defines the lasing threshold for a multi-mode spectrum. The material gain that provides lasing is taken as the same in both cases, allowing for the same g factor to appear in both equations.

Combining system (5.13) with equation (5.12), we obtain:

$$\frac{1}{K} = \sum_i \frac{1}{K_i} \tag{5.14}$$

The above mentioned equation (5.11) appears then as a result of formula (5.14). The emission cross-section is strongly wavelength-dependent, and so is K, which applying the conventional normalization can be presented as follows:

$$K(\lambda) = K^{max} \frac{\sigma_{em}(\lambda)}{\sigma_{em}^{max}} \tag{5.15}$$

For illustration we consider the spectra of a $150\mu m$ ribbon for DCM, RH640 and PM605, and calculate $K(\lambda)$ for each peak ($\tilde{\sigma}_{em}(\lambda_i) = \sigma_{em}(\lambda)/\sigma_{em}^{max}$):

$$K = K^{max} \left(\sum_{i=1}^{m} \left(\tilde{\sigma}_{em}(\lambda_i) \right)^{-1} \right)^{-1} \tag{5.16}$$

Then the result depends on the number of peaks we consider in the spectrum. The total number of peaks is rather large (limited by the emission cross-section curve), but only few of them actually contribute to the micro-laser emission. In order to explore the influence of the quantity of peaks on our estimated K value, we take as a criterion the respective value of peak intensity (compared to the spectrum maximum). Such calculations are made based on the experimental spectrum of a 150 μm ribbon laser for DCM, PM605 and RH640 and results are given in Tab.5.4. Apparently the 10% intensity criterion is too high, as it provides up to 40% error in the estimated K compared to the experimental value (except for RH640). The inaccuracy decreases for a 0.5% intensity criterion (except for RH640). It is possible that some parameters as the fluorescence lifetime or quantum yield are not correct, or that the refractive index of RH640-doped PMMA differs sufficiently from that of DCM case thus leading to an erroneous modal gain estimate.

Table 5.4: *Estimation of K [cm MW^{-1}] values for various dyes from Eq.*(5.10).

Dye, 5 wt%	DCM	RH640	PM605
K from Tab.5.2	48	15	82
Number of peaks, >10% of maximum	16	8	12
K estimated from Eq.(5.16)	72	15.5	140
Number of peaks, >0.5% of maximum	23	11	17
K estimated from Eq.(5.16)	50	11.5	99

In conclusion, we developed a model to predict the threshold values from the basic photo-physical properties of dyes and allowed to reach reasonable agreement with experimental data. Although the estimation accuracy varies with the number of spectral peaks taken into account our calculated values predict with less than 50% error the gain properties of the material.

5.2.3 Spectral shift with losses

In the previous section a model was developed to calculate the threshold of ribbon micro-lasers from the basic photo-physical properties of the dye. However the estimate was not purely theoretical, as some of the used parameters were actually obtained from micro-laser experiments: namely the central wavelength of the spectrum and the number of peaks. However, these data can be estimated theoretically as well. Some additional emission properties must be first discussed, making this part relatively independent from the previous one.

The central wavelength of a micro-laser spectrum should vary with the change of active medium, as was seen in a previous part (Tab.5.3, Fig.5.7). But the spectrum itself is not centered at the maximum of the stimulated emission cross-section, and depends in fact on the cavity size (for cavities made of the same dye). Experimentally we observed a clear blue shift of the spectrum with the decrease of ribbon width size (Fig.5.8), the absolute value of the shift being dye-dependent (Fig.5.8.b).

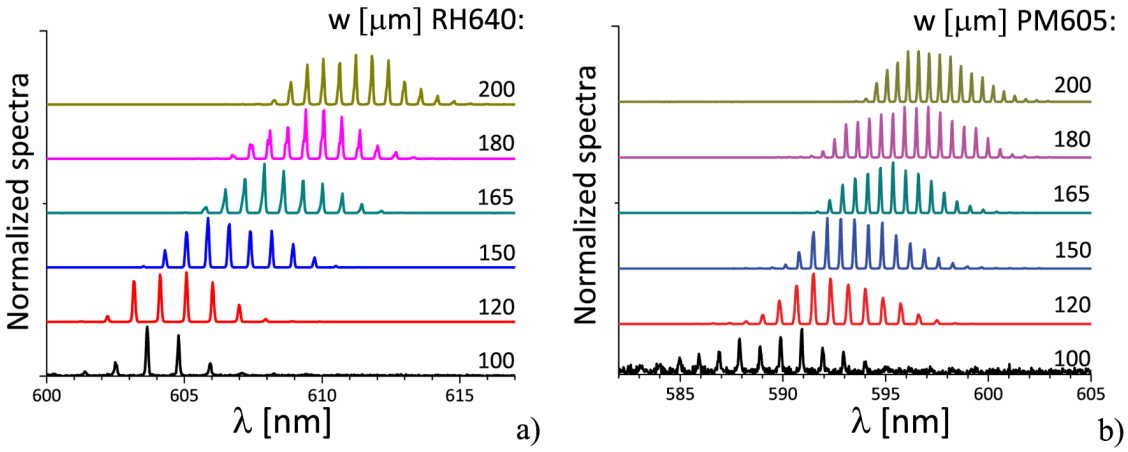

Figure 5.8: *Blue shift of the emission spectrum of the ribbon micro-laser with decrease of the cavity size for: a) RH640; b) PM605. The ribbon width is indicated for each spectrum.*

In the nineties some researchers working on dye-based systems were interested in the lasing of micro-droplets. It was also noticed, that the increase of dye concentration induced a red shift of the spectrum [149]. The reason why spectra appear at different wavelengths lies in the re-absorption process. Due to the overlap between absorption and emission spectra of dyes, unexcited molecules are bound to

absorb photons otherwise emitted from excited states:

$$g(\lambda) = \sigma_e(\lambda) N^* - \sigma_a(\lambda)(N - N^*) \tag{5.17}$$

Light amplification is then decreased, and the number of molecules that must be excited to reach the threshold is

$$N_c^* = \frac{g(\lambda) + \sigma_a(\lambda) N}{\sigma_e(\lambda) + \sigma_a(\lambda)} \tag{5.18}$$

In fact the increase of molecular density forces the emission to move into a region with lower re-absorption, thus red-shifting the spectrum.

Along the same lines, addition of absorber species (which do not contribute to the gain) [149] inside the droplet, or simply intense successive laser pumping [150] (resulting in creation of scattering objects), shifts the laser emission to the smaller wavelength (blue shift). Moreover, the shift becomes more prominent with the increase of absorber concentration. The quantity of amplifying dye molecules in this case remains the same, but there is a rise in round-trip losses induced by the absorber species. Thus by way of compensation of higher losses by a high gain the emission should take place closer to the maximum of the gain curve (which corresponds to the maximum of emission cross-section) leading to a blue-shift.

The spectral shift, observed in planar micro-lasers (Fig.5.8) can be explained similarly. Reduction of the cavity width results in a decay of the round-trip gain, while refraction losses remain unchanged. The difference between round-trip gain and losses decreases with cavity size in micro-lasers, very much like the rise in absorber concentration in micro-droplets, both resulting in a blue-shift.

Let us now proceed to a more quantitative estimate where $N_c^*(\lambda)$ should play a central role in its normalized form ($N_c^*(\lambda)/N$). This expression (known as $\gamma(\lambda)$) has been used to describe threshold conditions since the early days of dye lasers [88, 149]:

$$\gamma(\lambda) = \frac{N_c^*}{N} = \frac{g(\lambda)}{\sigma_a(\lambda) N + \sigma_e(\lambda) N} + \frac{\sigma_a(\lambda) N}{\sigma_a(\lambda) N + \sigma_e(\lambda) N} \tag{5.19}$$

At threshold, the gain balances the losses, and $g(\lambda)$ can be substituted by $-\ln r/L$ (r stands for losses per round-trip, and L is the length of this round-trip, Eq. 5.5). To find the lasing wavelength close to threshold, the minimum of this function should be localized, as shown on Fig.5.9. Indeed, this estimation provides the shift towards the shorter wavelength (blue-shift) with the decrease of ribbon size, consistent with experimental observation (see Fig.5.8). Moreover, the calculated shifts are of the same order of magnitude as experimentally observed ones.

We shall now focus on the number of peaks within a given spectrum. The peaks should normally fill all the gain curve, and their visibility in the emission spectrum is a matter of measurement precision and signal to noise ratio. The main emission (99.9 %) will take place in a more limited spectral region of extension $\triangle\lambda_{sp}$, and we are actually interested in the number of peaks within this range. If the spectrum width ($\triangle\lambda_{sp}$) is known in wavelength units, its frequency equivalent can be calculated from:

$$\triangle\nu_{sp} = \frac{c}{\lambda_{min}} - \frac{c}{\lambda_{max}} = \frac{4c\triangle\lambda_{sp}}{4\lambda_c^2 - (\triangle\lambda_{sp})^2} \tag{5.20}$$

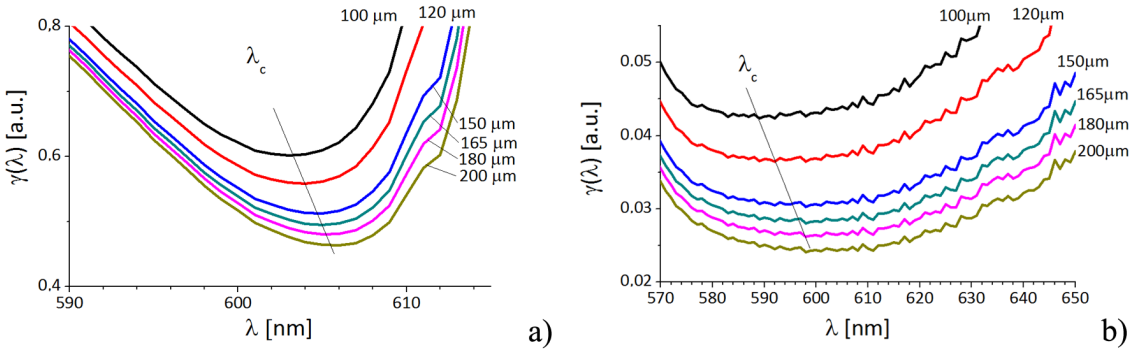

Figure 5.9: *Localization of the center of the emission spectrum by way of the γ function from expression (5.19): a) RH640; b) PM605.*

where $\lambda_{min} = \lambda_c - \triangle\lambda_{sp}/2$ and $\lambda_{max} = \lambda_c + \triangle\lambda_{sp}/2$. Then taking into account the distance between two peaks in the frequency spectrum of a ribbon of width w:

$$\triangle\nu = \frac{c}{2nw} \tag{5.21}$$

The number m of modes in the spectrum can be estimated from the condition that the frequency spectral range contains between m-1 and m inter-peak intervals $\triangle\nu_{sp}\,\epsilon\,[(m-1)\triangle v;\ m\triangle v]$:

$$\frac{8nw\triangle\lambda_{sp}}{4\lambda_c^2 - (\triangle\lambda_{sp})^2} \leq m \leq \frac{8nw\triangle\lambda_{sp}}{4\lambda_c^2 - (\triangle\lambda_{sp})^2} + 1 \tag{5.22}$$

Table 5.5: *Experimental width in [nm] of fluorescence, ASE and ribbon micro-lasers spectra ($\triangle\lambda$, defined at FWHM). In a ribbon case of width at 10% ($\triangle\lambda_{10\%}$) and 0.5% ($\triangle\lambda_{0.5\%}$) of the maximum are presented.*

Dye	σ_e	Fluorescence $\triangle\lambda$	ASE	Ribbon $\triangle\lambda$	Ribbon $\triangle\lambda_{10\%}$	Ribbon $\triangle\lambda_{0.5\%}$
PM605	97	71	17	5.5	9.8	13.7
PM597	115	89	18	-	-	-
DCM	127	102	23	6.2	10	16.5
RH640	50	45	16	4	6	9
RH590	51	42	23	-	-	-
MD7	62	57	13	3	4.5	7.3
MD48	45	46	8	-	-	-

Tab.5.5 presents the experimentally obtained values on FWHM[5] of spectra of a dye-doped PMMA system for fluorescence, ASE and in the case of a ribbon micro-laser. The empiric ratio between $\triangle\lambda$ of ASE over ribbon is 1/4. If the ribbon spectrum had a Gaussian envelope, the ratios of width at some height would be $\triangle\lambda_{10\%}(ribbon)/\triangle\lambda(ribbon) = 3.3$ and $\triangle\lambda_{0.5\%}(ribbon)/\triangle\lambda_{10\%}(ribbon) = 2.3$, whereas we observe experimentally 1.5 for both, (which gives $\triangle\lambda_{10\%}(ribbon)/\triangle\lambda(ASE) = \frac{3}{2}\cdot\frac{1}{4} = \frac{3}{8}$). The nature of this difference stays undetermined.

Finally the number of peaks was determined from a spectral range at 10% and 0.5% of the total emitted intensity, determined from FWHM of ASE (empiric value):

[5]FWHM is the abbreviation from "Full Width at Half Maximum".

$$\begin{aligned} \triangle\lambda_{10\%}(ribbon) &= \frac{3}{8}\triangle\lambda(ASE) \\ \triangle\lambda_{0.5\%}(ribbon) &= \frac{9}{16}\triangle\lambda(ASE) \end{aligned} \tag{5.23}$$

and presented on Tab.5.6 together with the experimentally obtained number of peaks, showing a good agreement.

Table 5.6: *Comparison of the number of peaks in the experimental spectrum of ribbon micro-lasers (exp.) and deduced (estim.) from Eq.(5.22), using spectrum FWHM defined from the one for ASE by Eq.(5.23). Data on RH640 and PM605 are presented.*

w, μm	PM605				RH640			
	10%		0.5%		10%		0.5%	
	exp.	estim.	exp.	estim.	exp.	estim.	exp.	estim.
100	8	8	11	12	4	5	8	8
120	10	10	15	14	6	6	9	9
150	12	12	16	17	8	8	11	11
165	13	13	17	19	9	9	12	12
180	14	14	21	20	9	9	12	13
200	16	16	22	22	10	10	14	14
$\triangle\lambda$ of ASE [nm] (from Eq.(5.23))	-	9	-	13	-	6	-	9

As already mentioned, the influence of re-absorption influence should be also taken into account in the expression for K. Combining equations (5.10), (5.18) and (5.8) it can be evidenced as follows:

$$\begin{aligned} K(\lambda_c, r_{loss}) &= \frac{K_0(\lambda_c)}{m}\left(1+\frac{\sigma_{ab}(\lambda_c)}{\sigma_{em}(\lambda_c)}\right)\frac{r_{loss}}{r_{loss}+\sigma_{ab}(\lambda_c)N} = \\ &= \frac{K_0(\lambda_c)}{m}\frac{r_{loss}}{\sigma_{em}(\lambda_c)}\frac{1}{\gamma(\lambda_c)} \end{aligned} \tag{5.24}$$

where $K_0(\lambda)$ is K in the absence of re-absorption (defined earlier in Eq.(5.10)), λ_c stands for the center of the spectrum defined from the minimum of the γ function(Eq.(5.19)), and m stands for the number of peaks in the spectrum defined by Eq.(5.22) ($\triangle\lambda_{sp}$ being taken as half of the ASE FWHM).

Equation (5.24) explains the reason why the threshold rises significantly for small ribbons. As the spectrum shifts towards small λ (blue-shift), the ratio $r_{loss}/\left(r_{loss}+\sigma_{ab}(\lambda_c)N\right)$, that was very close to unity, now decreases and $K(\lambda_c, r_{loss})$ becomes proportional to the losses. The threshold is than no more linear with the gain (losses), but scales to squared losses, as was evidenced on Fig.5.6.a.

We started this section with the demonstration of the relation between the gain and threshold, and proved it experimentally for ribbon micro-lasers. Then a simple model of threshold prediction based on photo-physical properties of dyes was proposed and proved to be valid up to no more than 20% error for large cavities. Finally the re-absorption losses were considered allowing to account for spectral shifts and the increase of threshold for small cavities.

5.2.4 Influence of the polarization anisotropy

The previous sections of this Chapter were dedicated to the estimation of the optically pumped threshold, without considering polarization effects. In fact, all

thresholds and gain values were obtained for a pump beam polarization orthogonal to the direction of propagation of the stimulated emission.

Here the influence of the pumping beam polarization on the gain and threshold will be examined based on the example of three dyes DCM, RH640 and PM605.

The direction of observation remains along the width of the ribbon (w on Fig.5.5a), while the pump beam polarization is kept linear within the substrate plane, while alternating from perpendicular ($\alpha = 90°$) to parallel ($\alpha = 0°$) to the direction of observation.

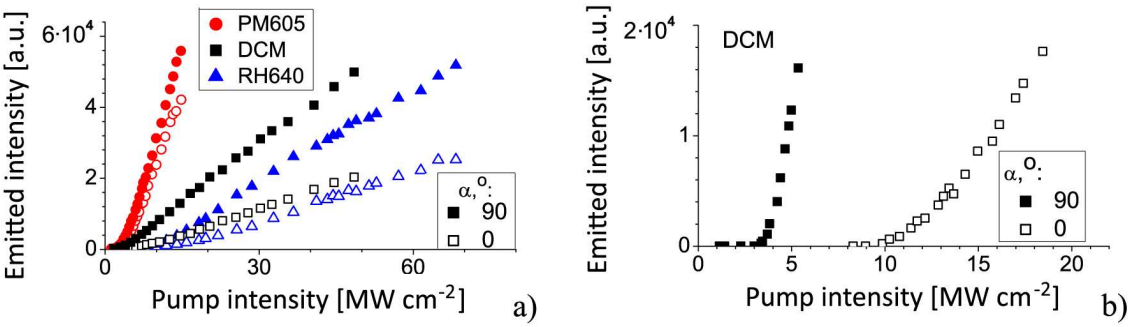

Figure 5.10: *Influence of the pump beam polarization angle α on the emitted versus pump intensity in the case of a) ASE, b) a 165 μm DCM ribbon micro-laser.*

Fig.5.10 presents the emitted intensity versus the pump intensity for ASE (a) and Fabry-Perot (b) configurations. It shows that the pump polarization α is a relevant parameter, which strongly influences the emitted intensity, depending of course on the molecular structure of the dye.

The slope of the ASE curve (Fig.5.10.a) is lower if the pump beam polarization is parallel to the observation direction (longitudinal pumping for $\alpha = 0°$). For some dyes the effect is more pronounced (DCM, RH640) than for others (PM605). These ASE curves can also serve for the determination of the gain value. However this demands an extension of the existing theory, which for a uniform 1-D beam profile provides the relation between ASE intensity and modal gain (Sub-section 2.3.4), in order to adapt it for a Gaussian beam profile. The latter is beyond the aim of this thesis work. Nevertheless, these ASE curves measured with a Gaussian beam profile evidence polarization-induced variation of gain, and the ratio of slopes at $\alpha = 0°$ and $90°$ should be proportional to the gain ratio at $\alpha = 0°$ over $\alpha = 90°$.

The threshold curves depicted on Fig.5.10.b leave no doubts concerning the change of the gain: the laser threshold is indeed reduced by a factor of two from $\alpha = 0°$ to $90°$ for DCM.

To predict the dependance in α, we use the model based on fluorescence anisotropy, developed in Chapter 3. For a change we now consider the total emitted intensity along the edge direction (Appendix B.5):

$$\frac{I(\alpha)}{I(\alpha = 90^o)} = \frac{\rho + 1}{2} + \frac{\rho - 1}{2} \cos 2\alpha, \tag{5.25}$$

where $\rho = I(0^o)/I(90^o)$ is a positive function of θ_0 and $\cos^2 \beta$.

For a linear dipole, $\beta = 0$, using the Eq.(3.9) it can be shown that $\rho = 1/3$ *for an isotropic distribution* (while in the case of 2-D distribution, i.e. $\theta_0 = 0^o$, $\rho = 1/2$), which implies that even excitation by a longitudinal polarization along the direction of observation ($\alpha = 0$) causes a non-negligible light emission in this direction (1/3) compared to the ideal case of perpendicular pumping ($\alpha = \pi/2$). This ρ factor can be calculated from the r_0 parameter, familiar in the fields of

fluorescence anisotropy. In practice ρ depends on the distribution of dyes (through θ_0) and then on the layer fabrication[6].

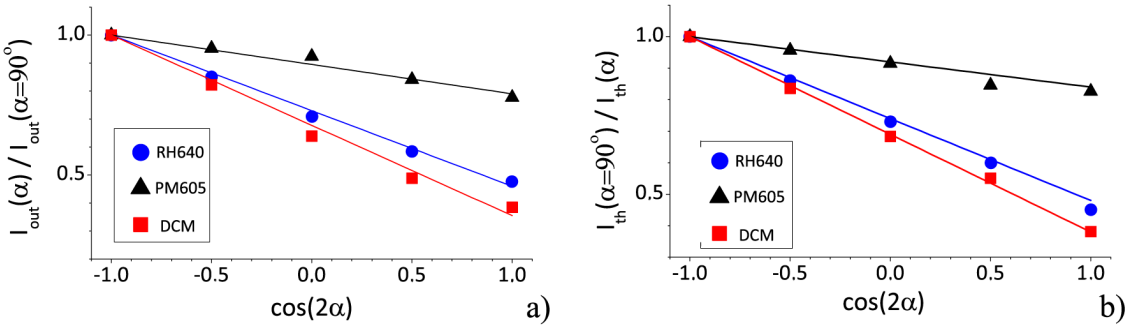

Figure 5.11: *Influence of the polarization on relative values of: a) ASE, b) threshold for a 165 µm ribbon micro-laser. Experimental data on all three dyes is plotted by points while solid lines follow Eq.(5.25) with ρ taken from experimental data (averaged over α to reduce the error)*

$I(\alpha)$ corresponds to the probability of fluorescence emission of the dyes. We note that the ASE intensity is proportional to I. We first checked that the ratio $I(0^o)/I(90^o)$ does not noticeably depend on the pump intensity, namely that the fluctuations remain in a range of $\pm 1\%$ for pump intensities varying from 20 to 60 MWcm^{-2}. Then the average ratio $I(0^o)/I(90^o)$ is plotted versus $\cos(2\alpha)$ in Fig.5.11.a for the three dyes. The curves display a linear behavior, which provides evidence for the validity of formula (5.25) which apply even in the stimulated regime. The ρ values for ASE presented in Table 5.7 are then inferred from the linear fits and formula (5.25).

The ρ values for fluorescence, given in Tab.5.7, resulted from calculations described in Chapter 3 for θ_0 and β values of each dye.

Table 5.7: ρ obtained for fluorescence in Chapter 3, and compared to ASE and the laser threshold inferred from Eq.(5.25) and Fig.5.11. Error is about ± 0.03.

ρ	DCM	PM605	RH640
Fluorescence	0.41	0.79	0.48
ASE	0.37	0.77	0.46
Threshold	0.38	0.84	0.48

The intensity of ASE in dye-doped PMMA layers at fixed pump intensity depends on the polarization of the pump beam (Fig.5.10.a). In other words, variation of the pump beam polarization results in a change of slope K between the gain and the pump intensity. Although the slope of the ASE curve shown on Fig.5.10.a does not correspond to K (as it was not inferred from VSL experiment), the ratio $K(\alpha)/K(90^o)$ at different pump polarization angles should scale to the ratio $I(\alpha)/I(90^o)$ of slopes of the intensities emitted in ASE at corresponding pump polarization angles (when the pumping region is the same for ASE measurements under different pump beam polarizations).

Accordingly, the validity of Exp.(5.25) can be checked for lasing thresholds as well. In fact they can be considered as working points where the non-linear behavior is still relatively moderate allowing for a fluorescence formula as Eq. (3.5). The gain value, necessary to attain the lasing threshold in planar Fabry-Perot

[6]For other values of β see Sub-section B.5 in Appendix B. For instance $\beta \to \pi/2$ implies $\rho > 1$ for both the 2-D and 3-D distribution laws, thus privileging a pump polarization parallel to the observation direction.

resonator is defined by the level of losses, leading to $K(\alpha)F_{th}(\alpha) = g_{th} = const.$ Thus the decrease of gain slope results in the increase of threshold value, we expect the ratio of threshold fluencies $F_{th}(\alpha)/F_{th}(90^o)$ of the ribbon-shaped micro-lasers to be inversely proportional to $K(\alpha)/K(90^o)$. Thresholds ratio being plotted versus $\cos(2\alpha)$ on Fig.5.11.b and consistently shows a linear behavior for the three dyes. If the $F_{th}(90^o)/F_{th}(\alpha)$ ratio is identified with the right part of formula (5.25), then a ρ value can be inferred for each dye. The results are gathered in Tab.5.7 where the error bars correspond to the fluctuations of the ribbon widths from 150 to 200 μm. Such satisfactory correlation between ρ values obtained from ASE and lasing suggests that the K parameter roots from the intrinsic molecular properties of dyes.

To the best of our knowledge, the early studies on the liquid dye lasers did not report on the pump polarization influence on the threshold. We suppose that in such configuration the effect is eliminated by rapid reorientation of the dye molecules in a solvent. For instance, a good quantitative agreement between ratio of fluorescence intensities $I(0^o)/I(90^o) = 0.5$ and lasing thresholds $F_{th}(90^o)/F_{th}(0^o) = 0.5$ was obtained under the orthogonal pump beam polarizations in Fabry-Perot laser, based on light-emitting polymer in solvent [124], while no difference in thresholds noticed by same author in liquid dye solution.

In summary, the polarization of the pumping beam can have an important impact on the emission efficiency in dye-doped systems, including gain and threshold. Quantitative predictions on this effect can be made based on the fluorescence anisotropy model developed in Chapter 3.

5.2.5 Numerical simulations of the threshold value based on rate-equations

This part is dedicated to an alternative analysis based on numerical simulations of the dynamics of the population density of the excited states of the molecule and of the emitted light intensity.

This simulation is based on a set of three equations, namely (1.32), (1.37) and (1.33) derived in Section 1.2):

$$\begin{aligned} \frac{d\eta^*}{dt} =& \sigma_a i_p - \left(\sigma_e i_e + \sigma_a i_p + \frac{1}{\tau_f}\right)\eta^* \\ \frac{di_e}{dt} =& \frac{c}{n}\left(\sigma_e i_e + \frac{1}{\tau_f}\right) N\eta^* - \frac{i_e}{\tau_{cav}} \\ i_p(t) =& \frac{2}{\sqrt{\pi}} i_{p0} exp\left[-\left(\frac{t}{\tau_p/2}\right)^2\right] \end{aligned} \tag{5.26}$$

The first equations describes the evolution of the excited state population density in the cavity ($N\eta^*$ [cm^{-3}], where $\eta^* = N_1/N$ is the relative population density) with the dye density N [cm^{-3}], whereas the second one accounts for the dynamics of the photon flux of the cavity mode (i_e [cm^{-2}s^{-1}]). The last expression defines the temporal profile of the pumping intensity (i_p [cm^{-2}s^{-1}]) in terms of a Gaussian. The characteristic times used in these equations are the fluorescence lifetime (τ_f), the photon lifetime in the cavity (τ_{cav}), the pump duration (τ_p) and i_{p0} stands for the mean pumping intensity during the pump pulse.

The third expression in (5.26) describes the pump beam temporal profile outside the cavity, which in general case is modified inside the cavity by dispersion processes and multiple reflections or refraction processes. However, the change of temporal profile inside 2-D micro-cavity can be considered negligibly small for

sub-nanosecond and longer pumping beam duration. A single round-trip of the pumping photon through the cavity height (600 nm) takes 9 fs. Apart from a very small percentage of scattered pumping photons, pump photons not absorbed by the dye or the wafer during a round-trip will leave the cavity in 10 fs. The propagation time within the cavity plane is typically 1 ps (to cover 200 μm distance in medium with refractive index n=1.5), which concerns only scattered pump photons. So it can be assumed that at a given moment in time, the number of pump photons in the cavity follows the distribution given by the third equation in the set (5.26).

The situation is opposite for the parameter i_e, describing the flux of emitted photons . Its value at a given time corresponds to the total number of photons that were created and remain till current time inside the cavity. And so the maximum of the i_e curve should be higher than i_p (under the condition $\sigma_e > 0$), but lower compared to the area of i_p.

We will examine the dynamics of the emission process on the example of the PM605 laser dye. First a 200 μm ribbon laser is considered. The following values were used in simulations: pump duration $\tau_p = 500$ ps, refractive index n = 1.54, fluorescence lifetime $\tau_f = 1.5$ ns (obtained experimentally with the streak camera set-up, Tab.3.7 in Sub-section 3.2.1), emission-cross section at 598 nm wavelength $\sigma_e = 3 \cdot 10^{-16}\text{cm}^2$ (calculated by Eq. (1.20), Sub-section 1.1.4, from the experimental fluorescence spectrum), absorption cross-section at pumping wavelength of 532nm $\sigma_a = 5.63 \cdot 10^{-16}$ cm^2 (calculated from the emission cross-section by Eq.(1.19), Sub-section 1.1.4), density of molecules $N = 2.3 \cdot 10^{19}\text{cm}^{-3}$ (estimated from the measured absorbance curve and the a fore-mentioned value of the absorption cross-section). As for the initial conditions, the excited population density and photon flux are set to zero before the arrival of the pump.

The dynamics of the emission at different values of pump intensity is shown on Fig.5.12. Far below the threshold, losses are too high and the system is only capable of spontaneous emission (Fig.5.12.a). Moderate increase (but still below threshold) of pumping intensity results in the creation of sufficient number of excited molecules to allow for avalanche de-excitation, however still too low to overcome the losses (Fig.5.12.b). In both cases, the emission is delayed with respect to the pump. Finally at threshold (14.8 kW cm^{-2}), the population of excited molecules rises so fast that the emission flux requires a much shorter build-up time than previously, and becomes predominant before the pump reaches half of its peak intensity (Fig.5.12.c). Moving further away from the threshold lowers the build-up time and the emission follows the temporal shape of the pumping curve (Fig.5.12.d). These results agree with our experimental observations with the streak-camera (Sub-section 3.2.1): the ASE follows the pumping signal and the fluorescence emission starts after the peak of the pump signal.

The dynamics is different in VECSOL configurations, where the active layer is set in the external resonator [106].

In fact the equations we used are somewhat over-simplified model, and they do not account for the re-absorption process and overestimate the impact of spontaneous relaxation of molecules into the emission flux (there is always a non-negligible percentage of molecules which undergo non-radiative de-excitation). We will refer to our basic model as A, the one containing quantum yield - B, and that containing both quantum yield and re-absorption - C.

In the case of model B, the quantum yield ϕ should decrease the flux of emitted photons:

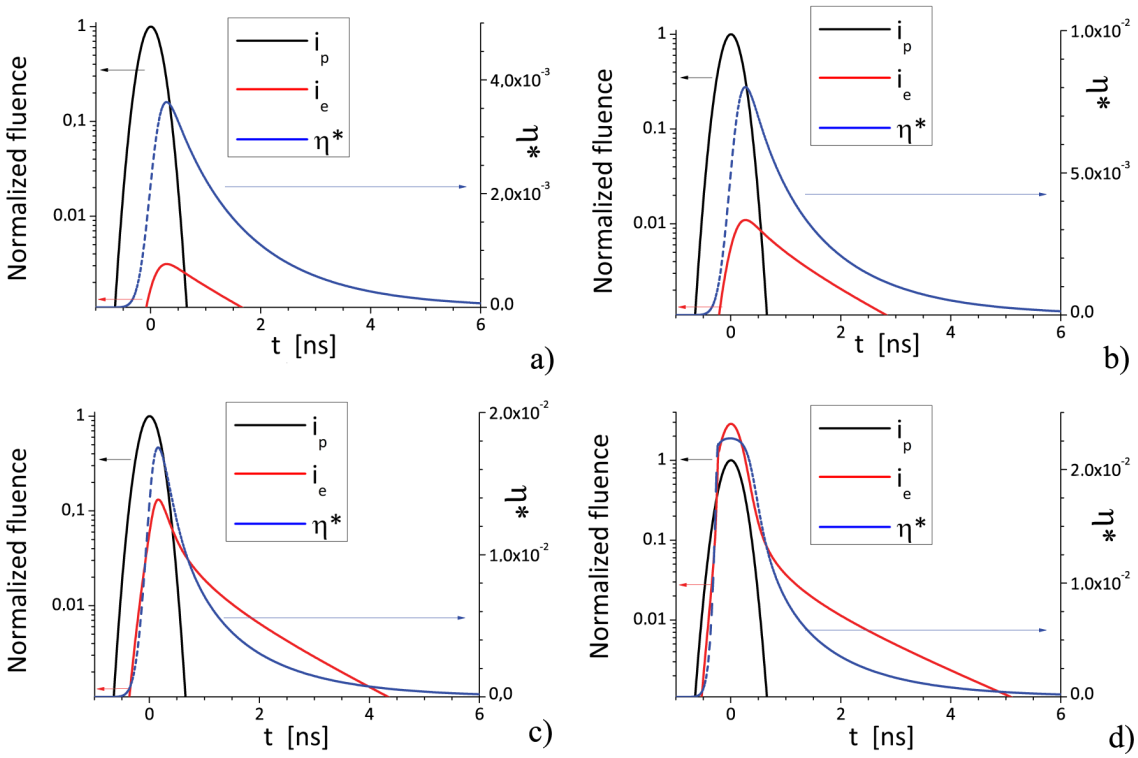

Figure 5.12: *Results of numerical simulations on a laser emission dynamics, performed by equations (5.26) depending on I_{p0} : a) fluorescence emission (6 kW/cm^2); b) just below threshold (12 kW/cm^2); c) just above threshold (40 kW/cm^2); d) further above the threshold (0.4 MW/cm^2). The left scale shows the normalized intensity (scaled by the ratio of emitted over pump energy), and the right one the relative number of excited molecules.*

$$\frac{di_e}{dt} = \frac{c}{n}\left(\sigma_e i_e + \frac{\phi}{\tau_f}\right) N\eta^* - \frac{i_e}{\tau_{cav}} \tag{5.27}$$

The re-absorption process (model C) is determined by the number of molecules in the ground state and the absorption cross-section at the emission wavelength $(\sigma_a(\lambda_e)(1-\eta^*)i_e)$. The first and second equations of the set (5.26) are then modified as follows:

$$\begin{aligned}\frac{d\eta^*}{dt} &= (\sigma_a(\lambda_a)i_p + \sigma_a(\lambda_e)i_e) - \left(\left(\sigma_e(\lambda_e) + \sigma_a(\lambda_e)\right) i_e + \sigma_a(\lambda_a)i_p + \frac{1}{\tau_f}\right)\eta^* \\ \frac{di_e}{dt} &= \frac{c}{n}\left(\left(\eta^*\left(\sigma_e(\lambda_e) + \sigma_a(\lambda_e)\right) i_e + \frac{\phi}{\tau_f}\right) - \sigma_a(\lambda_e)i_e\right) N - \frac{i_e(\lambda_e)}{\tau_{cav}}\end{aligned} \tag{5.28}$$

Obviously simulations with models B and C do not provide results identical to the ones discussed above, leading to several interesting differences. For instance - the introduction of a quantum yield leads to the transient oscillations in the number of excited molecules and the emission flux (Fig.5.13.a-b). It also increases the threshold (Fig.5.13.c, Tab.5.8).

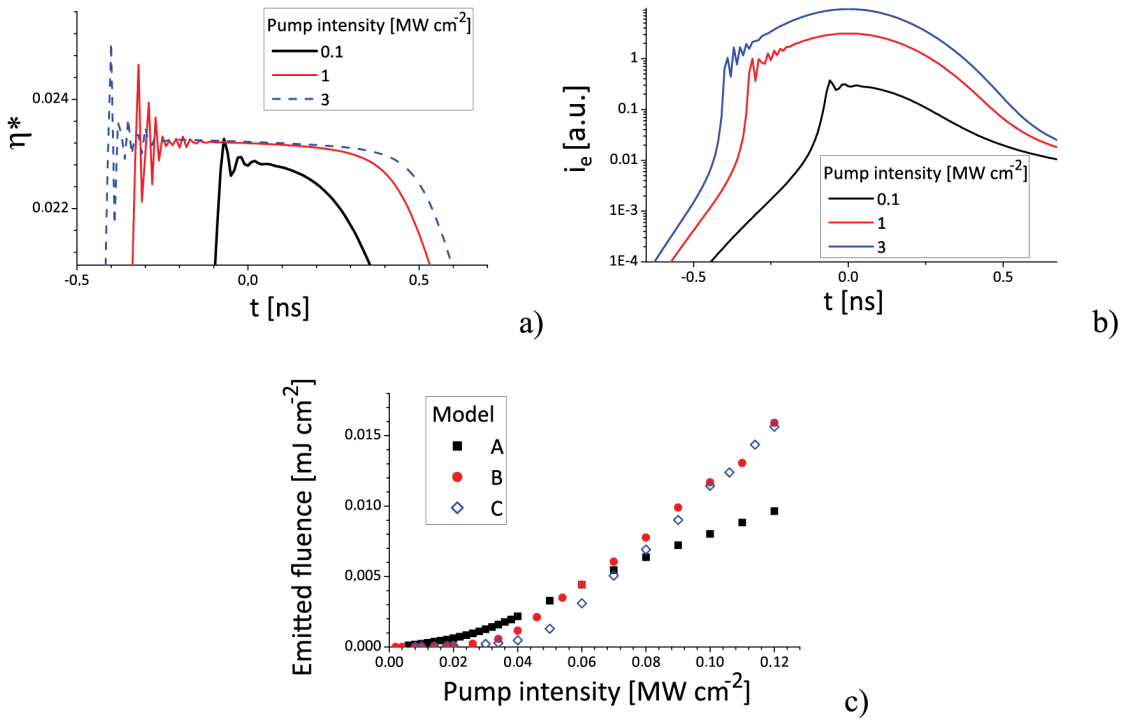

Figure 5.13: *Results of numerical simulations of the laser emission dynamics, performed by equations (5.28): a) transient oscillations in the number of excited molecules; b) transient oscillations in the emission flux; c) threshold curves by A, B and C models. Simulations performed for a 200 μm ribbon Fabry-Perot laser based on the PM605 dye.*

Table 5.8: Comparison of threshold values from our different models (for 5 wt% of PM605 in PMMA).

I_p [kW cm^{-2}]	Ribbon size [μm]	
	200	100
A	14.8	24
B	36	56.5
C	48	75
η^*_{max}	200	100
C	0.023	0.054

A more thorough study should be still performed for various ribbon sizes, based on different dyes and also taking into consideration the quantity of peaks in the emission spectrum.

These simulations advantage from ease in accounting for the gain anisotropy properties, which as well is left for the future studies.

Chapter conclusion

This Chapter focused on the gain properties in thin polymer films, studied experimentally on dye-doped polymers but can be easily extended for the case of light-emitting polymers.

After a thorough analysis of the values cited in literature to characterize the amplification in thin polymer films, we proposed to improve the existing terminology by introducing a new parameter K, which represents the slope between the gain and the pump intensity. Thus we attempted to simplify the comparison of the

gain in various materials in a fixed thin film configuration as well as fixed material in various film thickness values.

On the other hand, such approach allows to establish a simple expression to describe the relation between gain, losses and threshold. We obtained a satisfactory quantitative agreement between the the K parameter inferred from the gain measurements in the dye-doped thin polymer film and the one estimated from "gain-loss-threshold" relation based on measured experimental thresholds of ribbon micro-lasers. We also estimated K from known photo-physical properties of dyes, which gave a correct order of magnitude.

Such relation allows for the estimation of the gain, loss or threshold parameter from the others two, and thus enables to predict the optically pumped threshold and facilitates the design of optically pumped organic laser with optimal characteristics. In our opinion, this method can be also used to rule out materials with high optically-pumped thresholds for study of the electrically pumped ones.

The fluorescence anisotropy features the output polarization and also the intensity of the dye-doped micro-lasers emission. In the dye-doped media, anisotropy of fluorescence emission results in the gain anisotropy of stimulated emission, and thus the K parameter varies also with the polarization of the pump beam. We experimentally proved that for ribbon Fabry-Perot planar micro-lasers the threshold variation with pump beam polarization follows the same law as fluorescence intensity. Moreover we shown satisfactory agreement between the coefficients in both cases.

Some of these results were presented on the Matériaux et Nanostructures pi-Conjugués (MNPC) conference (Obernai, France, 2011).

Chapter 6

Thresholds of micro-lasers of various shapes

In the previous Chapter we proposed a model for the threshold estimation of dye-doped polymer micro-lasers based on standard photo-physical properties of dyes, and proved its validity in the case of ribbon-shaped micro-lasers. The basic idea relies on the well-known statement in laser physics, that at the threshold the modal gain compensates for the losses of the mode. A Fabry-Perot type cavity was chosen for the model experiment due to the ease of losses estimation (huge refraction losses happening at normal incidence on the dielectric borders).

The relation between mode threshold, gain and losses can be successfully used to address the inverse problem, that is to infer the cavity losses. For instance, one of the still open physical problems - namely diffraction effects on a dielectric corner, can be re-examined from this viewpoint.

However such analysis may be complicated in a case of simultaneous lasing modes in a multimodal cavity. As we will show in this Chapter, the respective localization of mode types defines their impact on the lasing properties.

The purpose of this Chapter is to generally and apply the previously developed model towards the analysis of the emission properties of various shapes of planar micro-lasers: square, rectangle and kite-shaped micro-laser. First the lasing properties of square micro-lasers are discussed, the light out-coupling mechanism is explored and their diffraction losses quantified. Then we address the co-existence in the cavity of modes with different quality factor: Fabry-Perot and diamond periodic orbits in rectangle micro-lasers, and finally whispering gallery modes and Fabry-Perot in kite-shaped micro-lasers.

6.1 Square-shaped micro-cavity

Our analysis of the emission properties of planar micro-lasers started from the simpler case of ribbon-like Fabry-Perot cavities. Next in complexity scale comes the rectangle, which can also act as a Fabry-Perot resonator, if its shorter side is much smaller than longer side. However depending on the aspect ratio of the rectangle, its other spacial modes can exist.

For the sake of simplicity, we proceed with our analysis at an intermediate level of complexity, which generally contains a single type of modes namely the square.

Square-shaped micro-lasers are extremely interesting objects from the point of view of fundamental physics, as their emission is tightly related to the still unsolved classic problem of diffraction on the dielectric corners. They also reveal very interesting polarization-dependent properties of their emission spectra. The study on square micro-lasers gave us an insight on the light refraction and polarization

phenomena occurring in micro-lasers emission (Sub-section 3.2.3).

The general emission properties of square micro-lasers are addressed first. Then, the influence of the pumping beam polarization on the emission properties are discussed. The following step in the study consists in the analysis of the simulated mode patterns and light out-coupling from a passive resonator. The latter is then confirmed by experimental observation. Finally diffraction losses are inferred from the experimentally measured threshold values.

6.1.1 General emission properties of square micro-lasers

In this section, the spectral properties and directionality of emission of square-shaped micro-lasers are described.

The analysis of passive square resonator states that there can exist many types of periodic orbits, as shown on Fig.6.1.b-e. Not all of them are confined in a cavity with refractive index n=1.5. Only those meeting the cavity border at an angle of incidence higher (for Fig.6.1.b-d) than the total internal reflection angle $\theta_c = 42^o$ on the boundary between PMMA and air can be sustained.

In fact, we have observed experimentally only two types of periodic orbits: Fabry-Perot and diamond (inscribed square, Fig.6.1.e). The fabrication with UV lithography gives generally lower precision comparing to electron-beam lithography. Such Fabry-Perot modes were experimentally reported in cavities made by UV lithography, but not by e-beam (except for RH640 dye, presumably due to its very low gain).

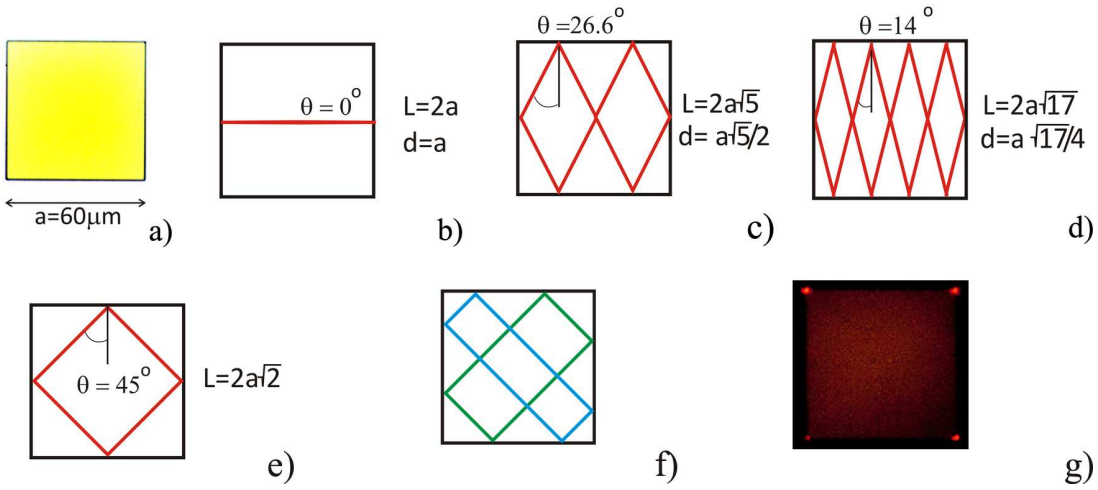

Figure 6.1: *Square micro-laser: a) optical microscope photo of a DCM-based cavity; b) Fabry-Perot periodic orbit; c), d) examples of non-confined orbits; e) inscribed diamond orbit; f) in-family diamond orbits; g) top view through the optical microscope of a lasing square cavity (hot points on the corner). The notations used in the graph are: a - cavity side, θ - internal angle of incidence, L - geometric length of an orbit, d - distance between successive reflective bounces (the latter is not given for a confined diamond orbit).*

The diamond orbit is not an isolated orbit in a square. There is an infinite number of inscribed rectangles that have exactly the same length as the diamond and the same angle, forming a so-called "in-family" diamond orbits (Fig.6.1.f).

All such diamond-family trajectories meet the boundary at the angle $\theta = 45^o$, which is larger than the total internal reflection angle $\theta_c = 42^o$ at the boundary between PMMA and air. Diamond orbits are then totally confined inside the cavity, and light can be extracted only due to 3-D wave diffraction effects at the corner (assuming a 2-D approximation). Observation of the cavity surface during

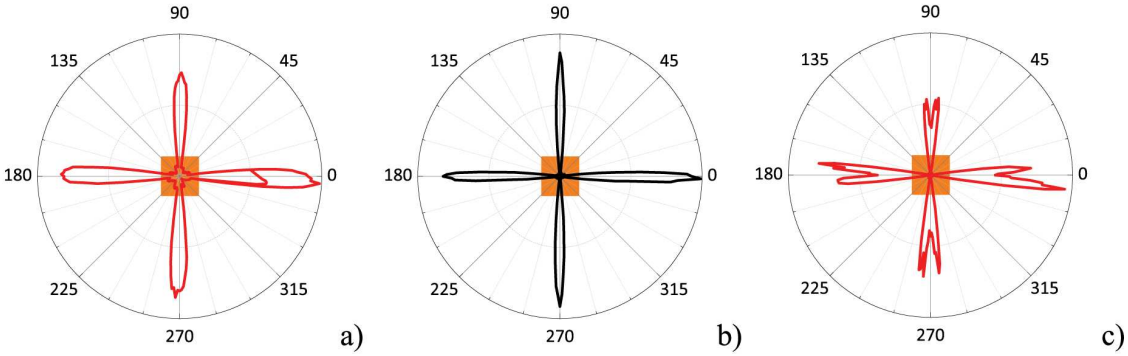

Figure 6.2: *Emission diagrams of a square micro-laser pumped with a 20 MWcm^{-2} circularly polarized light, corresponding to: a) total intensity of all peaks in the spectrum, b),c) maximum peak for each comb. The diagrams in (b) and (c) are plotted in different colors to depict different combs in emission spectra, consistently with the two combs spectrum on Fig.6.3.b.*

the lasing via a microscope objective (which we normally use for the alignment of the pumped region) evidences a strong diffraction effect at the corners as shown on Fig.6.1.g. This load us to assume, that diffraction at the corners must be the main mechanism for out-coupling and emission.

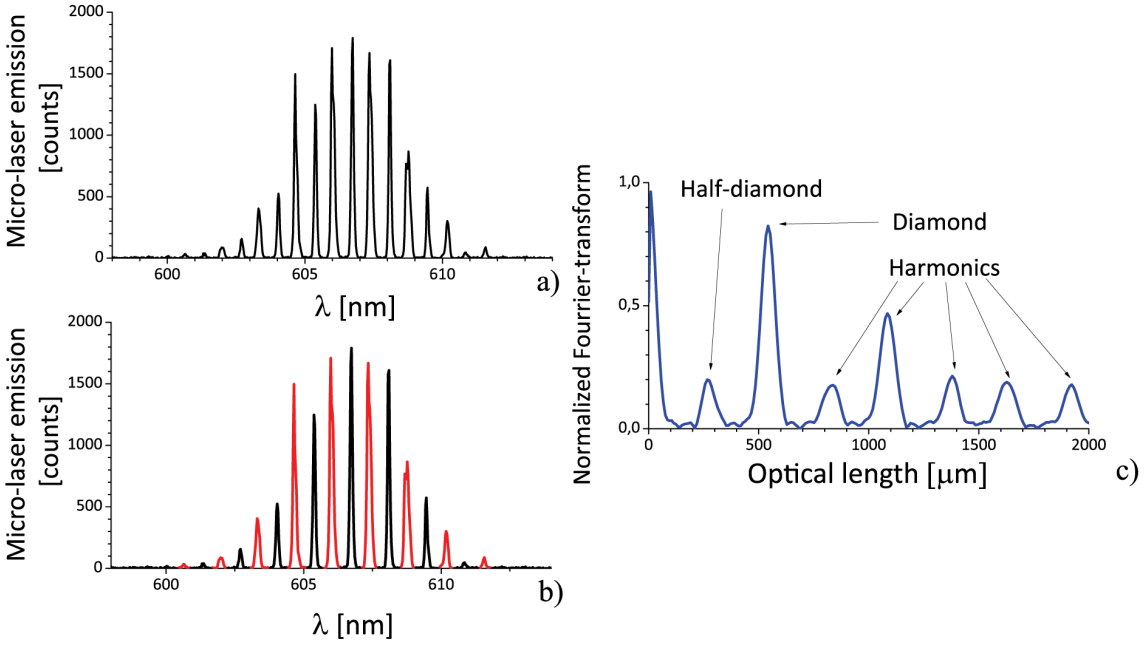

Figure 6.3: *Square micro-laser: a) spectrum in the direction of maximum emission, b) spectrum in (a) presented as superposition of two combs, c) Fourier-transform of the spectrum in (a).*

The emission diagram, depicted on Fig.6.2.a, may lead to the wrong conclusion, that the light leaves the cavity by refraction at normal incidence and that the emission directions are orthogonal to cavity sides. In fact, it is known from the previous study in our group [65], that light emission follows the cavity sides (verified for several shapes including the pentagon). Moreover, the square micro-laser emits light in four *relatively thin lobes* along its four sides (Fig.6.2.a) due to a mechanism still not well understood.

The spectrum in the direction of maximum emission is depicted on Fig.6.3.a. Fourier-transform (Appendix E.1) of this spectrum, shown on Fig.6.3.b, proves

that emission is sustained by the diamond periodic orbit. The FT also contains a series of peaks, which correspond to an orbit with a half diamond length originating form a numerical artifact.

Careful observation of the spectrum on Fig.6.3.a suggests this may be a superposition of two combs, as demonstrated on Fig.6.3.b. If the emission diagram is built separately for each comb (a result of the numerical treatment allowing for a decomposition of the experimental spectrum in two, where each represents a single comb), we see the stronger one happening along the maximum emission direction (Fig.6.2.b) and displaying thinner emission lobe, while the weaker one (Fig.6.2.c) has actually two lobes along each emission direction.

We evidenced that the experimental spectra of square micro-lasers contain the superposition of two combs, displaying different emission diagrams for each comb.

6.1.2 Influence of the pumping polarization on emission spectra

The pumping beam polarization leads to an interesting and unexpected effect on the emission spectra of square micro-lasers, the study of which is addressed in this section.

This effect was first observed for PMMA-DCM micro-squares, and further search with cavities based on other dyes proved it to be much less prominent. Thus the effect is strongly dye-dependent. As was mentioned in Sub-section 3.2.3, an in-plane polarization is dominant in the emission of square micro-lasers, properties discussed in this section will concentrate on such in-plane polarized component.

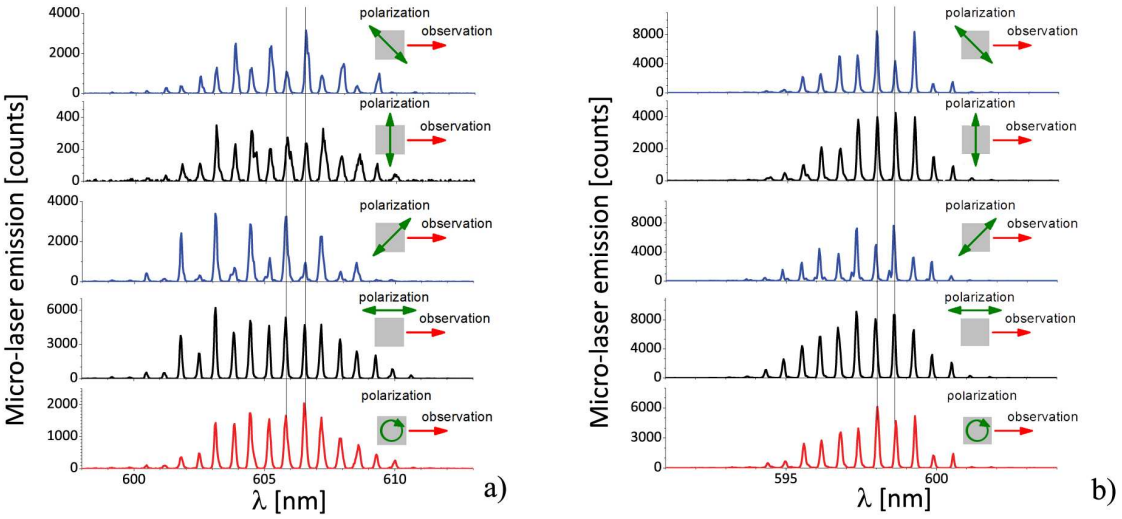

Figure 6.4: *Effect of pump polarization on the spectra of a square micro-laser (120 μm side): a) DCM-based square under 54 MWcm^{-2} pumping , b) PM605-based square under 7 MWcm^{-2}.*

One of two spectral combs becomes noticeably less intense when cavity is pumped with the polarization along one of its diagonals (Fig.6.4.a,b). Indeed pumping with a polarization along one diagonal reduces the intensity of different combs. The intensity of unchanged comb remains almost identical in both cases.

This effect was observed for several dyes, and apparently the relative decrease in combs intensities derives from the dye properties (the first and the third curves from the top in Fig.6.4.b).

Thorough alignment of the pumping beam with the center of the cavity (without fabrication defects at the boundary) is requested towards the observation of this effect.

As it happens, another particular polarization effect is present in the spectra depicted on Fig.6.4: the peak intensity of spectra obtained with a pumping polarization along the observation direction is considerably higher compared to the orthogonal polarization (2nd and 4th from the top on Fig.6.4). The ratio is about 10 for DCM and 2 for PM605. Even a circular polarization generates a lower output as compared to $\alpha = 0^o$.

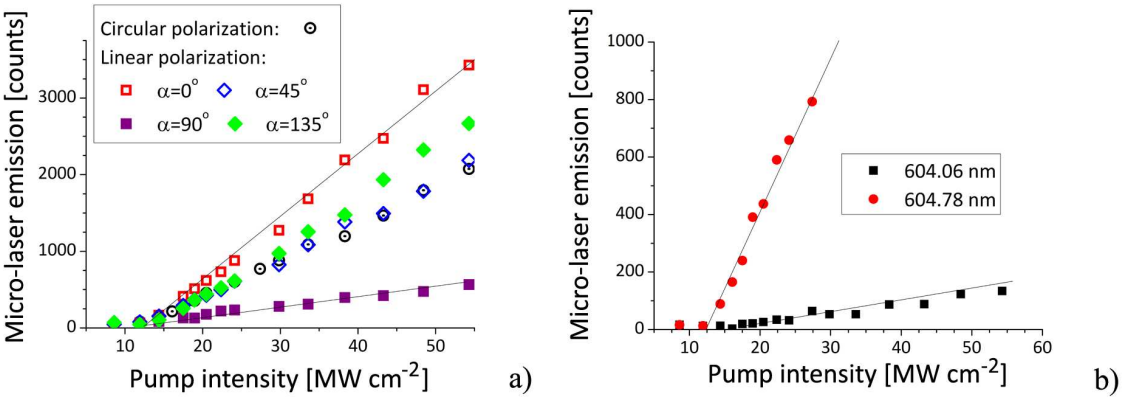

Figure 6.5: *Thresholds of square micro-laser emission in terms of pumping level: a) influence of pump beam polarization (threshold determined by the maximum peak), b) thresholds of two combs at $\alpha = 45^o$ (11.2±0.3 and 12.6±0.3 MWcm^{-2}). Measurements performed with a 120 µm side square made of PMMA-DCM (sample LPN7)*

The next important issue addressed in this part is that of the lasing threshold. It so appears that the orientation of the pump beam polarization does not influence the threshold, as determined from the peak intensity in the spectrum (depicted on Fig.6.5.a). Therefore the variation of the output intensity with the orientation of the pump beam polarization as reported above, refers to the emission slope (or efficiency). In other words, the emission of the maximal lobe, observed under various pump beam polarization angles corresponds to the same mode with an out-coupling efficiency set by the pumping polarization.

However the thresholds of the two combs present in the spectrum are found to differ slightly (Fig.6.5.b).

The experimental results presented in this section prove that the polarization state of the pumping beam plays an important role in the emission properties of square-shaped micro-lasers, in varying the out-coupling efficiency along the direction of observation. Analysis of the propagation and out-coupling of the mode should be undertaken in order to account for this effect.

6.1.3 Mode pattern of passive square resonators

The geometrical optics approach is only valid when the size of the object of interest is significantly large than the emission wavelength (say, $10 \times \lambda$ or above). Thus it cannot be applied to study the diffraction effect on a cavity corner while the edge confinement zone goes sub-λ. The system should then be considered from an electromagnetic point of view, but as the analytical solution for a dielectric cavity exists only for a sphere or an infinite cylinder with a circular cross-section, we resorted to "Finite-Difference Time-Domain" (FDTD) simulations to map the field distribution and eventually identify the out-coupling mechanism for square micro-cavities. This section is dedicated to the analysis of FDTD simulations.

Numerical computations presented in this section were performed on a commercially available Lumerical simulation package (Appendix F). Those simulations are

performed on passive cavities excited by a linear dipole with a variable polarization state. The dipole can be oriented orthogonally to the cavity plane - in this case it is referred to as TM-polarized, or at an arbitrary angle within the plane - then referred to as TE [1].

Relatively small 2-D cavities (10 μm side) were thoroughly examined at first, and several results on larger cavities were obtained thereafter. In fact, the time necessary for calculation of the field map at a given frequency grows steeply with the cavity size: from several minutes for a 10 μm square to 8-10 hours for 120 μm (considering quasi 2-D structures, full 3-D simulations would demand much more computer time). In this regard we performed 2-D simulations only.

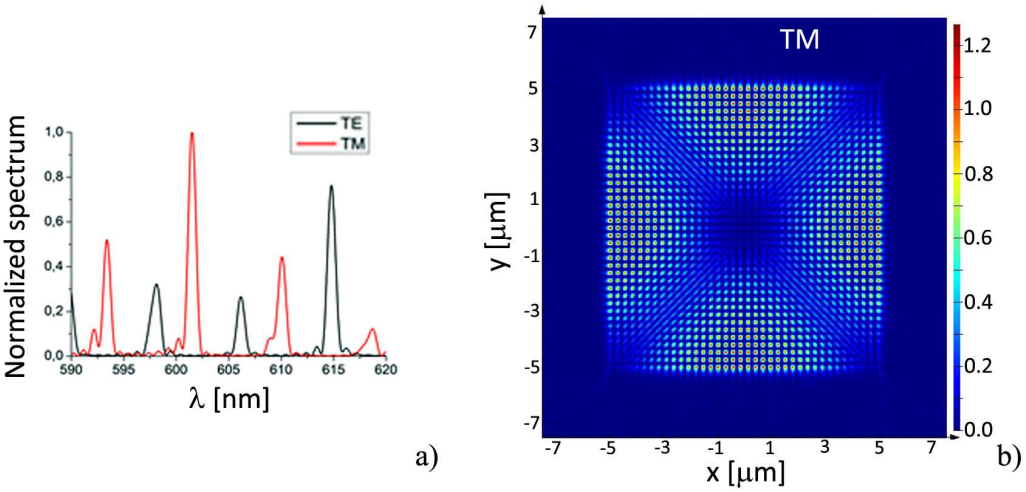

Figure 6.6: *FDTD simulations on a 10 µm side square micro-laser: a) calculated spectrum in the spectral region used for experimental observation; b) mode pattern of a TM-polarized wave at 593.5 nm.*

The spectrum of a 10 μm cavity is calculated and shown on Fig.6.6.a (in a spectral region typical of our experimental conditions for the observation of the emission of 2-D micro-lasers). The spectra of two polarization configurations, namely TE (in-plane, analog of I_P) and TM (orthogonal to the plane, analog of I_H) do not coincide, and this effect is particularly noteworthy for smaller cavities (with $ka \leq 100$, where k is the wave vector and a is the square side), Fig.6.6.a. The field maps and emission diagrams were calculated for several peak values in the spectrum of each polarization.

In the case of TM-polarization, the mode pattern varies with the wavelength, but generally exhibits a field minimum around the cavity center and the corners, as depicted on the field map Fig.6.6.b. The light is confined in the cavity and emission diagrams are quite chaotic and do not exhibit well-defined emission lobes (therefore they are not plotted in this work).

[1]Here we apply the TE/TM terminology, which is commonly-used in FDTD simulation tools for the description of polarization state.

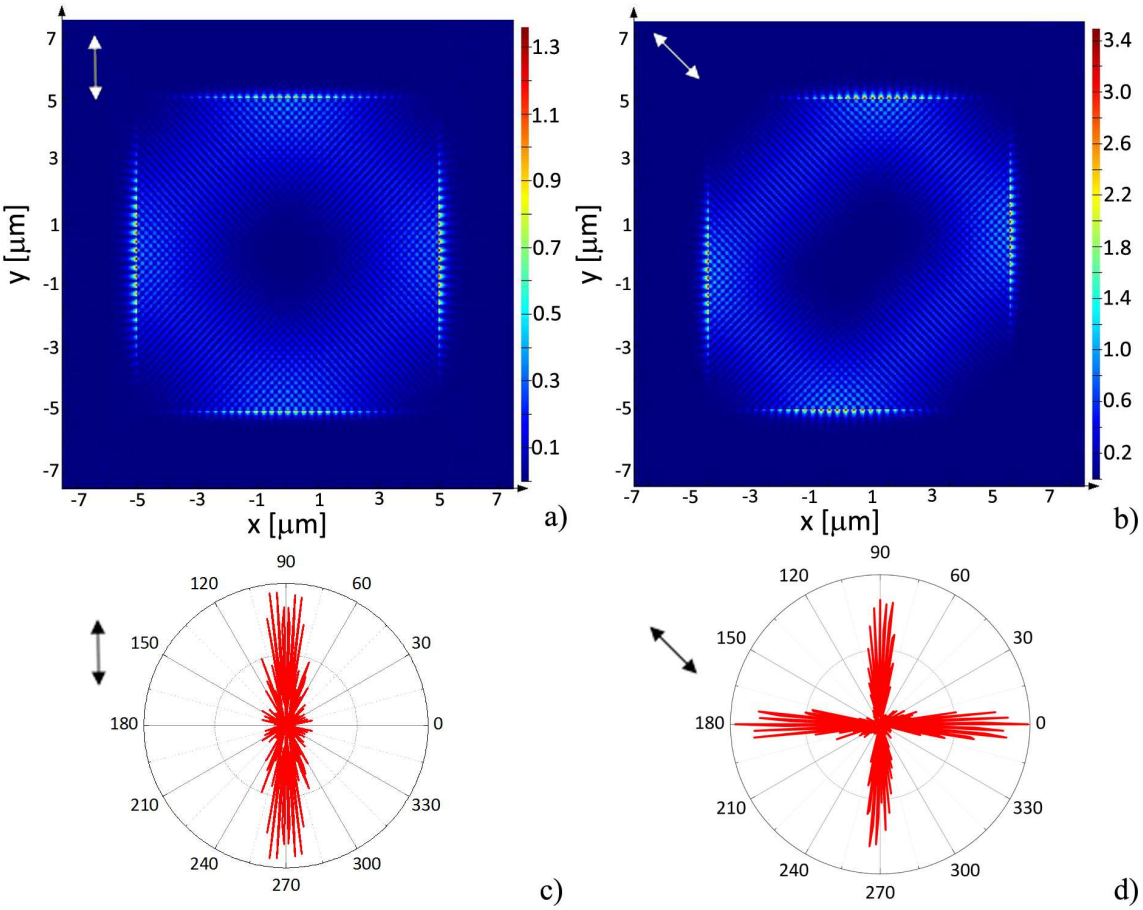

Figure 6.7: *FDTD simulations on a 10 µm side square micro-laser for an in-plane polarization (TE, at 598 nm peak). Mode patterns (a,b) and emission diagrams (c,d) for pump polarization at: a,c) $\alpha = 90^o$ (along the cavity side, represented by the arrow on (c)), b,d) $\alpha = 45^o$ (along the cavity diagonal, represented by the arrow on (d)).*

Unlike the TM-polarization, field maxima in the mode pattern for the TE-polarization are localized mainly at the vicinity of cavity borders (Fig.6.7.a). Moreover, the polarization of the excitation dipole has a strong influence on the mode pattern: an excitation dipole polarized along the cavity diagonal results in a shift in the pattern towards the direction of opposite diagonal, as shown on Fig.6.7.b. As for the emission diagram, it is in good agreement with experiments: an excitation polarization along the cavity side provides an emission maximum along the same direction (Fig.6.7.c).

Proper study of the out-coupling mechanism demands the analysis of a larger cavity size. Simulations were performed here for the in-plane polarization of a 60 μm cavity (Fig.6.8). The excitation polarization along the cavity diagonal results in a field maximum along the other diagonal, as shown on Fig.6.8.b. The light out-coupling happens at the cavity corner, as evidenced on Fig.6.8.c-d. Each corner provides two emission directions along the cavity sides, as shown for the zooming of the mode pattern with an appropriate intensity scale on Fig.6.8.d. These two lobes may origin from clock-wise and counter clock-wise waves.

Comparison of the field maps characterizing the in-plane polarization obtained respectively for a 10 (Fig.6.7.b) and 60 μm (Fig.6.8.c) side square suggests that an increase in the cavity size gives rise to the new field maxima (quite alike the in-family diamond orbits), which provides the visual effect of the field approaching the diagonal of a square cavity.

In summary, FDTD simulations on passive square cavities evidence the strong

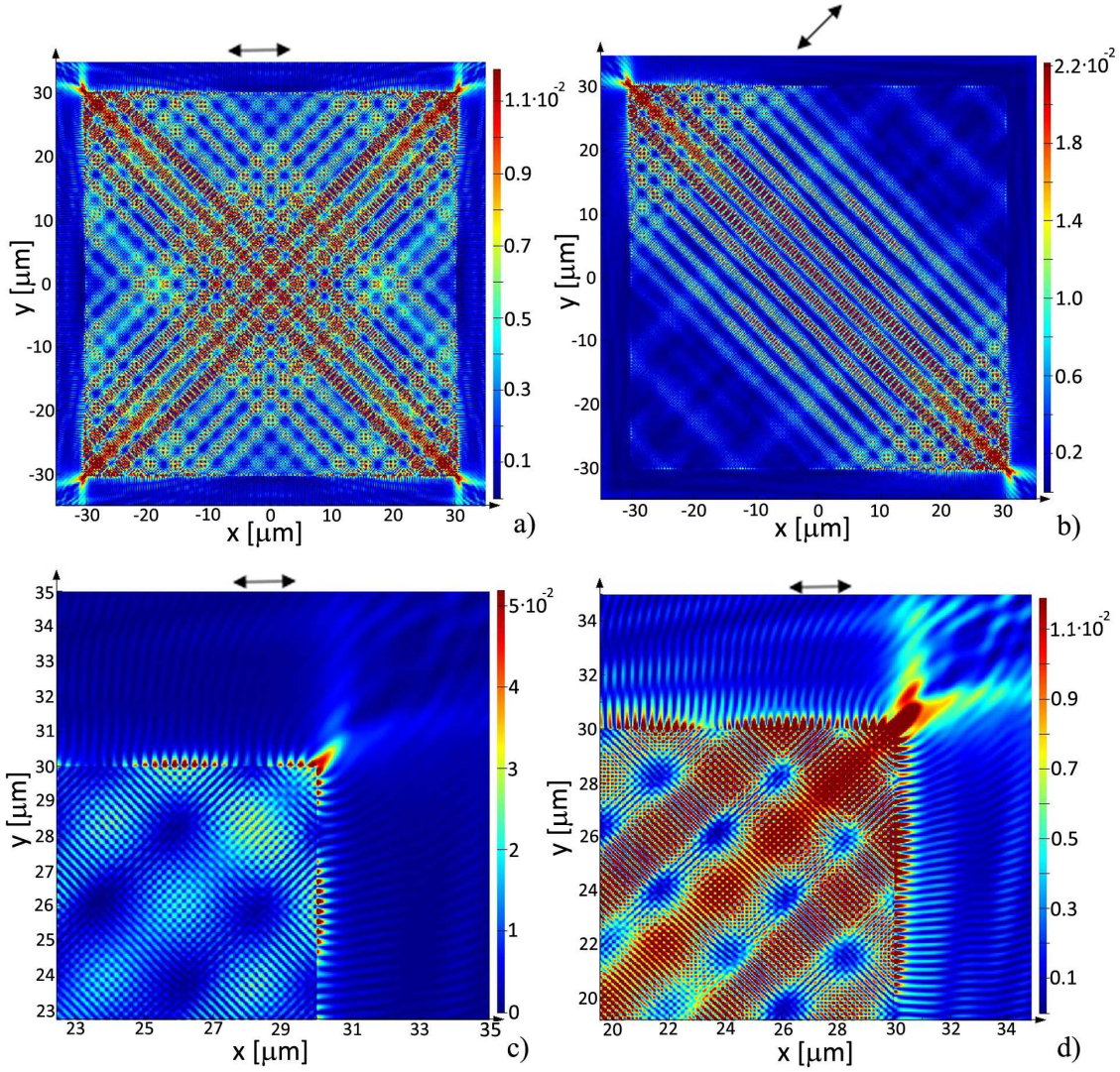

Figure 6.8: *FDTD simulations of a 60 μm side square micro-laser for an in-plane polarization (at 610.5 nm peak). Mode patterns for a cavity pumped with a pump polarization at: a) $\alpha = 0^o$, b) $\alpha = 135^o$; c-d) zoom at the corner of the cavity pumped with polarization at $\alpha = 0^o$ with different intensity scales for the mode pattern in a.*

influence of the pump beam polarization on the localization of field maxima in the mode pattern. The out-coupling mechanism is related to light diffraction at the cavity corner, while each corner seems to provide two emission lobes in the directions along the two adjacent cavity sides.

6.1.4 Extraction of light from the cavity

The striking difference in spectra obtained for different orientations of the linear pump beam polarization suggests that such polarization strongly influences the mode localization in the cavity. This assumption was supported in the previous section by FDTD simulations, and can also be checked experimentally. Here we discuss the experimental observations of light out-coupling under various pump polarization conditions.

The uEye CCD camera with teleobjective was used for the experiment. The system was aligned so as to provide a slight tilt away from an in-plane view on the sample (this procedure being necessary to distinguish a cavity from the surrounding polymer matrix, Fig.6.9). So the cavity is observed as in the standard 2-D

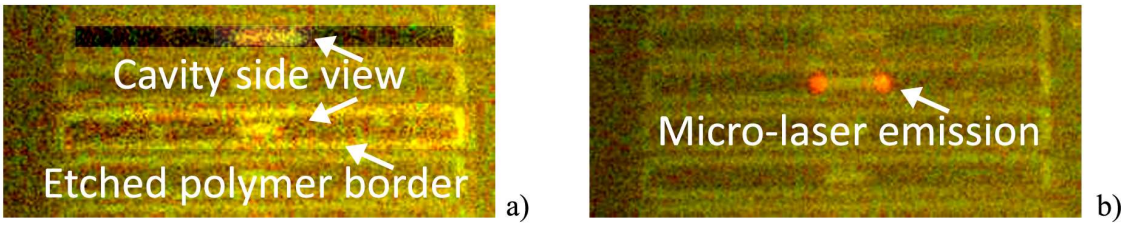

Figure 6.9: *Image from the uEye CCD camera (sample lightened by a table lamp): a) alignment, b) lasing.*

experiment but with the CCD camera instead of spectrometer. The sample was illuminated by a simple table lamp, when images depicted on Fig.6.9 were taken, and then the lightening was turned off during the experiment.

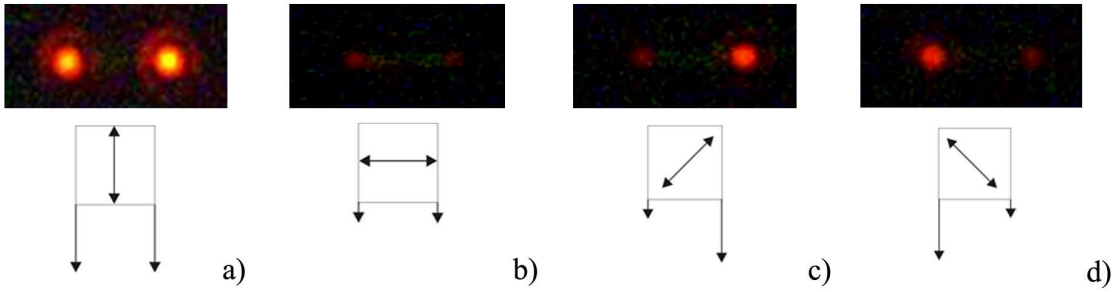

Figure 6.10: *Slightly oblique observation of light emission from square-shaped micro-laser for various orientations of pumping beam polarizations (with no sample illumination): a) $\alpha = 0^o$, b) $\alpha = 90^o$, c) $\alpha = 45^o$, d) $\alpha = 135^o$.*

At first the square was placed to face the camera from the side its side, allowing for two cavity corners to be visualized. The side images observed were completely different for linear pumping beam polarizations at $\alpha = 0^o$ (Fig.6.10.a), $\alpha = 90^o$ (Fig.6.10.b), $\alpha = 45^o$ (Fig.6.10.c) and $\alpha = 135^o$ (Fig.6.10.d). The two cavity corners facing the camera provide unequal emission intensity if the pump polarization is oriented along one of the cavity diagonals. The more intense emission comes out from the corner opposite to the polarization orientation (Fig.6.10.c,d). In the case where the pump polarization is aligned along the observation direction and orthogonal to it, both corners emit with the same intensity (Fig.6.10.a,b). And as in the case of emission spectra, the "magic" brightness is observed for $\alpha = 0^o$ pumping (Fig.6.10.a), in agreement with earlier reported emission spectra (Fig.6.4) and results from FDTD simulations (Fig.6.7.c).

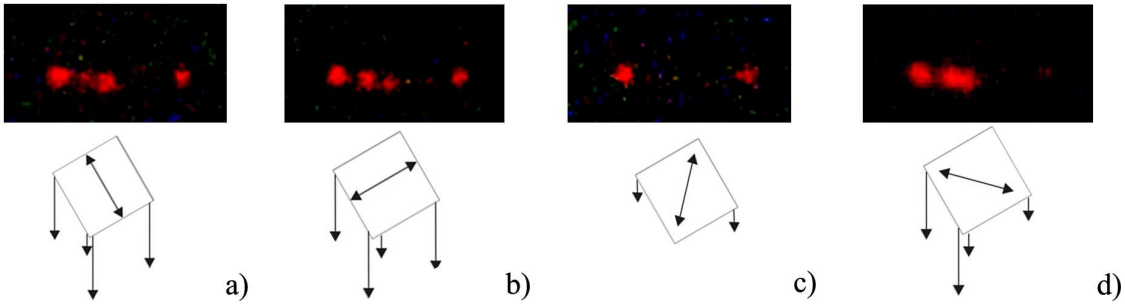

Figure 6.11: *Slightly tilted observation off symmetry of light emission from square-shaped micro-laser for various orientations of the pump beam polarizations: a) $\alpha = 0^o$, b) $\alpha = 90^o$, c) $\alpha = 45^o$, d) $\alpha = 135^o$.*

Then the square was turned by 30^o and made to face the camera by one of its corners. The experiment was repeated for a pump polarization orientation analogous to previous case (Fig.6.11), but this time unrelated related to the current observation direction. This graph evidences that light out-coupling along each corner takes place at several directions the same time.

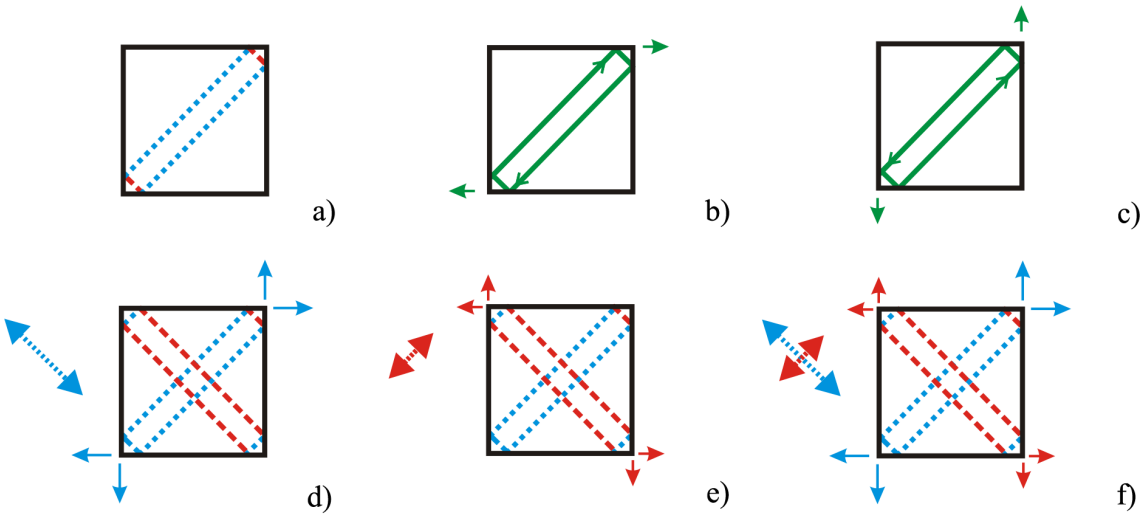

Figure 6.12: *Scheme of orbits inside the cavity and out-coupling: a) round trip of the diamond in-family periodic orbit, regions oriented along different diagonals are shown in dash and dot; b), c) out-coupling of same spatial mode with light propagating in opposite directions; d),e) cavity emission under linear pump beam polarization along the cavity diagonal; f) combination of d) and e), which accounts for the emission in the real system.*

Results are summarized on the schemes at Fig.6.12. Considering the diamond orbit along one of the cavity diagonals in Fig.6.12.a, we distinguish in its round-trip two unequal parts respectively oriented along the one diagonals (longer) and opposite to it (shorter part). The out-coupling of clock-wise (Fig.6.12.b) and counter-clock-wise (Fig.6.12.c) waves happen in two opposite directions along the same cavity side. Pumping with the beam polarized along the cavity diagonal provides a lasing mode that propagates along the other diagonal, as shown on Fig.6.12.d. At the meantime, due to the fluorescence anisotropy excitation of dye-doped layer with a linear pump beam polarization results in the triggering of gain in the orthogonal direction as well, and the opposite diagonal also gets excited (Fig.6.12.e). Thus, pumping along one of the cavity diagonals results in more intense emission from the corners of the opposite diagonal and less intense emission from corners along the pump polarization (Fig.6.12.f).

Observation of light out-coupling from the square micro-cavity confirmed the results of FDTD simulations. The emission in two orthogonal directions from each corner appears then to originate from clock-wise and counter-clock-wise waves, while the difference in the emission intensities under the pumping with linearly polarized beam is caused by fluorescence anisotropy. However, such approach does not explain the difference in the emission intensity between pumping with polarization $\alpha = 0^o$ and $\alpha = 90^o$. Still, it may be a resonator effect as FDTD simulations, presented in preceding Sub-section (see Fig.6.7.c), provides a similar result.

6.1.5 Threshold value

This section is focused on the quantitative estimation of the diffraction losses on

the dielectric corner, based on experimentally obtained thresholds of square micro-lasers.

This is the inverse problem to the one addressed in the previous chapter: the aim is to determine the losses from the threshold and *K factor* defined by Eq.(5.4) in Sub-section 5.2.1.

Threshold values have been measured for various cavity sizes and results are presented on Fig.6.13.a as a function of the diamond orbit length ($L = 2\sqrt{2}a$). The dependance is linear with L^{-1} with the exception of very small cavities, very much like for ribbon-shaped cavities (Fig.5.6.a). The nature of this effect (Fig.6.13.b) is described in Sub-section 5.2.3.

The linear part of the curve shown on Fig.6.13.a follows the predictions discussed in Sub-section 5.2.1, which establish the relation between the threshold value (I_{th}), cavity losses (r) and length of the round-trip performed by a mode (L): $I_{th} = -lnr/(KL)$ (equation (5.6), deduced from two assumptions: 1) the modal gain is proportional to the pumping intensity and 2) at threshold, the modal gain compensates the losses).

The K factor for a 600 nm PMMA-DCM layer was measured to be 50 cm/MW (section 5.1). Linearization of the curve on Fig.5.6.a provides a slope of 0.22±0.005. Thus we obtain a value of $r = (1.6\pm0.03)10^{-5}$, which gives an equivalent refractive coefficient R of about 10%.

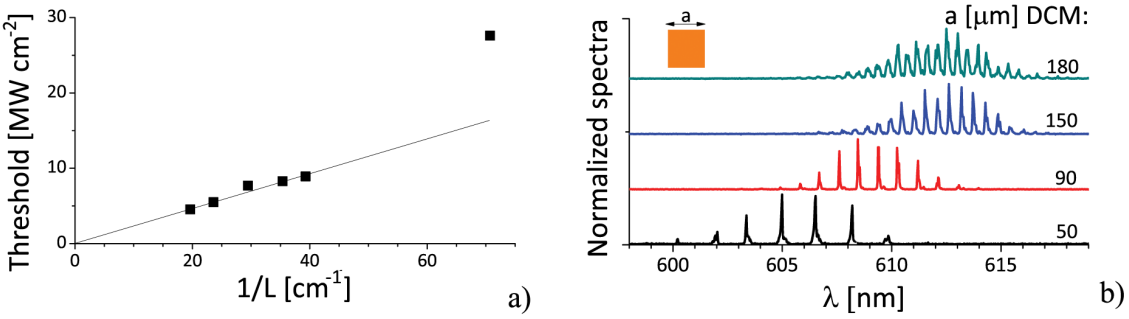

Figure 6.13: *Threshold (a) and spectra (b) of PMMA-DCM square micro-lasers of various sizes.*

The losses of the light diffraction on the dielectric corner are found to be slightly lower comparing to the refraction at normal incidence at the dielectric boundary: 90% of light leaves the cavity instead of 96%.

In summary, our study of square micro-lasers was very fruitful and provided interesting information on the mode structure and light out-coupling mechanisms. With the help of FDTD simulations and precise observations of the light out-coupling conditions, we have elaborated a model capable to account the somewhat a priori strange influence of the pump beam polarization on the spectral properties of square micro-lasers. This model, however, does not allow to conclude on the much higher spectrum intensity observed in the case of pumping at $\alpha = 0^o$ as compared to $\alpha = 90^o$. Still, FDTD simulations reproduce this difference in the emission diagram. Finally, considering the relation between mode threshold and losses, as derived in Section 5.2 for ribbon micro-lasers, we found that light diffraction at the dielectric corner can be described by an effective of refractive losses R coefficient the order of 10%.

6.2 Rectangle-shaped micro-cavity

A rectangular shape can be considered as a deformation of the square. If properly

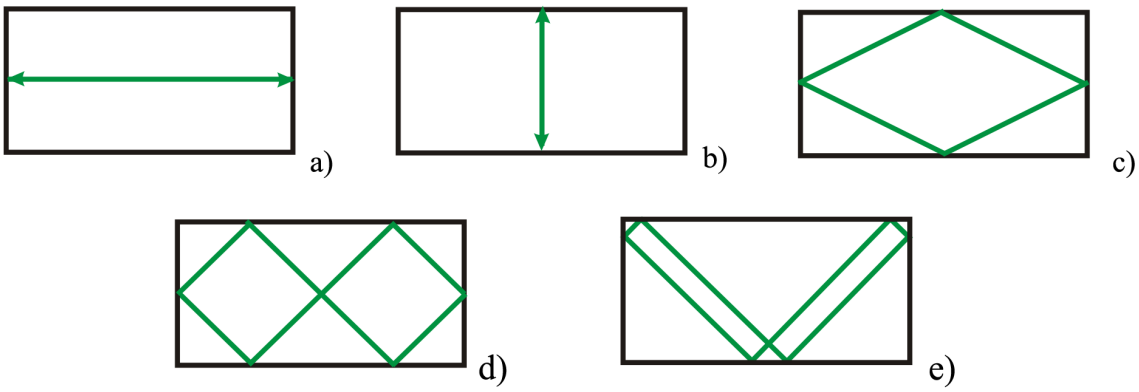

Figure 6.14: *Scheme of periodic orbits in a 2:1 rectangle resonator: Fabry-Perot (a,b), diamond (c), symmetric double diamond (d), general in-family double diamond (e) orbit. Only Fabry-Perot orbits depicted in (a) observed experimentally.*

scaled a rectangle micro-cavity can sustain two types of periodic orbits: multiple diamond (for instance single and double diamond in the rectangle with aspect ratio 2:1, as depicted respectively in Fig.6.14.c and Fig.6.14.d,e) and Fabry-Perot (Fig.6.14.a,b) [68]. In contrast with the square, the excitation of Fabry-Perot modes becomes feasible due to the elongation of one of the sides away from the reference square, resulting in a substantial increase in the length (at least 2 times, as shown on Fig.6.14.a-b, where Fabry-Perot modes from Fig.6.14.b are identical to the reference squares) of the amplification region of the mode (round-trip length). The double diamond becomes then a confined orbit, in contrast to the diamond (depicted on Fig.6.14.c), which may be the reason the last one is not observed experimentally.

The aim of this study is to analyze how the coexistence of two types of modes can modify the emission properties of rectangle micro-lasers. Experimental results were obtained with 2:1 cavities.

We first consider the emission properties of the double diamond periodic orbit in rectangle micro-lasers, followed by.the co-existence of different modes.

6.2.1 Emission properties of diamond modes in rectangles

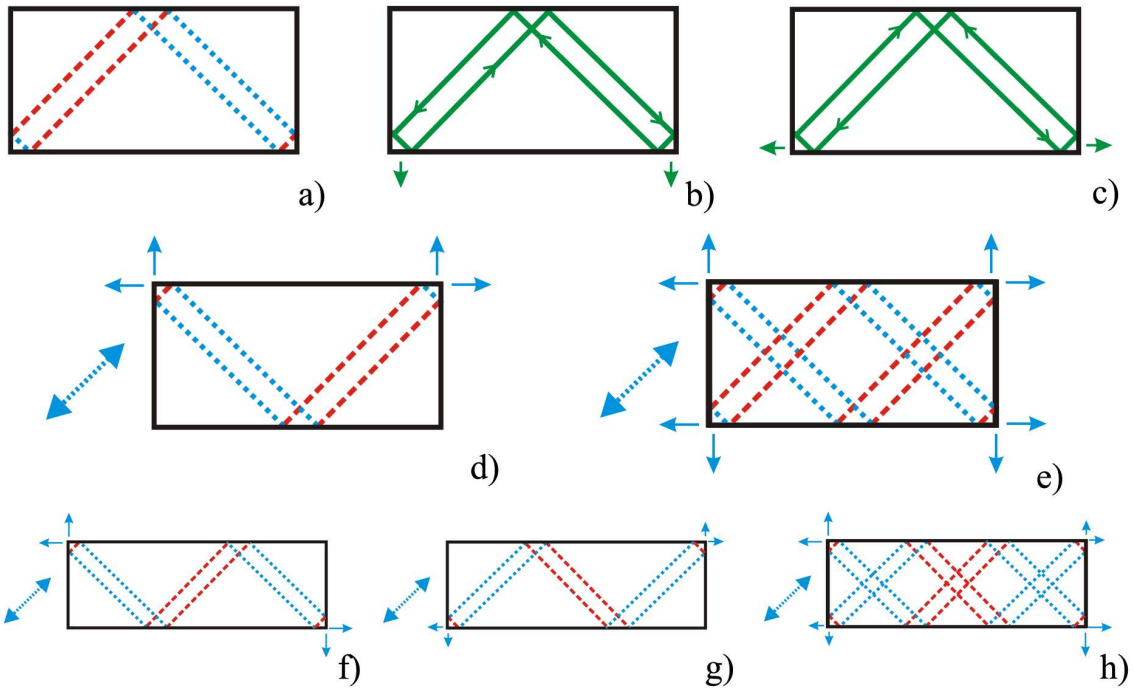

Figure 6.15: *Schemes of mode propagation in rectangle cavity and their out-coupling directions: 2:1 rectangle (a-e), 3:1 rectangle (f-h). Orthogonally oriented regions of round trip in different colours (a), out-coupling of the same spatial mode with light propagating in opposite directions (b,c), emission under linear polarization along the square diagonal (d, f, g - for a single orbit, e,h - for a couple of orbits).*

This section is focused on the peculiarities of the emission properties of double diamond periodic orbit in the case of rectangle micro-laser. The short overview is first given on the polarization effects, then the emission diagram of double diamond periodic orbit is described.

The emission properties of double diamond periodic orbit in rectangle do not correspond completely to the square case. Now the influence of the pumping beam polarization is defined by the scaling factor of cavity sides (Fig.6.15).

The mode propagation track may be decomposed into two groups of segments, respectively oriented along one diagonal of the unit square or the other. Whereas in a square these groups made highly uneven contribution to the in-family double diamond orbits, in the case of the rectangle this further ratio depends on the aspect ratio (m : 1) of the cavity sides. For instance the rectangle with an aspect ratio of 2 (2:1) can be decomposed into 2 squares, and the two groups of segments then equally contribute. Thus implies that the pump beam polarization does not affect the emission in the same as in the case of a square micro-laser.

The study of light out-coupling from such cavities confirmed this suggestion for a 2:1 rectangle: there is no significant dependance on the emission from the two corners on the orientation of pumping polarization (Fig.6.16).

A typical spectra for a double diamond periodic orbit in the rectangle is shown in Fig.6.17.b., and its emission diagram in Fig.6.17.a. Analysis of the Fourier transform plotted in Fig.6.17.c confirms that the emission does correspond to a double diamond periodic orbit.

In summary, the influence of polarization effects on double diamond periodic orbits in rectangle micro-laser is amenable to the aspect ratio of the cavity. In the case of a 2:1 rectangle the expected polarization effects are evidenced experimen-

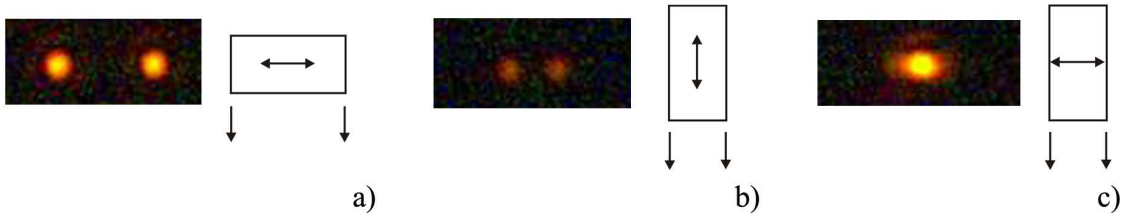

Figure 6.16: *CCD camera image on light out-coupling from a 2:1 rectangle with its long (a) and short (b,c) sides facing the camera. Double diamond orbits only are viewed when the long sides observed (a, $\alpha = 90^o$), weaker double diamond orbit from the small size (b, $\alpha = 0^o$) and Fabry-Perot (c, $\alpha = 90^o$) orbit (the double diamond is present as well when the small side is imaged, but much less intense and thus not clearly visible). The change of pumping polarization did not influence significantly the image from (a, similar for $\alpha = \{0^o, 45^o, 90^o, 135^o\}$) to (b, similar for $\alpha = \{0^o, 45^o, 135^o\}$).*

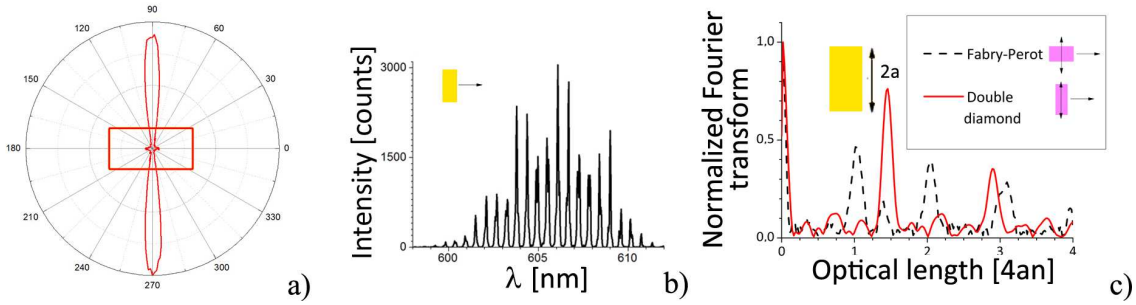

Figure 6.17: *Emission diagram (a) and spectrum (b) of the double diamond mode from a rectangle micro-laser (5 wt% DCM, pumped by a circularly polarized beam). Fourier transform (c) of the spectra, obtained under linear pumping beam polarization ($\alpha = 90^o$) along long (Fabry-Perot orbit) and short (double diamond orbit) cavity sides.*

tally and shown to be negligible for a double diamond orbits. The directions of emission maxima for a double diamond periodic orbit are orthogonal to the long cavity side (as depicted on Fig.6.17.a), which is non-intuitive but very important for the analysis proposed in the following sections.

6.2.2 Co-existence of different types of modes

We have already explored the emission properties of modes corresponding to Fabry-Perot and diamond periodic orbits in a case where each of them is the only lasing mode type acting in the cavity. In this section, we analyze the change in emission properties in the case where different modes coexist.

Modes that correspond to diamond periodic orbits exhibit theie emission maximum in the direction orthogonal to the long cavity side (Fig.6.17.a). As for Fabry-Perot, we experimentally succeeded in exciting of the longer Fabry-Perot mode only. Thus the emission properties are examined separately for each mode type in the direction of its emission maximum (in orthogonal directions).

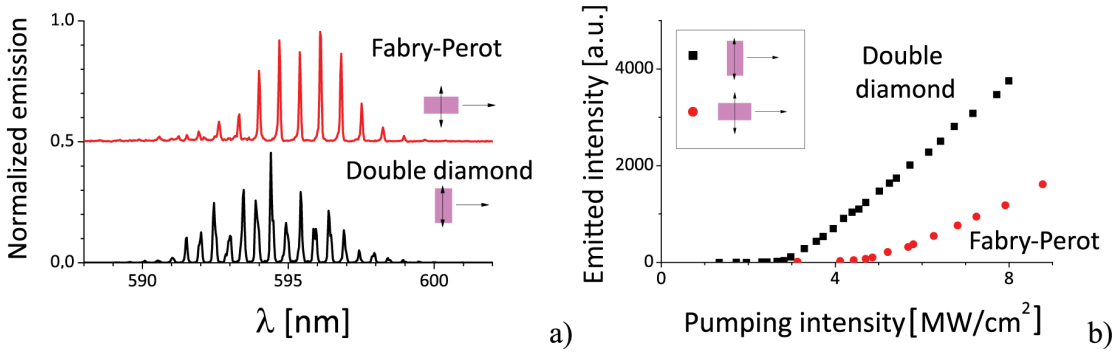

Figure 6.18: *Spectra (a) and thresholds (b) of double diamond (in black) and Fabry-Perot (in red) periodic orbits in 150*75 μm (2:1) rectangle micro-laser made of PMMA-PM605.*

Table 6.1: *Comparison of thresholds of diamond and Fabry-Perot periodic orbits in 150*75 μm rectangle micro-laser with the Fabry-Perot mode in a ribbon of the same size.*

Dye	I_{th}, MW cm^{-2}		
	Diamond	Fabry-Perot in	
		Rectangle	Ribbon
PM605	2.9	4.5	2.3

Spectra and thresholds are plotted on Fig.6.18. Contrary to expectations, the spectrum of the Fabry-Perot mode is red-shifted with respect to that of the diamond periodic orbit Fig.6.18.a. Such an effect could originate from spatial hole-burning[2]. Both modes are uniformly distributed in the resonator volume, and compete for the same gain medium. Having a lower threshold, the double diamond starts lasing first. The Fabry-Perot mode is forced to occupy the regions of field minima of the diamond, which results in the increase of its threshold compared to the case of ribbon resonators of the same size, as evidenced in Tab.6.1.

The important conclusion on the results presented in this section, is that mode competition and particularly hole-burning effects can result in an increase of the threshold of the mode. In this respect, one should be cautious when applying developed models that linearly relate gain, losses and thresholds as the one explained in the previous chapter as the experimentally observed process may not abide to its underlying assumptions.

6.3 Kite-shaped micro-cavities

A serious drawback of organic-dielectric optical resonators lies in their low light confinement, due to high refraction losses at the dielectric boundary. As a result, the photon lifetime in the cavity is small and a high pumping intensity (of the order of MWcm^{-2}) is necessary to reach threshold, as was already observed in this Chapter and the previous one.

The light confinement of a mode is generally governed by the quality factor:

$$Q = \frac{\lambda}{\triangle\lambda} = 2\pi\nu\tau_p \tag{6.1}$$

defined as the ratio of the emission wavelength λ over its full width at half

[2]Distortion of the gain shape in a laser medium caused by saturation effects of a standing wave.

maximum $\triangle\lambda$, or equivalently as the product of the emission frequency and τ_p photon lifetime in the cavity.

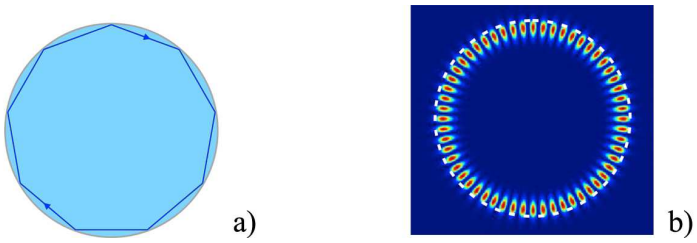

Figure 6.19: *Whispering gallery mode in a disk: a) schematic geometrical optics representation of the orbit propagation subject to periodic total internal reflections at the cavity border; b) simulated WGM field pattern.*

The role of the material refractive index in the mode confinement (via the quality factor) becomes less important if a mode track inside the cavity meets several total internal reflections. Such is the case for a set of convex resonator shapes, that sustain high quality factor modes - so called Whispering Gallery modes[3](WGM, shown on Fig.6.19 for a disk). Most noteworthy are micro-spheres (quality factor Q up to $8*10^9$ [151]), micro-toroids (10^8 [57]), micro-discs (lower Q, about 10^4reported for semiconductor cavity on a pillar [58]) etc.

Being the 2-D projection of a sphere, the disk should ne addressed at first. However, there are few experimental complications that arise in the study of cavities with low emission directionality when examined without evanescent out-coupling devices (waveguides or fibers). In this respect, we focused on disk deformations, that preserve the WGM behavior while allowing for directional emission.

Directionality of light emission can be obtained by a deformation of the contour or introduction of a local defect (on the boundary [152, 153, 154] as well as inside the cavity [155]). One of the first resonator shapes we studied extensively in this regard was a stadium [62], especially as it exhibits chaotic properties from the point of view of mathematical billiards. Still this cavity has two symmetry axis and thus at least four emission beams. It is possible to decrease the number of emission directions in stadium, down to a single one, for example by introduction of circular vacancies [156] (as we predicted by numerical simulations and proved experimentally). However, due to significant shape distortion from the circle, the stadium is an example of rather low-Q WGM resonator. Among other resonator shapes known for their WGM attached properties are spirals, notched or cut disk, and limaçon [157]. In order to avoid light diffraction on dielectric corners, we focused on smooth disk deformations. Limaçon cavity being already widely studied, we gave preference to the kite shape. The choice of kites was moreover motivated besides its ability to sustain WGMs, by additional possibility of Faby-Perot resonances as well, which provides us the opportunity to investigate the coexistence of two mode types.

The kite abides to the following contour function (which is infinitely continuously differentiable):

[3]Named by analogy with low-loss acoustic waves traveling along round walls, able to spread the whisper between two antipodes of the dome. First reported and explained by lord Rayleigh on St Paul's Cathedral in London.

$$x(t) = r\,(\cos t + \delta \cos 2t - \delta) \qquad (6.2)$$
$$y(t) = r \sin t$$

where $t \,\epsilon\, [0,\, 2\pi]$, r is the radius of an non-deformed disk and δ is the distortion parameter. When $\delta = 0$ equations (6.2) reduce to a disk. $\delta < 0.29$ defines a convex cavity (Fig.6.20.a), which turns to concave for $\delta > 0.29$ (Fig.6.20.b).

We investigated both convex (with $\delta = 0.165$) and concave (with $\delta = 0.5$) kite micro-lasers. The latter, however, exhibit rather moderate WGM features and for this reason their emission properties are summarized in Appendix G.

Figure 6.20: *Disk contour deformation into a kite: a) convex shape with $\delta = 0.165$, b) concave shape with $\delta = 0.5$.*

In this section the emission properties of kite-shaped resonators are addressed. First we describe the theoretical predictions on mode localization and emission. Then the influence of cavity size on the emission diagram is explored via FDTD simulations. Next we present experimental results in two parts: emission properties of cavities of various size and compositions (different dyes), and than comparison of threshold values for WGM and Fabry-Perot modes. In the framework of this project I supervised the internship student, Victor TSVIRKUN, who did his master thesis on the experimental study of kite micro-lasers.

6.3.1 Theoretical results on mode localization and emission in kite

The present section provides is devoted to a short overview of the Lasing Eigenvalue Problem as a calculation method and its application to kite-shaped micro-lasers.

This project was performed in collaboration with Elena SMOTROVA and Alex NOSICH from the Institute of Radiophysics and Electronics of the National Academy of Sciences of Ukraine, (Kharkov), who first established the WGM properties of kites, in the connection with the Lasing Eigenvalue Problem (LEP) as a theoretical tool [158].

The basis of this method consists in the solution of Maxwell equation with complex refractive index, whereby the imaginary part represents the gain properties.

They first set Maxwell equations into a 2-D linear eigenvalue problem subject to exact boundary radiation conditions. Then the problem is reduced to a set of Muller's boundary integral equations (with adequate quadrature formulas used for discretization). Finally the eigenvalues are found numerically as the roots of the corresponding determinant equation.

An example of simulation results on kite-shaped cavities [159, 160] is shown on the left-hand side of Fig.6.21. The dark-colored regions on the graph indicate the eigenvalues of the corresponding determinant equations for some lasing frequency (expressed as ka, being a product of the wave vector k with the cavity size a) and gain (γ - no reference to the parameter used in Chapter 5). After identification of

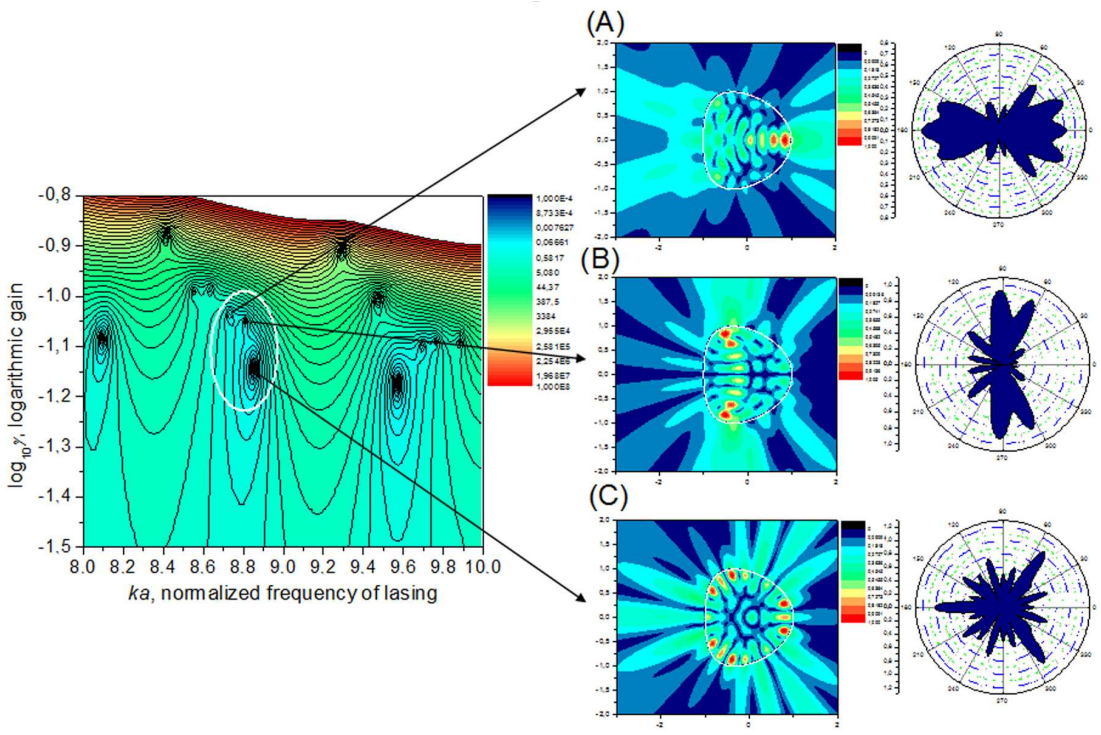

Figure 6.21: *LEP simulations: (left) map of the eigenvalues (dark colored regions) ine gain (γ - imaginary part of refractive index) and ka (cavity size) coordinates, (right) - field maps and emission diagrams for three adjacent eigenvalues from the map on the left. Simulation parameters: $\delta = 0.165$, refractive index n=1.5, discretization by N=50 quadratures.*

the eigenvalues, the field distribution map and emission diagrams can be drawn, as shown on Fig.6.21 for three adjacent eigenvalues on the gain map. The high gain value corresponds to a small threshold, so that the upper points on Fig.6.21 (left) depict modes with a lower threshold. The field pattern of those modes, that demand a higher gain (therefore located higher on the gain map, for example (A), (B) from Fig.6.21) are very similar to Fabry-Perot mode types. The low-gain mode (C), has its field maxima along the boundary, resembling a WGM profile.

This is a powerful formalism, that allows to calculate the mode profile and to determine the threshold from the modal losses. However there are two constraints in the direct application of the LEP method towards the analysis of 2-D micro-lasers:

- Calculations with high ka, which is the case for our micro-lasers as in general $ka > 1000$, demands to increase the number of discretization points and poses algorithm stability problems (an exceedingly large number of quadratures has to be considered).
- Deduced thresholds cannot be directly compared with the ones from experiments, as they do not account for modal gain distribution.

At the moment, the highest ka accessible to this simulation is of the order of 25. This corresponds to a rather small kite of about 1 μm in radius,when the emission wavelength is 600 nm. Thus the considered cavity scales to only a few emission wavelength and strictly speaking, the influence of cavity size on emission properties must be checked.

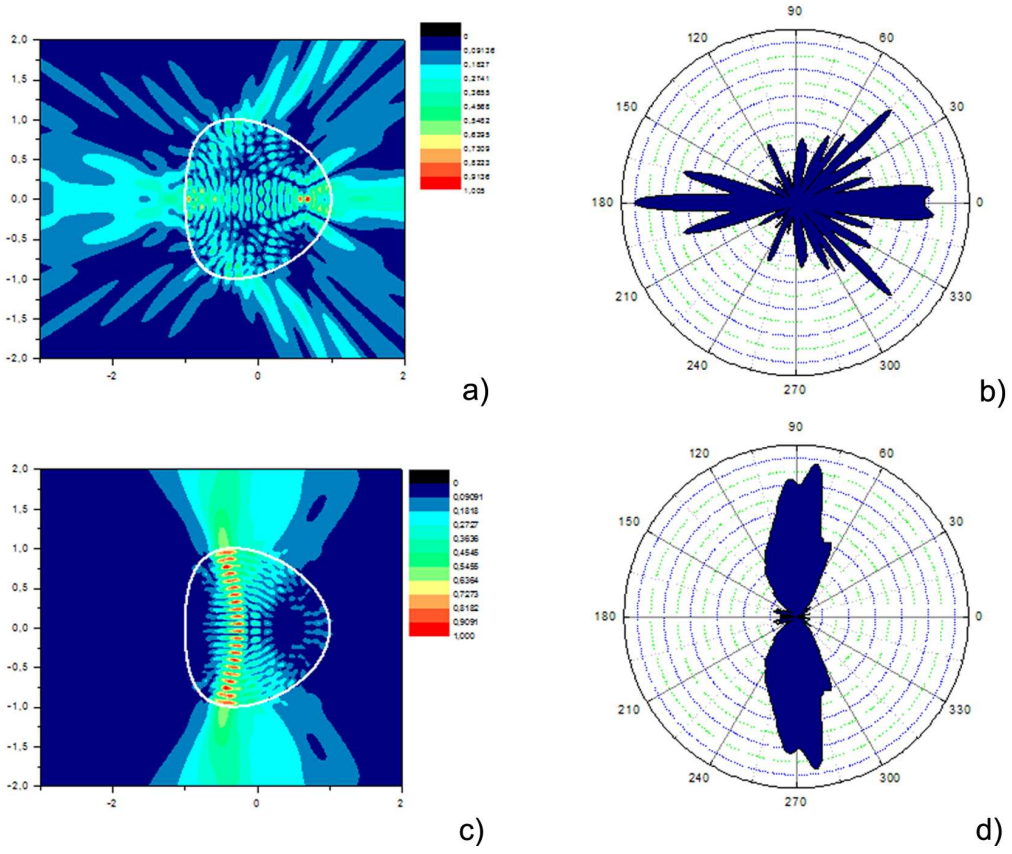

Figure 6.22: *LEP map fields (a,c) and emission diagrams (b,d) for a kite with* $\delta = 0.165$, *andith* $(ka; \gamma) = (23.37; 3.54 \cdot 10^{-2})$ *(a,b) and* $(23.49; 3.46 \cdot 10^{-2})$ *(c,d). Refractive index n=1.5, discretization over a set of N=100 points.*

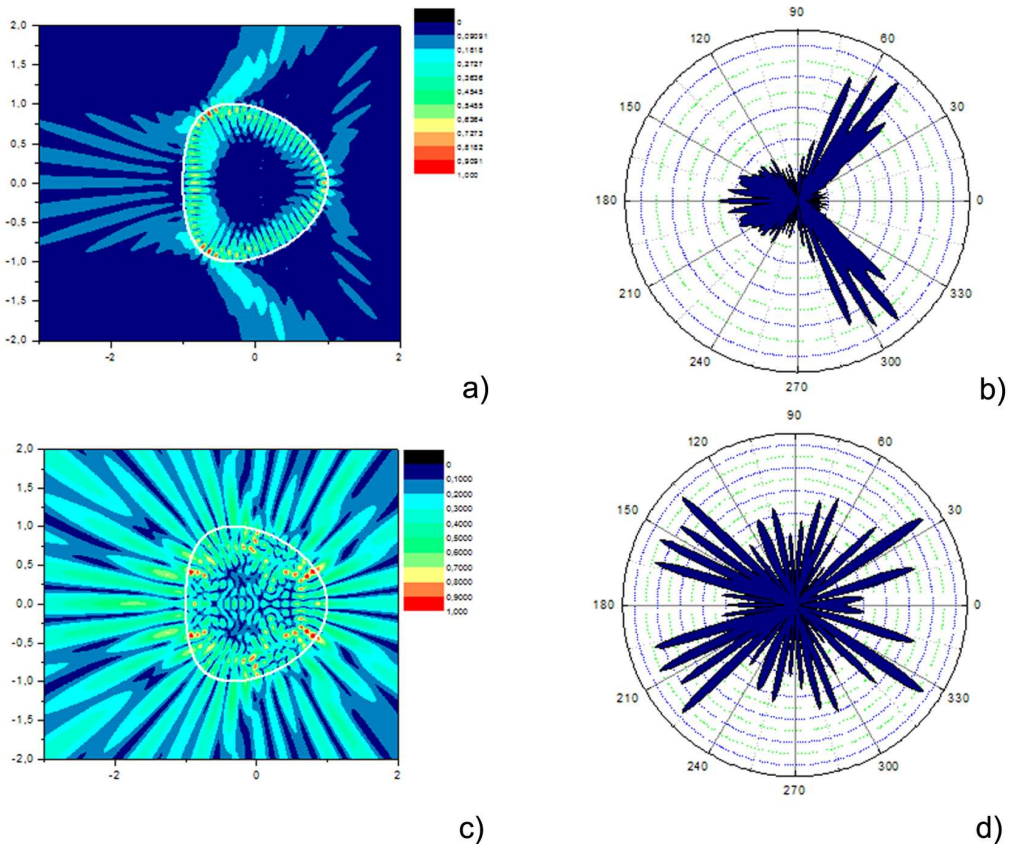

Figure 6.23: *LEP map fields (a,c) and emission diagrams (b,d) for a kite with* $\delta = 0.165$*, and* $(ka; \gamma) = (23.74; 9.55 \cdot 10^{-3})$ *(a,b) and* $(23.5; 4.56 \cdot 10^{-2})$ *(a,b). Refractive index n=1.5, discretization over a set of N=100 points.*

The example of several simulated mode fields and emission profiles for $ka = 25$ are shown on Fig.6.22 (Fabry-Perot type modes) and Fig.6.23 (WGM). The profile of modes depicted on Fig.6.23.a is akin to a classic WGM pattern, while the mode on Fig.6.23.c-d is given merely as an example of non-Fabry-Perot mode.

In summary, the LEP method predicts the co-existance of WGM and Fabry-Perot mode types in kite-shaped cavities of small size ($ka = 25$). The directions of maximum emission of different mode types do not coincide. In contrast to rectangle micro-laser, the peak emission of one mode matches to a non-zero emission of the other modes, making thus the expected emission spectra highly multimodal.

The influence of the cavity size on the emission properties of kite micro-laser is addressed in the following section.

6.3.2 FDTD simulations

In this section we present the results of FDTD simulations, that were performed on commercially available Lumerical simulation package (Appendix F), in order to check the cavity size influence on the emission properties of kite micro-lasers.

FDTD simulations allow to compute the mode pattern and the emission diagram, but fail to provide information on the emission threshold. However, as LEP simulations cannot be performed on large cavities, we took advantage of the FDTD method to further investigate the influence of a cavity sizes on their emission properties.

The first simulations were performed for a cavity with 5 μm radius, which is slightly larger than in the former study by LEP (1 μm) and lies in another range in terms of wavelength scaling ($> 10\ \lambda$).

To begin with, a spectrum was calculated for TE (in plane) and TM-polarized (orthogonal to the plane) modes, as depicted on Fig.6.24.a. Then the field patterns (Fig.6.24.b-d) and emission diagrams (Fig.6.25.b-d) were mapped for several peak wavelengths in the spectrum.

A clear WGM structure of a mode can be noticed at first glance with field maxima localized at the vicinity of the cavity boundary, as shown on Fig.6.24.b. An additional proof of strong light confinement in the cavity can be inferred from the field map with a strong zoom on the intensity, as on Fig.6.25.a, the emission clearly evidencing pattern.

The difference in field distributions between TE and TM polarized components can be evidenced only when the mode map is zoomed at any region near the cavity border (Fig.6.24.c-d), sowing that the TE mode actually is less confined.

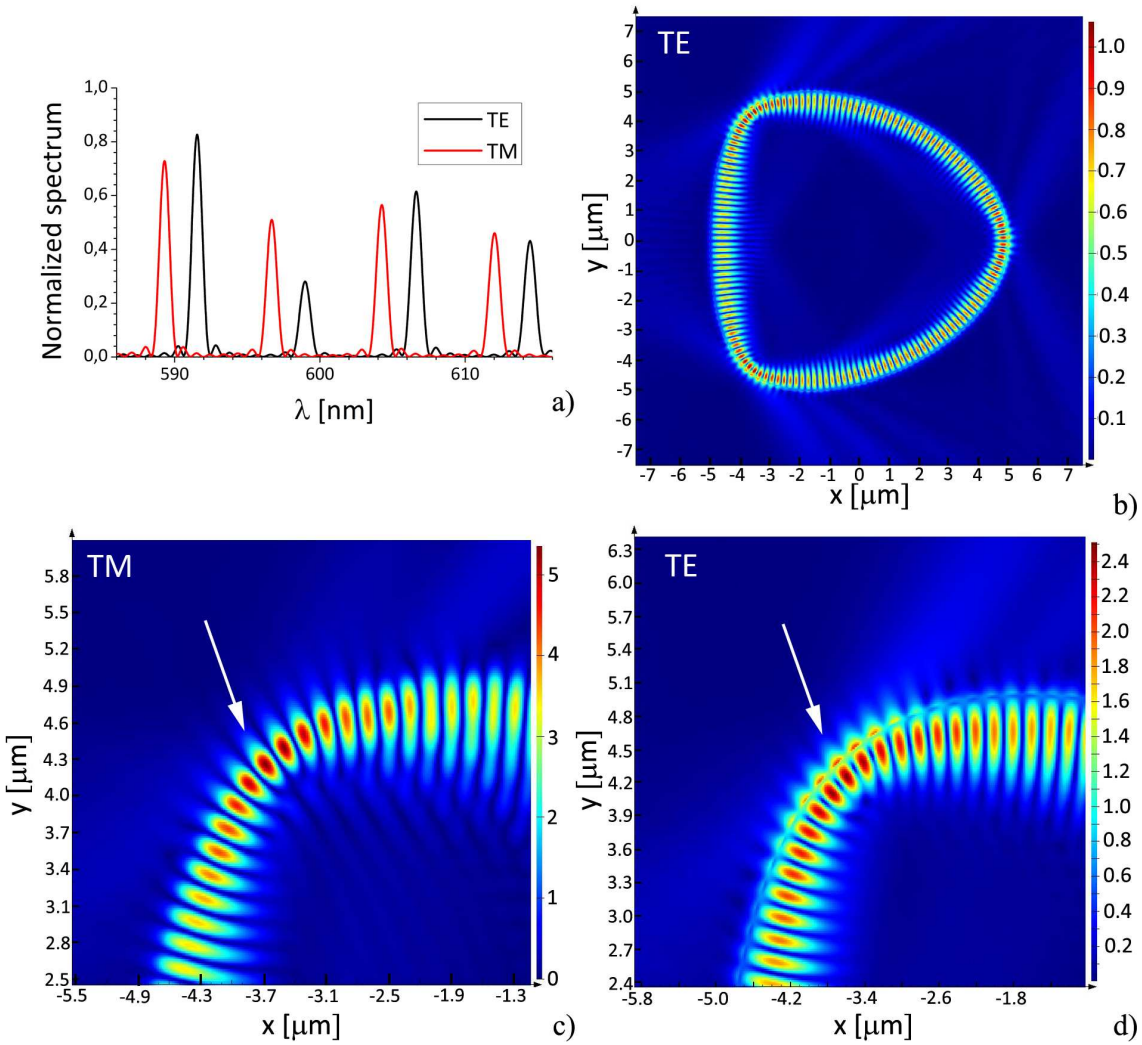

Figure 6.24: *Mode patterns obtained with FDTD simulations for a $r = 5$ μm kite with $\delta = 0.165$: a) spectra of TE and TM-polarized mode; b) mode pattern at 606.5 nm resonance (TE-polarized). c),d) zoom of the mode map: c) 597nm resonance (TM), d) 606.5 nm resonance (TE).*

The advantage of mode field patterns of dielectric cavities is that they permit the visualization of mode structure inside the cavity as well as the out-coupling mechanism (by zoom into the intensity level on the plot, as depicted on Fig.6.25.a). The latter facilitates an understanding of the emission diagrams, built on Fig.6.25.b-d, namely the origin of the emission peaks. For instance, the emission within 0-45° on diagrams Fig.6.25.b-d is provided by the upper cavity corner, as well as the

lobe at 210°, while the emission in range 45-90° origins from the right-hand corner (other emission directions are symmetrical to those explained and given by lower corner and a nose).

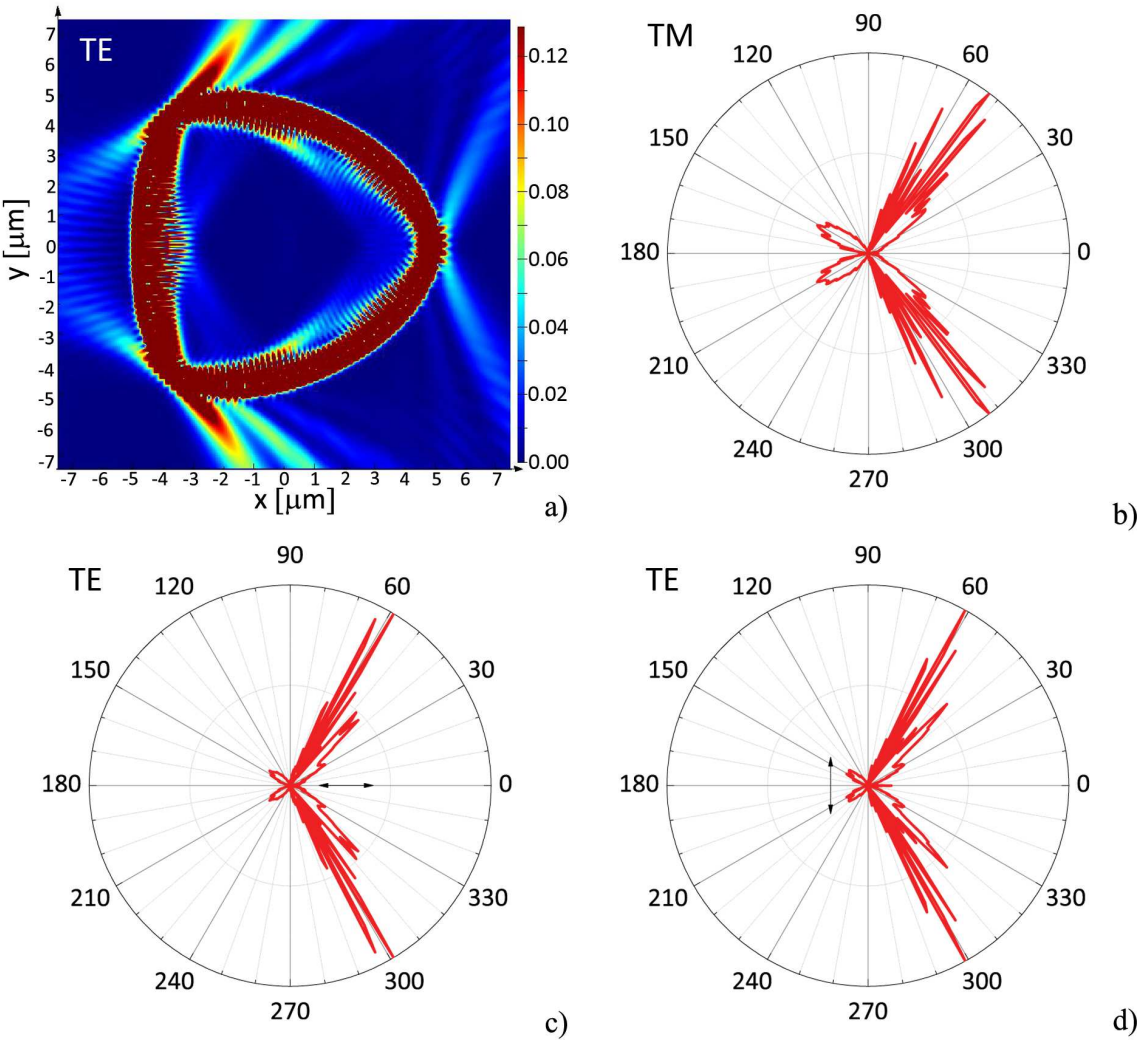

Figure 6.25: *FDTD simulations for a $r = 5$ μm kite with $\delta = 0.165$: a) zoom of a TE mode map (606.5 nm); angular emission diagrams for b) TM (604.3 nm); c) TE (606.5 nm, $\alpha = 0^o$) d) TE (606.5 nm, $\alpha = 90^o$).*

An interesting fact is that there is a tiny emission peak along 0° direction on emission diagram depicted on Fig.6.25.d. This is the Fabry-Perot periodic orbit, which appears with pumping polarization $\alpha = 90^o$. The relatively small emission of Fabry-Perot does not have physical basis, and is caused by limitations of the used numerical tool (passive simulations do not account for the gain properties of the medium, which results in an increased inaccuracy for weakly confined modes, such as Fabry-Perot periodic orbit, Appendix F).

Emission along 150° is more intense for TM mode than for TE. Still there is a good correspondence between emission patterns of 5 μm kite provided by FDTD simulations (Fig.6.25.b-d) and 1 μm kite obtained with LEP (Fig.6.23.b).

An increase in the cavity size leads in appearance of WGMs with several maximums along the cavity radius, as depicted on Fig.6.26. At the same time this does not affect the emission properties (Fig.6.26).

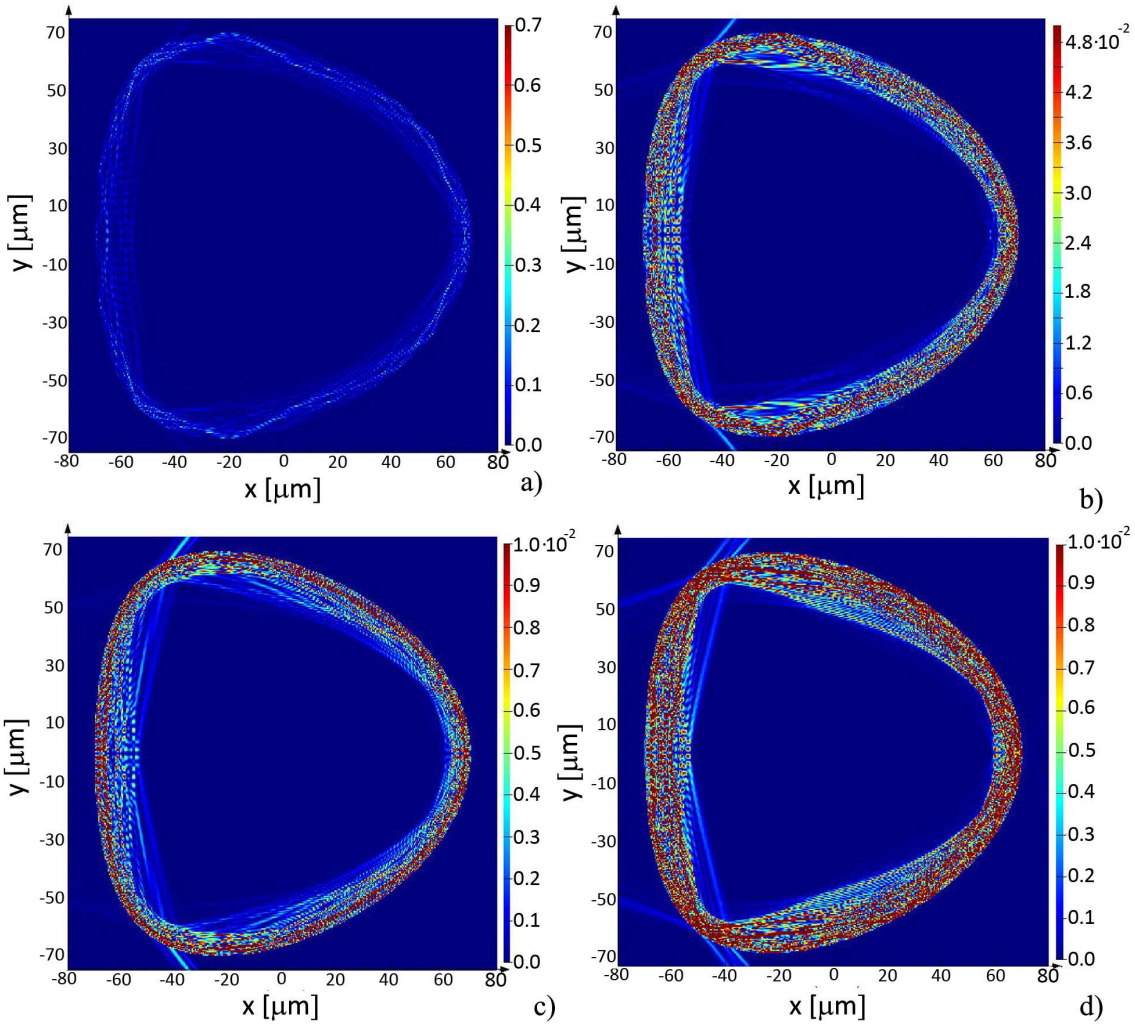

Figure 6.26: *FDTD simulations for a r = 70 μm kite with δ = 0.165 (TE): a) 613 nm; maps zoomed in intensity: b) 613 nm; c) 615.7 nm; d) 620.4 nm.*

FDTD simulations show, that the emission directionality does not change with the increase of the cavity size, at least in our examined range. Moreover, there is a good correspondence between emission patterns of kites as from FDTD simulations compared to those obtained by LEP. The first step in the experimental study on kite micro-lasers will be in the comparison of experimental emission diagrams with those predicted by simulations.

6.3.3 Experimentally observed emission properties

This section analyzes the experimentally obtained emission spectra, in terms of emitted power diagrams and thresholds for kite micro-lasers. The data processing is explained first on the example of relatively big cavities (70 μm in radius). Then the emission spectra and emission diagrams are shown for various cavity sizes and for samples based on several dyes. Viktor TSVIRKUN performed the main part of this experimental work in the framework of his master thesis under my guidance.

6.3.3.1 Analysis of the emission properties

The experimental spectra of micro-lasers of various shapes presented earlier in this work, contain combs, corresponding to a single type of modes. Even in a case of co-existence of several lasing mode types in a resonator (as for instance Fabry-Perot and diamond periodic orbits in a rectangle), the directions of maximum

emission were completely different, and the presence of one mode type did not seem to interfere significantly with the spectrum of another. At the beginning of the investigation of kite micro-lasers we faced the problem of spectral superposition of combs with comparable intensities, representing different mode types.

The Fourier transform provides the information on the modal content of the spectrum, however it fails to spectrally single-out the different modes. In order to proceed with thise study, it was necessary to develop a new method , allowing to distinguish mode types in the spectrum.

The additional tool we called for is the analysis of the polarization of the micro-laser emission (in the layer plane or orthogonally to it), where a thoroughly studied polarization state of the Fabry-Perot type mode ($P \approx 0.9$) was taken as a reference. Another criterion for the analysis was the quality factor of the mode. In the absence of hole-burning effects the mode with lower Q should be blue-shifted compared to the higher-Q one (Sub-section 5.2.3). To our advantage, the hole-burning effect should be negligible for kite emission, as the gain region for the Fabry-Perot and WGM modes are localized in different parts of the cavity (Sub-sections 6.3.1, 6.3.2).

First the experiment was performed on a 5 wt% DCM-based kite of 70 μm in radius. The emission diagram representing the total intensity in spectrum is plotted on Fig.6.27.a, showing satisfactory correspondence with the simulated emission diagrams. As for the spectra, their structure is rather complicated, and varies strongly with the emission direction, as depicted on Fig.6.27.b. According to simulations, emission at 60° and 165°, are expected to be mainly of WGM nature, while, if present at all, Fabry-Perot modes should appear mainly at 0° and 80°. Comparing spectra at 0°, 80° (eventual Fabry-Perot modes) and 60°, 135° (WGM), we note that the first group (0°, 80°) emits mainly in the spectral region below 613 nm, whereas the second (60°, 135°) is mainly in the red-shifted portion above. As the quality factor of a Fabry-Perot mode is presumably lower for a WGM, a blue-shifted emission (towards shorter wavelength) of the Fabry-Perot mode can be indeed expected.

Fourier-transform of spectra depicted on Fig.6.27.b contains clear Fabry-Perot peaks (a quasi doubled diameter radial optical length of *4 rn*, Fig.6.27.c) for 0° and 80° only, while the peaks for the 60° and 135° directions may be interpreted as WGM's (optical length of *12 rn* and their harmonics, Fig.6.27.c).

As we learned from the study of ribbon micro-lasers, the threshold of Fabry-Perot modes depends strongly on the pumping beam polarization. Here the variation of the pumping beam polarization did not affect substantially the spectra at 60° and 165°, while a part of spectrum below 613nm at 0° and 80° was seen only at a pumping polarization direction orthogonal to emission.

Finally, we examined the polarization state of the kite emission (Fig.6.27.e). There is no notable TM-component in the spectrum below 613 nm emission, and the WGM part sustains both TE and TM polarized peaks at different wavelength. The emission diagram can be plotted for each of these WGM peaks, and except for the thinner peaks their structure is very similar to those plotted on Fig.6.27.a: two main lobes in the range 45°-70° (symmetrical with respect to the 0° axe) and two minor lobes at about 165° (and 195°). The diagram of the emission for a 623 nm window in Fig.6.27.d, is representative of TM-polarized emission. FDTD predictions appeared in satisfactory agreement with experiments, displaying TM-polarized mode with lobes at a 165° angle slightly larger than for the TE-polarized ones.

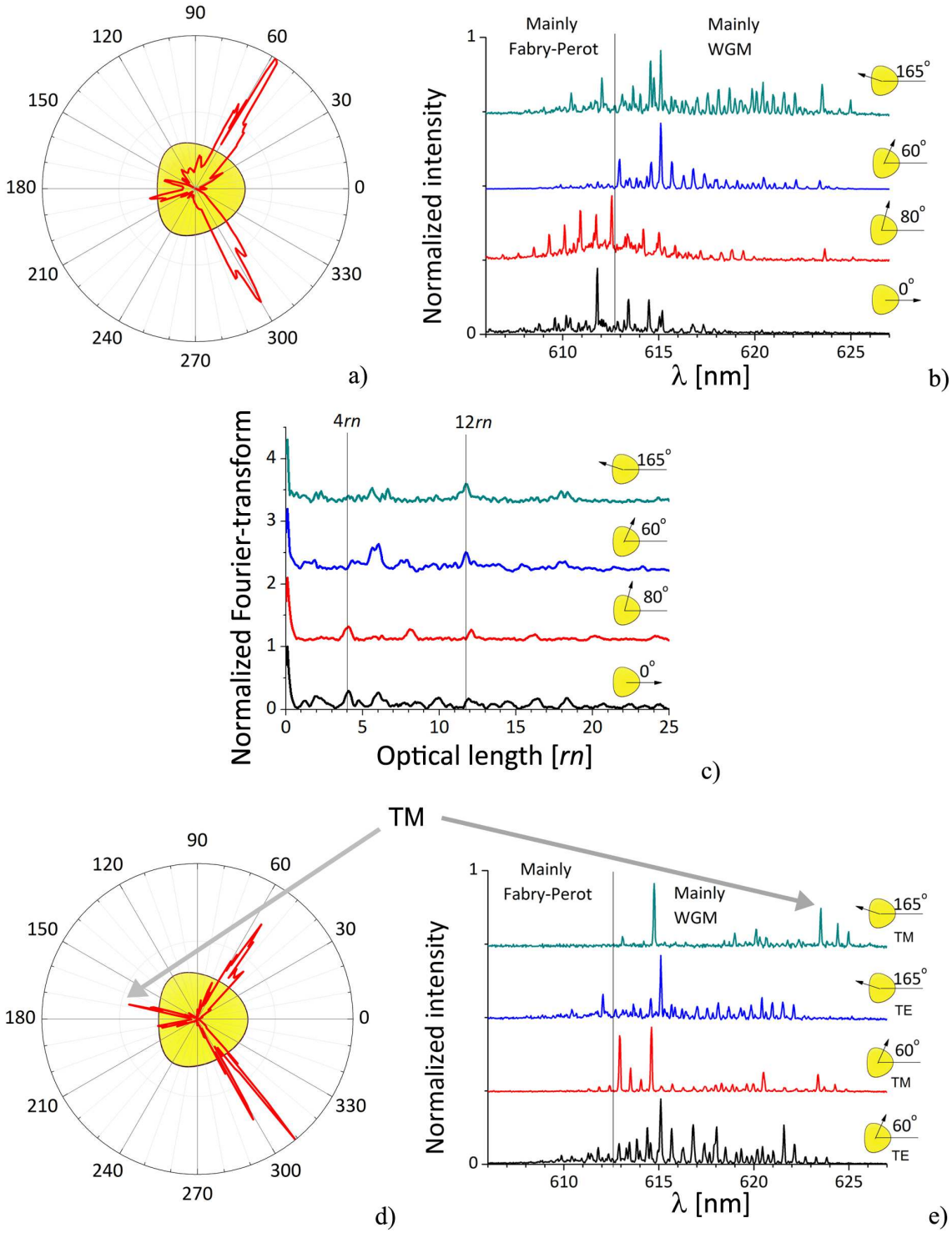

Figure 6.27: *Experimental emission properties of a $r = 70\mu m$ kite made of DCM: a) emission diagram representing the total intensity in spectrum; b) spectra at some directions of emission maxima; c) Fourrier-transform of the spectra given in (b); d) diagram of emission at 623 nm; e) polarization components of the emission spectra at 60° and 165° (TE - within the cavity plane, TM- orthogonal to the plane).*

We developed and validated several methods for the analysis of experimental data, based on polarization and quality-factor analysis. This set of methods form a powerful tool-box, that allows to distinguish the influence of different mode types on the emission properties of micro-lasers, probably beyond the specific but still representative case embedding kite micro-cavities.

6.3.3.2 Emission properties of various kite sizes and dyes

Here we focus on the influence of the nature of dye molecules and of the cavity size on the emission properties of kite-shaped micro-lasers.

The first experiment on kite micro-lasers, presented in the previous section, was held on DCM-based cavities, as a standard in our group for years. The choice of a rather big cavity size (70 μm in radius) was motivated by the possibility to excite both WGM and Fabry-Perot modes.

Experimental study of smaller cavities is interesting for two reasons:

- the decrease in the mode round-trip length results in bigger distance between the peaks in the spectrum, and thus easing the interpretation of the spectral properties;
- possibility to conduct the analysis of the influence of cavity size on the mode thresholds and to compare with values predicted by LEP in the limit of small cavities.

However experimental difficulties shown up for smaller cavities.

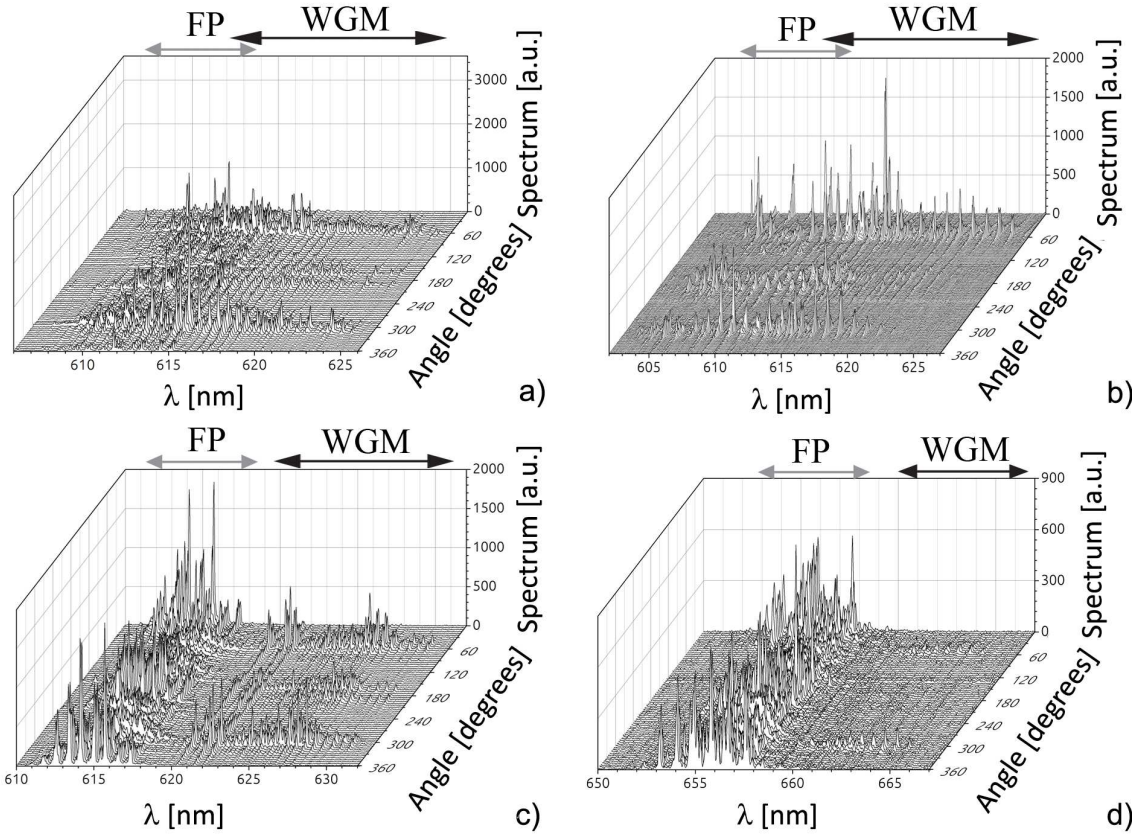

Figure 6.28: *Emission spectra of kite micro-lasers at various angle observation: a) 70 μm radius, DCM-based; b) 40 μm radius, DCM-based; c) 70 μm radius, MD7-based; d) 70 μm radius, MD48-based.*

The experimental emission diagrams of a 70 μm DCM-based kite, presented in the previous section, do not posses a perfect symmetry. The reason is in the variable angular step, used during the recording of the spectra in order to prevent bleaching (e.g. smaller angular step used for registering spectra along the maxima mission directions), which resulted in the recording of spectra at non-symmetric angles (with respect to the cavity axis, as is clear on Fig.6.27.a, which instead of displaying two symmetrical peaks at about 60° and 300° has one of them is few

degrees tilted). The emission diagram exhibit a fine structure along the directions of maximum emission, and the very first measurement was performed with a 2° angular step over [0°, 360°], which caused a blue spectral shift of the finally measured spectrum compared to the initial one.

Such a shift evidences the degradation of dye molecules in the cavity [65]. We observed this effect for various shapes of cavities, when a much higher pumping intensity was applied over dozens of minutes. However such a quick degradation was rather surprising for a DCM-based cavity of 140 μm size.

Decrease in the kite size indeed resulted in a larger spacing between peaks in the spectrum: spectra of a 70 μm radius DCM-based kite, depicted on Fig.6.28.a, shows a denser structure as compared to spectra of a 40 μm radius DCM-based kite, as shown for comparison on Fig.6.28.b. These graphs encompass the full emission spectrum. Each graph contains four regions of emission maxima at 60, 170, 190 and 300°, the spectra were recorded from 0° till 360°. Unfortunately the decrease in the peaks density in the emission spectrum of kite micro-lasers did not facilitate the analysis in case of DCM-based cavities. The close observation of the graph Fig.6.28.b of a 40 μm radius DCM-based kite shows that the spectrum along the 300° emission direction is blue-shifted by about 5 nm as compared to the 60° direction. Such a rapid degradation should be caused by the strong light confinement attached to a WGM mode. Thus the increased intensity in the maxima of fields for WGM compared to Fabry-Perot modes enhances the dye degradation. Molecules around the cavity border undergo more absorption-emission cycles and thus degrade faster.

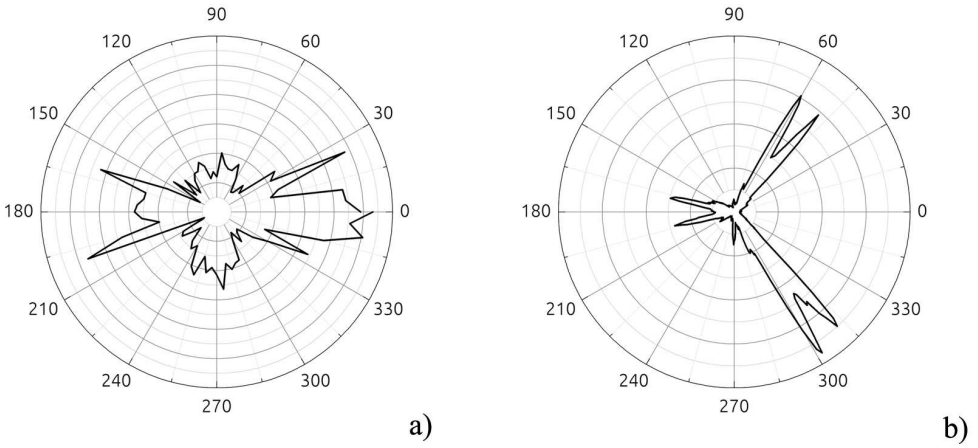

Figure 6.29: *Experimental emission diagram of a 70 μm radius MD7-based micro-laser: a) Fabry-Perot mode; b) WGM mode.*

Still it was possible to conclude that emission diagrams of WGMs modes for 55, 40 and 30 μm radius DCM-based kites are identical to that for 70 μm, although peak intensities in the diagrams are affected by degradation. For instance, the emission diagram of a Fabry-Perot mode in a 55 μm radius cavity exhibits a well-behaved lobe at about 90°, but degradation prevented the observation of the symmetrical lobe at 270°.

In this regard, dye molecules with enhanced photo-stability were used to proceed with experimental studies on kite micro-lasers, namely MD7 and MD48 from Bodipy family (Appendix C), supplied by our collaborators Gilles CLAVIER and Rachel MEALLET-RENAULT from PPSM laboratory at ENS de Cachan and synthesized by Marina DVORKO an internship student.

A most impressive consequence lies in the spectral separation of Fabry-Perot and WGM modes, as may be seen from Fig.6.28.c-d (Fabry-Perot below 618 nm

for MD7 and below 659 for MD48). Secondly, the emission diagram of Fabry-Perot mode (as shown on Fig.6.29.a) is in better correspondence with theoretical predictions, than the one observed with a DCM-based kite. And finally, the experimental study on MD7-based cavities did not suffer from degradation problems.

The directionality of the emission is not affected by cavity decrease or the change in dye content. However, our first experiments on smaller cavities failed due to rapid cavity degradation (presumably related to the strong confinement of WGM). In order to overcome this problem, highly photo-stable dye molecules must be used for experimental study of kite-shaped micro-lasers.

6.3.3.3 Threshold

The initial scope of the present study on kite micro-lasers was to determine the ratio of emission thresholds of different modes and examine the variation of this ratio with the change in cavity size. We expect the threshold of WGM mode to increase less steeply for small cavities compared to Fabry-Perot mode.

The serious degradation of the emission in the case of DCM-based cavities makes experimentally deduced thresholds rather doubtful. Especially as a 55 μm radius kite displays higher thresholds compared to 40 μm (Tab.6.2). Still, as shown in Tab.6.2, the ratio of deduced thresholds is stable with cavity size in case of DCM-based kites.

Table 6.2: *Comparison of emission thresholds of Fabry-Perot and WGM modes, measured at a 60° off-axis direction for various cavity sizes and contents.*

	I_{th} [MWcm^{-2}]		Ratio
Radius [μm]	Fabry-Perot	WGM	
DCM			
70	9±0.2	6.2±0.8	1.5
55	16.2±0.4	10.2±1.6	1.6
40	12.4±0.4	8±1	1.6
MD7			
70	5.2±0.5	2.8±0.3	1.9

The enhanced photo-stability of MD7-based kites allowed to perform a thorough study of the micro-laser emission. Unfortunately the sample contained 70 μm-size cavities only, and the analysis of the influence of the cavity size on the mode threshold was not possible and is left for the future studies.

Chapter conclusion

Modal structure plays an important role on the emission properties of dye-doped micro-lasers. Due to the intrinsic emission anisotropy properties of dye molecules, the pumping beam polarization can alter the spectral properties of the modes showing a two-dimensional in-plane structure, as was witnessed in the case of square micro-lasers.

We provided a thorough study on the emission properties of square and kite micro-lasers. The FDTD simulations were used to understand the polarization effects and light out-coupling mechanisms, and provided a good basis for the interpretation of experimental data.

Emission properties of planar square micro-laser, such as spectrum and intensity, are proved to vary significantly with the orientation of the pump beam polarization. Direct observation of emission confirmed the predictions provided by the analysis of FDTD simulations, that light out-coupling happens at the cavity corners. Moreover, pumping with polarization along one of the cavity diagonals

favors the gain along the opposite diagonal. Thus the variation of the pump beam polarization switches the distribution of intensity out-coupled at different cavity corners. Although the nature of the striking increase of output intensity under the pump polarized along the observation direction (and orthogonally to cavity side) remains unknown, we consider these properties as potentially interesting for integrated optics applications.

The application of "gain-loss-threshold" balance into the study of dielectric cavities in which light is out-coupled at the corners allows for the study of light diffraction. We have deduced the analog of the Fresnel reflection coefficient R = 0.1 at the dielectric corner with n = 1.5 for the light of about 600 nm wavelength.

We were also interested to study experimentally the influence of the co-existence of different mode types in the cavity on their thresholds. The kite micro-lasers were thoroughly examined in this regard, as those capable to sustain our standard Fabry-Perot periodic orbit as well as the Whispering Gallery Modes. The predictions on the emission diagram, provided by LEP and FDTD simulations, are in good quantitative agreement with measured ones. There was no influence of the cavity size on the emission diagram structure for kites of the size in the range from 40 to 70 μm. The absence of hole-burning effects in kites is also noteworthy. However we failed to perform a proper study on cavity size influence on the thresholds of different modes due to enhanced degradation of cavity based on our standard DCM dye. The verification of these properties on the cavity doped with dye with increased photo-stability is left for future studies.

Some of these results were presented on the French Israeli Symposium on Nonlinear and Quantum Optics (Aussois, France, 2011).

General conclusions

In this thesis we have undertaken to study the influence of the pump beam polarization and photo-physical properties of dyes on the emission features of dye-doped polymer micro-lasers.

We started by a setting formalized definitions of the photo-physical properties of dyes in view of their solid-state applications, thus advantaging a future research in the group.

Then we moved on to study the spontaneous emission of dyes, from the point of view of their polarization properties. We extended the existing fluorescence anisotropy model to the more general case of non-isotropic dye distribution in the medium, where dye exhibit the non-collinear absorption and emission dipoles. This model predicted that the emission anisotropy would vary with the direction of observation, which we could experimentally confirm. Moreover, contrary to the general earlier assumption in liquid dye lasers, the absorption and emission dipoles of examined dyes excited to S_1 energy level were proved to be non-collinear. Fluorescence anisotropy features of the dye emission are proved to be important towards stimulated emission and lasing in particular, as they define the gain anisotropy and thus the system sensitivity to the pump beam polarization. On the other hand the output polarization properties of dye-doped micro-lasers were proved to be mainly influenced by the electromagnetic properties of the lasing mode.

We proposed a more general and quantitative description of the amplification in dye-doped or conjugated polymer layers, by introducing the K parameter, which represents the linear ratio between gain and pump intensity (in the limit of validity of such linearity). This approach simplifies gain comparison between materials for a given configuration. This also allows to derive a simple relation between gain, losses and threshold, which can be used to infer one of these properties based on the others two. We experimentally validated this "gain-loss-threshold" relation in the benchmarking case of ribbon-shaped planar micro-lasers. We also inferred an estimate of K from known photo-physical properties of dyes, which proved in agreement with the expected order of magnitude. Thus, we propose to use this method in order to estimate the optically-pumped threshold, thus assisting the selection of materials towards lasing at a desired wavelength, thus also indirectly guiding research towards an improved material starting point for electrical pumping.

We also examined experimentally the out-coupling mechanisms from square-shaped micro-lasers, and showed it to be caused by light diffraction at the corner. In this regard, the "gain-loss-threshold" relation proved helpful towards the study of this fundamental physical problem. For the investigated dye-doped thin polymer films, we have found an equivalent of the Fresnel reflection coefficients for light diffraction on the dielectric corner. The pump polarization was found to greatly impact the emission of planar square micro-lasers, as it allows to select the cavity corner(s) responsible for out-coupling and moreover influences the emission angular diagram for such cavities.

Among the perspectives towards future work, we believe that the improvement of the evaluation methods for the K parameter based-on photo-physical properties of the dyes should be done, so as to allow for proper selection of gain materials towards light amplification and laser applications.

Developed "gain-loss-threshold" relation we consider to be a powerful tool towards the analysis of gain and mode coupling, which should be explored in the micro-lasers of arbitrary shapes.

Light diffraction at the dielectric corner can be examined for thin polymer layers of various thickness and corner angles, which may be a relevant empirical basis towards more fundamental physical investigations.

Square micro-lasers are shown to be highly interesting objects in terms of the light coupling applications, especially thanks in particular to the sensitivity of their emission features with respect to the pump beam polarization that we have evidenced in this work for the first time and could be generalized to other shapes. Polarization of the pump, is added to the palette of other control parameters disclosed earlier (such as the contour shape itself, holes in the cavity), thus further opening-up the possibility to control the emission features of lasing micro-cavities, which had been from its inception a decade ago, one of the main initial motivations of this domain of research.

Appendix A

Sample fabrication

Technical details on the sample fabrication are explained here.

A.1 Polymer-dye solution preparation

Various commercially available polymers in solution were used for fabrication: PMMA 495 A6 manufactured by MicroChem (anisole based solution with 6 wt% of PMMA with an average chain length of $495{\cdot}10^3$ units), PMMA 950 A15 (for VECSOL).

The required quantity of dye powder (5 wt% of DCM as the standard concentration, the percentage indicating the mass ratio of dye over polymer after solvent evaportaion) is blended with the polymer solution in a clean room environment under yellow light. A magnetic stirrer inside the bottle is used to homogenize the solution over a couple of hours. The bottle is then closed and carefully isolated by an aluminum foil (to avoid detrimental exposure to light that might induce partial polymerization of polymer chains or their aggregation).

The non-commercial dyes used in study were synthesized in the PPSM lab of ENS Cachan in the group of Gilles CLAVIER and Rachel MEALLET-RENAULT, and are basically BODIPY derivatives. High purity commercial dyes (99.9%) purchased from Exciton, and used without further purification. First trials were made with dyes from other manufacturers, but due to their lower quality there was no lasing effect. The names and abbreviations of all dye molecules studied in the present work are listed at the beginning of Appendix C.

A.2 Substrates

We use three types of substrates for the following experimental purposes: standard commercial 2 inches Si wafer (A.C.E.) for tests on fluorescence and ellipsometric measurements of the refractive index; standard 3 inch Si wafer covered by a 2 μm SiO_2 layer for ASE and laser emission study (the SiO_2 layer from thermal oxidation, provides the light guiding effect inside the polymer layer, Section 1.3) or a glass slide to study the photo physical properties of dyes inside the polymer matrix and for fluorescence anisotropy measurements.

In general, wafers are kept in a closed box in a clean-room in order to prevent exposure to dust. However a 10 minutes surface cleaning by UV-ozone improves the quality of polymer deposition. It activates bonds on the surface of the wafer, thus improving the substrate wetting by the polymer solution. Droplets spread faster over the surface and consequently the liquid deposition time is reduced. In the case of glass substrates, a primary cleaning procedure is necessary, namely a

10 minutes ultrasonic cleaning by acetone, then by isopropanol, followed by drying in a nitrogen flow.

A.3 Spin-coating

The optimal parameters of spin coating can be found in the manufacture data for each polymer solution. Yet there remains a possibility of slight variation depending on the substrate type, and surely as a consequence of dye molecules incorporation. Spin-coating parameters used here result from an experimental optimization search made by Melanie LEBENTAL.

In the case of a PMMA 495-dye solution, the following parameters are set (speed, acceleration, time): 500 rpm, 500 rpm/s, 5 s with opened cover followed by 1000 rpm, 1000 rpm/s, 18 s with closed cover. Polymer films further used for e-beam lithography are spun-coated with the use of a special cover (GR7) in order to reduce surface roughness. It also provides a decrease of the film thickness by about 50-100 nm and is thus to be avoided for films prepared for UV-lithography. We use the Microposit S1805 photo-resist for UV-lithography, with spinning speeds at 1000 rpm, 1000 rpm/s, 20 s (with open cover).

Baking of the polymer layers is needed in order to evaporate the residual solvent and in some cases to partially polymerize. Working with active polymer layers, we perform two hours baking in the oven at a relatively low temperature (120°C for PMMA). The samples are withdrawn from the oven a few hours after the curing, left to cool slowly down to room temperature so as to prevent layer from cracking due to a too fast change in temperature of surroundings. The photo-resist baking is less demanding and is performed on a hot plate at 95°C during 2 minutes.

After curing each layer, its thickness is checked by a DEKTAK profilometer (typical values are ranging from 0.6 to 1.1 μm for active polymer alone and together with the photo-resist correspondingly).

A.4 UV lithography

UV exposure of the sample is applied through a chrome[1] optical mask (made by Photronics LTD with electronic mask designed in "Layout Editor") with a 6 s dose. After transfer of the geometrical pattern of the mask to the resist, irradiated areas are easily removed by 1 minute rincing in a developer solution (6:1 ratio of DI water to developer DEL). The sample is finally rinsed by DI water.

Etching is performed in an oxygen plasma (RIE - reactive ion etching), the duration of which depends on the exact thickness of the layers and is of the order of a few minutes. The etching speed of the resist is faster than that of the polymer, which forces us to depose thicker layers of resist upon the active polymer layer. In opposite cases, the time necessary to etch the resists is insufficient to fully encode the active polymer portions on the uncovered parts. The procedure duration is calculated so as to etch as well the thin layer (30-50 nm) between the resist and polymer, which inevitably appears during the resist spinning.

A.5 E-beam lithography

As explained in Chapter 2.1 electronic mask is necessary to perform e-beam lithography. This may be either a positive or negative electronic mask (cavity exposed

[1]Several other materials can be used as well, for instance Aluminum. As a result, the mask cost is reduced, however the quality of cavities is altered strongly and a number of the fabrication cycles is reduced as well.

or not, Fig.A.1) depending on the polymer being the negative (for example SU8) or positive (our standard PMMA) resist towardsr the electron beam.

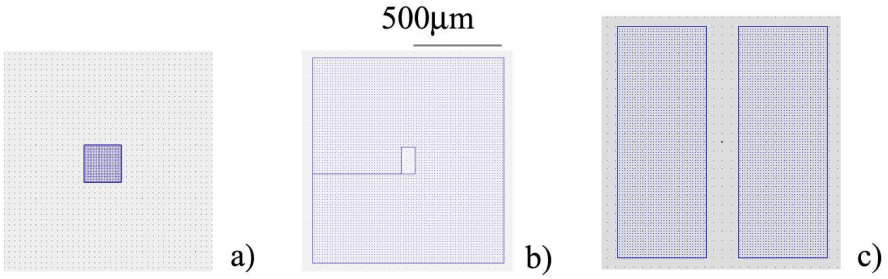

Figure A.1: *Electronic mask fragments for e-beam lithography: a) positive; b),c) negative.*

During the e-beam lithography with a negative electronic mask, all the sample surface except for cavities (which amount 0.1-0.5% of the sample area) is exposed to the electron beam. In such case, the fabrication duration may exceed 20 hours, which is exceeding realistic limits for future applications. It is however possible to simplify and accelerate the process by deliberate exposure of well-defined areas around each cavity (Fig.A.1.b). A standard size of the step between the cavity and etched area border is taken of the order of 500 μm. Except for few very efficient dyes, such a gap size preserves from significant absorption by the surrounding polymer layer of the scattered part of the pump beam. The Fig.A.1.c demonstrates the advantage of negative mask e-beam lithography for the fabrication of ribbon-shaped micro-lasers: such a ribbon has only two borders that limit its width and thus only transverse resonances which eliminates the problem of mode competition with longitudinal resonances.

After the exposition the samples are developed during 45 s in a 3:1 mixture of MIBK/IPA (Methyl isobutyl ketone), than washed in isopropanol and dried.

All the e-beam lithography samples were performed on a Leica EBPG 5000+ set-up at the "Laboratoire de Photonique et Nanostructures" (LPN) of CNRS by Christian ULYSSE from the dye-doped polymer layers fabricated in the clean room of LPQM. Since 2007 the samples to and from LPN are send by post. The sample are packed in separate boxes so as to avoid any contact of polymer layers with the box. The cover is scotched to prevent dust and liquids penetration inside the box.

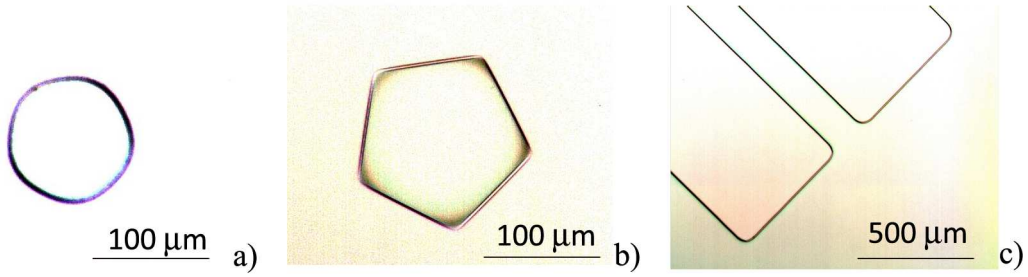

Figure A.2: *Optical microscope photographs of defects caused by electron-beam lithography in the polymer layers containing Alq_3: a,b) "pentagon" micro-cavity; c) ribbon micro-cavity. (a) was obtained with first trials and (b,c) with smaller radiation dose.*

Still, there remain e-beam lithography problems with samples containing small organo-metalic molecule Alq_3. The first attempts lead to cavities with rounded corners in the plane (Fig.A.2.a) and non-vertical sidewalls. Afterward attempts

to solve this problem by the changing the radiation dose (Fig.A.2.c), however the quality of the sidewalls of Alq_3-based cavities remained much lower than for normal cavities (Fig.A.2.b). It is possible, that the e-beam damages layers containing Alq_3 and thus decreases significantly the layer emission. However, this spurious phenomenon did not prevent lasing in the DCM-Alq_3 doped PMMA planar micro-lasers.

A.6 Edge cleaving methods

Edge cleaving appeared to be an essential, however non-trivial technological bottleneck issue towards proper ASE measurements. As mentioned in Section 2.1, spun-coating results in access of the polymer along the sample edge (Fig.2.1.c). The wafer itself can be cleaved easily by scratching along the Si crystalline axis (the orientation of which is always marked on a wafer by rectangular part of the edge). However in the presence of a polymer layer covering the wafer, the scratch on the wafer top (polymer side) leading to good wafer cleavage provides a quite irregular polymer border (Fig.A.3.a).

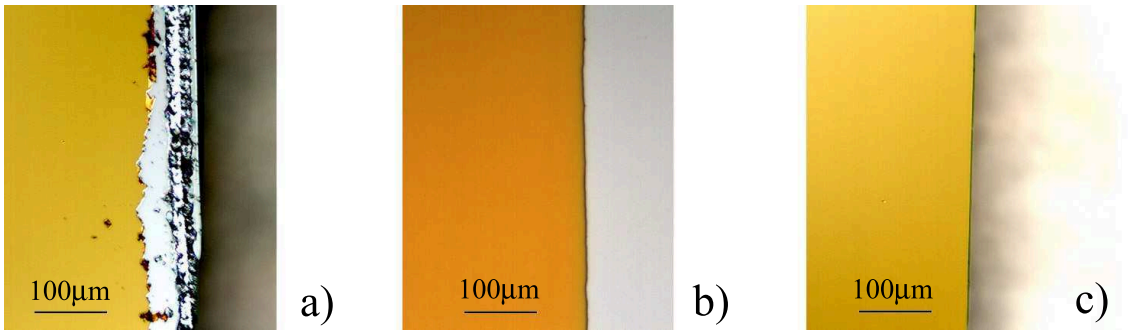

Figure A.3: *Optical microscope photographs of edge cleaving methods: a) polymer side cut b) plasma etching (layer covered by a glass plate), c) wafer side cut.*

Attempts at etching some area along the border by oxygen plasma helped slightly improve the situation (Fig.A.3.b). From our trials the optimal method consists in scratching the bottom side of the wafer (Fig.A.3.c). Although it may result in defects on the sample surface (during cleaving the sample stands on the polymer layer), the border irregularities being then almost absent (Fig.A.3.c). In as much as ASE measurements require only a tiny line along the border, its quality is essential.

Appendix B

Calculation of fluorescence anisotropy

This appendix develops calculations concerning fluorescence anisotropy in the case of a non-isotropic dipole distribution.

B.1 Some critical issues in the calculation

The calculation track is rather straightforward in the case of a collinear orientation of the absorption and emission moments, the integration being then done over all possible orientations of one dipole (θ variable). But in the general case of $\beta \neq 0$ the integration must be performed over two inter-related variables θ and θ_a (Fig.B.1.a), thus further demanding a choice of independent angular variables so as to be able to proceed to a sound integration.

As already discussed in the main text of this thesis, the angle β between absorption and emission dipoles is set at exact pumping wavelength. Even for an assembly of molecules, the variation of β can be considered as negligibly small. The orientation of the absorption moment might be tuned by changing the pump wavelength, thus consider the orientation of the emission moment as an independent variable.

At the outcome of the search of the suitable trigonometric representation of the angular relation between the moments, we call on the trihedral angle formula, which for trihedral ABCO from Fig.B.1.b is:

$$\cos C = \frac{(\cos \angle BOA - \cos \angle COA \cos \angle BOC)}{\sin \angle COA \sin \angle BOC}, \tag{B.1}$$

where C is a dihedron formed by ACO and BCO planes. Applied respectively to the two trihedral conformations ABCO and DEFO (the DEF plane is parallel to the xOy plane) shown on Fig.B.1.b,c we obtain

$$\begin{aligned} \cos(\pi - \mu) &= \frac{(\cos \theta_a - \cos \theta \cos \beta)}{\sin \theta \sin \beta} \\ \cos |\psi| &= \frac{(\cos \beta - \cos \theta_a \cos \theta)}{\sin \theta_a \sin \theta} \end{aligned} \tag{B.2}$$

Finally, simple mathematical derivations and substitution of the first expression (B2) into the second one provide the set of equations underlying all calculations in this Appendix:

$$\begin{aligned} \cos \theta_a &= \cos \theta \cos \beta - \cos \mu \sin \theta \sin \beta, \\ \cos |\psi| \sin \theta_a &= \cos \beta \sin \theta + \sin \beta \cos \theta \cos \mu; \end{aligned} \tag{B.3}$$

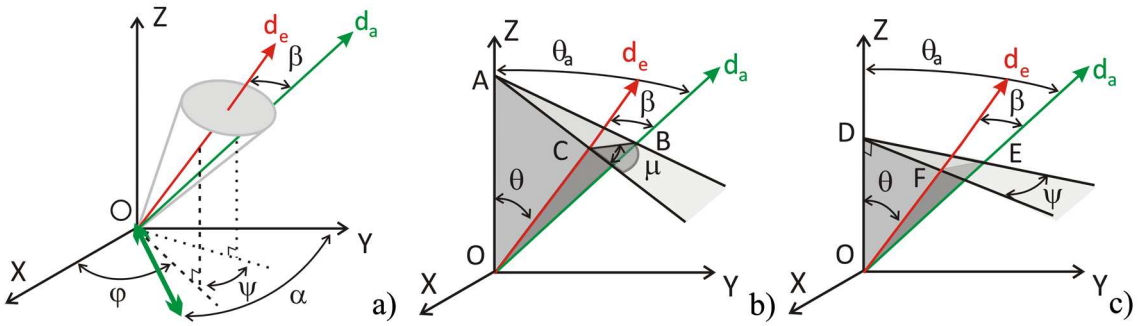

Figure B.1: *Illustration of the trihedral formula applied to the issue of relating the angles between absorption and emission dipoles: a) depiction of the orientation of the moments; trihedrons b)ABCO and c) DEFO in this system.*

This couple of expressions (B3) allows for straightforward calculations of the absorption probability over all possible orientations of the absorption moment of an arbitrary molecule (Appendix B.2).

B.2 Absorption probability calculation

As mentioned in Appendix B.1, the orientation of the absorption dipole of a dye can be defined within a cone of angle 2β around the emission dipole. All d_a positions on this cone are considered equiprobable and should be taken into account, leading to the following expression:

$$P_a(\Omega) = \frac{1}{2\pi}\int_0^{\pi} \left(P_a(\Omega,\mu,|\psi|) + P_a(\Omega,\mu,-|\psi|)\right) d\mu, \tag{B.4}$$

The absorption probability is a scalar product of the vectorial excitation and absorption dipoles: $P_a(\Omega,\mu,\psi) \propto \|\mathbf{e}\cdot\mathbf{u}_a\|^2$. The expression under the integral in (B4) can be then shown to be:

$$\begin{aligned} P_a(\Omega,\mu,|\psi|) + P_a(\Omega,\mu,-|\psi|) = &\sin^2\theta_a\left(1+\cos\left(2\alpha+2\varphi\right)\right) - \\ &- 2\cos\left(2\alpha+2\varphi\right)\left(\cos|\psi|\sin\theta_a\right)^2 \end{aligned} \tag{B.5}$$

Here only θ_a and ψ are functions of μ and, with the aid of the set of equations (B3) one may replace μ by other angular variables (namely θ and β):

$$P_a(\Omega) = \frac{1}{4}\left(A - B\sin^2\theta\left(1-\cos\left(2\alpha+2\varphi\right)\right)\right), \tag{B.6}$$

where the functions

$$\begin{aligned} A(\beta) =& 2 - 2\cos^2\beta, \\ B(\beta) =& 1 - 3\cos^2\beta, \end{aligned} \tag{B.7}$$

have been introduced to simplify expression B.6 and following ones.

B.3 Expressions for the intensity components and the polarization degree P

The intensity components of the emission along any axis emission $\boldsymbol{\gamma}$ can be calculated from the starting point of formula (3.5) recalled here:

$$I_\gamma = I_{\gamma\,0} \int_\Omega P_a(\Omega) \Pi_{e\,j}(\Omega) f(\Omega) d\Omega$$

$\Pi_{e\,\gamma}$ stands for the Poynting vector component along this axis, proportional to the squared sine of the angle between dipole orientation $\mathbf{u}_\mathrm{e}$ and the observation direction $\mathbf{j}$ (written as a norm of their vector product, to facilitate the presentation for arbitrary observation direction and dipole orientation): $\Pi_{e\,\gamma}(\Omega) = \Pi_{e\,\gamma}(\theta, \varphi) \propto \|\mathbf{j} \times \mathbf{u}_\mathrm{e}\|^2$.

The observation direction $\boldsymbol{\gamma}$ can be defined in any suitable way. We chose here to refer it to the angle γ, which is counted from the z axis within the y-z plane, in consistence with our the experimental arrangement. Such an approach allows us to consider the general case of the arbitrary emission direction, of which expressions for edge and vertical emission are special cases. Then the emission probability along any arbitrary emission direction, defined by the angle γ, is given by:

$$\Pi_{e\,\gamma}(\Omega) \propto \underbrace{\sin^2\theta \cos^2\varphi}_{I_{P'}} + \underbrace{\left(\cos\theta \sin\gamma + \sin\theta \sin\varphi \cos\gamma\right)^2}_{I_{H'}} \tag{B.8}$$

where two orthogonal polarizations, namely $I_{P'}$(parallel to the sample plane) and $I_{H'}$, can be clearly distinguished from the start. In fact the emission can always be decomposed into a set of two orthogonally polarized components: for the edge emission it will be I_P and I_H, while along the vertical emission configuration one can introduce several orthogonal polarization pares such as ($I_{||}$, $I_\perp$) or (I_X; I_Y) (polarized along x and y-axis). Applying the previous formula to the cases of vertical emission ($\gamma = 0$) and edge emission ($\gamma = \pi/2$) we get:

$$\begin{aligned}
\Pi_{e\,y}(\Omega) &\propto \underbrace{\sin^2\theta \cos^2\varphi}_{I_P} + \underbrace{\cos^2\theta}_{I_H} \\
\Pi_{e\,z}(\Omega) &\propto \sin^2\theta = \underbrace{\sin^2\theta \cos^2\varphi}_{I_X} + \underbrace{\sin^2\theta \sin^2\varphi}_{I_Y} = \\
&= \underbrace{\sin^2\theta \sin^2(\varphi + \alpha)}_{I_{||}} + \underbrace{\sin^2\theta \cos^2(\varphi + \alpha)}_{I_\perp}
\end{aligned} \tag{B.9}$$

The corresponding overall intensity integrals are:

$$
\begin{aligned}
I_{P'} &= \frac{I_{E'0}}{4\pi \sin\theta_0} \int_0^{2\pi} d\varphi \int_{\frac{\pi}{2}-\theta_0}^{\frac{\pi}{2}+\theta_0} P_a(\Omega) \sin^2\theta \cos^2\varphi \sin\theta d\theta \\
I_{H'} &= \frac{I_{E'0}}{4\pi \sin\theta_0} \int_0^{2\pi} d\varphi \int_{\frac{\pi}{2}-\theta_0}^{\frac{\pi}{2}+\theta_0} P_a(\Omega) \left(\cos\theta \sin\gamma_0 + \sin\theta \sin\varphi \cos\gamma_0\right)^2 \sin\theta d\theta \\
I_{||} &= \frac{I_{E'0}}{4\pi \sin\theta_0} \int_0^{2\pi} d\varphi \int_{\frac{\pi}{2}-\theta_0}^{\frac{\pi}{2}+\theta_0} P_a(\Omega) \sin^2\theta \sin^2(\varphi+\alpha) \sin\theta d\theta \\
I_{\perp} &= \frac{I_{E'0}}{4\pi \sin\theta_0} \int_0^{2\pi} d\varphi \int_{\frac{\pi}{2}-\theta_0}^{\frac{\pi}{2}+\theta_0} P_a(\Omega) \sin^2\theta \cos^2(\varphi+\alpha) \sin\theta d\theta
\end{aligned}
\tag{B.10}
$$

while I_P and I_H can be inferred from those expressions respectively via $I_P = I_{P'}$ and $I_H = I_{H'}(\gamma_0 = 0)$.

The integration over φ is carried-out first:

$$
\int_0^{2\pi} d\varphi \begin{pmatrix} P_a(\Omega) \\ P_a(\Omega)\cos^2\varphi \\ P_a(\Omega)\cos^2(\varphi+\alpha) \end{pmatrix} = \frac{\pi}{8} \begin{pmatrix} 4(A - B + B\cos^2\theta) \\ 2(A-B) + B\cos 2\alpha + B(2-\cos 2\alpha)\cos^2\theta \\ 2A - B + B\cos^2\theta \end{pmatrix}
\tag{B.11}
$$

The integrals over $\sin^2\varphi$ or $\sin^2(\varphi+\alpha)$ may be easily obtained by linear superposition.

The following step is the integration over θ :

$$
\frac{1}{4\pi \sin\theta_0} \int_{\frac{\pi}{2}-\theta_0}^{\frac{\pi}{2}+\theta_0} d\theta \begin{pmatrix} \sin\theta \\ \cos^2\theta \sin\theta \\ \cos^4\theta \sin\theta \end{pmatrix} = \frac{1}{30\pi} \begin{pmatrix} 15 \\ 5\sin^2\theta_0 \\ 3\sin^4\theta_0 \end{pmatrix}
\tag{B.12}
$$

Performing simple mathematical operations, the following expressions can be reached:

$$
\begin{aligned}
I_{P'} = I_P &= \frac{I_{E'0}}{240}(10A(3-\sin^2\theta_0) - \\
&\quad - B(2-\cos 2\alpha)(15 - 10\sin^2\theta_0 + 3\sin^4\theta_0)) \\
I_{H'} &= \frac{I_{E'0}}{480}(10A(3C + D\sin^2\theta_0) - 2B(15C + 5(D-C)\sin^2\theta_0 - \\
&\quad - 3D\sin^4\theta_0) - \cos 2\alpha BC(15 - 10\sin^2\theta_0 + 3\sin^4\theta_0))
\end{aligned}
\tag{B.13}
$$

$$
I_H = \frac{I_{E'0}\sin^2\theta_0}{60}\left(5(A-B) + 3B\sin^2\theta_0\right)
\tag{B.14}
$$

$$
\begin{aligned}
I_{||} &= \frac{I_{E'0}}{240}(10A(3-\sin^2\theta_0) - \\
&\quad - 3B(15 - 10\sin^2\theta_0 + 3\sin^4\theta_0)) \\
I_{\perp} &= \frac{I_{E'0}}{240}(10A(3-\sin^2\theta_0) - \\
&\quad - B(15 - 10\sin^2\theta_0 + 3\sin^4\theta_0))
\end{aligned}
$$

where $C = 1 + \cos 2\gamma$ and $D = 1 - 3\cos 2\gamma$ have been introduced for the sake of simplifying notations.

As far as the dipole distribution within the xOy plane is isotropic for both 2-D and 3-D models, there should be no difference between the $I_{||}$ and I_P components if the pump beam polarization is along the x-axis (or $I_\perp$ and I_P for a polarization along y-axis). Indeed, it can be noticed in (B.12) that:

$$\begin{aligned} I_{||} &= I_P\left(\alpha = \frac{\pi}{2}\right) \\ I_\perp &= I_P\left(\alpha = 0\right) \end{aligned} \tag{B.15}$$

The emission anisotropy at an arbitrary angle γ is defined by analogy with the theory of fluorescence anisotropy:

$$\begin{aligned} P_\gamma(\alpha) =& \frac{I_{P'} - I_{H'}}{I_{P'} + I_{H'}} = \\ =& \frac{\left(\begin{array}{c} \cos 2\alpha(3+\cos 2\gamma)(1-3\cos^2\beta)+ \\ +(C_1 + C_2\cos^2\beta)(1-\cos 2\gamma) \end{array}\right)}{\left(\begin{array}{c} \cos 2\alpha(1-\cos 2\gamma)(1-3\cos^2\beta)+ \\ +(C_1 + C_2\cos^2\beta)(3+\cos 2\gamma)+ \\ +2(C_3 - C_1 + \cos^2\beta(C_1 - C_2)) \end{array}\right)} \end{aligned} \tag{B.16}$$

Although somewhat cumbersome, this expression is general and cannot be further reduced. Thus the expressions for the emission anisotropy in the case of VECSOL configurations and planar micro-lasers, namely P_V (vertical emission) and P_E (edge emission) respectively defined as:

$$\begin{aligned} P_E &= \frac{I_P - I_H}{I_P + I_H} \\ P_V &= \frac{I_{||} - I_\perp}{I_{||} + I_\perp} \end{aligned} \tag{B.17}$$

can be obtained from (B.16) using $P_E = P_{\gamma=\frac{\pi}{2}}(\alpha)$ and $P_V = P_{\gamma=0}(\alpha = \frac{\pi}{2})$. After few simplification steps, the following relatively compact expressions are obtained:

$$\begin{aligned} P_E &= \frac{C_1 + C_2\cos^2\beta + \cos 2\alpha\,(1 - 3\cos^2\beta)}{C_3 + C_1\cos^2\beta + \cos 2\alpha\,(1 - 3\cos^2\beta)} \\ P_V &= \frac{3\cos^2\beta - 1}{2}\frac{1}{C_4 + C_5\cos^2\beta} \end{aligned} \tag{B.18}$$

where:

$$\begin{aligned} C_1(\theta_0) &= 2\frac{15 - 10\sin^2\theta_0 - 9\sin^4\theta_0}{15 - 10\sin^2\theta_0 + 3\sin^4\theta_0} \\ C_2(\theta_0) &= 6\frac{5 - 10\sin^2\theta_0 + 9\sin^4\theta_0}{15 - 10\sin^2\theta_0 + 3\sin^4\theta_0} \\ C_3(\theta_0) &= 2\frac{15 + 10\sin^2\theta_0 + 3\sin^4\theta_0}{15 - 10\sin^2\theta_0 + 3\sin^4\theta_0} \\ C_4(\theta_0) &= \frac{C_1 + C_3}{4} \\ C_5(\theta_0) &= \frac{C_1 + C_2}{4} \end{aligned} \tag{B.19}$$

B.4 VECSOL configuration

In order to analyze the polarization properties in the case of VECSOL emission, one needs to examine the behavior of the I_X emission component from (B.9) as a function of the linear pump beam polarization angle α for fluorescence. The VECSOL cavity contains a glass plate at Brewster angle to fix the emission polarization for example along the x-axis. Consequently, the same origin of the influence of the variation of pump beam polarization orientation should be the same in the case of VECSOL emission and the I_X component of fluorescence in a vertical emission direction.

The expression for I_X is identical to I_P (as easy to notice from (B.9)), and taking into account formula (B.13) the dependance of I_X on α is linear with $\cos 2\alpha$ (functions I_{X1} and I_{X2} are independent of α):

$$\begin{aligned} I_X &= I_{X1}(\beta,\theta_0) + I_{X2}(\beta,\theta_0)\cos 2\alpha \\ I_{X1} &= \frac{I_{E'0}}{120}\left(5A(3-\sin^2\theta_0) - B(15-10\sin^2\theta_0+3\sin^4\theta_0)\right) \\ I_{X2} &= \frac{I_{E'0}}{240}B\left(15-10\sin^2\theta_0+3\sin^4\theta_0\right) \end{aligned} \tag{B.20}$$

It is useful to present the expression of I_X in terms of a value for pump polarization parallel to the analyzed observation polarization ratio:

$$\begin{aligned} \frac{I_X(\alpha)}{I_X(\alpha=0)} &= \frac{1-P_V}{1+P_V} + \frac{2P_V}{1+P_V}\cos 2\alpha = \\ &= A + (1-A)\cos 2\alpha \end{aligned} \tag{B.21}$$

B.5 Total intensity along the edge emission direction and the related polarization effect

Using the expressions derived in Appendix B.3, we show here how the emission intensity along the edge direction varies with the pumping beam polarization.

As was established in Appendix B.3, the I_H emission component is a constant with respect to the pumping beam polarization, I_P being linear with $\cos 2\alpha$. Using expression in (B.13) for the I_P component we can now rewrite in a more compact form:

$$I_P = I_P(\alpha=45^o) + \cos 2\alpha\left(\frac{I_P(\alpha=0^o) - I_P(\alpha=90^o)}{2}\right) \tag{B.22}$$

The total emitted light along edge direction is just a sum of I_P and I_H components :

$$\begin{aligned} I(\alpha) = I_P(\alpha=45^o) + I_H + \\ + \cos 2\alpha\left(\frac{I_P(\alpha=0^o) - I_P(\alpha=90^o)}{2}\right) \end{aligned} \tag{B.23}$$

If we now normalize it by $I(\alpha=90^o)$:

$$\frac{I(\alpha)}{I(\alpha=90^o)} = \frac{I_P(\alpha=45^o)+I_H}{I_H+I_P(\alpha=90^o)} + \\ + \cos 2\alpha \frac{I_P(\alpha=0^o)-I_P(\alpha=90^o)}{2\left(I_H+I_P(\alpha=90^o)\right)} \tag{B.24}$$

This expression can be further condensed into:

$$\frac{I(\alpha)}{I(\alpha=90^o)} = \frac{\rho+1}{2} + \frac{\rho-1}{2}\cos 2\alpha$$

where

$$\rho = \frac{I_P(\alpha=45^o) + \frac{1}{2}\left(I_P(\alpha=0^o)-I_P(\alpha=90^o)\right)+I_H}{I_H+I_P(\alpha=90^o)} = \tag{B.25}$$
$$= \frac{I(\alpha=0^o)}{I(\alpha=90^o)}$$

Finally, expressions on ρ for a several cases of the dye transition dipoles orientation are summarized in TableB.1.

Table B.1: *Comparison of the values of ρ parameter for several orientations of dye transition moments (angle β) and distribution law (θ_0).*

β [degrees]	ρ	ρ(3-D)	ρ(2-D)
0	$\frac{15+10\sin^2\theta_0-9\sin^4\theta_0}{45-10\sin^2\theta_0-3\sin^4\theta_0}$	1/3	1/2
45	$3\frac{25+10\sin^2\theta_0-3\sin^4\theta_0}{105+10\sin^2\theta_0-3\sin^4\theta_0}$	5/7	6/7
90	$\frac{45+22\sin^4\theta_0-3\sin^4\theta_0}{15+42\sin^4\theta_0-9\sin^4\theta_0}$	3	4/3

Appendix C

Photo-physical properties of dyes

This appendix is devoted to a more detailed description of the main photo-physical properties of the dyes and fluorophores exploited over this research work.

In total, five commercial dyes (from Exciton) were used, namely:

- DCM ([4-dicyanomethylene-2-methyl-(4-dimethylaminostyryl)-4H-pyran]),
- PM605 (Pyrromethene 605; 8-acetoxymethyl-2,6-diethyl-4,4-difluoro–1,3,5,7-tetramethyl-4-bora-3a,4a-diaza-s- indacene),
- PM597 (Pyrromethene 597; 4,4-difluoro-2,6-diisopropyl-1,3,5,7,8-pentamethyl-4-bora-3a,4a-diaza-s- indacene),
- RH590 (Rhodamine 590; Rhodamine 6G; 2-[6-(ethylamino)-3-(ethylimino)-2,7-dimethyl-3H-xanthen-9-yl]-benzoic acid, methyl ester, perchlorate),
- RH640 (Rhodamine 640; Rhodamine 101; 9-(2-carboxyphenyl)-2,3,6,7,12,13,16,17-octahydro-1H,5H,11H,15H,-xantheno[2,3,4-ij:5,6,7-i'j']- diquinolizin-4-ium perchlorate);

one commercial fluorophore (from Sigma Aldrich):

- Alq_3(Tris(8-hydroxyquinolinato)aluminium);

and two non-commercial dyes from the Bodipy family (synthesized in the PPMS laboratory, ENS de Cachan):

- MD7 (4,4-difluoro-8-mesityl-3,5-di(naphthalen-1-yl)-4-bora-3a,4a-diaza-s-indacene),
- MD48 (4,4-difluoro-8-mesityl-2,6-dipropyl-3,5-di(thiophen-2-yl)-4-bora-3a,4a-diaza-s-indacene).

Table C.1: *Molecular structure, molar mass (M), fluorescence quantum yield (ϕ) and fluorescence lifetime (τ_f) of the examined fluorophores.* [1]*If not given directly in literature, value is deduced from other mentioned parameters. In matrix:* [2]*PMMA,* [3]*p(HEMA-MMA)*

Abbreviation	Chemical formula	M [g/mol]	ϕ	τ_f [ns]
DCM	$C_{19}H_{17}N_3O$	303.36	0.76 [91]	2 [91]
			0.66 [162][2]	1.31[162][2]
PM605	$C_{20}H_{27}N_2O_2BF_2$	376.25	0.65	5
PM597	$C_{22}H_{33}N_2BF_2$	374.32	0.77[163]	6.3 [112]
RH640	$C_{32}H_{31}N_2O_3ClO_4$	591.05	0.8 [117][1]	7.5 [117]
RH590	$C_{27}H_{29}ClN_2O_7$	543.02	0.79[162][2]	4.8 [77][2]
			0.84[126][3]	3.3[126][3]
Alq_3	$Al(C_9H_6NO)_3$	459.3	0.32	10 [164]
MD7	$C_{38}H_{29}BF_2N_2$	562.46	0.95 [165]	5.5[165]
MD48	$C_{32}H_{33}BF_2N_2S_2$	558.56	0.72	6.39

The molecular structure of those dyes is sketched on Fig.C.1. Their chemical formulas and some important parameters are presented in Tab.C.1. For the majority, their 3-D molecular structures are displayed in the first section together with calculated orientation of their respective absorption dipoles. Unfortunately, current version of Gaussian© software available for our collaborators in the PPSM laboratory allows for calculation of the absorption dipoles only.

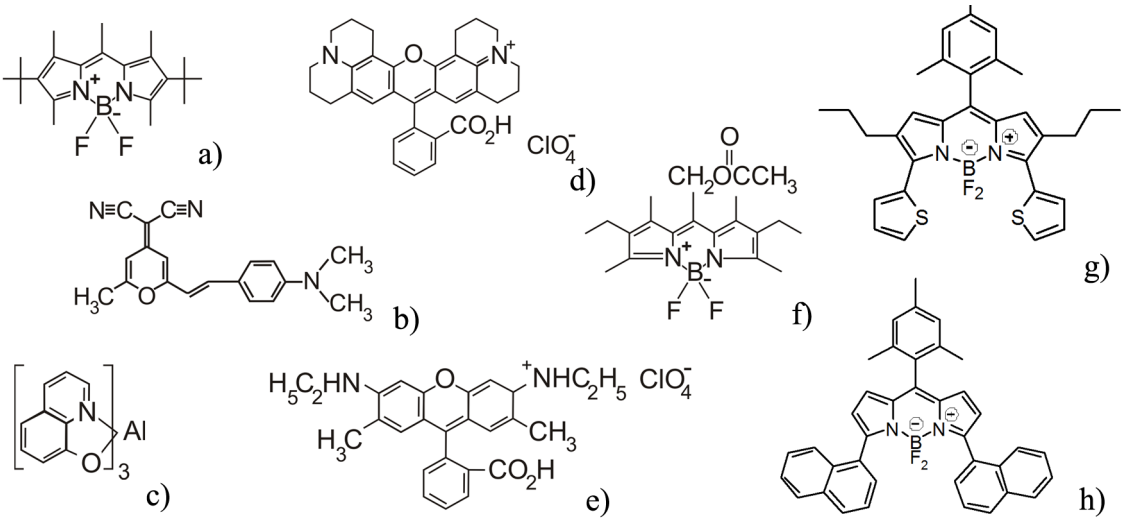

Figure C.1: *The molecular structure of the dyes and fluorophores used in this work: a) PM597; b) DCM; c) Alq_3; d) RH640; e) RH590; f) PM605; g) MD48; h) MD7.*

C.1 Absorption and emission properties of the examined dyes

C.1.1 Density of dye molecules in a unit volume

Density of dye molecules in the polymer unit volume is defined by their molar number (ν) per occupied volume (V), namely:

$$N = N_A \nu \frac{1}{V} \tag{C.1}$$

Their molar number can be related to the polymer mass via the dye molar density:

$$\nu = \frac{m_d}{M_d} = c\,(wt\%)\,\frac{m_p}{M_d} \tag{C.2}$$

(indexes "p" and "d" stand for polymer and dye correspondingly). The average volume occupied by the dye molecules is referred to the polymer free volume. It amounts to volumic spacing between chain units, and can be estimated [148] from the polymer density (ρ) and the molar volume related to Van der Waals volume (V_w, M_{mu} - the molecular weight of the monomeric repeat unit):

$$V_f = \frac{1}{\rho} - \frac{1.3V_w}{M_{mu}} \tag{C.3}$$

The V_f for PMMA is known to be 0.127 cm^3/g.

The volume that can be occupied by dyes in the volume associated with the polymer mass m_p is then: $V = V_f m_p$. The substitution of last expression and equation (C.2) into (C.1) provides the formula (1.5) from Sub-section 1.1.2:

$$N = N_A c(wt\%)\frac{1}{M_d}\frac{1}{V_f}$$

C.1.2 Absorbance and absorption cross-sections of dyes

Information on experimentally obtained (2.3.1) absorbance and molar extinction factors for the studied dye molecules incorporated into a PMMA bulk matrix are presented in Tab.C.2. This Table contains the peak values, and those at 355 and 532 nm pump wavelength).

Table C.2: *Comparison of the absorption properties of the examined dyes and fluorophores. λ_{max} is given in nm, $\sigma_A N$ in cm^{-1} and ε_A in $mol^{-1}cm^2$. Measurement relative errors are less than 2% (as inferred from the error in the measurement of a layer thicknesses).*

Molecule	Maximum			532 nm		355 nm	
	λ_{max}	$\sigma_A N$	ε_A	$\sigma_A N$	ε_A	$\sigma_A N$	ε_A
DCM	461	$1.61{\cdot}10^4$	$3.55{\cdot}10^7$	$3.29{\cdot}10^3$	$7.28{\cdot}10^6$	$5.08{\cdot}10^3$	$1.12{\cdot}10^7$
PM605	545	$1.92{\cdot}10^4$	$5.28{\cdot}10^7$	$1.3{\cdot}10^4$	$3.58{\cdot}10^7$	$1.44{\cdot}10^3$	$3.95{\cdot}10^6$
PM597	525	$1.93{\cdot}10^4$	$5.27{\cdot}10^7$	$1.63{\cdot}10^4$	$4.46{\cdot}10^7$	$1.63{\cdot}10^3$	$4.46{\cdot}10^6$
MD7	542	$1.11{\cdot}10^4$	$4.56{\cdot}10^7$	$1.05{\cdot}10^4$	$4.32{\cdot}10^7$	$1.81{\cdot}10^3$	$7.42{\cdot}10^6$
RH640	578	$1.88{\cdot}10^3$	$8.12{\cdot}10^6$	$6.45{\cdot}10^2$	$2.78{\cdot}10^6$	$2.03{\cdot}10^2$	$8.75{\cdot}10^5$
RH590	531	$3.68{\cdot}10^2$	$1.46{\cdot}10^6$	$3.63{\cdot}10^2$	$1.44{\cdot}10^6$	2.8	$1.11{\cdot}10^5$
Alq_3	389	$1.89{\cdot}10^3$	$4.18{\cdot}10^6$	12.2	$2.7{\cdot}10^6$	$1.16{\cdot}10^3$	$2.56{\cdot}10^6$
MD48	593	$9.54{\cdot}10^3$	$3.9{\cdot}10^7$	$2.03{\cdot}10^3$	$8.27{\cdot}10^6$	$1.27{\cdot}10^3$	$5.18{\cdot}10^6$

Tab.C.3 compares the peak values of the absorption cross-sections cited in the literature and is estimated in two different ways:

- from absorbance curves (Tab.C.2), using an estimated value from Exp.(1.5) value for the density of dye molecules in the polymer;
- from stimulated emission cross-sections via Exp.(1.19):

$$\frac{\sigma_a^{max}}{\sigma_e^{max}} = \frac{1}{\phi}\frac{\lambda_e}{\lambda_a}$$

Table C.3: *Peak values of the absorption cross-section of the examined dyes and fluorophores ($\sigma_A^{max}(\lambda_{max})$[$10^{-16}$ cm^2]). Dyes from [1]Kodak, [2]Exciton. Matrix: [3]PMMA, [4]COP(MMA-TMSPMA).*

Molecule	Cited in literature	Estimated from		
		Exp.(1.19)	Exp.(1.5)	
			$V = V_f \cdot m_p$	$V = m_p \cdot \rho(PMMA)$
DCM	5.2[162][1,3]	4.68	$4.21 \cdot 10^{-2}$	0.28
PM605	-	5.6	0.21	1.36
PM597	1.77[112][2,4]	1.23	0.26	1.7
RH640	-	5.5	$1.6 \cdot 10^{-2}$	0.11
RH590	4.4[162][1,3]	1.9	$8.3 \cdot 10^{-3}$	$5.5 \cdot 10^{-2}$
Alq_3	-	0.53	$2.4 \cdot 10^{-4}$	$1.56 \cdot 10^{-3}$
MD7	-	2.6	0.25	1.6
MD48	-	3.5	$4.8 \cdot 10^{-2}$	0.31

Proper estimate of the peak value of the absorption cross-section resulted from an in-depth study. It is therefore preferable to present here the absorption cross-section values at the pumping wavelength only in a relative way. Tab.C.4 shows the absorption cross-sections at 532 and 355 nm scaled to the maximum of the absorption cross-section curve.

Table C.4: *Absorption cross-section values of examined dyes at the wavelength used in experiments (scaled to the peak value of the absorption cross-section σ_A^{max} [cm^2]).*

molecule	$\sigma_A(532nm)/\sigma_A^{max}$	$\sigma_A(355nm)/\sigma_A^{max}$
DCM	0.2	0.31
PM605	0.68	0.075
PM597	0.84	0.084
RH640	0.34	0.11
RH590	0.99	$7.6 \cdot 10^{-3}$
Alq_3	$6.5 \cdot 10^{-3}$	0.61
MD7	0.95	0.16
MD48	0.21	0.13

C.1.3 Calculated absorption dipole

Here we present in details the results of Gaussian© computations on the absorption transition dipoles of dyes used herein.

Table C.5: *Calculated absorption properties of the dyes and fluorophores used herein (η - angle between absorption moment for $S_0 \rightarrow S_1$ and $S_0 \rightarrow S_2$ transitions, except for Alq_3, where the angles between the three absorption moments for possible $S_0 \rightarrow S_1$ transitions are given)*

	λ [nm]	Oscillator strength	x	y	z	η [degrees]
DCM	428	1.17	4.04	0.45	$-1 \cdot 10^{-4}$	38.4
	296	0.23	-0.80	-1.27	$2 \cdot 10^{-4}$	
PM605	434	0.54	2.41	1.35	0.17	
	360	0.13	-1.06	-0.6	-0.11	1.69
	341	0.037	0.29	0.54	0.2	89.9
RH640	465	0.83	3.56	0	0	90
	331	0.11	0	1.07	$-3.4 \cdot 10^{-2}$	
RH590	424	0.8	-3.35	-1.2E-3	$-4 \cdot 10^{-4}$	89.8
	317	0.17	$-4.8 \cdot 10^{-3}$	1.33	$-2.8 \cdot 10^{-2}$	
Alq_3	427	$1.66 \cdot 10^{-2}$	-0.38	0.29	$7.4 \cdot 10^{-2}$	49.7
	420	$6.14 \cdot 10^{-2}$	-0.9	-0.19	$8.7 \cdot 10^{-2}$	86.3
	412	$2.99 \cdot 10^{-2}$	$-6.7 \cdot 10^{-2}$	0.60	0.20	45.4
MD7	531	0.43	2.86	0.01	-0.44	89.9
	429	0.1	-0.008	1.26	-0.004	

C.1.4 Estimated emission cross-section

The definition of emission cross-section was subject of a long study, and finally we came to conclusion that proper expression to use is Eq.(1.20):

$$\sigma_e = \frac{\phi \lambda^4}{8\pi n^2 c \tau} \frac{f(\lambda)}{\int f(\lambda) d\lambda}$$

Table C.6 contains the estimated emission cross-section and wavelength λ_{max} at which the curve reaches its maximum as well as the values cited in the literature for used dyes.

Table C.6: *Comparison of the emission properties of the examined dyes and fluorophores. Dyes from [1]Kodak, [2]Exciton. Matrix: [3]PMMA, [4]COP(MMA-TMSPMA).*

σ_E	Estimated			Cited in literature	
	λ_{max} [nm]	τ_f [ns]	$\sigma_E(\lambda_{max})$[cm^2]	λ_{max}[nm]	$\sigma_E(\lambda_{max})$[cm^2]
DCM	607	2	$2.5 \cdot 10^{-16}$	560	$3.6 \cdot 10^{-16}$ [162] [1,3]
PM605	575	1.5	$3.45 \cdot 10^{-16}$	-	-
PM597	586	6.3	$0.85 \cdot 10^{-16}$	569	$0.5 \cdot 10^{-17}$ [112][2,4]
RH640	608	2.5	$4.2 \cdot 10^{-16}$	-	-
RH590	555	4.8	$1.45 \cdot 10^{-16}$	548	$1.6 \cdot 10^{-16}$ [162][1,3]
Alq_3	537	10	$1.15 \cdot 10^{-17}$	-	-
MD7	613	5.5	$2.2 \cdot 10^{-16}$	-	-
MD48	650	6.4	$2.3 \cdot 10^{-16}$	-	-

C.2 FRET process in examined dyes

Here we present the data on calculated RETs in examined dyes.

Table C.7: *FRET characteristics for used dyes and Alq_3-dye combinations. Dyes taken in a quantity corresponding to 5 wt% in PMMA.*

Molecule	R_0 [nm]	N [10^{20} cm^{-3}]	$< r >$ [nm]	$< r > /R_0$	E
DCM	2.5	7.8	1.1	0.44	0.99
PM605	3.6	6.3	1.2	0.33	1
RH640	3.0	4.0	1.4	0.47	0.99
PM597	3.2	6.3	1.2	0.38	1
RH590	2.2	4.4	1.3	0.59	0.96
MD7	3.5	4.2	1.3	0.37	1
MD48	3.9	4.25	1.3	0.33	1
RH590-Alq_3	2.0	9.6	1.0	0.5	0.98
RH640-Alq_3	2.8	8.8	1.05	0.38	1
DCM-Alq_3	3.4	17	0.85	0.25	1
PM605-Alq_3	3.7	14	0.90	0.24	1

C.3 Experimental values on fluorescence anisotropy

C.3.1 Guided fluorescence (in a glass substrate)

The values of the P parameter for a guided fluorescence in sample on a glass substrate are presented in Tab.C.8, and those measured in a spectrofluorimetre in Tab.C.10.

Table C.8: *Comparison of P values measured for different dyes from an edge emission configuration of guided fluorescence.*

Dye molecule	[wt%]	P_E	P_V	Dye molecule	[wt%]	P_E	P_V
PM605 (on Si)	5	-0.1	0.07	RH590	5	0.28	0.23
PM605	5	0.08	0.08	RH640	2.3	0.11	0.9
DCM	5	0.18	0.18	DCM-Alq_3	5	0.1	0.17
PM597	5	0.04	0.04	MD7	5	0.04	0.01

Table C.9: *Fluorescence anisotropy of the emission at $\gamma_0 = 40°$ (under cw pumping at 532 nm wavelength) obtained with 3-D set-up.*

Dye	Concentration [wt%]	$P_{\gamma_0}(90)$	$P_{\gamma_0}(0)$	d_H
DCM	0.5	0.4±0.1	-0.3±0.1	0.5±0.1
	5	0.4±0.1	0.1±0.1	0.8±0.1
PM605	5	0±0.1	0.2±0.1	1.5±0.1

C.3.2 Polarization ratio obtained with spectrofluorimeter

Table C.10: *P and d_H obtained for various dyes by measurements in a spectrofluorimeter. Measurement error is estimated to be about ± 0.02.*

Dye	%	532 nm			355 nm		
		P(90)	P(0)	d_H	P(90)	P(0)	d_H
DCM	0.5	0.59	-0.12	0.46	0.27	0.17	0.91
	3.47	0.36	0.1	0.76	0.23	0.20	0.97
	5	0.34	0.16	0.83	0.23	0.19	0.94
PM605	1.3	0.254	0.23	0.95	0.19	0.18	0.99
	4.3	0.251	0.24	0.95	0.2	0.19	0.99
	5	0.245	0.24	0.97	0.22	0.21	0.98
	6	0.24	0.24	0.97	-	-	-
Alq_3		-	-	-	0.26	0.18	0.92
Dcm-Alq_3	5	0.35	0.11	0.77	0.24	0.2	0.93
RH590	5	0.54	-0.08	0.5	0.08	0.33	1.32
RH640	0.9	0.36	0.09	0.75	0.19	0.24	1.05
	1.96	0.32	0.11	0.79	0.21	0.23	1.02
	3.12	0.29	0.14	0.85	-	-	-
	5	0.28	0.15	0.86	0.21	0.22	1.03
	10	0.23	0.18	0.93	-	-	-
MD7	5	0.23	0.228	0.95	0.22	0.21	0.98
	10	0.23	0.22	0.95	0.20	0.19	0.98
MD48	5	0.20	-0.15	0.49	0.21	0.20	1.00
	10	0.19	0.17	0.98	0.18	0.16	0.98

Appendix D

Fluorescence anisotropy measurements

An important place in this work was deducted to the experimental verification of the fluorescence anisotropy properties of dye molecules embedded in a polymer matrix in the thin-film configuration. The experimental arrangement itself causes a significant modification of the detected fluorescence signal. This effect surely must be taken into account.

This appendix is devoted to the explanation on the estimation of the depolarization factor in the FLIM set-up and spectrofluorimeter, which is crucial for the treatment of data, reported in Section 3.1.3.

D.1 Depolarization effect of the FLIM set-up

After breaking down the initial fluorescence signal into two orthogonal polarizations, these are made to propagate in different branches of our set-up. Precisely, the component sent to the pentaprism reaches the detector at a time delayed by $\triangle t$ with respect to the other component, as shown on Fig.D.1.a. One more unavoidable distortion introduced by the set-up affects the intensity values of the orthogonally polarized components (described by the G factor from Eq.(2.1)).

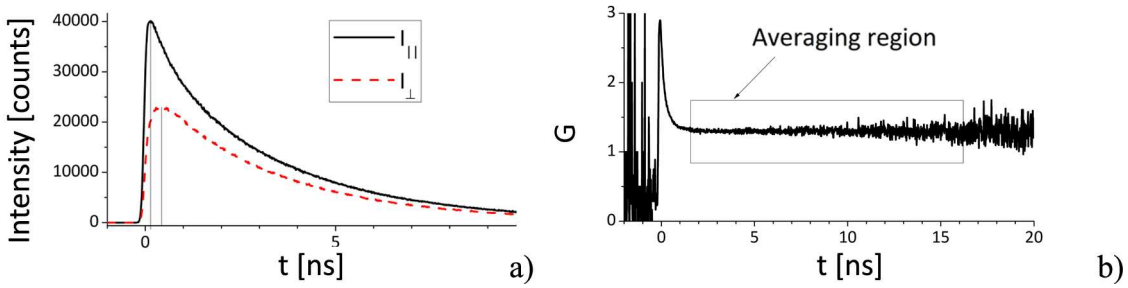

Figure D.1: *set-up-induced depolarization factor G and delay between polarized components, measured in a reference experiment with RH640 in anisole solvent: a) registered polarized components $I_{||}$ and $I_{\perp}$ (as it is seen, the maximum of $I_{\perp}$ is delayed with respect to $I_{||}$); b) the definition of G factor (delay between polarized components is taken into account).*

The G factor is not constant, but depends on the wavelength of the detected signal due to the dispersion of the dichroic mirror. A callibrating measurement should be then done for each dye prior to the experiment itself.

The delay $\triangle t$ is wavelength-dependent as well, although the variation is of the order of a few ps in the visible part of spectrum. Compared to an average value

of 160 ps and a typical fluorescence duration of a few ns, the obtained results are not influenced much in general. The exact value can be inferred from the reference measurement.

The aim of these reference measurements is to define the system response in the case of an isotropic emission with equal polarization components. It is normally made in non-viscous solution at room temperature[1], as in this case the characteristic time of rotation of dye molecules is comparable with the excited state lifetime[70, 69]. Then due to molecular rotation the fluorescence emission becomes isotropic ($I_{||} = I_{\perp}$), but the experimentally obtained fluorescence anisotropy is still not equal to zero due to residual instrumental anisotropy from the set-up itself (the G factor from formula (2.1)). This procedure allows to infer the value of the G factor:

$$G = \left(\frac{I_{||}}{I_{\perp}}\right)_{ref} \tag{D.1}$$

The delay between orthogonally polarized signals should be taken into account priory to the calculation of G factor.

Table D.1: G and $\triangle t$ deduced for various dyes from reference measurement

Dye	515 nm		343 nm	
	G	$\triangle t$ [ps]	G	$\triangle t$ [ps]
DCM	1.3 ± 0.07	182 ± 6	1.45 ± 0.07	167 ± 6
PM605	1.53 ± 0.06	150 ± 13	1.3 ± 0.07	157 ± 6
RH640	1.3 ± 0.07	156 ± 6	1.63 ± 0.08	155 ± 13

The fluorescent properties of dye molecules may vary significantly with the change of surrounding medium (Sub-section 1.1.7). As a result, the solvatochromic shift in the fluorescence of some dyes, will reflect the change in surroundings or dye concentration. So attention should be paid while applying the above described technique to samples containing solvatochromic molecules, as the large shift between the fluorescence spectra of dye in solution and polymer matrix is bound to modify significantly the G-factor.

Likewise, in the case of a given dye, the deduced r will vary with the polymer matrix. Such r value may also be quite different from the one, obtained from classical fluorescence anisotropy measurements in solution at cryogenic temperatures.

D.2 Instrumental depolarization effect from the spectrofluorimeter

The spectrofluorimeter used in the study is described in Sub-section 2.3.3. It allows to detect the polarized components of the emission, as well as excite the sample with linearly polarized light.

The factor G in this set-up is caused by wavelength-dependent response of the emission optics and detectors to polarization. The definition of G-factor proposed in the manual of the device and described in Eq.(2.3): $G = I_{HV}/I_{HH}$ is similar to Eq.(D.1) (given in previous section). The first letter in abbreviation (V or H) stands for the polarization of the excitation beam ($\alpha = 90^o$ or 0^o correspondingly), and the second - polarization of detected light (P or H correspondingly, as depicted on Fig.2.11).

[1]The reference measurement only is made in a solution, the fluorescence anisotropy is examined in a thin film

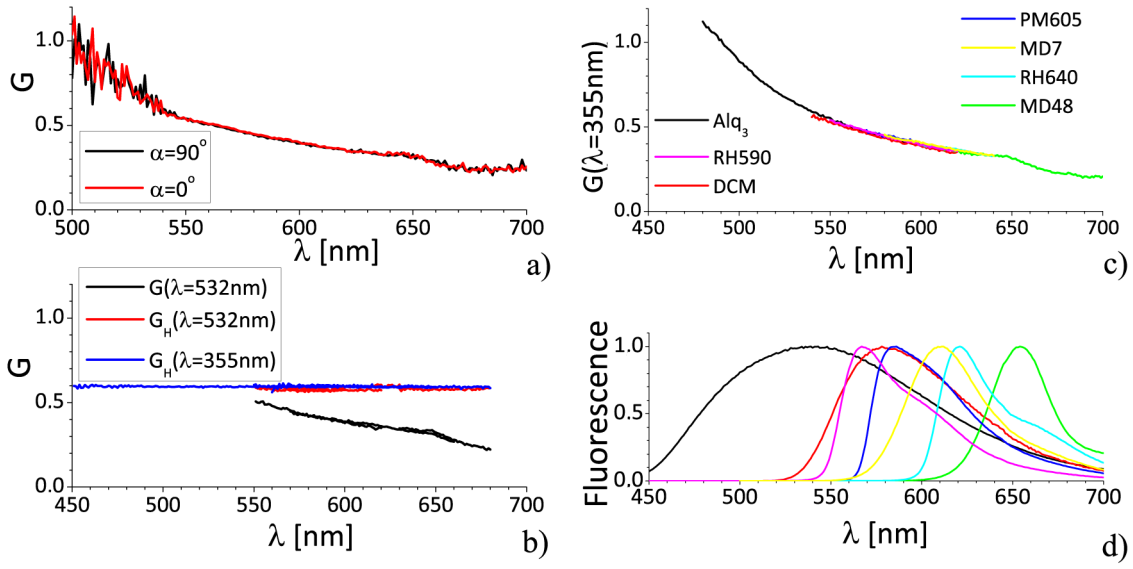

Figure D.2: *Set-up-induced depolarization factors G and G_H: a) G value for RH590 solution under pumping with different α, b) G_H values under 532 and 355 nm pumping and G (532 nm); c) illustration of the G parameter on the example of G (355 nm) as from the peak emission of the corresponding fluorescence spectra (d).*

It is based on the assumption that the emitted intensities I_P and I_H are equal. This is generally correct for measurements in a solution, then excitation with polarization $\alpha = 0^o$ or in other words incident light polarization along the measured direction, provides two equally intense orthogonally polarized components. And the registered values thus differ due to unequal response of the detecting part.

With this respect all measurements of G factor were performed in liquid solution of dye in anisole. The G is wavelength-dependent, and so must be checked for all the examined range of the wavelength. The G-factor of a dye solution, as shown on Fig.D.2.a, has a big definition error on the sides of fluorescence curve. So it should be defined at the maximum of fluorescence spectra, meaning that single measurement is inconsistent to provide the proper value of G and several dye solutions should be examined. We recorded polarized fluorescence spectra for all used dyes in order to cover their fluorescence emission band (Fig.D.2.b, d).

A low-concentration liquid dye solution and anisole as a solvent is used in the study.

In fact, the entrance polarizer which defines the polarization of the excitation beam, alters the excitation power as well. This effect was taken into account with the G_H parameter, defined from the solution as the ratio $I_H(\alpha = 0°)/I_H(\alpha = 90°)$. G_H is a constant throughout the visible spectrum and does not depend on the excitation wavelength, as proved on Fig.D.2.c.

The measured G and G_H parameters were used for the treatment of data, presented in sub-sub-section 3.1.3.4.

Appendix E

Analysis of micro-laser emission

During the PhD work several techniques were implied for the interpretation of modal properties from the spectrum, the emission diagram and the threshold. Some of these methods were actually developed from the results obtained in the thesis work. This appendix serves to clear out all the details on the interpretation of modal properties from the emission of micro-laser.

E.1 Spectrum

For the sake of simplicity, the tools we use for the spectrum analysis will be explained on the example of the most straight forward cavity shape - ribbon micro-laser (Section 5.2).

As light propagates in the optical resonator it becomes an object of interference effects. Only waves meeting in phase at the boundary point will remain. These are so-called constructive resonances, that form a spatial electromagnetic mode of resonator.

Such waves travel the same trajectory, and that the phase shift is proportional to the length of round-trip path L:

$$\begin{aligned} k_m nL &= 2\pi m \\ \triangle k &= 2\pi \frac{\triangle \lambda}{\lambda^2} \end{aligned} \tag{E.1}$$

Thereby the distance between peaks in spectrum is related to the orbit length. And the light refracted from the cavity will posses the spectral comb structure even if the light source itself is a broad-band (Fig.E.1.a).

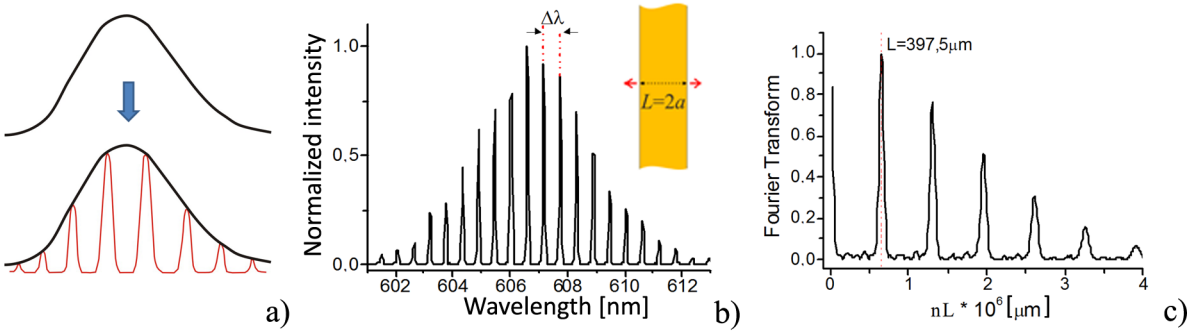

Figure E.1: *Illustration on the analysis of a micro-laser spectrum: a) resonator combs as result of constructive interferences; b) typical spectrum of planar ribbon Fabry-Perot micro-laser; c) Fourier transform of the spectrum depicted on (b).*

The micro-laser spectrum is something like a fingerprint of resonance mode on the gain curve of the active medium. The ribbon cavity supports Fabry-Perot type modes, which can be represented by light bouncing along the cavity width between two parallel walls. The light gets refracted in the same direction (as depicted on the inset in Fig.E.1.b), where we the spectrum is registered (the typical spectrum of ribbon micro-laser is shown on Fig.E.1.b).

The orbit length can be derived from the distance between peaks (combining both equations given above):

$$\triangle\lambda = \frac{\lambda^2}{nL} \tag{E.2}$$

And $\triangle\lambda$ can be directly measured in spectrum as a distance between two neighbor peaks.

Another way to define the orbit length is to perform the Fourier transform of the spectrum, as depicted on Fig.E.1.c. It is a highly advantageous method in the case of the complex spectrum structure or coexistence of several modes (when manual measurement of the distance between peaks becomes a challenge).

It is convenient to express the spectrum in wave-numbers before the transformation is applied. This way the obtained Fourier transform (FT) represents optical length units along its x-axis.

FT always contains several peaks - the optical length of each resonance round-trip nL and its harmonics mnL. The position of the maximum peak indicates the optical length of the main lasing orbit in the cavity. In case of ribbon micro-laser the first peak is maximum, but in cavities with coexisting several types of modes it is generally not the case [101].

The FT presented on Fig.E.1.c was made on the spectrum of 200 μm width ribbon laser and evidences the main orbit length is L=*397* μm, which reproduces the real value of 400 μm ($2w$) with tiny error. The error of the definition of obit length from the FT is basically defined by FWHM of corresponding peak in FT, for instance in the FT shown on Fig.E.1.c this value is $\pm$ 23 μm. The width of FT in its turn is defined by the quality of initial spectrum (resolution as well as signal to noise ratio), but also by readability of the modes superposition (in case of coexistence of several modes types).

The refractive index value used in Fourier-transform data treatment should account for dispersion:

$$n_{total} = n_{eff}\left(k_m\right) + k_m \frac{\partial n_{eff}}{\partial k}\left(k_m\right) \tag{E.3}$$

which results in about 10% increase of its value (n_{total} with respect to n_{eff})[64].

E.2 Lasing threshold

This Section is devoted to the peculiarities of the threshold analysis, performed in the present work.

A lasing threshold is generally defined as pump unity value (intensity, power, fluence, voltage etc.), characterizing the very beginning of lasing process. Lasing threshold (for example, Fig.E.2.a) constitutes the transition between two separate regions of respectively spontaneous and stimulated emission in the output power curve as well as in the emission spectrum [43].

The threshold value is generally inferred from linearization of the stimulated emission region of the output power curve.

Traditionally in the group the threshold was built by the intensity of a maximum peak in the spectrum (Fig.E.2.a left). Which is correct for a cavity with one mode type actually lasing (Fabry-Perot, square). Still, we proved during this thesis that inferring the threshold value from the curve by the total intensity in the emission spectrum allows for the decrease of the inaccuracy caused by deviations in the intensity of maximum peak (Fig.E.2.a left).

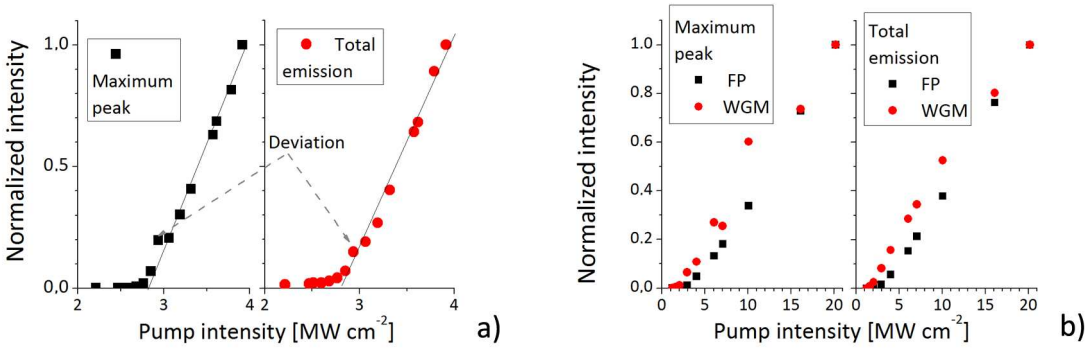

Figure E.2: *Illustration on the threshold analysis of a micro-laser emission: a) influence of the small peak intensity deviation on the threshold curve, built by maximum (left) or total (right) intensity in the spectrum of a 200 µm ribbon Fabry-Perot micro-laser; b) influence of a co-existence of different modes on the threshold curve, built by maximum (left) or total (right) intensity in the spectral region occupied by a mode.*

However the situation changes drastically in the case of the coexistence of several modes in the emission spectrum, as we witnessed in kite micro-lasers. The deviations of peak intensities especially for Whispering Gallery Modes become rather a rule (Fig.E.2.b left), and thus integration in spectrum is advised for the proper data treatment. Different modes types can be localized in spectrum by the analysis of their polarization state (see Sub-section 3.2.3).

Appendix F

FDTD simulations

The Finite-Difference Time-Domain (FDTD) method is one of the most frequently used for modeling the electromagnetic wave propagation. This is perhaps the most accurate method, as it is based on the Maxwell equations themselves. It also posses important advantages of monitoring the system response in wide frequency range at the time and observation of temporal evolution of propagating wave. The basic principle of this simulation is explained in the first part of this Appendix.

From all the available programs on FDTD simulations, we chose commercial Lumerical simulation tool. For the first trials showed its numerous advantages in our particular case of quasi 2-D resonators. The details on simulation routine are explained in second part of this Appendix.

F.1 FDTD basics

The FDTD deals with spatial disctretization of simulated region (examined object and its surroundings) and temporal discretization of wave propagating process. And it basically performs the solution of Maxwell equation for discretized components of electromagnetic field. The material properties are typically defined by the electric and magnetic permittivities. And there are no limitations on source type (initial excitation), except for it should be time-dependent.

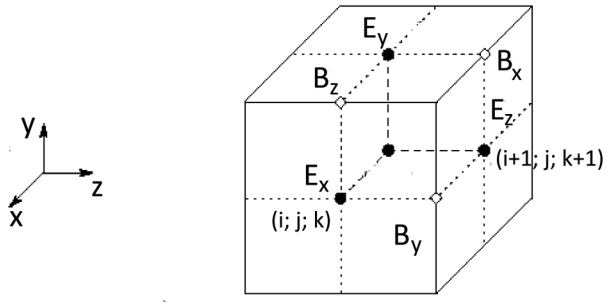

Figure F.1: *FDTD cell.*

The standard FDTD algorithm is organized as follows. The calculations are made for whole simulated region within cycles that correspond to sequent moments of time. During one cycle the Maxwell equations are solved for each point of grid and all six components of electric and magnetic fields are found in each and single point.

The simulation is numerically unstable if the spatial resolution of the grid (Δx_i) and temporal step Δt are independent and chosen in a random way. There is a criterion to fulfill for the simulation to be stable (Courant criterion):

$$\Delta t \leq \frac{1}{c\sqrt{\sum \frac{1}{\Delta x_i^2}}} \tag{F.1}$$

This method allows for calculation of the distribution of fields in the object of interest in a wide frequency range during simulated period of time. At the meantime, the natural limitations of the method origin from Cartesian discretization grid, which will distort any curved surface into a staircase one (application of a nonlinear mesh at the cavity boundary, however, decreases the meshing error).

Another useful tool commonly used in modern FDTD simulations packages: Perfectly Matched Layers (PML), which surround the simulated region. These PMLs aim to absorb all the emission reaching them, in order to prevent the back-reflections into the simulated region.

The FDTD simulations presented in this work were performed with the commercial Lumerical FDTD Solutions software.

F.2 Lumerical simulation package

We chose this software for our study as among simulation tools of this sort available in the laboratory, Lumerical allowed for simulation of an arbitrary cavity shape.

The schematic presentation of simulated region is given on Fig.F.2.a. We performed simulations of square and kite micro-cavities of various size (from 1 to 70 μm) with refractive index 1.54. Simulation region was $5\mu m$ bigger in each dimension compared to the cavity size.

Mesh parameter corresponds to the number of cells per wavelength. Its minimum value allowing for quantitative results is about 10-15, therefore the simulations for cavities with $ka > 100$ (about 1000 in our experimental samples) demand a tremendous amount of time. Calculation of a field map at a given frequency grows steeply with the cavity size: from several minutes for a 10 μm square to 8-10 hours for 120 μm (considering quasi 2-D structures, full 3-D simulations would demand much more computer time).

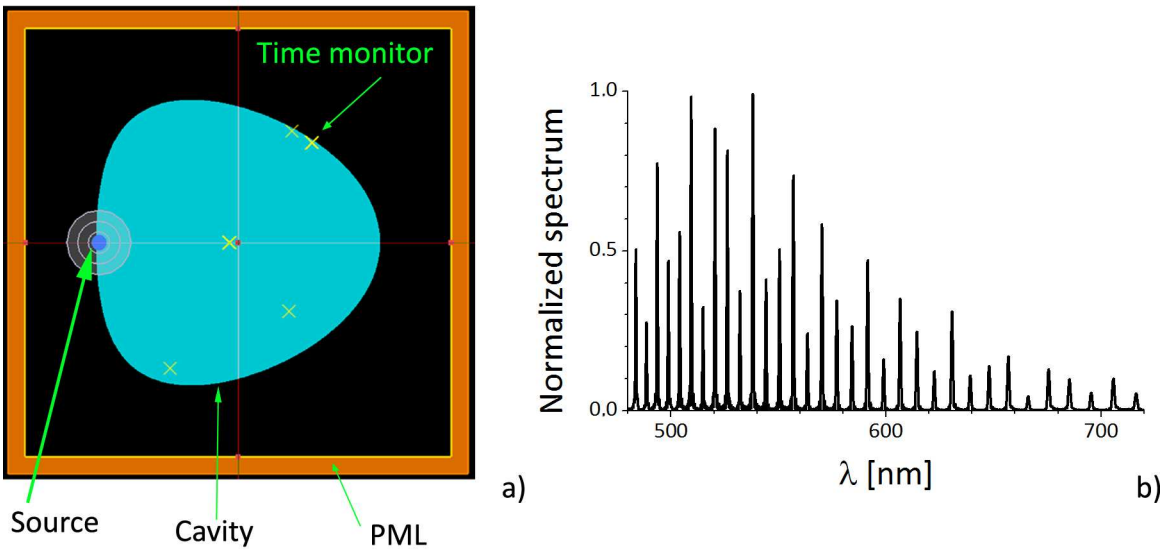

Figure F.2: *Illustration of FDTD simulations: a) visualization of the simulated region and field detectors; b) simulated spectrum for kite cavity with $r = 5\mu m$.*

In this regard all the simulations presented in this work were passive 2D simulations.

A linear dipole with a variable polarization state was used for excitation. The dipole can be oriented orthogonally to the cavity plane - in this case it is referred to as TM-polarized, or at an arbitrary angle within the plane - then referred to as TE. Source had a Gaussian-shaped temporal profile with FWHM of 3 fs, centered at 600 nm with the span of 160 nm in spectral domain.

The simulation time was chosen in order to allow for 4-5 round-trips of a mode in the cavity.

We used three types of monitors in the study: time monitor (depicted on Fig.F.2.a), 1-D and 2-D field profiles.

A time monitor records the time dependency of electric and magnetic fields ($\overrightarrow{E}(t)$ and $\overrightarrow{H}(t)$). It can be put anywhere inside the cavity, on its border and in the free space around the cavity. In our simulations we have noticed that placing the time monitor on the cavity boundary provides a more neat spectrum compared to one localized inside the cavity.

The field intensity can then be plotted, visualizing the moments of time at which mode passes through the monitor. Afterward the spectrum (as shown on Fig.F.2.b) can be obtained by applying the chirped Z-transform[1] by the software to all the filed components recorded by a monitor.

Only after calculation of the spectrum the mode profile and emission diagram can be calculated within second simulation, as those should be done for a single peak in the spectrum (detecting the the field in the frequency range centered on the peak frequency with FWHM equal to the one of the peak).

In order to obtain the emission diagram we used four 1-D field profile monitors, placed at the edge of the simulated region and PMLs. And then plotted the emission diagram from intensity values of recorded field components. The 2-D field profile monitors (rectangles with user-defined dimensions) were used to record the filed maps. Both 1-D and 2-D field profile monitors utilize a above-described Z-transform technique.

The serious drawback of the passive simulation of dielectric micro-cavities is in a high losses value (4% of light remains in the cavity at normal incidence at the border between the dielectric with a refractive index n = 1.5 and the air). For the cavities with relatively low quality factor a Z-transform technique on any chosen frequency will visualize the transient processes happening at the very beginning of simulation. The use of temporal apodization tool is then advised for simulations of dielectric cavities, allowing to minimize the influence of a source on the simulated field maps. It consists in the application of a window function to the simulated temporal field dependency prior to Z-transform. However, the temporal size of the apodization window must be chosen carefully, to include the frequency at which the field monitor is centered and avoid the overlap with neighboring peaks in spectrum.

[1] A generalization of the discrete-time Fourier transform, allows for conversion of the time domain signal to a frequency-domain one.

Appendix G

Concave kite

Here we address the emission properties of concave kite micro-lasers. The results of FDTD simulations are considered first, as they provide the theoretical basis for the analysis. The experimentally obtained emission spectra and diagrams are then discussed.

The deformation parameter $\delta = 0.5$ causes a stronger distortion away from the circular shape, resulting in lower light confinement inside the cavity and vanishing of the whispering gallery modes. The first LEP simulations in these cavities were made for small ka values (equivalent kite radius r about 0.1 μm) and show moderate WGM features, which tend to vanish as the cavity size increases up to 1 μm.

The results of FDTD simulations on a 5 μm radius cavity are depicted on Fig.G.1: the left column shows the TE-polarized component, while the right one shows TM component. The latter appears to be more confined, which is evidenced by the field pattern and more intense peaks on the emission diagram by two orders of magnitude.

The experimental emission properties were examined with 70 μm radius kites based on MD7 and MD48 dyes. Due to the high similarity of results, only spectra and emission diagrams on MD7-based cavities are reported on Fig.G.2.

The small spectral shift between the Fabry-Perot and other modes suggest much lower quality factor for such mode as compared to WGM as discussed above.

We provided numerical and experimental proof on the fact that strong distortion from the circle shape results in loss of WGM properties.

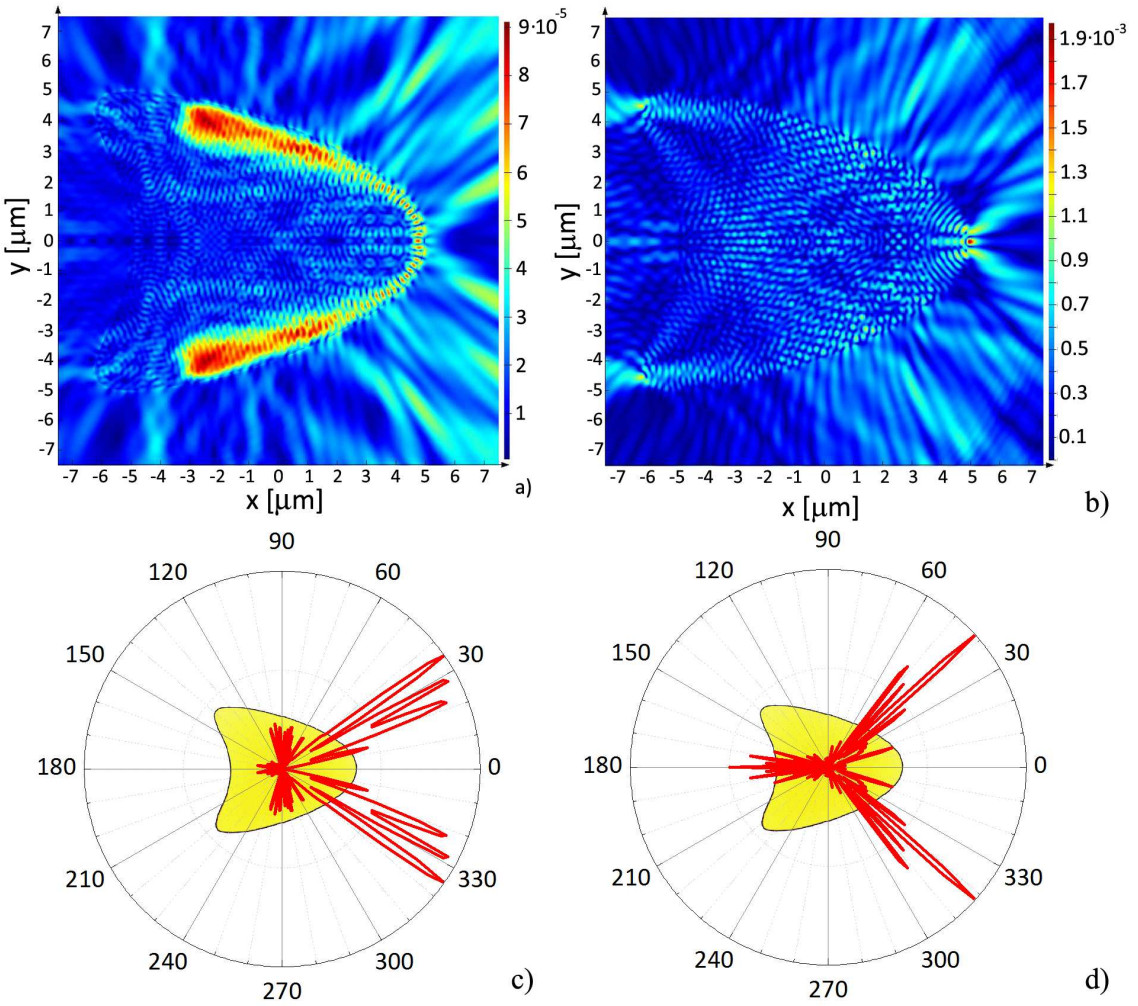

Figure G.1: *FDTD simulations on 5 μm radius kite with $\delta = 0.5$: field patterns (a,b) and emission diagrams (c,d) for TE-polarized at 611 nm (a,c) and TM-polarized emission at 614 nm (b,d).*

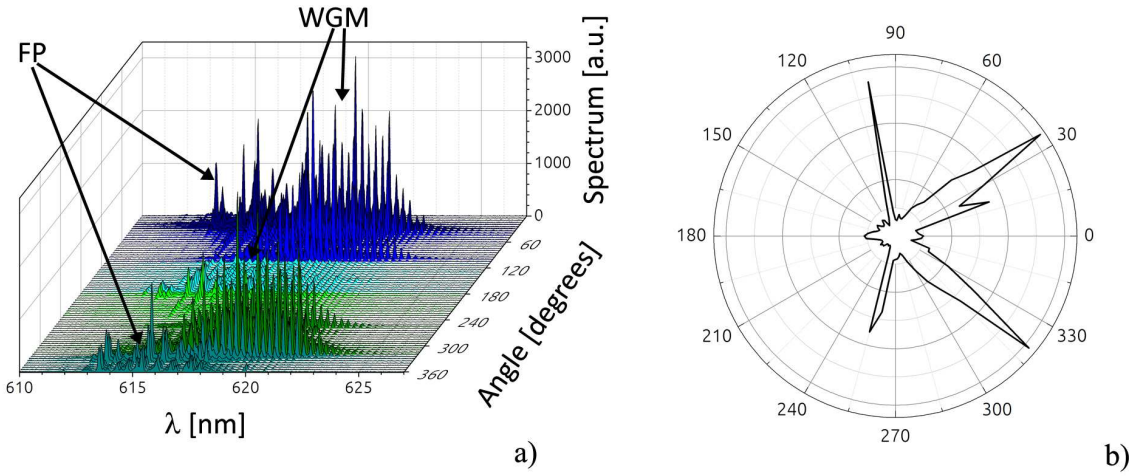

Figure G.2: *Emission properties of 70 μm radius MD7-based concave kite ($\delta = 0.5$): a) emission spectra; b) emission diagram from the full spectrum.*

Appendix H

Random lasers

Lasing from strongly scattering gain media, non-embedded into external resonator, was reported in 1990s [166, 167][1] and is widely known as *random lasing*. This effect originates from multiple scattering of gain-provided stimulated photons in the random dielectric structure, resulting in the frequency-disordered distribution of constructive resonances.

Since its discovery, random lasing has been associated with Anderson localization [169], and for this reason random media have been extensively studied during last decades. Random lasers are also advantageous for practical applications: fabrication by relatively simple and low-cost techniques (with no necessity in high-precision methods for cavity processing), use as a coating on the arbitrary-shaped surfaces [170] etc. Some recent findings on the spatial coherence of random lasers [171] suggest a high potential of the latter in speckle-free full-field imaging [172].

In this Appendix we briefly discuss the state of the art in the random laser exploration and show some experimental proofs on random lasing in our dye-doped thin polymer films.

H.1 Theoretical basis

Random laser follows the standard threshold features of a conventional laser: the passage from ASE to lasing is characterized by the intensity threshold and the reduction in the peak width from about 10 nm for ASE to sub nm lasing peak (see Tab.H.1).

Gain medium may provide the efficient feedback in a scattering system, when the light mean free path l_s exceeds the optical gain length l_g (in [cm] estimated as inverse of a gain value).

Random systems can have one of these two different feedback mechanisms:

- non-resonant (i.e. intensity feedback, light propagates through diffusion, typically corresponds to weak scattering regime; is represented by single-frequency emission spectrum [173]);
- resonant (i.e. field feedback [174], light localization happens in closed loops, where interference between counter-propagating waves is very important [173], typically corresponding to strong scattering but also possible for weak scattering).

[1] Both following the pioneering work of Letokhov [168], who discovered lasing in non-resonant feedback system made of rubidium crystal placed between a laser mirror and a scatterer.

In fact, Anderson localization can appear only in systems with strong scattering. Moreover, such strongly scattering medium is expected to meet few more necessary conditions in order to experience Anderson localization.

Firstly, a random medium must match the (modified) Ioffe-Regel criterion [167]:

$$kl_s < 1 \tag{H.1}$$

where k is the light wave-vector, meaning the electric field can not perform a complete single oscillation between two scattering events. For instance, light-emitting polymers are far from fitting this condition as $l_s \gg \lambda$, while semiconductor powders are rather good candidates.

Secondly, as Anderson localizations influence inevitably the transmission properties: the transmission coefficient should decrease exponentially with the sample thickness (instead of linear Beer–Lambert–Bouguer law $\ln T = -L/L_o$ for non-localized state [167]).

Finally, laser effect in strongly scattering random medium is not by itself a proof of Anderson localization. Extensive study of the various random media revealed several mechanisms apart from the Anderson localization, that can cause the lasing effect in such systems, for instance the random resonators created by random fluctuations of the refractive index.

H.2 Problems

In spite of numerous proofs of random lasing in various materials (fine powders [175], translucent ceramics [176], polymer films [177], porous materials [178] and colloidal solutions of nano-particles [179], dye-doped micro-porous glass [180]; small summary on their properties is given in Tab.H.1), the deeper physical mechanisms standing beyond this phenomenon are still argued in the community:

1) presence of Anderson localization in strongly scattering samples (in 2D and 3D cases is doubted by some authors [173]);

2) nature of the photonic states in random lasers: are they created within passive dielectric random system or shaped by the gain [181]? Indeed, the extend of lasing modes in the sample is naturally reduced by the reabsorption of the emission in the unpumped regions.

3) narrow peaks in the emission spectrum [182]: do they correspond to specific spatially localized resonators (localized modes [183]) or delocalized resonance covering a large volume of sample (extended modes [180]), or even the coexistence of both localized and extended modes as claimed in [184]? [2]

[2]Experimental technique adopted in [184] consisted of the excitation of the whole sample combined with local probing.

*Table H.1: Features of random lasing in various materials. $\Delta\lambda$ stands for the peak full-width, P_{th} - the excitation intensity threshold, PF - power fluctuations, LM - localized modes, EM- extended modes. N/p indicates that information was not provided in the cited article. *Fourier transform of spectrum provided and is periodic. ** Strong localization mentioned.*

Medium	Ref.	$\Delta\lambda$ [nm]	P_{th} [$MWcm^{-2}$]	Resonances	PF
DOO-PPV*	[185]	0.2	≈ 0.6	LM	-
Colloidal solutions of nano-particles	[179]	0.12	≈ 0.06	LM	+
Nanocrystalline ZnO powder**	[184]	n/p	2	LM+EM	+
	[186]	0.3	≈ 0.7	n/p	n/p
ZnCdO/ZnO QD fine powders	[187]	0.1	≈ 0.06	n/p	+
$Nd_{0.5}La_{0.5}Al_3(BO_3)_4$ ceramic	[176]	n/p	≈ 20	LM	n/p
Porous gallium phosphide with methanol-RH640 solution	[178]	0.1	≈ 0.55	more LM	+
Porous glass with methanol-RH590 solution	[180]	0.2	610	EM	+

Thereby, complete understanding of the random lasing phenomenon demands an extensive study of these three problems.

H.3 Experimental results

Random lasing was demonstrated in π-conjugated light-emitting polymers (for example DOO-PPV [185]) and dye-doped porous materials ([178, 180] see Tab.H.1). Consequently, it is probable to achieve random lasing in dye-doped thin polymer films, which actually has already been witnessed by our group [64]. In current thesis work we addressed some basic features of random lasing in dye-doped polymer layers.

The samples used in this study were our standard thin dye-doped PMMA films deposited according to the protocol described in Appendix A.3 on the silicon wafer (with 2 μm SiO_2 layer). Since no cavity is necessary for random laser experiment, lithography was not applied. Moreover, in order to prevent the influence of polymer access along the sample edge (caused by spun-coating), we applied cleaving technique described in Appendix A.6. DCM and RH640 dyes of 5 wt% concentration were examined (still, random lasing was systematically achieved in standard ASE measurements for $>$ 3 wt% of DCM and $>$ 2 wt% of RH640).

The experimental configuration was similar to ASE measurements described in Sub-section 5.1.4: a dye-doped polymer layer was placed on our 2-D detection setup (Sub-section 2.2.1), pumped at 532 nm with approximately 200 μm in diameter Gaussian beam, while lateral emission in the direction orthogonal to the sample edge was analyzed with a CCD camera. But this time pumping was applied at variable distance (from several mm to several cm) from the sample side.

A typical lasing spectrum of our polymer layer is shown on Fig.H.1.a. It has an arbitrary shape, while presence of several peaks suggests a coherent feedback. Fourier transform of such spectrum (depicted on Fig.H.1.b) has rather complex structure (which by the way differs from the Fourier transform reported in [185] for light-emitting polymers). However, if the pumping was applied in the vicinity (several mm) of the previously pumped area, emission spectrum appeared to be

more structured (see Fig.H.1.c). The latter may be a result of the local effect of the pumping or emitted photons on the random medium.

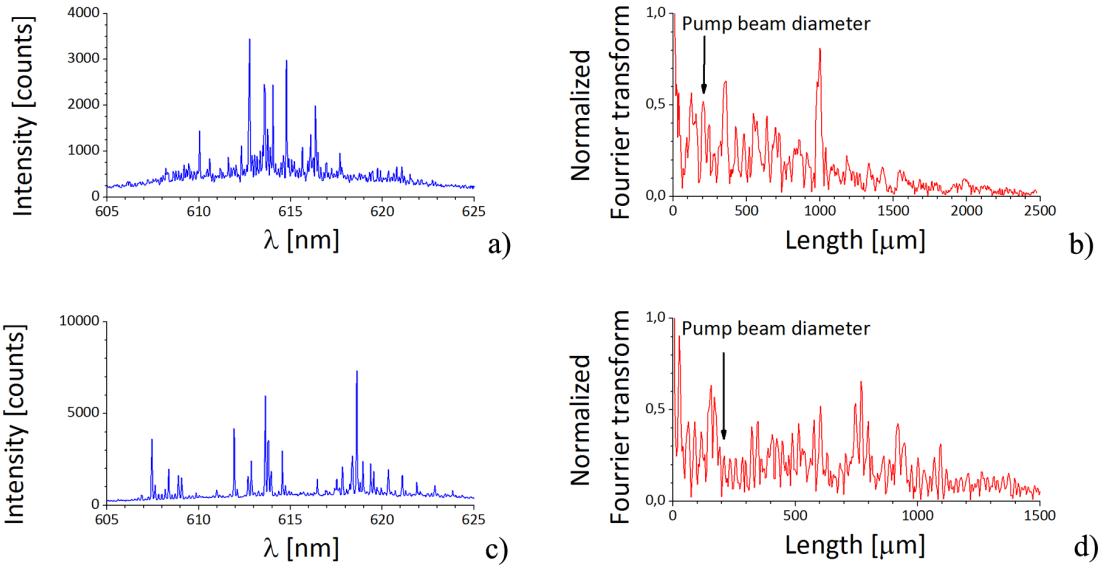

Figure H.1: *Random lasing in PMMA thin film doped with 5 wt% of DCM: a),c) emission spectra; b,d) their Fourrier transform. Measurements were taken at two different pumping points (a,b) and (c,d), where the second point (c,d) was found in close vicinity of previously pumped region.*

Random laser in our system exhibits a threshold behavior in the intensity threshold (see Fig. H.2.a) and reduction in the peak width from about 20 nm for ASE to about 0.05 nm lasing peak (for example Fig.H.4.b), thus following the features of random lasing stated for other media (see Tab.H.1).

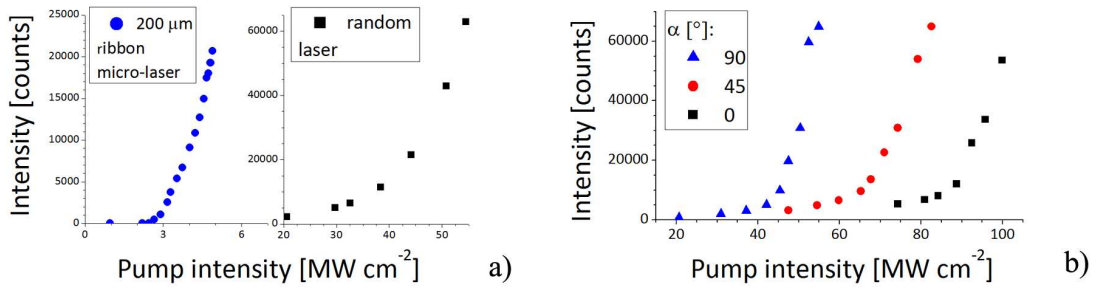

Figure H.2: *Threshold curves of the random laser in thin PMMA film doped with 5 wt% of dye: a) DCM; b) RH640. (a) random laser threshold versus 200 μm large ribbon micro-laser, both had pump beam polarization a orthogonal to the emission direction (a = 90°). (b) influence of the pump beam polarization a on the random laser threshold for RH640-based sample. These curves were built from 3 s integration spectra.*

In the DCM-based samples, random laser was never achieved with pump beam polarization parallel to the emission direction ($\alpha = 0°$). However, the pump intensity was first kept below 80 MW cm^{-2} for DCM dye, which does not compensate for factor of about 3 in K reduction under $\alpha = 0°$ pumping (Sub-section5.2.4). We then examined emission spectra for wider range of pump intensities for both DCM and RH640-based samples (for RH640 the pump beam polarization has smaller effect on K factor - about 2). There was still no lasing from DCM-based sample, while for Rh640 we achieved about 2 times higher threshold under $\alpha = 0°$ pump

beam polarization compared to $\alpha = 90°$ (see Fig.H.2.b).

We have also occasionally witnessed an interesting evolution of the emission spectra in our system under constant pumping intensity (example depicted on Fig.H.3): at relatively low pumping intensities random lasing appeared only after several pump pulses, while intensity emitted by this random laser reached its maximum in several tenth of pump pulses.

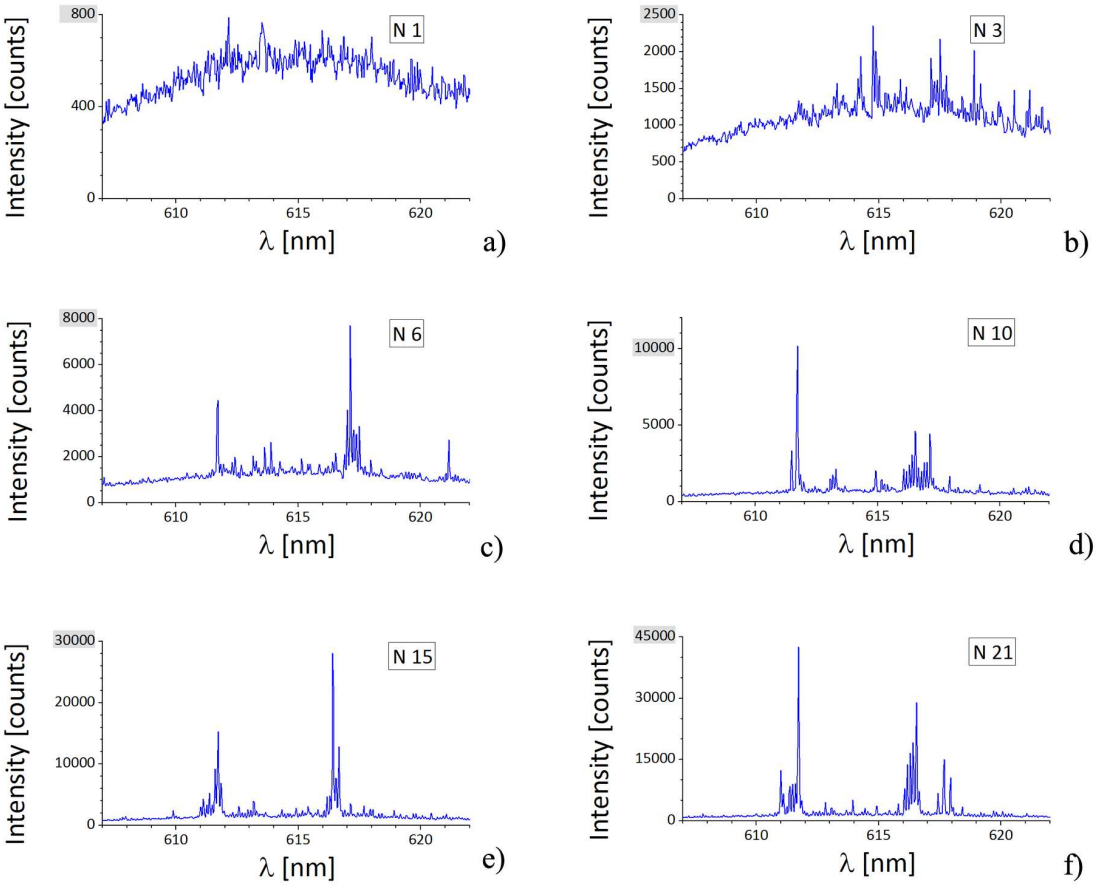

Figure H.3: *Emission spectra from the same measurement serie. Each spectrum was accumulated during 0.1 s (a single pump pulse used for excitation) under the fixed pump intensity of 68 MWcm^{-2}. Spectrum number: a) 1; b) 3; c) 6; d) 10; e) 15; f) 21. Measurement performed in the PMMA thin film doped with 5 wt% of DCM.*

In contrast to the light-emitting polymers [185], the random lasing spectra in the dye-doped polymer is a subject of strong fluctuations. For instance, several consequently taken spectra accumulated during a single pump pulse under a fixed pump intensity level exhibit strong arbitrary intensity variation (as depicted on Fig.H.4.a). Still the positions of peaks remain static (as depicted on Fig.H.4.b).

However, the variation of the pump intensity results in the displacement of some peaks in the emission spectrum, as evidenced by Fig.H.5.

Finally, spectra obtained at two different pumping points have non-similar envelopes, and both wavelength matching and mismatching peaks (see Fig. H.6).

We also examined the polarization state of random laser for DCM-based sample, and as depicted on Fig. H.7 it is TE-polarized.

As for future prospects, the 3-D emission pattern of random lasing in our dye-doped polymer films should be addressed. The role of the polymer matrix should be examined with both variation of the gain material as well as incorporation of scatterers into the polymer matrix (for instance silica nano-particles). Finally, influence of the pump beam polarization on the random laser threshold should

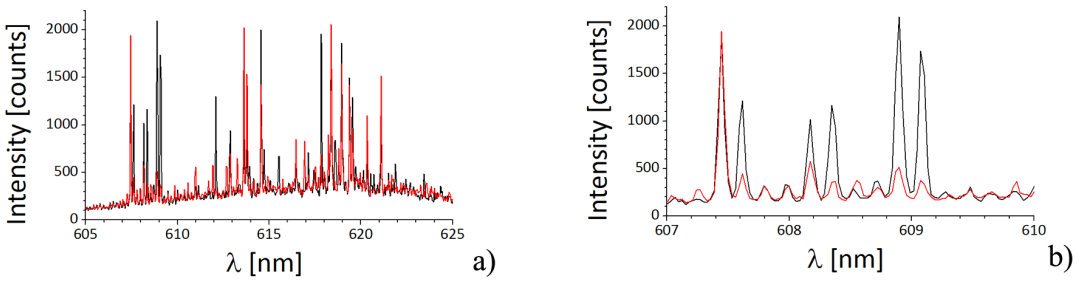

Figure H.4: *Fluctuations in the emission spectrum under fixed pump intensity level (95 MWcm^{-2}): a) whole spectrum; b) spectrum in the narrow wavelength range for better visualization. These are emission spectra accumulated during 0.1 s (a single pump pulse used for excitation) taken at the same pumping point.*

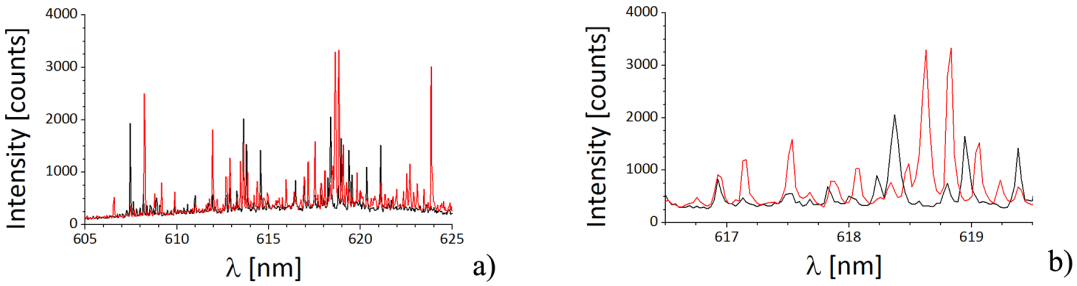

Figure H.5: *Fluctuations in the emission spectrum with the pump intensity variation: a) whole spectrum; b) spectrum in the narrow wavelength range for better visualization. These are emission spectra accumulated during 0.1 s (a single pump pulse used for excitation) taken at the same pumping point. Pump intensities applied are 95 MWcm^{-2} for spectrum presented in black and 110 MWcm^{-2} for spectrum presented in red.*

be studied more thoroughly and theoretical model on threshold fluctuations [188] should be verified.

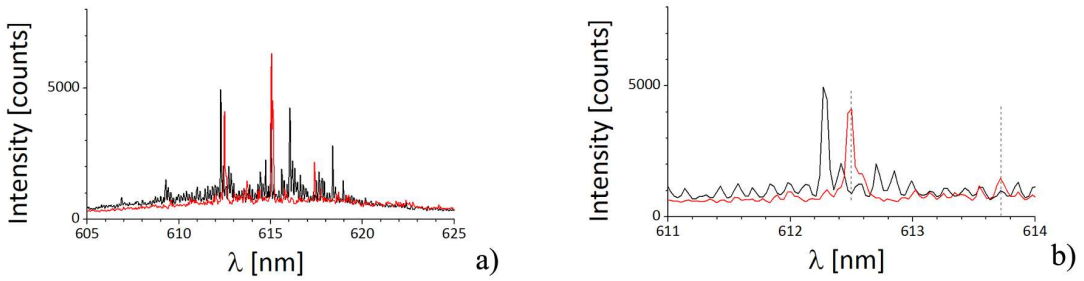

Figure H.6: *Fluctuations in the emission spectrum with variation of the pumping point location: a) whole spectrum; b) spectrum in the narrow wavelength range for better visualization. These are emission spectra accumulated during 0.1 s (a single pump pulse used for excitation) taken in two different pumping points at the pump intensity of 73 MWcm^{-2}.*

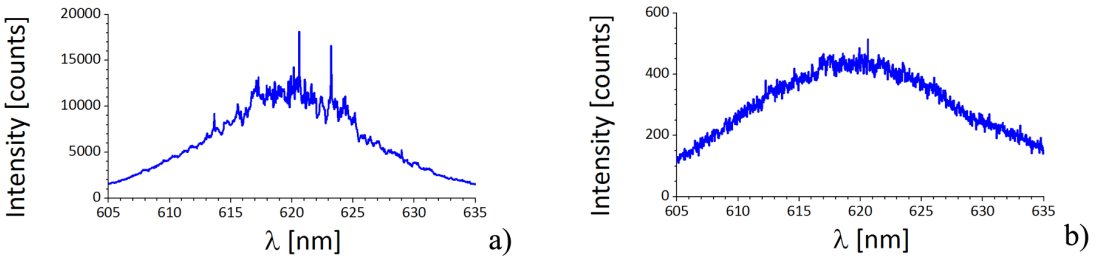

Figure H.7: *Polarized emission spectrum (integrated over 3 s): a) TE polarization (in the sample plane); b) TM polarization - ASE only (orthogonal to the sample plane). Measurement performed in the PMMA thin film doped with 5 wt% of DCM.*

Appendix I

Coupled micro-lasers

This appendix details the experimental study we performed on two micro-lasers spaced by a sub-micron air-gap (example of two square micro-resonators is shown on Fig.I.1). The results presented here were obtained by two internship students Salim ZERKANI (whom I co-supervised together with Clement LAFARGUE) and Viktor TSVIRKUN. The samples used in experiments were 5 wt% PMMA-DCM fabricated by the electron-beam lithography at LPN by Christian ULYSSE.

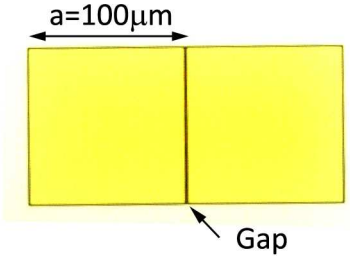

Figure I.1: *Optical microscope photo of the couple of closely spaced 100µm PMMA-DCM square micro-lasers.*

I.1 Motivation

Coupled-cavity lasers began to be intensively studied in 1970s in the context of stabilization of laser emission and coupled-mode theory for coupled-cavity lasers was developed for semiconductor lasers [189].

Recent developments in the filed of dielectric micro-resonators allowed for design of novel sensors and all-optical signal processing devices. In this regard research activities of numerous groups were focused on coupling between optical resonators of various shapes (micro-disks [190], micro-rings [191], micro-toroids[192], micro-spheres[193]) with resonators and waveguides and also coupled resonators optical waveguides (CROWs [194]).

Majority of publications on this subject deals with at least partially passive structures, while near-field coupling of micro-lasers stays much less explored. Moreover, coupled micro-lasers are expected have specific properties of their own [195], which is the reason we conducted experiments described in this Appendix.

I.2 Experiment description

Aiming to study the coupling effects, we designed two types of experiment:

- both cavities pumped at the same time, hereafter referred as the *symmetric*

pumping geometry (pumping beam centered with the symmetry center of the system as depicted on Fig.I.2) ;

- one cavity is fully-pumped while another only partially, hereafter referred as the *non-symmetric pumping geometry* (depicted on Fig.I.3).

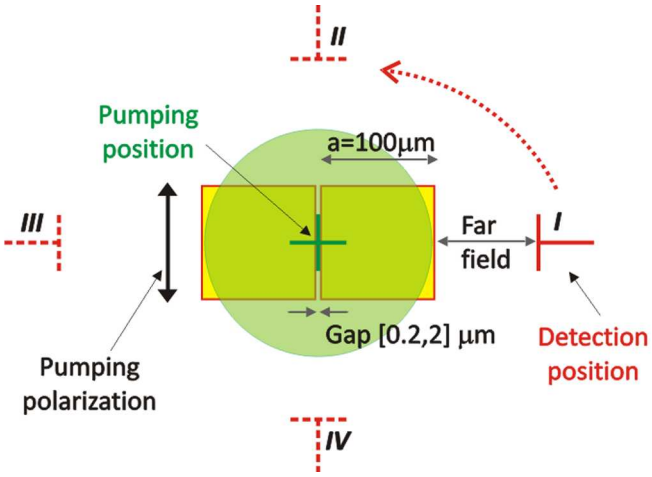

Figure I.2: *Scheme on the symmetric pumping configuration. Pumping beam is centered with the symmetry center of the system, while the detection in the far field is performed in the sample plane at several angular positions depicted by I, II, III and IV. Pumping beam dimensions are realistic.*

In both pumping geometries the detection was performed with the 2-D setup (see Sub-section 2.2.1) in the far field at several angles (mostly at directions I and III shown on Fig.I.2) if not the whole circumference. The pump beam polarization was mainly linear oriented along ($\alpha = 0^o$) or orthogonally ($\alpha = 90^o$) with respect to the emission direction, while several tests with circularly polarized pump beam were performed as well.

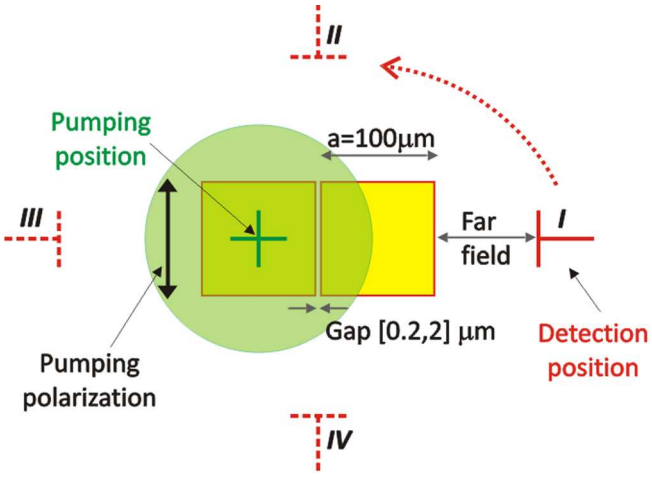

Figure I.3: *Scheme on the non-symmetric pumping configuration. Pumping beam is centered with the symmetry center of the system, while the detection in the far field is performed in the sample plane at several angular positions depicted by I, II, III and IV. Pumping beam dimensions are realistic.*

Close spacing between cavities may result in coupling between cavities, but it surely creates interference effects. The emission pattern is modified in both cases. Thus the interference may be mistakenly taken as the proof of coupling. In order to distinguish the role of each resonator in the system and reveal the coupling

effects if such are present, we applied the symmetric and non-symmetric pumping schemes.

I.3 Two squares

System of two closely placed square micro-resonators has specific spectral and intensity properties, which are presented in this Section.

I.3.1 Spectral properties

As was mentioned in Sub-section 6.1.1, we have never experimentally observed a Fabry-Perot periodic orbit in the electron-beam fabricated DCM-doped square micro-lasers. Only diamond periodic orbit was present in the Fourier-transform of such spectra.

However, Fabry-Perot periodic orbit appears in the emission spectra of two closely placed squares. Indeed, spectra along *I* and *III* emission directions (see Fig.I.3) always contain diamond periodic orbit[1] independently on the pumping configuration and polarization of the pump beam. As for Fabry-Perot periodic orbit it was noticed under specific pumping beam polarization conditions (circular polarization and some orientations of linear $\alpha = 90^o$, $\alpha = 45^o$ but not $\alpha = 0^o$).

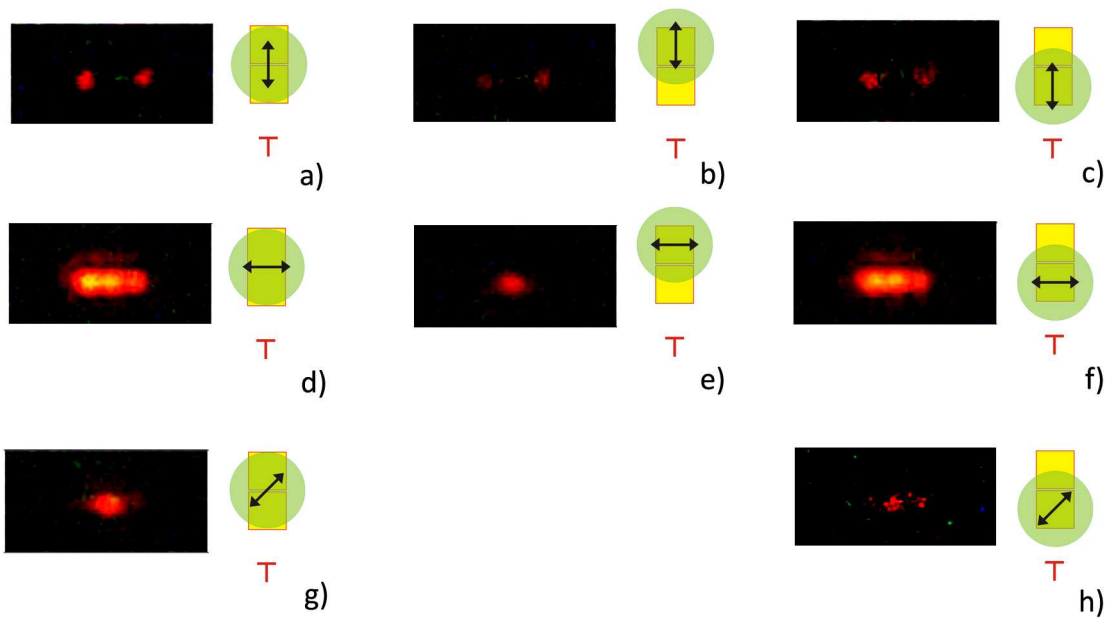

Figure I.4: *Slightly oblique observation of light emission from a system of closely-placed square-shaped micro-lasers (1 μm gap) for various orientations of pumping beam polarization (with no sample illumination): a), b), c) $\alpha = 0^o$; d), e), f) $\alpha = 90^o$; g), h) $\alpha = 45^o$. Both symmetric (a, d, g) and non-symmetric pumping geometries applied (b, c, e, f, h). Pumping beam intensity was 50 MWcm^{-2}.*

We experimentally observed light out-coupling from the system of two square micro-lasers under various pump polarization conditions (with CCD camera, following the routine explained Sub-section 6.1.4). The results are presented on Fig.I.4. Similar study on single rectangle micro-lasers (see Sub-section 6.1.4) proved that emission representing different periodic orbits may be out-coupled from different parts of the cavity: at the corners (diamond) or at the cavity side

[1]Except for the small gap when threshold of emission corresponding to the diamond orbit is higher compared to Fabry-Perot one.

(Fabry-Perot). In the case of two closely placed cavities we can distinguish the diamond periodic orbit (Fig.I.4.a-c, pumping beam polarized along the emission direction), the Fabry-Perot (Fig.I.4.e,g) and their combination (Fig.I.4.d,f,h). Still, obtained information is insufficient to localize the cavity responsible for observed emission.

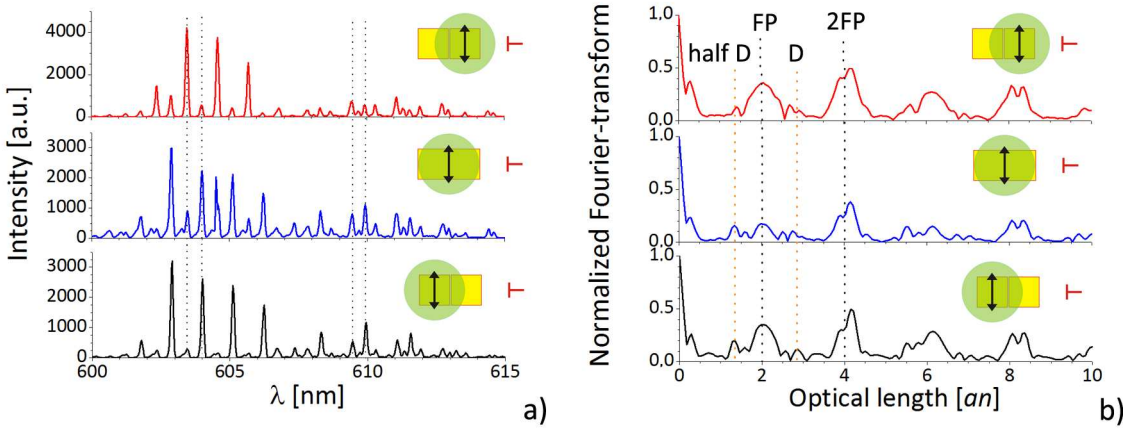

Figure I.5: *Emission of the system of two closely placed micro-lasers (1 μm gap) with excitation geometry varied (indicated by the scheme next to each plot): a) emission spectra; b) normalized Fourier-transform (lengths of periodic orbits are indicated with FP and D: Fabry-Perot FP = 2an; diamond D = $2\sqrt{2}an$). Excitation was made with the intensity of 38.5 MWcm^{-2} with polarization orthogonal to the emission direction ($\alpha = 90^o$).*

In order to explore this question further, we studied the emission spectra at various excitation geometries (see Fig.I.5). In all three cases (one symmetric and two non-symmetric excitations) the emission contains two types of periodic orbits (Fig.I.5.b): diamond (with optical length $2an\sqrt{2}$, thus corresponding to a single cavity) and Fabry-Perot (with optical length $2an$ for a single square and $4an$ - its harmonic or Fabry-Perot in rectangle formed by two squares). Each spectrum (Fig.I.5.a) contains two clearly different spectral regions, which are shown below to correspond to the Fabry-Perot ($\lambda < 607$ nm) and the diamond ($\lambda > 607$ nm) periodic orbits. These spectral regions contain superposition of combs, which in the case of symmetric pump geometry have about equal amplitudes (middle spectrum on Fig.I.5.a), and non-equal if pump geometry is non-symmetric. Vertical dashed lines on this figure allow to see that choice of pumped cavity in the non-symmetric pumping geometry (upper and lower spectra) favors one of the two combs in each spectral region.

As such combs may represent the emission coming from different cavities, the obvious question is how this emission is excited: directly by the pump or through the coupling from neighbor cavity. We decided to shift the center of the pump beam in non-symmetric pump geometry in a way to excite only one cavity and compare results with the previous case (see Fig.I.6). There is always one Fabry-Perot comb but it is impossible to say if it corresponds to the pumped or unpumped cavity.

Thereby, center of the pump beam in non-symmetric pump geometry was farther shifted away from system center (see Fig.I.7). The beam size on the graph corresponds to FWHM of the beam profile. Thus experiments with non-symmetric excitation presented on upper and lower plots on Fig.I.7 are single-cavity pumping. No Fabry-Perot periodic orbit observed in this case, although taking into account non-homogeneous pumping, the reason may be in excitation below threshold of the Fabry-Perot.

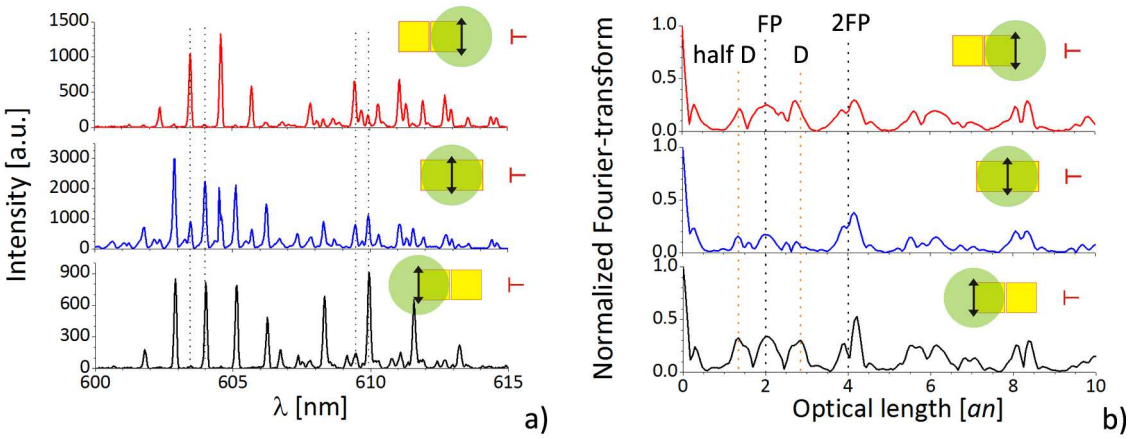

Figure I.6: *Emission of the system of two closely placed micro-lasers (1 μm gap) with excitation geometry varied (indicated by the scheme next to each plot): a) emission spectra; b) normalized Fourier-transform (lengths of periodic orbits are indicated with FP and D: Fabry-Perot FP = 2an; diamond D = $2\sqrt{2}an$). Excitation was made with the intensity of 38.5 MWcm^{-2} with polarization orthogonal to the emission direction ($\alpha = 90^o$).*

Still this experiment is highly informative for the spectral properties of modes corresponding to different periodic orbits: the Fabry-Perot one lays in region $\lambda <$ 607 nm while thee diamond in $\lambda >$ 607 nm, meaning Fabry-Perot is shifted towards lower wavelength in the above-discussed example. However it is not always the case, as it was in fact opposite in some experiments (superposed Fabry-Perot and diamond spectra were also observed). There are several factors that may influence relative spectral position of the emission of different periodic orbits: sample aging, local fabrication defects, alignment problems or the gap size influence.

Summarizing the analysis of spectral properties, there are at least two possible explanations of presence of the Fabry-Perot periodic orbit in case of two closely placed cavities:

- presence of the second cavity modifies the reflection coefficient on the cavity border next to it and thus influences the threshold of Fabry-Perot;
- Fabry-Perot occurs in one cavity as a result of coupling of the emission from the second cavity.

I.3.2 Intensity effects

First series of experiments on non-symmetric pumping configuration gave rather curious results on the intensity emitted along the *I* and *III* directions. It seemed that the ratio of intensities registered *I* and *III* was gap-dependent: $I(III) < I(I)$ for 0.2-0.3 μm gaps and $I(III) > I(I)$ for 1 and 2 μm gap. However these results were not reproduced in following experimental series, which suggests either sample aging effects or the misalignment during first tests.

On the other hand, lasing threshold is the most reliable among intensity parameters. Thereby we focused our attention on threshold curves. The results of this study are presented in Fig.I.8 and Tab.I.1. Variation of the Fabry-Perot threshold with the excitation geometry is small compared to measurement error, which is not always the case for the diamond. Meanwhile we observe a clear dependance of the Fabry-Perot threshold on the gap size: in case if gap is small (0.2 μm) Fabry-Perot starts lasing before the diamond, while it's the opposite for big gaps (1 μm, see

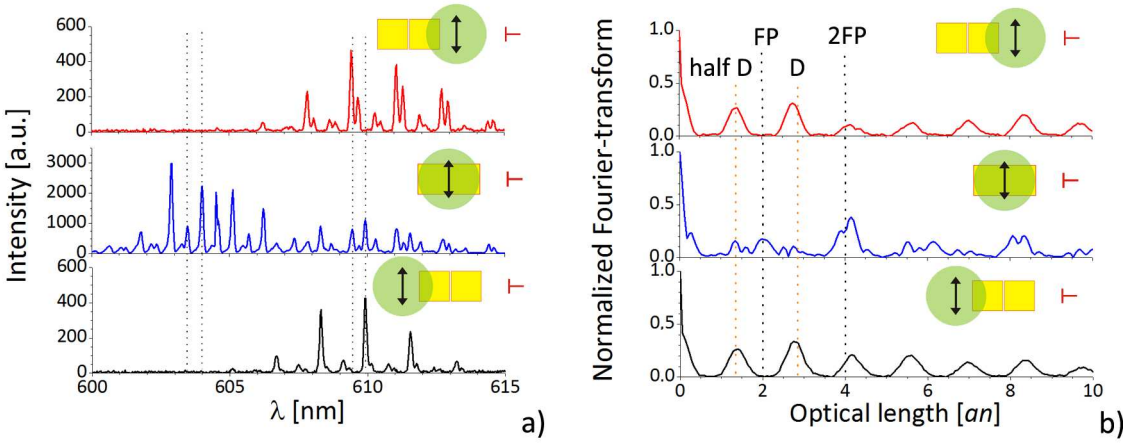

Figure I.7: *Emission of the system of two closely placed micro-lasers (1 μm gap) with excitation geometry varied (indicated by the scheme next to each plot): a) emission spectra; b) normalized Fourier-transform (lengths of periodic orbits are indicated with FP and D: Fabry-Perot FP = 2an; diamond D = $2\sqrt{2}an$). Excitation was made with the intensity of 38.5 MWcm^{-2} with polarization orthogonal to the emission direction ($\alpha = 90^o$).*

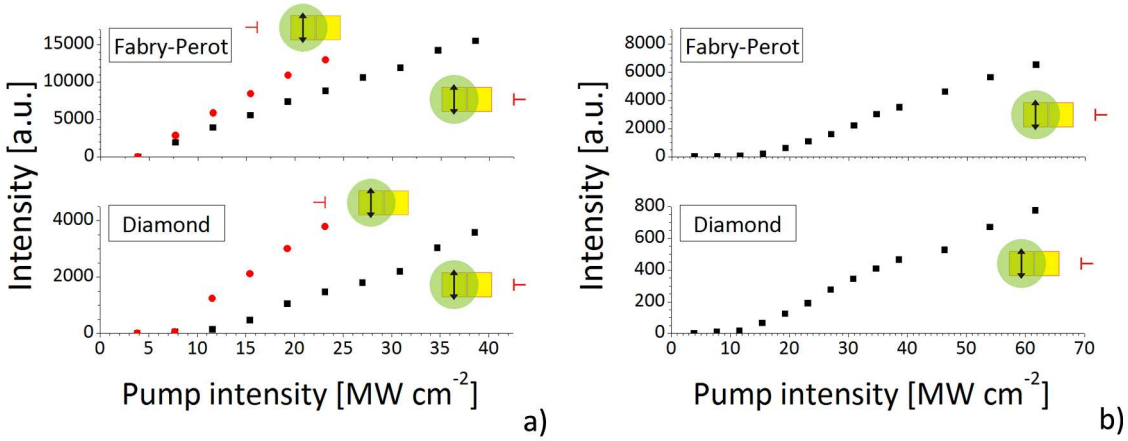

Figure I.8: *Lasing thresholds curves of Fabry-Perot and diamond modes in a system of two closely placed square micro-lasers for various gap sizes: a) 0.2 μm; b) 1 μm. Excitation geometry is indicated by the scheme next to each plot.*

Fig.I.8 and Tab.I.1). Several threshold graphs obtained on the very beginning of the study exhibited the change in linear behavior of the emitted intensity exactly at the threshold of the other mode, suggesting that modes share the same gain medium. However, this result should be confirmed by a test experiment with a new sample and thorough attention payed to the alignment.

Table I.1: Lasing thresholds of Fabry-Perot and diamond modes in a system of two closely placed square micro-lasers for various gap sizes, pump beam polarizations orientations and emission directions I and III (see Fig.I.3). Measurements were performed in non-symmetric pump beam configuration.

Gap [μm]	Polarization	Fabry-Perot		Diamond	
		Threshold [MWcm^{-2}]			
		I	*III*	*I*	*III*
0.2	$\alpha = 90^o$	2.9	3	12	6
0.3	$\alpha = 0^o$	-	-	9	9
	$\alpha = 90^o$	8	9	-	-
	Circular	14	17	9	10
1	$\alpha = 0^o$		-	13	9
	$\alpha = 90^o$	14	15	-	-
	Circular	15	-	10	-

Finally, we examined the emission diagrams using symmetric pump beam geometry and circular polarization (see Fig. I.9). The directionality of emission in a system of two closely placed squares depends on the size of gap between cavities: the main emission direction follows the cavities line in the case of sub-micron gap (0.3μm, Fig. I.9.a) or the system mirror-axis for micron-order gap (1μm, Fig. I.9.b). Moreover, emission diagram of the system with 1μm gap is similar to the one of a 2:1 rectangle micro-laser. In fact, the variation of the emission pattern with the gap size is caused by the change of the first lasing mode from diamond to Fabry-Perot with the decrease of the gap size.

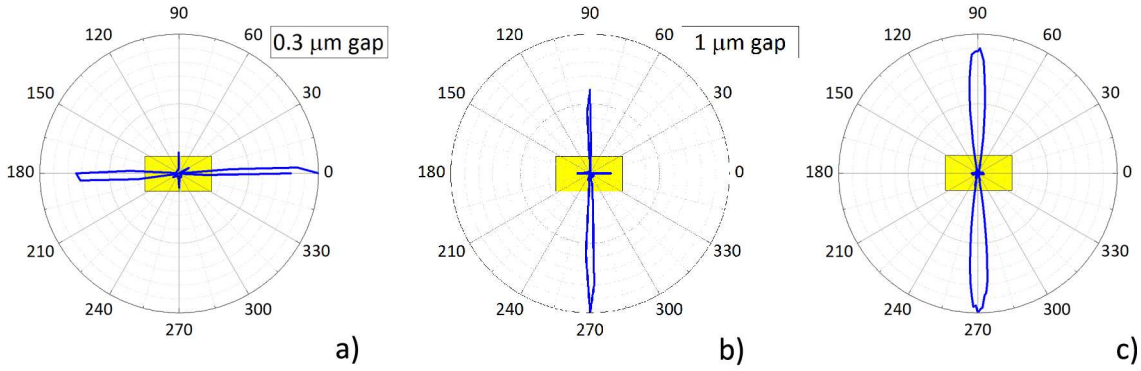

Figure I.9: *Emission diagrams obtained under circular pumping beam polarization: a) couple of squares with 0.3μm gap; b) couple of squares with 1μm gap; c) rectangle 2:1. Diagrams represent integration of the whole emission spectrum.*

We demonstrated the change in the emission properties of square micro-laser in the presence of another cavity in close vicinity. However, analysis of the emission properties as well as recognition of the emitting cavity is complicated by the symmetry of the system (as two cavities are identical). In this regard, several tests were made on the system of closely placed square and rectangle.

I.4 Square and rectangle

System of 100μm-side square and 100μm*xμm rectangle (two different sizes 100μm*120μm and 100μm*170μm) we examined with non-symmetric excitation geometry (Fig.I.3).

Let us start with 100μm*120μm rectangle. Experiment was done with non-symmetric excitation of the system with varied linear pump beam polarization

(Fig.I.10). First the square was pumped (Fig.I.10.a,b), and due to the pump beam size caused also some partial pumping of the rectangle. In order to distinguish the role of each cavity, equivalent experiment with partial excitation of rectangle from another side was performed (Fig.I.10.c,d). This allowed to preserve the experimental conditions (beam size and observation direction) and leave the square non-pumped.

Periodic orbits found in each emission spectra on Fig.I.10 are summarized in Tab.I.2. In fact, partial excitation of rectangle independently on the pump beam polarization results in excitation of the Fabry-Perot in square (Fig.I.10.d). As the square cavity was non-pumped even partially, such emission should originate from interaction between cavities through the gap.

Comparison of the square-rectangle and rectangle excitation under $\alpha = 90^o$ pumping beam polarization, suggests the similar effect of excitation of the Fabry-Perot in rectangle through the square. Strictly speaking comparison of spectra excited with different pumping beam polarizations is not correct at the current stage of the study. This demands a thorough study of the impact of pumping beam polarization on thresholds of different modes.

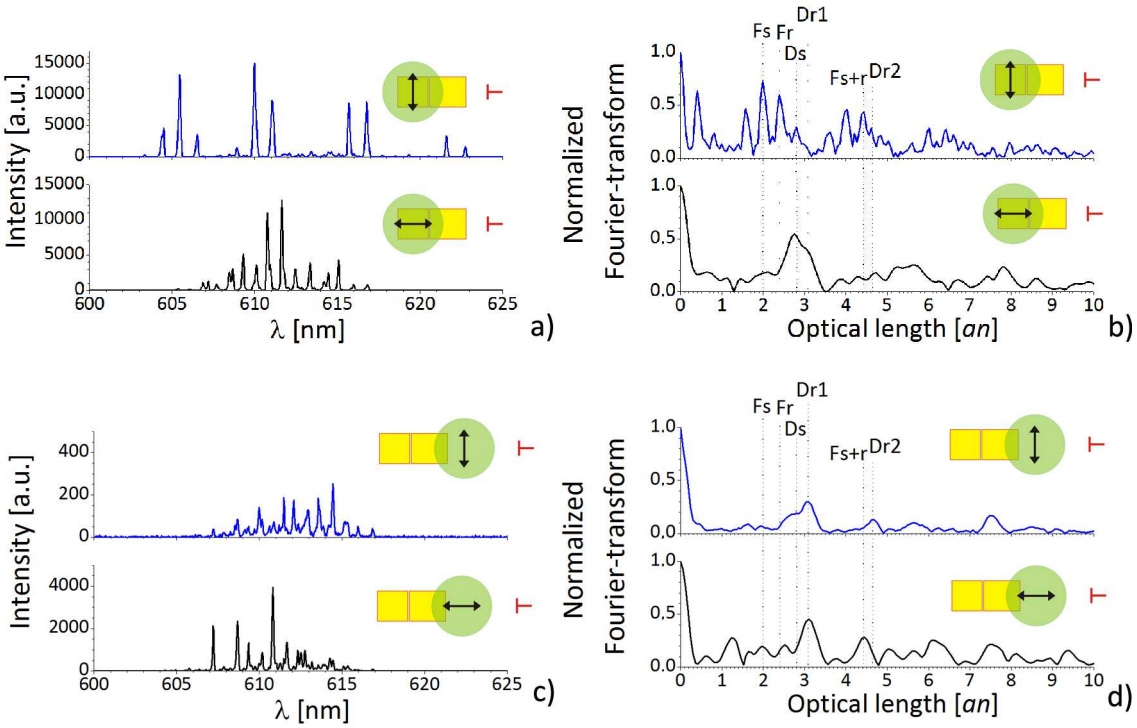

Figure I.10: *Emission of the system of two closely placed micro-lasers (1 μm gap) with pump beam polarization varied (indicated by the scheme next to each plot): a)c,) emission spectra; b),d) normalized Fourier-transform. Pumping geometry was non-symmetric with: a),b) homogeneously pumped square and partially non-homogeneously excited rectangle; c),d) partially non-homogeneously excited rectangle. Lengths of periodic orbits are indicated with Fs, Fr, Fs+r, Ds, Dr1 and Dr2: Fabry-Perot in the square Fs = 2an, in the rectangle Fr = 2.4an, in the whole system Fs+r = 4.4an; diamond in the square Ds = $2\sqrt{2}an$, in the rectangle Dr1 = $2\sqrt{2.44}an$; double diamond in the rectangle Dr2 = $2\sqrt{5.44}an$. Excitation was made with the intensity of 77 MWcm^{-2}.*

Table I.2: Summary on periodic orbits deduced by Fourier-transform technique in experiments presented on Fig.I.10. Lengths of periodic orbits are indicated with Fs, Fr, Fs+r, Ds, Dr1 and Dr2: Fabry-Perot in the square Fs = 2an, in the rectangle Fr = 2.4an, in the whole system Fs+r = 4.4an; diamond in the square Ds = $2\sqrt{2}an$, in the rectangle Dr1 = $2\sqrt{2.44}an$; double diamond in the rectangle Dr2 = $2\sqrt{5.44}an$

		Fabry-Perot	*Diamond*
Square+rectangle	$\alpha = 90^o$	Fs, Fr, Fs+r	Ds, Dr1, Dr2
	$\alpha = 0^o$	Fs	Ds, Dr1, Dr2
Rectangle	$\alpha = 90^o$	Fs	Ds, Dr1, Dr2
	$\alpha = 0^o$	Fs, Fs+r	Dr1

There was a single test made on $100\mu m$*$120\mu m$ rectangle. Although the pumping beam intensity was twice lower, all three Fabry-Perot modes (in square, rectangle and system of square and rectangle) and several diamonds (in square, rectangle and double diamond in rectangle) were excited under $\alpha = 90^o$ pumping.

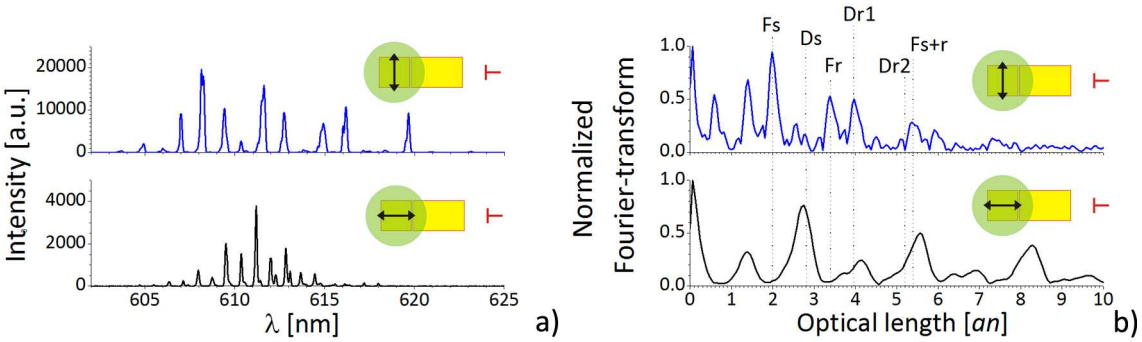

Figure I.11: *Emission of the system of two closely placed micro-lasers (1 μm gap) with non-symmetric excitation geometry and pump beam polarization varied (indicated by the scheme next to each plot): a) emission spectra; b) normalized Fourier-transform (lengths of periodic orbits are indicated with Fs, Fr, Fs+r, Ds, Dr1 and Dr2: Fabry-Perot in the square Fs = 2an, in the rectangle Fr = 3.4an, in the whole system Fs+r = 5.4an; diamond in the square Ds = $2\sqrt{2}an$, in the rectangle Dr1 = $2\sqrt{3.9}an$; double diamond in the rectangle Dr2 = $2\sqrt{6.9}an$). Excitation was made with the intensity of 38.5 MWcm^{-2}.*

Further study of the effects described in this Appendix should consist of study of identical (with one and several orbit types, as for instance Fabry-Perot, squares, rectangles) and as well as non-identical combination of cavities.

Appendix J

Transistors based on hybrid materials

Despite numerous advantages of organic materials, as for instance structural diversity, ease of processing, efficient luminescence and tunability of emission wavelength, their application to the electrically-driven devices stays limited due to a poor electrical mobility. The latter together with mechanical and thermal stability, band gap tunability are distinct properties of inorganic materials. Therefore, the organic-inorganic hybrids advantage from the combination of the unique properties of both classes of materials [196, 197, 198, 199, 200, 201, 202, 203].

During this thesis work we attempted to perform the light emitting diodes and transistors based of hybrid material. This project was held between four laboratories from Paris region and one researcher from foreign institution: Laboratoire de Photonique Quantique et Moleculaire (LPQM) and Laboratoire de Photophysique et Photochimie Supramoléculaires et Macromoléculaires (PPSM) at ENS de Cachan, Laboratoire de Physique des Interfaces et des Couches Minces (LPICM) at Ecole Polytechnique, Laboratoire de Physique des Lasers (LPL) at Paris 13 University and Eduard TUTIS from Institute of Physics in Zagreb, Croatia.

Study of the organic-inorganic hybrids type known as "perovskite" is one of research interest of the "Optical properties of hybrid nanostructures" group at LPQM, ENS de Cachan [204]. This group, headed by Emmanuelle DELEPORTE, works since a decade on the optical properties of various perovskite components, synthesized by their collaborators Pierre AUDEBERT and Laurant GALMICHE from PPSM laboratory at ENS de Cachan.

At the meantime, the LPICM laboratory at Ecole Polytechnique has all necessary equipment for the production and characterization of the OLEDs, organic photovoltaic devices and organic light-emitting transistors. These are the research interest of our collaborators from LPICM, namely Bernard GEFFROY, Denis TONDELIER and Jean-Charles VANEL.

Eduard TUTIS is experienced in modeling the electronic transport in organic and inorganic materials, as well as exciton formation and light emission.

Unfortunately the project did not provide expected results due to several technological problems, impossible to resolve during this PhD work. However, we consider the future work in this direction perspective, especially as some technological issues were localized during this project. This appendix aims to summarize the work performed so far.

Appendix is organized as follows. First we give short review on the perovskite properties. Then the aim of the project is explained together with a comparative description of the planned devices architecture. Finally we discuss the peculiarities

of all the fabrication stages and problems related with each stage.

J.1 General information on perovskites

The organic–inorganic perovskites are crystalline hybrids and were extensively studied in nineties [197, 198, 199, 200, 201, 202].

Crystal structure of the perovskite corresponds to the one of calcium titanium oxide ($CaTiO_3$, Fig.J.1.a), and thus such materials were named after a "perovskite" rock first known for this crystalline structure. Organic-inorganic perovskite consists of inorganic anions (shaped as an extended network of MX_6 corner-sharing metal halide octahedra, where M is generally a divalent metal and X a halide Fig.J.1.a,b) and organic cations (forming a separate layer, Fig.J.1.c).

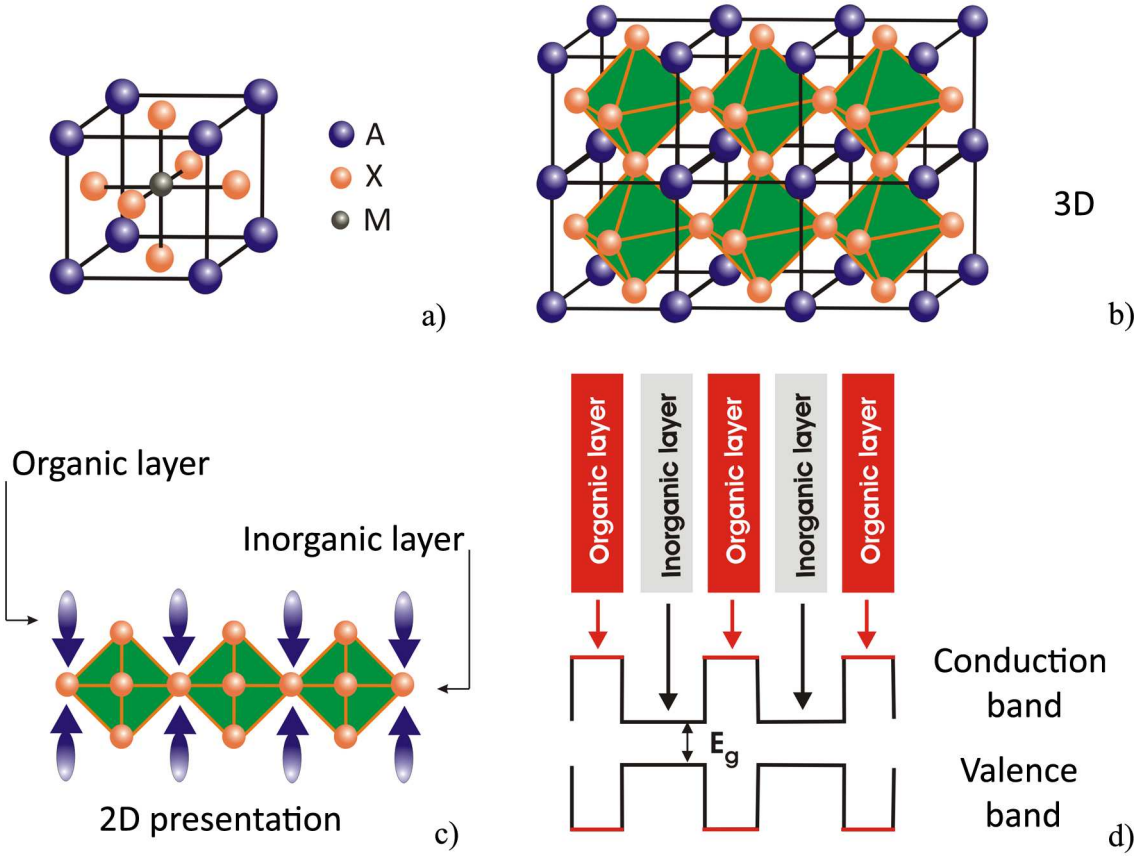

Figure J.1: *Perovskite materials: a) unit perovskite cell; b) 3D presentation of periodic repetition of the unit cells; c) 2D presentation of organic and inorganic layers; d) schematic organic-inorganic perovskite structure and a possible energy-level scheme.*

The resulting quantum well structure (see Fig.J.1.d) can be influenced by the variation of both organic and inorganic compounds, allowing for a wide design flexibility. A careful choice of inorganic compound, as so to meet the conditions of the carrier injection and confinement, results in efficient electroluminescence in such hetero-structure devices[198, 196, 200].

Perovskites tend to self-assemble into crystals from a room-temperature solutions (or from a vapor phase)[1]. Thereby perovskite layers can be fabricated

[1]The MX_6 structure is formed by covalent/ionic bonding, the organic cations are tied to halogens (X) in inorganic sheets by means of hydrogen/ionic bonding, and finally relatively weaker interactions (π-π, van der Waals) create the bounds between the R-groups.

through relatively simple (compared to molecular beam epitaxy) techniques, such as spun-coating, thermal evaporation, ink-jet printing etc. Also several substrate types can be used for this: glass, quartz, plastic, sapphire, silicon etc.; under condition of the proper choice of the solvent.

J.2 Project description

In non-crystalline organic materials the charge mobility is known to be in the range $10^{-6} \div 10^{-2}$ [$cm^2V^{-1}s^{-1}$] [206, 207] with generally imbalanced mobility for electrons and holes. The electrical mobility is naturally higher in perovskite materials, as charge transport happens within a halide layer. Tin-based halides are reputed for best mobility characteristics, for instance $CH_3NH_3SnI_3$[2] was reported for value of 50 [$cm^2V^{-1}s^{-1}$] at room temperature[205]. The values reached in tin-based perovskite TFT transitor with inorganic layer consisting of a single halide layer ($(C_6H_5C_2H_4NH_3)_2SnI_4$) exhibit mobility 0.6 [$cm^2V^{-1}s^{-1}$][3].

The efficient "Organic-Inorganic Light Emitting Diodes" (OILEDs) and "Thin-film Field-Effect Transistors" (TFT) based on perovskites have been already demonstrated [198, 200, 202, 203]. The aim of our project was to create the light-emitting diode based on perovskite materials. The first step towards realization of the hybrid-material diode was in creation of the OILEDs and transistors based on with the perovskites synthesized at PPSM (PEPI, to be detailed below), and then move towards our principal goal by successive improvement of the device architecture together with incorporation of the organic dyes to perovskite structure[4]. The work on this project stuck on the very first stage, as we did not manage to achieve any working OLED or transistor device.

J.3 Devices architecture

Here we give a brief description on the perovskite material implemented in our study as well as chosen architecture of TFT and OLED devices.

Among the various perovskite materials previously studied in collaboration between LPQM and PPSM, the best film quality, emission stability and satisfactory photo-luminescence efficiency were noted in the PEPI perovskite (biphenethylammonium tetraiodoplombate, $(C_6H_5C_2H_4 - NH_3)_2\, PbI_4$)[204]. Thereby, this material was chosen to conduct the first experiments. PEPI exhibits a sharp absorption peak at 516.8 nm and photo-luminescence at 522.6 nm [204], the band-gap is located at 450 nm (which corresponds to 2.8 eV). The thicknesses of inorganic and organic layers were measured to be respectively 6.3 and 10 Å.

We used the transistor scheme (depicted on Fig.J.2.a) similar to presented in publication of perovskite-based field-effect transistors (Fig.J.2.b) [203], with several modification towards a standard organic material based transistor architecture (Fig.J.2.c), used in LPICM laboratory. For instance, we used as gate the Cr layer on a glass substrate instead of the $n{+}{+}\ Si$ layer with In contact, then we chose to use a spun-coated polymer layer (either PMMA or SU8) as a gate dielectric (instead of thermally grown silica [203]). The drain/source contacts we fabricated by evaporation of Al or Au above the perovskite layer, while Kagan et all. [203] mention

[2] SnI_3indicates close to infinite number of halide layers within single inorganic layer.

[3] Such perovskites act as the p-type metals

[4] Especially as the external quantum efficiency in TFT device can be substantially increased with recombination layer distancing from the contacts, as was recently demonstrated [208].

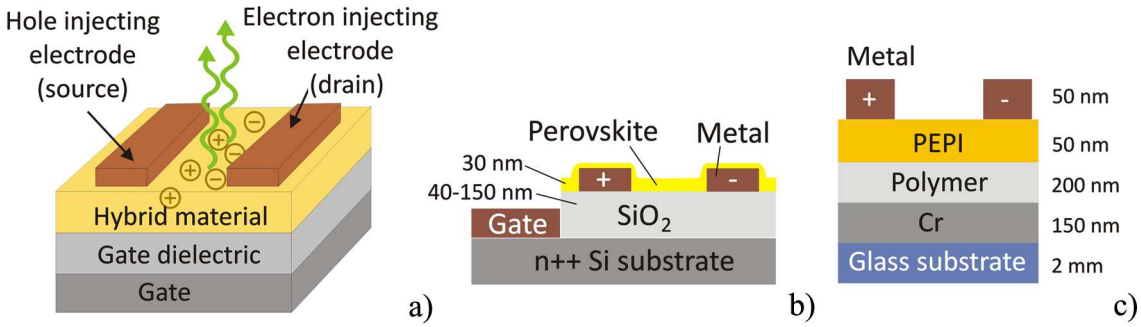

Figure J.2: *Field-effect transistor scheme (a), perovskite-based transistor configuration reported in* [203] *(b) and examined in terms of our project (c).*

evaporation *Pd*, *Pt* and *Au* either before or after the spun-coating of perovskite layer[5]. Finally the reported hybrid TFT was based on $(C_6H_5C_2H_4NH_3)_2SnI_4$ perovskite.

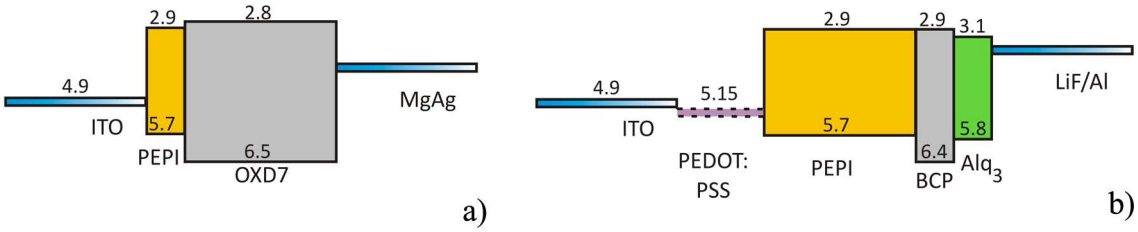

Figure J.3: *OLED architecture together with HOMO-LUMO levels in electron volt: a) reported in [198]; b) used in our experiments.*

The first reported perovskite-based OILED [198] had the architecture depicted on Fig.J.3.a (the thickness of different layers was as follows: 100 nm ITO, 10 nm PEPI[6], 50 nm OXD7, 200 nm MgAg). It exhibited efficient electroluminescence (12 000 [cd m^2] at 2 A cm^{-2}, 24V) at liquid nitrogen temperatures. However emission efficiency reduced drastically with the passage to the room temperatures, which authors explained with thermal ionization of the excitons.

Another group reported the OILED working at room temperatures but in nitrogen atmosphere [200]. They used more complex $PbCl_4$-based perovskite, which organic part contained the AEQT dye molecule (chemical structure of overall hybrid was $(H_3NC_2H_4C_{16}H_8S_4C_2H_4NH_3)_2PbCl_4$). Device architecture was similar to the one depicted on Fig.J.3.a, except for silica deposited on the ITO in a shape of several rectangular areas in order to avoid shorting between anode and cathode, and also additional Ag layer on the top of MgAg contact to hinder oxidation. The given thickness of OLED layers is follows: 150 nm ITO, 130 nm SiO_2, 300 nm perovskite, 60 nm MgAg, 120 nm Ag. Device maximum efficiency was 0.1 lm W^{-1}at 8V and 0.24 A.

We also used an architecture modified compared to depicted Fig.J.3.a (see Fig.J.3.b): BCP was used instead of OXD7 (being a material currently used in LPICM and exhibiting similar to OXD7 HOMO-LUMO characteristics), Alq_3 layer was added to improve the electrons injection from cathode and in half of devices we also incorporated PEDOT:PSS layer between ITO and PEPI. The layer thick-

[5]Although there is a soft remark in this paper concerning the deposition order of a hybrid layer and source/drain contacts, mentioning that the evaporation of contacts prior to perovskite deposition prevents the latter from exposure to potentially harmful temperatures.

[6]PEPI was referred in this article as PAPI

nesses are 25 nm/ 25 nm/ 50 nm/ 10 nm/ 10 nm/ 1.2 nm/ 100 nm for the ITO / PEDOT / PEPI / BCP / Alq_3/ LiF / Al respectively.

J.4 Experimental results

The first stage of the project consisted in the acquisition of working skills for PEPI material processing (solution preparation, layer fabrication on the substrate itself and a polymer layer) at clean-room environment. After the films of good quality were obtained, we skipped to second stage, involving the TFT transistor and OILED fabrication (following architectures described in the Section J.3) in the glove-box facilities. In this Section, we provide an explicit description of the fabrication routine and problems, that we faced during both of these stages. I would like to acknowledge PhD students Yi WEI and Gaetan LANTY from hybrid nanostructures group at LPQM for guiding the perovskites processing and fruitful discussions. I would also like to express my appreciation to Bernard GEFFROY, Denis TONDELIER and Jean-Charles VANEL for training my skills in OLEDs and transistors routine as well as their patience and hopefulness in the moments of technical failures.

J.4.1 PEPI preparation

Pb-based perovskites have worse electrical mobility properties compared to *Sn*-based. However, we started the project with PEPI, which is *Pb*-based hybrid, for two reasons:

- PEPI was carefully studied by our collaborators from LPQM and PPSM, leading to a robust preparation and deposition work-flow.
- *Sn*-based structures must be processed in the inert atmosphere only, thereby the first experiments aiming the optimization of device architecture should be done with a material that can be processed in room conditions.

We prepared PEPI ($(C_6H_5C_2H_4 - NH_3)_2\, PbI_4$, biphenethylammonium tetraiodoplombate) 10 wt% solution in DMF (dimethyl foramide) solvent by mixing following components:

$$2\,[C_6H_5C_2H_4 - NH_3I] + PbI_2 \rightarrow [C_6H_5C_2H_4 - NH_3]_2\, PbI_4$$

where $C_6H_5C_2H_4 - NH_3I$ salt is prepared in PPSM laboratory and high purity PbI_2 is purchased from Sigma Aldrich.

For each 10 ml of DMF (density 0.9487 [kg L^{-1}] at 20° C) the following total amount of powder was used: 0.949 [g]. In order to respect the stochiometric ratio:

$$m\,[C_6H_5C_2H_4 - NH_3I] = 2\frac{M\,[C_6H_5C_2H_4 - NH_3I]}{M\,[PbI_2]} m\,[PbI_2]$$

when mixing the salts we used salt in quantities $m\,[PbI_2]$ and $m\,[C_6H_5C_2H_4 - NH_3I]$ respectively 0.456 and 0.493 [g] ($M\,[C_6H_5C_2H_4 - NH_3I]$=249.1 [g mol^{-1}]; $M\,[PbI_2]$ =249.1 [g mol^{-1}]).

Solution is spun-coated with parameters (speed, acceleration, time): 2000 rpm, 2000 rpm/s, 30 s with closed cover, followed by 1 min bake at 95° C on a hot plate. Obtained PEPI film is about 50 nm thick and is of a color between yellow and green.

J.4.2 Polymer deposition

Perovskites are known to self-organize on limited number of substrates (listed in Section J.1) such as silica, quartz and some plastics. Without facilities to grow the silica layer on the *Cr* layer, we decided to try the spun-coated polymer films. And as previous findings of hybrid nanostructures group at LPQM stated the self-organization of PEPI on PMMA, this polymer was initially chosen as a gate dielectric (Fig.J.2.a) in our transistor configuration.

There are several limitations on the thickness of gate dielectric:

- less than 100 nm thick layer is insufficient to prevent shorting between top contacts and gate (Fig.J.2.a);
- more than 300 nm thick layer may eliminate the gate effect on transistor characteristics.

Thus, a 200-250 nm thickness of polymer was chosen.

PMMA The solution of PMMA in anisole we normally utilize as matrix for planar micro-lasers (PMMA 495 A6 manufactured by MicroChem, see Appendix A) appeared to be unsuitable for this application. It provides either homogeneous layers with thicknesses of no less than 400 nm or thin but non-homogeneous layers[7] (depending on the spun-coating parameters).

Consequently we followed the protocol of PMMA-toluene solution preparation, used at nanostructures group at LPQM, suggesting next empiric relation between x the spun-coated film thickness (in nm) and $c[wt\%]$ the PMMA powder mass concentration in toluene: $c[wt\%$. Resulting x nm thick PMMA layer is obtained, while deposited with following spun-coating parameters (speed, acceleration, time): 2200 rpm, 2200 rpm/s, 40 s; by 20 min bake at 95° C on a hot plate.

For some unexplained reason, obtained films were all of < 140 nm thick, with the average surface roughness of about 30 nm. Moreover, we faced a serious problem of the PEPI film quality, when deposited above such layer (as depicted on Fig.J.4.a). Thereby a toluene-based PMMA solution also appears unsuitable for transistor applications. Being a strong solvent, DMF may penetrate into the polymer during the spun-coating process, which concerns in the first place such easily soluble polymers as PMMA.

SU8 The very first series of PEPI films deposited upon the SU8 polymer exhibited considerably better quality compared to PMMA (see Fig.J.4.b). For this reason we adopted SU8 polymer as gate dielectric in transistor architecture, depicted on Fig.J.2.c. The optimal deposition parameters of SU8 2000.5 in order to obtain 200-250 nm thick films were found to be as follows (speed, acceleration, time): 2000 rpm, 1000 rpm/s, 30 s; followed by 2h bake at 180° C in the oven.

Surface treatment The film roughness is a very important issue in organic electronics, and its the relevance increases with the number of layers in final sandwich-alike structure. As it is seen on the Fig.J.4.c-d, a rather small defect on the bottom layer (dust on Fig.J.4.c) increases drastically on the following level of the device (roughness spreads around the dust particle Fig.J.4.d).

[7]For instance 4000 rpm, 4000 rpm/s, 40 s (speed, acceleration, time) deposition resulted in the film thickness varied from 140 to 180 nm (corresponding to 40 nm roughness).

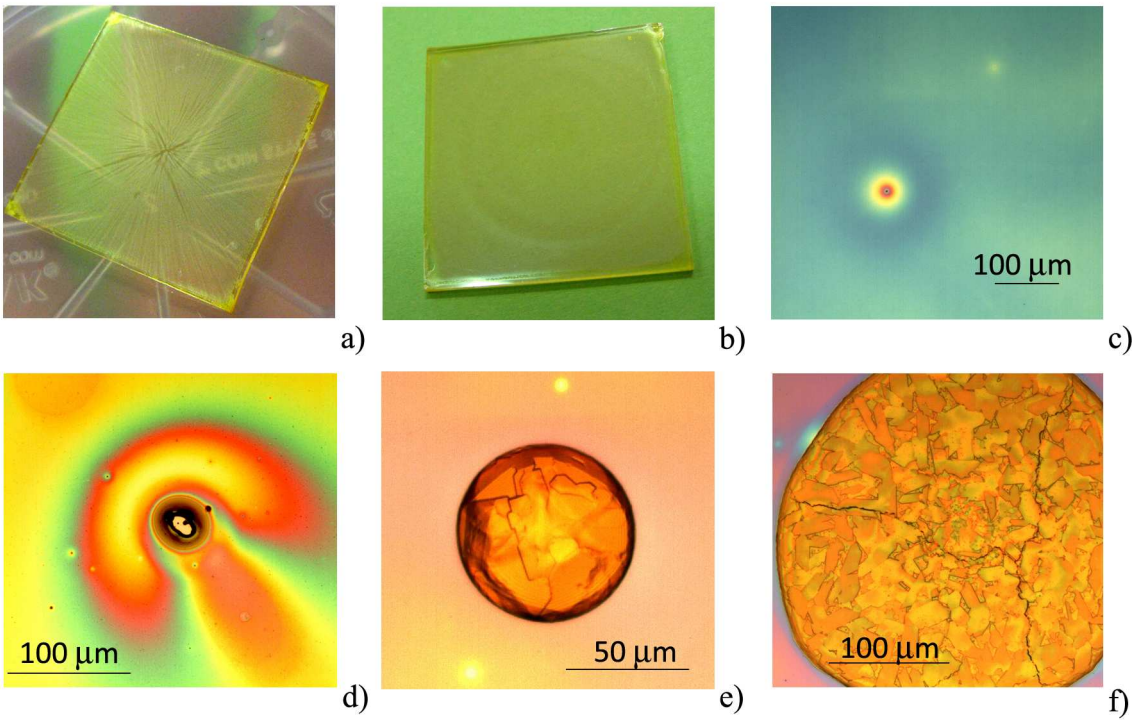

Figure J.4: *Photographs on PEPI deposition on the polymer: a) PEPI on PMMA (toluene solution); b) PEPI on SU8; c) defect within SU8 deposition (dust); d) expansion of the (c)-type defect within PEPI deposition above SU8 layer; e), f) PEPI crystalline droplets. Here (a,b) were deposited on a glass substrate, while (c-f) on glass substrate covered with a Cr layer.*

Prior to the perovskite deposition, a surface must be treated in order to release the bonds and overcome the wetting issue (for instance with KOH or O_2)[8]. In the opposite case the perovskite does not form a homogeneous layer, but shapes into the droplets of a various size, as shown on Fig.J.4.e-f (the crystalline structure and domains can be clearly seen from these optical microscopy photos).

Fig.J.5 represents the experimental comparison of both surface treatment methods. There is no substantial difference between surface roughness for PEPI deposited on glass slide (Fig.J.5.a,b). Meanwhile PMMA treatment with O_2 provides considerably better result than with KOH (Fig.J.5.c,d). We thereby adopted the surface treatment with O_2 as a standard technique during the work on this project.

J.4.3 OILED device

The architecture of perovskite-based OILED we attempted to make was described in Section J.3 and depicted on Fig.J.3.b. Here we concentrate on fabrication routine and technical problems arising at different steps.

The preliminary study on the PEPI deposition on PEDOT and ITO demonstrated satisfactory PEPI film quality in both cases.

The substrate used in our work was glass slide with deposited ITO layer and gold contacts. It was cleaned with propanol (15 min in supersonic) and O_2(15 min in UV-ozone), and afterward introduced into the glove-box. All following operations were performed in the inert atmosphere or in the vacuum (evaporation).

For each spun-coated layer ITO-free region was cleaned before the layer baking. PEDOT deposition parameters were as follows (speed, acceleration time, time):

[8]Treatment with KOH is generally utilized in hybrid nanostructures group, while surface treatment with O_2 is a standard method in organic electronics.

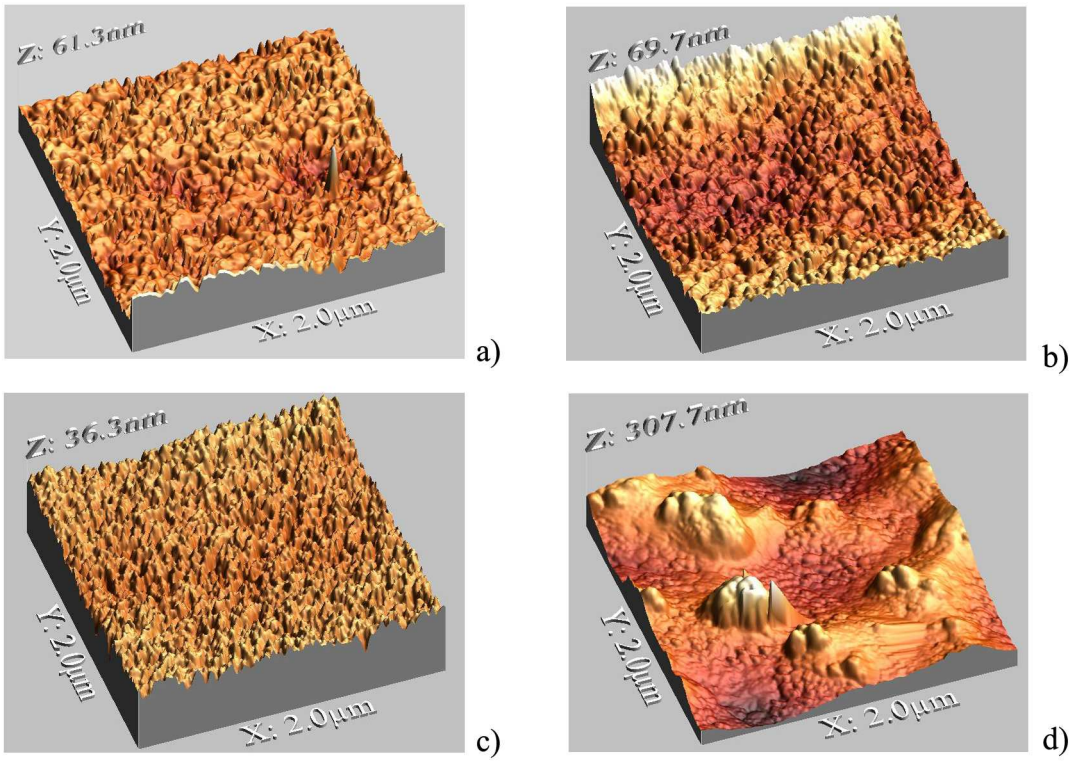

Figure J.5: *Atomic force microscope images on PEPI film roughness. The left column corresponds to surface treatment with O_2 prior to PEPI deposition, while the right - with KOH. Following substrates were used for PEPI deposition: glass (a, b) and PMMA deposited on the glass (c, d).*

3000 rpm / 5 s/ 15 s + 3500 rpm / 5 s/ 30 s, followed by 2 min bake at 105° C on a hot plate. PEPI deposition parameters were (speed, acceleration time, time): 4000 rpm / 4 s/ 30 s, followed by 1 min bake at 95° C on a hot plate.

Other layers were deposited by vacuum evaporation at about 10^{-7} mbar vacuum.

Testing of resulting device took place in the ambient atmosphere, and the degradation of metal contacts was noticed even before the current was applied to the system. Moreover, all the samples exhibited rapid degradation with current injection, and before 20 mA the metal contacts were in inoperable condition, as evidenced by photographs on Fig.J.6.a,b. No light emission observed. One of the possible reasons for that is in rather high surface roughness of studied PEPI films (as shown in Fig.J.5), due to high sensitivity of OLEDs to peak current.

Although PEPI is known to degrade under oxygen atmosphere, it normally takes up to 24 hours before the photo-luminescence quenching. Thereby the observed rapid degradation should have another origin, as for instance the presence of solvent in the device due to short baking time of PEPI layer.

At the meantime, high temperature has a destructive influence on the PEPI, which may decrease the electroluminescence efficiency in the device.

J.4.4 Transistor device

We worked on the PEPI perovskite-based thin-film transistor, which architecture is depicted on Fig.J.2.c. (with SU8 as a gate dielectric). Here we describe the fabrication routine and issues faced at various stages.

A glass slide covered with 150 nm Cr layer served as a substrate for following spun-coating of SU8 and PEPI layers, and vacuum evaporation of top contacts (Au or Al). Consequent electrical tests were made in glove-box with the aid of

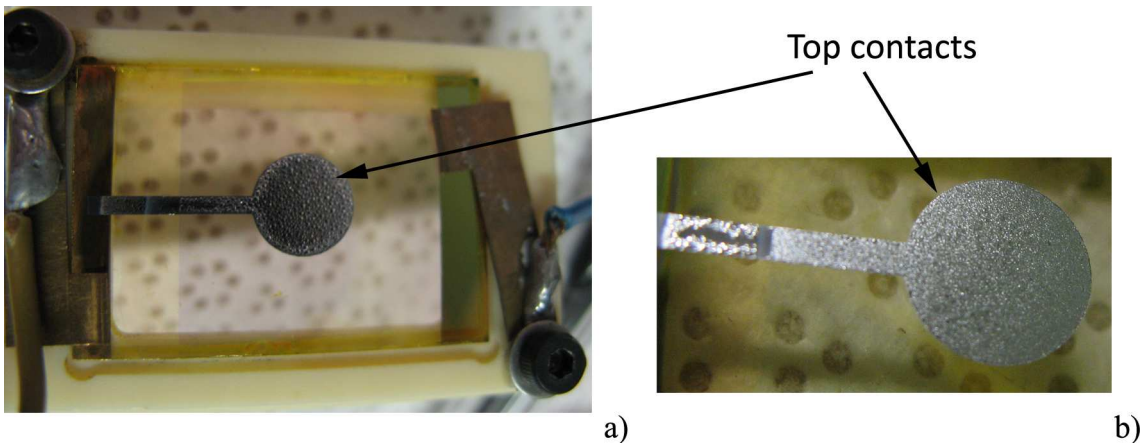

Figure J.6: *OLED photographs: a) OLED in the measurement cell; b) zoom on the top contacts.*

contacts positioning system depicted on Fig.J.7.

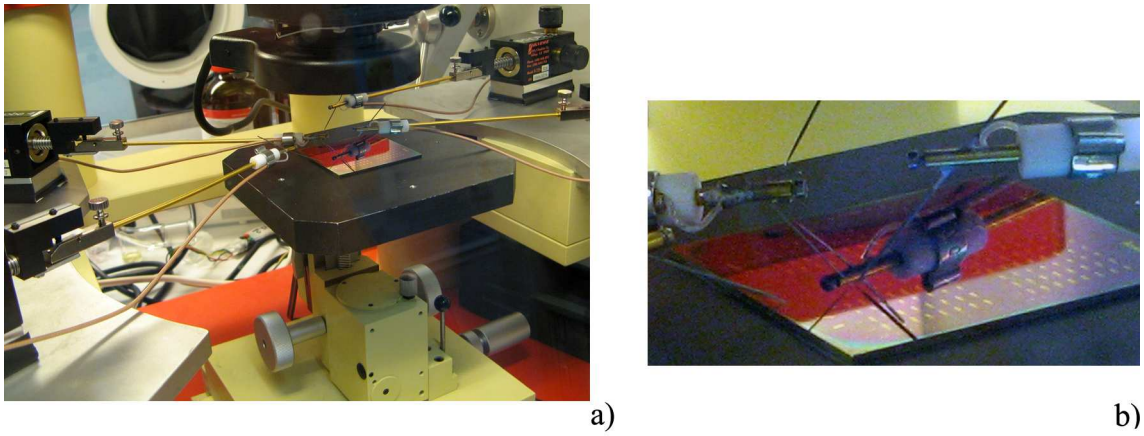

Figure J.7: *Photographs on the set-up utilized for the measurement of current-voltage characteristics of transistor: a) needle-contact micro-positioning system; b) zoom to the sample area.*

We have evidenced current passage through the perovskite layer (for instance, the same order of mobility for holes and electrons) but never managed to achieve properly working transistor due to several problems:

- Sample contamination within transportation

As for our first attempts, transistors fabrication included transportation from LPICM to LPQM (SU8 and PEPI deposition) and back, which inevitably results in the surface contamination and should be avoided. Moreover, due to perovskite sensitivity to oxidation, the duration of sample exposure to the room atmosphere should be reduced to the minimal possible (e.g. ideally fabricated and tested in the glove-box).

- Glove-box vibrations

The set-up we used to test the IV characteristics of transistors (shown on the photographs on Fig.J.7) was situated in the glove-box, situated just above the primary vacuum pump, causing serious vibrations. As result, the needle contacts depicted on Fig.J.7.b eventually pierced the sandwiched structure during the IV-curves

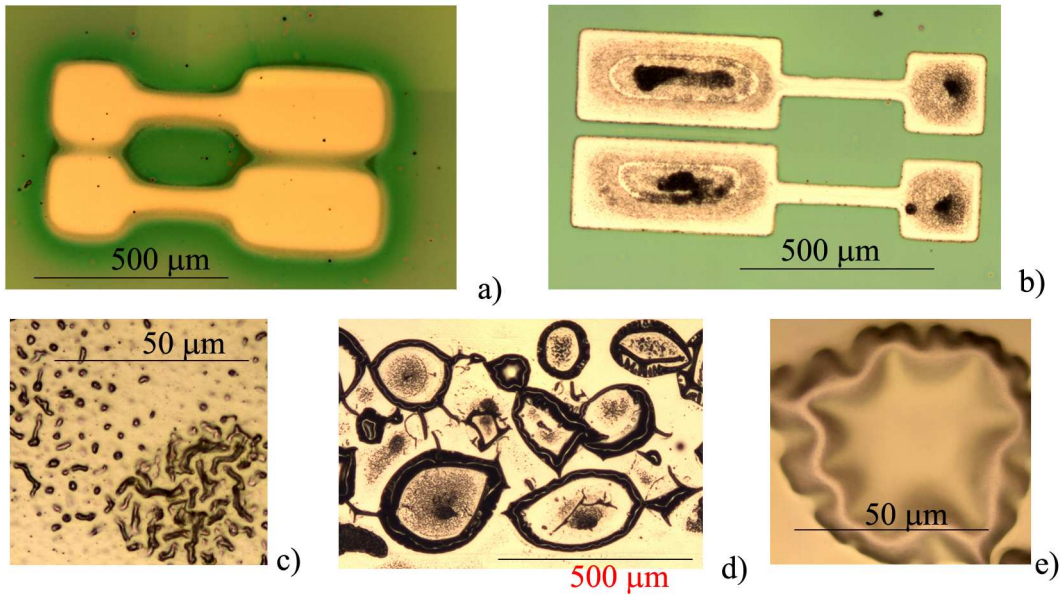

Figure J.8: *Optical microscope photographs on the top contacts: a) Au deposited on the PEPI film fabricated at LPQM; b)-d) Al deposited on PEPI fabricated i glove-box. c) and e) are represent a zoom of respectively b) and d). A separation between contacts is absent on (a) due to fabrication problems with this sample, still the photograph evidences the absence of degradation on the surface of the contacts.*

measurements. Meanwhile, the absence of expected current-voltage characteristics while measured in the analogous set-up situated outside the glove-box in the room atmosphere may be related to perovskite sensitivity to oxidation.

- Solvent evaporation

As was mentioned in previous subsection, the degradation of top contacts was noticed when the PEPI films were fabricated in the glove-box, as it is seen on Fig.J.8. Thereafter a longer bake period should be applied. Meanwhile, it was experimentally verified in hybrid nanostructures group that up to 20 minutes bake does not alter the photo-physical properties of PEPI.

- Contact with high temperatures

In TFT configuration we chose for experimental verification the metal contacts were evaporated just on the top of PEPI layer. It is strictly advisable to modify the device architecture in order to prevent perovskite film from harmful exposure to high temperatures.

J.4.5 Self-organization issue

We have also performed a study of the surface quality and self-organization of PEPI deposited on the quartz substrate. Scanning electron microscope images shown on Fig.J.9 suggest that the self-organization appears in domains of up to several micrometer in size, which stays much smaller compared to $20 \div 200$ μm width of the transistor channel. Thereby the attempts of fabrication should be stopped until a larger self-organization domains are obtained.

It is worse noticing, that all reported TFT and OILED perovskite-based devices [198, 203] were fabricated with the use of the perovskite solution obtained from dissolved perovskite crystals. These papers describe a following fabrication scheme: after the different salts are mixed in the solvent (as described in Sub-section J.4.1),

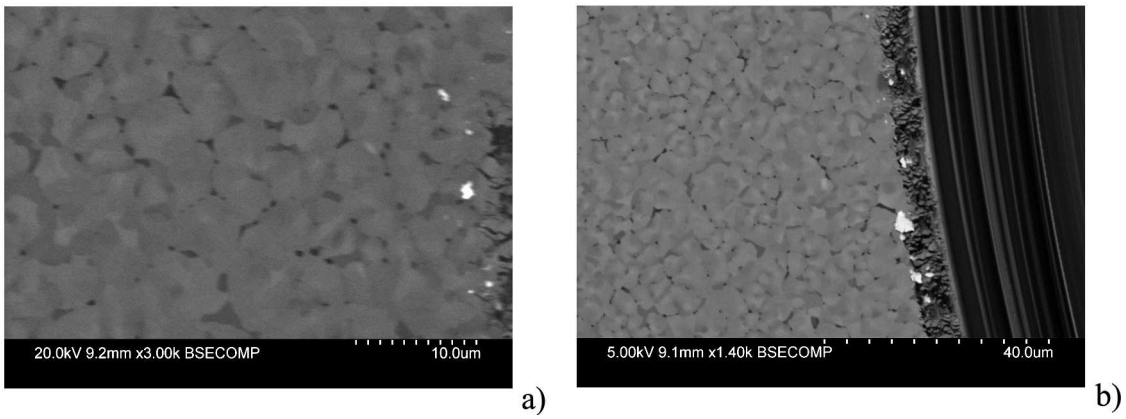

Figure J.9: *Scanning electron microscope images of PEPI layer deposited upon a quartz substrate. Image scale: a) 10 μm; b) 40 μm.*

the perovskite crystals are precipitated and then dissolved in the solvent, and only the latter was used for spun-coating.

Such fabrication sequence contains an extra purification stage (by crystallization) compared to the one we used, which may be crucial for the size of self-organization domain.

Bibliography

[1] Soffer B.H. and McFarland B.B., "Continuously Tunable Narrow-Band Organic Dye Lasers" Appl. Phys. Lett.,10, p. 266-268 (1967).

[2] Fork R.L., Brito Cruz C. H., Becker P. C., and Shank C. V., "Compression of optical pulses to six femtoseconds by using cubic phase compensation" Opt. Lett., 12, p. 483-485 (1987).

[3] Tang C. W., VanSlyke S. A., "Organic electroluminescent diodes" Appl. Phys. Lett., 51, p. 913-915 (1987).

[4] Burroughes J. H., Bradley D. D. C., Brown A. R., Marks R. N., MacKay K., Friend R. H., Burns P. L., Holmes A. B., "Light-emitting diodes based on conjugated polymers" Nature, 347, p. 539 - 541 (1990).

[5] Delezoide C., Salsac M., Lautru J., Leh H., Nogues C., Zyss J., Buckle M., Ledoux-Rak I., Nguyen C. T., "Vertically Coupled Polymer Microracetrack Resonators for Label-Free Biochemical Sensors" IEEE Photonics Technology Letters, 24, p. 270-272 (2012).

[6] Kobayashi T., Nakatsuka S., Iwafuji T., Kuriki K., Imai N., Nakamoto T., Claude C. D., Sasaki K., Koike Y., "Fabrication and superfluorescence of rare-earth chelate-doped graded index polymer optical fibers" Appl. Phys. Lett. 71, p. 2421-2423 (1997).

[7] Yang Y., Turnbull G. A., Samuel I. D. W., "Hybrid optoelectronics: A polymer laser pumped by a nitride light-emitting diode" Appl. Phys. Lett., 92, p.163306.1-3 (2008).

[8] Bernanose A., Comte M., Vouaux P., "Sur un nouveau mode d'émission lumineuse chez certains composés organiques" J. Chim. Phys. Phys.- Chim. Biol., 50, p. 64-68 (1953).

[9] Zhu D. X., Zhen H. Y., Ye H., Liu X., "Highly polarized white-light emission from a single copolymer based on fluorene," Appl. Phys. Lett., 93, p. 163309.1-3 (2008).

[10] Cimrova V., Remmers M., Neher D., Wegner G., "Polarized light emission from LEDs prepared by the technique," Adv. Mater., 8, p. 146–149 (1996).

[11] Era M., Tsutsui T. , Saito S., "Polarized electroluminescence from oriented p-sexiphenyl vacuum-deposited film," Appl. Phys. Lett., 67, p. 2436–2438 (1995).

[12] Pichler K., Friend R. H., Burn P. L., Holmes A. B., "Chain alignment in poly(p-phenylene vinylene) on oriented substrates" Synth. Met., 55, p. 454–459 (1993).

[13] Sakamoto K., Miki K., Misaki M., Sakaguchi K., Chikamatsu M., Azumi R., "Very thin photoalignment films for liquid crystalline conjugated polymers: Application to polarized light-emitting diodes," Appl. Phys. Lett., 91, p. 183509.1-3 (2007).

[14] Grell M., Bradley D. D. C., "Polarized luminescence from oriented molecular materials," Adv. Mater. 11, p. 895–905 (1999).

[15] Park B., Huh Y. H., Jeon H.G., "Polarized electroluminescence from organic light-emitting devices using photon recycling" Optics Express, 18, p. 19824-19830 (2010).

[16] Peterson O.G., Snavely B.B., "Stimulated Emission From Flashlamp-Excited Organic Dyes In Polymethyl Methacrylate" Appl. Phys. Lett., 12, p. 238-240 (1968).

[17] Hermes R.E., Allik T. H., Chandra S., Hutchinson J. A., "High-Efficiency Pyrromethene Doped Solid-State Dye-Lasers" Appl. Phys. Lett., 63, p. 877-879 (1993).

[18] Faloss M., Canva M., Georges P., Brun A., Chaput F., Boilot J.P., "Toward millions of laser pulses with pyrromethene- and perylenedoped xerogels" Appl. Opt., 36, p. 6760-6763 (1997).

[19] Tessler N., Denton G.J., Friend R.H., "Lasing from conjugated-polymer microcavities" Nature, 382, p.695-697 (1996).

[20] Dumarcher V., Rocha L., Denis C., Fiorini C., Nunzi J.-M., Sobel F., Sahraoui B., Gindre D., "Polymer thin-film distributed feedback tunable lasers" J. Opt. A: Pure Appl. Opt., 2, p. 279-283 (2000).

[21] Vasdekis A. E. , Turnbull G. A., Samuel I. D. W., Andrew P., Barnes W. L. "Low threshold edge emitting polymer distributed feedback laser based on a square lattice" Appl. Phys. Lett., 86, p. 161102.1-3 (2005).

[22] Mele E., Camposeo A., Stabile R., Del Carro, P., Di Benedetto F, Persano L., Cingolani R., Pisignano D., "Polymeric distributed feedback lasers by room-temperature nanoimprint lithography" Appl. Phys. Lett., 89, p.131109.1-3 (2006).

[23] Suganuma N., Seki A., Tanaka Y., Ichikawa M., Koyama T., Taniguchi Y., "Organic polymer DBR laser by softlithography" J. Photopolym. Sci. Tech., 15, p. 273-278 (2002).

[24] Frolov S.V., Fujii A., Chinn D., Vardeny Z. V., Yoshino K., Gregory R. V., "Cylindrical micro-lasers and light emitting devices from conducting polymers" Appl. Phys. Lett., 72, p.2811-2813 (1998).

[25] Dou S.X., Toussaere E., Ben-Messaoud T., Potter A., Josse D., Kranzelbinder G. and Zyss J., "Polymer microring lasers with longitudinal optical pumping" Appl. Phys. Lett., 80, p. 165-167 (2002).

[26] McGehee M.D., Heeger A.J., "Semiconducting (conjugated) polymers as materials for solid-state lasers" Adv. Mater., 12, p. 1655-1668 (2000).

[27] Gupta R., Stevenson M., Heeger A. J., "Low threshold distributed feedback lasers fabricated from blends of conjugated polymers: Reduced losses through Förster transfer" J. Appl. Phys., 92, p.4874-4877 (2002).

[28] Kozlov V.G., Parthasarathy G., Burrows P.E., Khalfin V.B., Wang J., Chou S.Y., Forrest S.R., "Structures for organic diode lasers and optical properties of organic semiconductors under intense optical and electrical excitations" IEEE Journal of Quantum Eletronics, 36, p.18-26 (2000).

[29] Samuel I. D. W., Turnbull G. A., "Organic Semiconductor Lasers" Chem. Rev., 107, p. 1272–1295 (2007).

[30] Segal M., Baldo M. A., Holmes R. J., Forrest S. R., Soos Z. G., "Excitonic singlet-triplet ratios in molecular and polymeric organic materials" Phys. Rev. B, 68, p.075211.1-14 (2003).

[31] Baldo M. A., Holmes R. J., Forrest S. R., "Prospects for electrically pumped organic lasers" Phys. Rev. B, 66, p.035321.1-16 (2002).

[32] Giebink N.C. Forrest S.R., "Temporal response of optically pumped organic semiconductor lasers and its implication for reaching threshold under electrical excitation" Phys. Rev. B, 79, p.073302.1-4 (2009).

[33] Wallikewitz B.H., de la Rosa M., Kremer J. H.-W. M., Hertel D., Meerholz K. "A Lasing Organic Light-Emitting Diode" Adv. Mater., 22, p. 531-534 (2010).

[34] Gärtner C., Karnutsch C., Lemmer U., and Pflumm C. "The influence of annihilation processes on the threshold current density of organic laser diodes" J. Appl. Phys., 101, p. (2007).

[35] Tessler N. , Pinner D. J. , Cleave V., Thomas D. S., Yahioglu G., Barny P. Le, and Friend R. H. "Pulsed excitation of low-mobility light-emitting diodes: Implication for organic lasers" Appl. Phys. Lett., 74, p.2764-2766 (1999).

[36] Inoue Y., Sakamoto Y., Suzuki T., Kobayashi M., Gao Y., Tokito S., "Organic Thin-Film Transistors with High Electron Mobility Based on Perfluoropentacene" Jap. J. Appl. Phys., 44, pp. 3663–3668 (2005).

[37] Hosokawa C., Tokailin H., Higashi H., and Kusumoto T. "Transient electroluminescence from hole transporting emitting layer in nanosecond region" Appl. Phys. Lett., 63, p.1322-1324 (1993).

[38] Kozlov V. G., Bulovic V., Burrows P. E., Baldo M., Khalfin V. B., Parthasarathy G., Forrest S. R., You Y., Thompson M. E., "Study of lasing action based on Förster energy transfer in optically pumped organic semiconductor thin films" J. Appl. Phys., 84, p. 4096-4108 (1998).

[39] Bulovic V. , Kozlov V. G., Khalfin V. B., Forrest S. R., "Transform-Limited, Narrow-Linewidth Lasing Action in Organic Semiconductor Microcavities" Science, 279, p. 553-555 (1998).

[40] Reufer M., Riechel S., Lupton J. M., Feldmann J., Lemmer U., Schneider D., Benstem T., Dobbertin T., Kowalsky W., Gombert A., Forberich K., Wittwer V., Scherf U., "Low-threshold polymeric distributed feedback lasers with metallic contacts" Appl. Phys. Lett., 84, p. 3262-3264 (2004).

[41] Stehr J., Crewett J., Schindler F., Sperling R., von Plessen G., Lemmer U., Lupton J.M., Klar T.A., Feldmann J., Holleitner A.W., Forster M., Scherf U. "A low threshold polymer laser based on metallic nanoparticle gratings" Adv. Mater., 15, p. 1726-1729 (2003).

[42] Gwinner M.C., Khodabakhsh S., Song M. H., Schweizer H., Giessen H., and Sirringhaus H., "Integration of a Rib Waveguide Distributed Feedback Structure into a Light-Emitting Polymer Field-Effect Transistor" Adv. Func. Mater., 19, p. 1360-1370 (2009).

[43] Samuel I. D. W., Namdas E. B., Turnbull G. A. "How to recognize lasing " Nature Photonics, 3, p. 546 - 549 (2009).

[44] Voss T., Scheel D., Schade W., "A microchip-laser-pumped DFB-polymer-dye laser" App. Phys. B: Lasers and Optics, 73, p. 105-109 (2001).

[45] Riedl T., Rabe T., Johannes H.-H., Kowalsky W., Wang J., Weimann T., Hinze P., Nehls B., Farrell T., Scherf U., "Tunable organic thin-film laser pumped by an inorganic violet diode laser" Appl. Phys. Lett., 88, p. 241116.1-3 (2006).

[46] Vasdekis A. E. , Tsiminis G., Ribierre J.-C., O' Faolain L., Krauss T. F., Turnbull G. A., Samuel I. D. W., "Diode pumped distributed Bragg reflector lasers based on a dye-to-polymer energy transfer blend" Opt. Express, 14, p. 9211-9216 (2006).

[47] Garrett C. G. B., Kaiser W., Bond W. L., "Stimulated emission into optical whispering modes of spheres" Phys. Rev., 124, p.1807-1809 (1961).

[48] Tzeng H.-M., Wall K.F., Long M.B., Chang R.K., "Laser emission from individual droplets at wavelengths corresponding to morphology-dependent resonances" Optics Letters, 9, p. 499-501 (1984).

[49] Gorodetsky M. L., Savchenkov A. A., Ilchenko V. S., "Ultimate Q of Optical Microsphere Resonators," Opt. Lett., 21, pp. 453–455 (1996).

[50] Savchenkov A.A., Ilchenko V.S., Matsko A.B. and Maleki L., "Tunable filter based on whispering gallery modes" Electron. Lett., 39, p. 389-391 (2003).

[51] Sandoghdar V., Treussart F., Hare J., Lefevre-Seguin V., Raimond J.-M., Haroche S., "Very low threshold whispering-gallery-mode microsphere laser" Phys. Rev. A , 54, p. R1777-R1780 (1996).

[52] Lissillour F., Messager D., Stephan G., and Feron P., "Whispering-gallery-mode laser at 1.56 mm excited by a fiber taper" Opt. Lett., 26, p.1051-1053 (2001).

[53] Vassiliev V.V., Velichansky V.L., Ilchenko V.S., Gorodetsky M.L., Hollberg L., Yarovitsky A.V., "Narrow-line-width diode laser with a high-Q microsphere resonator" Opt. Commun., 158, p. 305–312 (1998).

[54] Vernooy D. W., Furusawa A. , Georgiades N. Ph., Ilchenko V. S., Kimble H. J., "Cavity QED with high-Q whispering gallery modes " Phys. Rev. A, 57, p. R2293-2296 (1998).

[55] Arnold S., Khoshsima M., Teraoka I., Holler S., Vollmer F. "Shift of whispering-gallery modes in microspheres by protein adsorption" Opt. Lett., 28, p. 272-274 (2003).

[56] Vollmer F., Arnold S., and Keng D. "Single virus detection from the reactive shift of a whispering-gallery mode" PNAS, 105, p. 20701–20704 (2008).

[57] Armani, D. K., Kippenberg, T. J., Spillane S. M., Vahala, K. J., "Ultra-high-Q toroid microcavity on a chip" Nature, 421, p. 925–928 (2003).

[58] Gayral B., Gérard J. M. , Lemaître A., Dupuis C., Manin L., Pelouard J. L., "High-Q wet-etched GaAs microdisks containing InAs quantum boxes" Appl. Phys. Lett. 75, p. 1908–1910 (1999).

[59] Kippenberg T. J. , Spillane S. M., Armani D. K., Vahala K. J., "Fabrication and coupling to planar high-Q silica disk microcavities "Appl. Phys. Lett., 83, p. 797-799 (2003).

[60] Srinivasan K., Barclay P. E., Painter O. "Fabrication-tolerant high quality factor photonic crystal microcavities" Opt. Express, 12, p.1458-1463 (2004).

[61] Yang L., Vahala K. J., "Gain functionalization of silica microresonators" Opt. Lett., 28, p. 592-594 (2004).

[62] Lebental M., Lauret J. S., Hierle R., Zyss J., "Highly directional stadium-shaped polymer microlasers" Appl. Phys. Lett. 88, p. 031108.1-3 (2006).

[63] Ben Messaoud T., "Effet laser en microcavités symétriques et asymétriques à base de polymère luminescent", PhD thesis, Ecole Normale Superieure du Cachan, Cachan, France, p.1-228 (2003).

[64] Lebental M., "Chaos quantique et micro-lasers organiques", PhD thesis, Université Paris Sud, Orsay, France, p.1-183 (2007).

[65] Djellali N., "Vers le contrôle géométrique de l'émission de microcavités laser à base de polymères", PhD thesis, Ecole Normale Superieure du Cachan, Cachan, France, p.1-144 (2009).

[66] Lozenko S. "Heavy metal ion sensors based on organic microcavity lasers", PhD thesis, Ecole Normale Superieure du Cachan, Cachan, France, p.1-125 (2011).

[67] Bogomolny E., Dubertrand R., Schmit C., "Trace formula for dielectric cavities: General properties" Phys. Rev. E, 78, p. 056202.1-16 (2008).

[68] Bogomolny E., Djellali N., Dubertrand R., Gozhyk I., Lebental M., Schmit C., Ulysse C., Zyss J., "Trace formula for dielectric cavities II: Regular, pseudo-integrable, and chaotic examples" Phys. Rev. E, 83, p. 036208.1-16 (2011).

[69] Valeur B., *Molecular fluorescence: Principles and Applications*, 4th edition, Wiley-VCH: Germany, 2007.

[70] Lakowicz J. R., *Principles of Fluorescence Spectroscopy*, 3rd edition, Springer: Singapore, 2006.

[71] Schaefer R. B., Willis C. R., "Quantum-mechanical theory of the organic-dye laser", Phys. Rew. A, 13, p. 1874-1890 (1976).

[72] Jacques V. , Murray J. D., Marquier F., Chauvat D., Grosshans F., Treussart F., Roch J.-F., "Enhancing single-molecule photostability by optical feedback from quantum jump detection" Appl. Phys. Lett., 93, p. 203307.1-3 (2008).

[73] Srinivas N. K. M. N., Rao S. V., Rao D. N., "Saturable and reverse saturable absorption of Rhodamine B in methanol and water" J. Opt. Soc. Am. B, 20, p. 2470-2479 (2003).

[74] Meyer M., Mialocq J.C., "Ground state and singlet excited state of laser dye DCM: dipole moments and solvent induced spectral shifts", Opt. Commun., 64, p. 264-268 (1987).

[75] Magde D., Wong R., Seybold P. G., "Fluorescence Quantum Yields and Their Relation to Lifetimes of Rhodamine 6G and Fluorescein in Nine Solvents: Improved Absolute Standards for Quantum Yields" Photochem. Photobiol., 75, p. 327–334 (2002).

[76] Green A. P., Buckley A., "Application of gauge R&R to the rigorous measurement of quantum yield in fluorescent organic solid state systems" Rev. Sci. Instrum., 83, p. 0731108.1-8 (2012).

[77] Lam S. Y., Damzen M. J., "Characterisation of solid-state dyes and their use as tunable laser amplifiers" Appl. Phys. B, 77, p. 577-584 (2003).

[78] Tagaya A. , Teramoto S., Nihei E., Sasaki K., Koike Y., "High-power and high-gain organic dye-doped polymer optical fiber amplifiers: novel techniques for preparation and spectral investigation" Appl. Opt., 36, p. 572-578 (1997).

[79] Penzkofer A., Sperber P., "Measurement of absorption cross-section in the long-wavelength region of the S0-S1 absorption band" Chem.Phys, 88, p.309-313 (1984).

[80] Ruckebusch C., Sliwa M., Pernot P., de Juan A., Tauler R., "Comprehensive data analysis of femtosecond transient absorption spectra: A review" J. Photochem. Photobiol. C Photochem. Rev., 13, p. 1–27 (2012).

[81] Koechner W., *Solid-State Laser Engineering*, 6th edition, Springer: USA, 2006.

[82] Siegman A. E., *Lasers*, 1st edition, University Science books: USA, 1986.

[83] McCumber D. E., "Einstein relation connecting broadband emission ans absorption spectra" Phys. Rew. A, 136, p. 954-957 (1964).

[84] Barnes W. L., Laming R. I., Tarbox E. J., Morkel P. L., "Absorption and emission cross-section of Er3+ doped silica fibers" IEEE Journal of Quantum Electronics, 27, p. 1004-1010 (1992).

[85] Fowler W.B., Dexter D.L., "Relation between absorption and emission probabilities in luminescent centers in ionic solids" Phys. Rev. A, 128, p. 2154-2165 (1962).

[86] Koch T. L., Chiu L. C., Yariv A., "Analysis and performance of a picosecond dye laser amplifier chain" J. Appl. Phys., 53, p. 6047-6059 (1982).

[87] Krupke W. F., Shinn M. D., Marion J. E., Caird J. A., Stokowski S. E., "Spectroscopic, optical, and thermomechanical properties of neodymium- and chromium-doped gadolinium scandium gallium garnet" J. Opt. Soc. Am. B, 3, p. 102–114 (1986).

[88] Peterson O. G., Webb J. P., McColgin W. C., Eberly J. H., "Organic Dye Laser Threshold " J. Appl. Phys., 42, p.1917-1928 (1971).

[89] Selenyi P., "Wide angle interferences and the nature of elementary light sources" Phys. Rev., 56, p. 477-479 (1939).

[90] Braslavsky E., "Glossary of terms used in photochemistry" Pure Appl. Chem, 79, p. 293-465 (2007).

[91] Bondarev S. L. , Knyukshto V. N., Stepuro V. I., Stupak A. P. Turban A. A. "Fluorescence and Electronic Structure of the Laser Dye DCM in Solutions and in Polymethylmethacrylate" J. Appl. Spectrosc., 71, p. 194-201 (2004).

[92] Gadella T. W. J., *FRET and FLIM Techniques*, Laboratory Techniques in Biochemistry and Molecular Biology, 33, Elsevier: Amsterdam, 2009.

[93] Le Floc'h V., Brasselet S., Roch J.-F., Zyss J. "Monitoring of Orientation in Molecular Ensemblesby Polarization Sensitive Nonlinear Microscopy" J. Phys. Chem. B, 107, p. 12403-12410 (2003).

[94] McClellan A. L., *Tables of experimental dipole moments*, W. H. Freeman and Company: San Francisco, 1963, p. 254.

[95] Kasarova S. N., Sultanova N. G., Ivanov C. D., Nikolov I. D. "Analysis of the dispersion of optical plastic materials" Optical Materials, 29, p.1481-1490 (2007).

[96] Palik E. D., *Handbook of Optical Constants of Solids*, Academic Press: Boston, 1985.

[97] Malitson I. H. "Comparison of the Refractive Index of Fused Silica" J. Opt. Soc. Am. A, 55, p. 1205-1208 (1965).

[98] Pauli W., *Pauli Lectures on physics. Volume 1. Electrodynamics*, Dover publications, Inc.: New York, USA, 2000.

[99] Unger H. G., *Planar Optical Waveguides and Fibres*, Oxford University Press: USA, 1993.

[100] Chemla D. S., Zyss J., *Nonlinear optical properties of organic molecules and crystals,* Academic Press: Orlando, USA, 1987.

[101] Lebental M., Djellali N., Arnaud C., Lauret J.-S., Zyss J., Dubertrand R., Schmit C., and Bogomolny E. "Inferring periodic orbits from spectra of simply shaped microlasers" Phys. Rev. A, 76, p. 023830.1-13 (2007).

[102] Thiel M., Fischer J., von Freymann G., Wegener M., "Direct laser writing of three-dimensional submicron structures using a continuous-wave laser at 532 nm", Appl. Phys. Lett., 97, p. 221102.1-3 (2010).

[103] Rabbani-Haghighi H., Forget S., Chénais S., Siove A., "Highly efficient, diffraction-limited laser emission from a vertical external-cavity surface-emitting organic laser", Opt. Lett., 35, p. 1968-1970 (2010).

[104] Chenais S., Forget S., "Recent advances in solid-state organic lasers", Polym. Int., 61, p. 390–406, (2012).

[105] Gozhyk I., Forget S., Chénais S., Ulysse C., Brosseau A., Méallet-Renault R., Clavier G., Pansu R., Zyss J., Lebental M., "Towards polarization controlled organic micro-lasers" Proc. SPIE 8258, 82580K, http://dx.doi.org/10.1117/12.909102. (2012).

[106] Rabbani-Haghighi H., Forget S., Siove A., Chénais S., "Analytical study of vertical external-cavity surface-emitting organic lasers" Eur. Phys. J. Appl. Phys., 56, p. 34108.1-7 (2011).

[107] Spitz J.-A., Yasukuni R. , Sandeau N., Takano M., Vachon J. - J., Meallet-Renault R., Pansu R. B., "Scanning-less wide-field single-photon counting device for fluorescence intensity, lifetime and time-resolved anisotropy imaging microscopy", J. Microsc. (Oxf.), 229, p. 104–114 (2008).

[108] Clayton A. H. A., Hanley Q.S., Arndt-Jovin D.J., Subramaniam V., Jovin T.M., "Dynamic Fluorescence Anisotropy Imaging Microscopy in the Frequency Domain (rFLIM)" Biophys. J ., 83, p. 1631-1649 (2002).

[109] Shaklee K.L., Nahory R.E., Leheny R.F., "Optical gain in semiconductors" J. Lumin., 7, p. 284-309 (1973).

[110] Dal Negro L., Bettotti P., Cazzanelli M., Pacifici D., Pavesi L., "Applicability conditions and experimental analysis of the variable stripe length method for gain measurements", Opt. Commun., 229, p. 337-348 (2004).

[111] Rabbani-Haghighi H., Forget S., Chénais S., Siove A., Castex M.-C., Ishow E., "Gain measurement and low-threshold laser operation in non-doped thin films made of a small-molecule organic red-emitter" Appl. Phys. Let., 95, p. 033305.1-3 (2009).

[112] Susdorf T., Del Agua D., Tyagi A., Penzkofer A., Garcia U. O., Sastre R., Costela A., Garcia-Moreno I., "Photophysical characterization of pyrromethene 597 laser dye in silicon-containing organic matrices", Appl. Phys. B, 86, p. 537–545 (2007).

[113] Wright D., Brasselet E., Zyss J., Langer G., Kern W., "Dye-doped organic distributed-feedback lasers with index and surface gratings: role of pump polarization and molecular orientation" J.Opt.Soc.Am. B, 21, p. 944-950 (2004).

[114] Visser T. D., Demeulenaere B., Haes J., Lenstra D., Baets R., Blok H., "Confinement and modal gain in dielectric waveguides" J. Lightwave Techn., 14, p. 885-887 (1996).

[115] Bittner S., Dietz B., Miski-Oglu M., Oria Iriarte P., Richter A., Schäfer F., "Experimental test of a two-dimensional approximation for dielectric microcavities" Phys. Rev. A , 80, p. 023825.1-9 (2009).

[116] Wang X., Linke R. A., Devlin G., Yokoyama H., "Lasing threshold behavior of microcavities: Observation by polarization and spectroscopic measurements" Phys. Rev. A, 47, p. R2488-R2491 (1993).

[117] Ramon M. C., Ariu M., Xia R., Bradley D. D. C., Reilly M. A., Marinelli C., Morgan C. N., Penty R. V., White I. H., "A characterization of Rhodamine 640 for optical amplification: Collinear pump and signal gain properties in solutions, thin-film polymer dispersions, and waveguides", J. Appl. Phys., 97, p. 073517.1-8 (2005).

[118] Lebental M., Lauret J.-S., Zyss J., Schmit C., Bogomolny E., "Directional emission of stadium-shaped microlasers" Phys. Rev. A, 75, p. 033806.1-5 (2007).

[119] Lozenko S., Djellali N., Gozhyk I., Delezoide C., Lautru J., Ulysse C., Zyss J., Lebental M., "Enhancing performance of polymer-based microlasers by a pedestal geometry" J. Appl. Phys., 111, p. 103116.1-9 (2012).

[120] Frateschi N., Kanjamala A., Levi A. F. J., Tanbun-Ek T., "Polarization of lasing emission in microdisk laser diodes" Appl. Phys. Lett., 66, p.1859-1861 (1995).

[121] Balaban M. V., Smotrova E. I., Shapoval O. V., Bulygin V. S., Nosich A. I., "Nystrom-type techniques for solving electromagnetics integral equations with smooth and singular kernels" Int. J. Numer. Model.: Electron. Networks, Devices and Fields, 25, DOI: 10.1002/jnm.1827, p. 1-22 (2012).

[122] Liang P., Chen Q., Zhang S., Lei J., "Polarization and power characteristics of pulsed dye lasers with transverse pumping" Appl. Phys. B, 55, p. 494-500 (1992).

[123] Yaroshenko O.I., "Theory of pulsed dye lasers with account of optical anisotropy and rotational diffusion" J. Opt. A, 5, p. 328-334 (2003).

[124] van de Berg S. A., 't Hooft G. W., Eliel E. R., "Orientational relaxation in polymer and dye solutions and its consequence for laser threshold" Chem. Phys. Lett., 347, p. 167-172 (2001).

[125] Dyumaev K. M., Manenkov A. A., Maslyukov A. P., Matyushin G. A., Nechitailo V. S., Prokhorov A. M., "Dyes in modified polymers: problems of photostability and conversion efficiency at high intensities" J. Opt. Soc. Am. B, 9, p. 143-151 (1992).

[126] Holzer W., Gratz H., Schmitt T., Penzkofer A., Costela A., Garcia-Moreno I., Sastre R., Duarte F. J., "Photo-physical characterization of rhodamine 6G in a 2-hydroxyethyl-methacrylate methyl-methacrylate copolymer" Chem. Phys., 256, p. 125-136 (2000).

[127] Yariv A., *Quantum Electronics*, 3rd ed., Wiley: USA, 1988.

[128] Casalboni M., de Matteis F., Merlo V., Prosposito P., Russo R., Schutzmann S., "1.3 m light amplification in dye-doped hybrid sol-gel channel waveguides" Appl. Phys. Lett., 83, p. 416-418 (2003).

[129] Lu W., Zhong B., Ma D., "Amplified spontaneous emission and gain from optically pumped films of dye-doped polymers" Appl. Opt., 43, p. 5074-5078 (2004).

[130] Costela A., Garcia O., Cerdan L., Garcia-Moreno I., Sastre R., "Amplified spontaneous emission and optical gain measurements from pyrromethene 567 – doped polymer waveguides and quasi-waveguides" Opt. Express, 16, p. 7023-7036 (2008).

[131] Calzado E. V., Villalvilla J. M., Boj P. G., Quintana J. A., Gómez R., Segura J. L., Díaz García M. A., "Amplified spontaneous emission in polymer films doped with a perylenediimide derivative" Appl. Opt., 46, p. 3836-3842 (2007).

[132] Oton C. J., Navarro-Urrios D., Capuj N. E., Ghulinyan M., Pavesi L., González-Pérez S., Lahoz F., Martin I. R., "Optical gain in dye-impregnated oxidized porous silicon waveguides," Appl. Phys. Lett., 89, p. 011107.1-3 (2006).

[133] Tagaya A., Koike Y., Nihei E., Teramoto S., Fujil K., Yamamoto T., Sasaki K., "Basic performance of an organic dye-doped polymer optical fiber amplifier" Appl. Opt., 34, p. 988-992 (1995).

[134] Peng G. D., Chu P. L., Xiong Z., Whitbread T., Chaplin R. P., "Broadband tunable optical amplification in Rhodamine B-doped step-index polymer optical fibre" Opt. Commun., 129, p. 353-357 (1996).

[135] Howell B. F., Kuzyk M. G., "Amplified spontaneous emission and recoverable photodegradation in polymer doped with Disperse Orange 11" J. Opt. Soc. Am. B, 19, p. 1790-1793 (2002).

[136] Zhang D., Ma D., "Improved amplified spontaneous emission by doping of green fluorescent dye C545T in red fluorescent dye DCJTB:PS polymer films" Appl. Opt., 46, p. 2996-3000 (2007).

[137] Jordan G., Flämmich M., Rüther M., Kobayashi T., Blau W. J., "Light amplification at 501 nm and large nanosecond optical gain in organic dye-doped polymeric waveguides" Appl. Phys. Lett., 88, p.161114.1-3 (2006).

[138] Kretsch K. P. , Belton C., Lipson S., Blau W. J., Henari F. Z., Rost H., Pfeiffer S., Teuschel A., Tillmann H., Hörhold H.-H., "Amplified spontaneous emission and optical gain spectra from stilbenoid and phenylene detrivative model compounds" J. Appl. Phys., 86, p. 6155-6159 (1999).

[139] Saraidarov T., Reisfeld R., Kazes M., Banin U., "Blue laser dye spectroscopic properties in sol-gel inorganic-organic hybrid films" Opt. Lett., 31, p. 356-358 (2006).

[140] McGehee M. D., Gupta R., Veenstra S., Miller E. K., Dıaz-Garcıa M. A., Heeger A. J., "Amplified spontaneous emission from photopumped films of a conjugated polymer" Phys. Rev. B, 58, p. 7035-7038 (1998).

[141] de la Rosa-Fox N., "Optical gain at room temperature in PPV-related materials" Opt. Mat., 12, p. 267-271 (1999).

[142] Lawrence J. R., Turnbull G. A., Samuel I. D. W., Richards G. J., Burn P. L., "Optical amplification in a first-generation dendritic organic semiconductor" Opt. Lett., 29, p. 869-871 (2004).

[143] Tsiminis G., Wang Y., Shaw P. E., Kanibolotsky A. L., Perepichka I. F., Dawson M. D., Skabara P. J., Turnbull G. A., and Samuel I. D. W. "Low-threshold organic laser based on an oligofluorene truxene with low optical losses" Appl. Phys. Lett., 94, p. 243304.1-3 (2009).

[144] Karve G., Bihari B., Chen R. T., "Demonstration of optical gain at 1.06 μm in a neodymium-doped polyimide waveguide" Appl. Phys. Lett., 77, p. 1253-1255 (2000).

[145] Wong W. H., Pun E. Y. B., Chan K. S., "Er3+–Yb3+ co-doped polymeric optical waveguide amplifiers" Appl. Phys. Lett., 84, p. 176-178 (2004).

[146] Shaklee K. L., Nahory R. E., Leheny R. F., "Optical gain in semiconductors" J. Lumin., 7, p. 284-309 (1973).

[147] Forget S., Chenais S., Tondelier D., Geffroy B., Gozhyk I., Lebental M., Ishow E., "Red-emitting fluorescent organic light emitting diodes with low sensitivity to self-quenching" J. Appl. Phys., 108, pp. 064509.1-6 (2010).

[148] Tsutsumi N., Kawahira T., Sakai W., "Amplified spontaneous emission and distributed feedback lasing from a conjugated compound in various polymer matrices" Appl. Phys. Lett., 83, p. 2533-2535 (2003).

[149] Mazumder M. M., Chen G., Kindlmann P. J., Chang R. K., Gillespie J. B., "Temperature-dependent wavelength shifts of dye lasing in microdroplets with a thermochromic additive" Opt. Lett., 20, p. 1668-1670 (1995).

[150] Taniguchi H., Tomisawa H., "Wavelength shifts of a suspended-single-droplet dye laser by successive laser pumping" Opt. Lett., 22, p. 1852-1854 (1994).

[151] Vernooy D. W., Ilchenko V. S., Mabuchi H., Streed E. W., Kimble H. J. "High-Q measurements of fused-silica microspheres in the near infrared" Opt. Lett., 23, p. 247–249 (1998).

[152] Wang Q. J., Yan C., Yu N., Unterhinninghofen J., Wiersig J., Pflügl C., Diehl L., Edamura T., Yamanishi M., Kan H., Capasso F., "Whispering-gallery mode resonators for highly unidirectional laser action" PNAS, 107, p. 22407–22412 (2010).

[153] Schwefel H. G. I., Rex N. B., Tureci H. E., Chang R. K., Stone A. D., Ben-Messaoud T., Zyss J., "Dramatic shape sensitivity of directional emission patterns from similarly deformed cylindrical polymer lasers" J. Opt. Soc. Am. B, 21, p. 923-934 (2004).

[154] Courvoisier F., Boutou V., Wolf J. P., Chang R. K., Zyss J., "Deciphering output coupling mechanisms in spiral microcavities with femtosecond light bullets" Opt. Lett., 30, p. 738-740 (2005).

[155] Dettmann C. P., Morozov G. V., Sieber M., Waalkens H., "Directional emission from an optical microdisk resonator with a point scatterer " EPL, 82, p. 34002.1-5 (2008).

[156] Djellali N., Gozhyk I., Owens D., Lozenko S., Lebental M., Lautru J., Ulysse C., Kippelen B., Zyss J., "Controlling the directional emission of holey organic microlasers" Appl. Phys. Lett., 95, p. 101108.1-3 (2009).

[157] Song Q., Fang W., Liu B., Ho S.-T., Solomon G. S., Cao H., "Chaotic microcavity laser with high quality factor and unidirectional output" Phys. Rev. A, 80, p. 041807R.1-4 (2009).

[158] Smotrova E. I., Nosich A. I., "Mathematical study of the 2-D lasing problem for the whispering-gallery modes in a circular dielectric microcavity," Opt. Quant. Electron., 36, p. 213-221 (2004).

[159] Smotrova E. I., Nosich A. I., "Simulation of Lasing Modes in a Kite-Shaped Microcavity Laser" proceedings of CAOL, Sevastopol, Ukraine, p.144-146 (2010).

[160] Smotrova E. I., Nosich A. I., "Directional Light Emission from a Kite-Shaped Microcavity Laser" proceedings of ICTON, Stockholm, Sweden, We.A4.4 (2011).

[161] Prazeres T. J. V., Fedorov A., Barbosa S. P., Martinho J. M. G., Berberan-Santos M. N., "Accurate Determination of the Limiting Anisotropy of Rhodamine 101. Implications for Its Use as a Fluorescence Polarization Standard" J. Phys. Chem. A , 112, p. 5034-5039 (2008).

[162] Tagaya A., Kobayashi T., Nakatsuka S., Nihei E., Sasaki K., Koike Y., "High gain and high power organic dye-doped polymer optical fiber amplifiers: absorption and emission cross sections and gain characteristics" Jpn. J. Appl. Phys., 36, p. 2705-2708 (1997).

[163] Boyer J. H., Haag A., Soong M.-L., Thangaraj K., Pavlopoulos T. G., "Laser action from 2,6,8-trisubstituted- 1,3,5,7-tetramethyl-pyrromethene-BF2 complexes: part 2" Appl. Opt., 30, p. 3788-3789 (1991).

[164] Humbs W., Zhang H., Glasbeek M., "Femtosecond fluorescence upconversion spectroscopy of vapor-deposited tris(8-hydroxyquinoline) aluminum" Chem. Phys., 254, p. 319-327 (2000).

[165] Schmidt E. Yu., Zorina N. V., Dvorko M. Yu., Protsuk N. I., Belyaeva K. V., Clavier G., Mallet-Renault R., Vu T. T., Mikhaleva A. I., Trofimov B. A., "A General Synthetic Strategy for the Design of New BODIPY Fluorophores Based on Pyrroles with Polycondensed Aromatic and Metallocene Substituents" Chem. Eur. J., 17, p. 3069 – 3073 (2011).

[166] Lawandy N. M., Balachandran R. M., Gomes A. S. L., Sauvain E., "Laser action in strongly scattering media" Lett. to Nature, 368, p. 436-438 (1994).

[167] Wiersma D. S., Bartolini P., Lagendijk A., Righini R., "Localization of light in a disordered medium" Lett. to Nature, 390, p. 671-673 (1997).

[168] Letokhov V. S., "Generation of light by a scattering medium with negative resonance absorption" Sov. Phys. JETP, 26, p.835– 840 (1968).

[169] John S., "Electromagnetic Absorption in a Disordered Medium near a Photon Mobility Edge" Phys. Rev. Lett, 53, p. 2169-2172 (1984).

[170] Wiersma D. S., "The physics and applications of random lasers" Nature Phys., 4, p. 359-367 (2008).

[171] Redding B., Choma M. A., Cao H., "Spatial coherence of random laser emission" Opt. Lett, 36, p. 3404–3406 (2011).

[172] Redding B., Choma M. A., Cao H., "Speckle-free laser imaging using random laser illumination" Nat. Photonics, 6, p. 355-359 (2012).

[173] Zaitsev O., Deych L., "Recent developments in the theory of multimode random lasers" J. Opt., 12, p. 024001.1-14 (2010).

[174] Cao H., "Review on latest developments in random lasers with coherent feedback" J. Phys. A: math. Gen., 38, p. 10497-10535 (2005).

[175] Cao H., Zhao Y. G., Ho S. T., Seelig E. W., Wang Q. H., Chang R. P. H., "Random Laser Action in Semiconductor Powder" Phys. Rev. Lett., 82, p. 2278-2281 (1999).

[176] Bahoura M., Morris K. J., Noginov M. A., "Threshold and slope efficiency of $Nd_{0.5}La_{0.5}Al_3(BO_3)_4$ ceramic random laser: effect of the pumped spot size" Opt. Commun., 201, p.405-411 (2002).

[177] Polson R. C., Chipouline A., Vardeny Z. V., "Random Lasing in π-Conjugated Films and Infiltrated Opals" Adv. Mater., 13, p. 760 (2001).

[178] van der Molen K. L., Tjerkstra R. W., Mosk A. P., Lagendijk A., "Spatial Extent of Random Laser Modes" Phys. Rev. Lett., 98, p. 143901.1-4 (2007).

[179] Wu X., Fang W., Yamilov A., Chabanov A. A., Asatryan A. A., Botten L. C., Cao H., "Random lasing in weakly scattering systems" Phys. Rev. A, 74, p. 053812.1-11 (2006).

[180] Mujumdar S., Türck V., Torre R., Wiersma D. S., "Chaotic behavior of a random laser with static disorder" Phys. Rev. A, 76, p. 033807.1-6 (2007).

[181] Andreasen J., Asatryan A. A., Botten L. C., Byrne M. A., Cao H., Ge L., Labonté L., Sebbah P., Stone A. D., Türeci H. E., Vanneste C., "Modes of random lasers" Adv. in Opt. and Photon., 13, p. 88-127 (2011).

[182] Wiersma D. S., "Random lasers explained?" Nature Photon., 3, p. 246-248 (2009).

[183] Vanneste C., Sebbah P., "Selective Excitation of Localized Modes in Active Random Media" Phys. Rev. Lett., 87, p.183903.1-4 (2001).

[184] Fallert J., Dietz R. J. B., Sartor J., Schneider D., Klingshirn C., H. Kalt, "Co-existence of strongly and weakly localized random laser modes" Nature Photon., 3, p. 279-282 (2009).

[185] Tulek A., Polson R. C., Vardeny Z. V., "Naturally occurring resonators in random lasing of π-conjugated polymer films" Nature Phys., 6, p.303-310 (2010).

[186] Cao H., Zhao Y. G., Ho S. T., Seeling E. W., Wang Q. H., Chang R. P. H, "Random laser action in semiconductor powder" Phys. Rev. Lett., 82, p.2278-2281 (1999).

[187] Kalusniak S., Wunsche H. J. , Henneberger F., "Random Semiconductor Lasers: Scattered versus Fabry-Perot Feedback" Phys. Rev. Lett., 106, p. 013901.1-4 (2011).

[188] Apalkov V. M., Raikh M. E., "Universal fluctuations of the random lasing threshold in a sample of a finite area" Phys. Rev. B, 71, p. 054203.1-8 (2005).

[189] Lang R.J., Yariv A., "An exact formulation of coupled-mode theory for coupled-cavity lasers" IEEE Journal of Quantum Electronics, 24, p. 66-72 (1988).

[190] Ryu J.-W., Lee S.-Y., Kim C.-M., and Park Y.-J., "Directional interacting whispering-gallery modes in coupled dielectric microdisks" Phys. Rev. A, 74, p. 013804.1-7 (2006).

[191] Liu B., Shakouri A., Bowers J. E., "Passive microring-resonator-coupled lasers" Appl. Phys. Lett., 79, p. 3561-3563 (2001).

[192] Liang W., Yang L., Poon J. K. S., Huang Y., Vahala K. J., and Yariv A., "Transmission characteristics of a Fabry–Perot etalon–microtoroid resonator coupled system" Opt. Lett., 31, p. 510-512 (2006).

[193] Dumeige Y., Trébaol S., Tavernier H., Féron P., "Dispersion properties of high-Q passive and active single or coupled resonators" Proc. of SPIE, 7226, p. 72260S.1-13 (2009).

[194] Mookherjea S., Yariv A., "Coupled Resonator Optical Waveguides" IEEE Journ. of Select. Topics in Quant. Electron.,8, p. 448-456 (2002).

[195] Liertzer M., Ge L., Cerjan A., Stone A. D., Türeci H. E., and Rotter S., "Pump-Induced Exceptional Points in Lasers" Phys. Rev. Lett., 108, p.173901.1-5 (2012).

[196] Hattori T., Taira T., Era M., Tsutsui T., Saito S., "Highly efficient electroluminescence from a heterostructure device combined with emissive layered-perovskite and an electron-transporting organic compound" Chem. Phys. Lett., 254, p. 103–108 (1996).

[197] Era M., Morimoto S., Tsutsui T., Saito S., "Electroluminsecence device using two dimensional semiconductor $(C_6H_5C_2H_4NH_3)_2PbI_4$ as an emitter" Synth. Met., 71, p. 2013-2014 (1995).

[198] Era M., Morimoto S., Tsutsui T., Saito S., "Organic-inorganic heterostructure electroluminescent device using a layered perovskite semiconductor $(C_6H_5C_2H_4NH_3)_2PbI_4$" Appl. Phys. Lett., 65, p. 676-678 (1994).

[199] Mitzi D. B., Felld C. A., Harrison W. T. A., Guloy A. M., "Conducting tin halides with a layered organic-based perovskyte structure" Nature, 369, p. 467-469 (1994).

[200] Chondroudis K., Mitzi D. B., "Electroluminescence from an Organic-Inorganic Perovskite Incorporating a Quaterthiophene Dye within Lead Hallide Perovskyte Layers" Chem. Mater., p. 3028-3030 (1999).

[201] Mitzi D. B., "Templating and structural engineering in organic-inorganic perovskytes" J. Chem. Soc., Dalton Trans., p.1-12 (2001).

[202] Mitzi D. B., Chondroudis K., Kagan C. R., "Organic-inorganic electronics" IBM. J. Res. & Dev., 45, p. 29-45 (2001).

[203] Kagan C. R., Mitzi D. B., Dimitrakopoulos C. D., "Organic-Inorganic Hybrid Materials as Semiconducting Channels in Thin-Film Field-Effect Transistors" Science, p. 945-947 (1999).

[204] Zhang S., Lanty G., Lauret J.-S., Deleporte E., Audebert P., Galmiche L., "" Acta Mater., 57, p. 3301-3309 (2009).

[205] Mitzi D.B., Feild C.A., Schlesinger Z., Laibowitz R.B.,"Transport, Optical, and Magnetic Properties of the Conducting Halide Perovskite $CH_3NH_3SnI_3$" J. Solid State Chem., 114, p. 159–163 (1995).

[206] Dimitrakopoulos C. D., Malenfant P. R. L., "Organic thin film transistors for large area electronics" Adv. Mater., 14, p. 99-117 (2002).

[207] Cicoira F., Santano C., "Organic light emitting field effect transistors: advances and perspectives" Adv. Funct. Mater., 17, p. 3421-3434 (2007).

[208] Capelli R., Toffanin S., Generali G., Usta H., Facchetti A., Muccini M., "Organic light-emitting transistors with an efficiency that outperforms the equivalent light-emitting diodes" Nat. Mat., 9, p. 496–503 (2010).

Polarization properties of solid-state organic lasers

I. Gozhyk,[1,*] G. Clavier,[2] R. Méallet-Renault,[2] M. Dvorko,[2] R. Pansu,[2] J.-F. Audibert,[2] A. Brosseau,[2] C. Lafargue,[1] V. Tsvirkun,[1] S. Lozenko,[1] S. Forget,[3] S. Chénais,[3] C. Ulysse,[4] J. Zyss,[1] and M. Lebental[1]

[1]*Laboratoire de Photonique Quantique et Moléculaire, CNRS UMR 8537, Institut d'Alembert FR 3242, Ecole Normale Supérieure de Cachan, 61 Avenue du Président Wilson, F-94235 Cachan, France*

[2]*Laboratoire de Photophysique et Photochimie Supramoléculaires et Macromoléculaires, CNRS UMR 8531, Institut d'Alembert FR 3242, Ecole Normale Supérieure de Cachan, F-94235 Cachan, France*

[3]*Université Paris 13, Sorbonne Paris Cité, Laboratoire de Physique des Lasers, CNRS UMR 7538, F-93430, Villetaneuse, France*

[4]*Laboratoire de Photonique et Nanostructures, CNRS UPR20, Route de Nozay, F-91460 Marcoussis, France*

(Received 24 July 2012; published 12 October 2012)

The polarization states of lasers are crucial issues both for practical applications and fundamental research. In general, they depend in a combined manner on the properties of the gain material and on the structure of the electromagnetic modes. In this paper, we address this issue in the case of solid-state organic lasers, a technology which enables one to vary independently gain and mode properties. Different kinds of resonators are investigated: in-plane microresonators with Fabry-Perot, square, pentagon, stadium, disk, and kite shapes, and external vertical resonators. The degree of polarization P is measured in each case. It is shown that although transverse electric modes prevail generally ($P > 0$), the kite-shaped microlaser generates negative values for P (i.e., a flip of the dominant polarization which becomes mostly transverse magnetic polarized). In general, we demonstrate that both the pump polarization and the resonator geometry can be used to tailor the polarization of organic lasers. With this aim in view, we, at last, investigate two other degrees of freedom, namely upon using resonant energy transfer and upon pumping the laser dye to a higher excited state. We then demonstrate that significantly lower P factors can be obtained.

DOI: 10.1103/PhysRevA.86.043817 PACS number(s): 42.55.Sa, 42.55.Mv, 42.60.Da, 05.45.Mt

I. INTRODUCTION

Light-matter coupling issues are firmly based on quantum electrodynamics foundations. However, practical consequences on real systems are often difficult to derive due to sometimes complicated quantum formulations. Maxwell-Bloch equations provide a semiclassical expression more appropriate for lasers [1], which are usually macro- or mesoscopic systems. The resulting nonlinear coupled equations could be handled by means of numerical simulations, which nevertheless face major problems for large systems due to huge meshes. This obstacle is even increased when polarization states of electromagnetic modes are involved, since they require the treatment of three-dimensional and vectorial Maxwell equations. And yet, polarization remains a key point for many photonics components.

We would like to address this issue by way of micron- and millimeter-sized lasers of various resonator geometries, which are out of reach of full electromagnetic simulations due to their large scale, but where validity of the semiclassical (or geometrical optics) limit is expected to provide a simplified insight [2]. In this work, we propose to evidence and analyze polarization effects in solid-state organic laser systems, and demonstrate the possibility to modify the output polarization by playing on cavity shape or on material related features.

Previous works have been devoted to microresonators of circular geometry [3–5], coated fibers [6,7], and distributed feedback lasers (see, for instance, [8]). In this work, we focus on vertical emitting devices [vertical external cavity surface emitting organic lasers (VECSOLs) [9]], where the properties of the gain material can be quite easily decoupled from the cavity shape, and on thin-film planar microlasers of various contours, such as square, pentagon, kite, etc. Actually planar microresonators have become widely used in photonics systems, from integrated optics [10] to fundamental physics (see, for instance, [11] or [12]). But in general, their use is limited to Fabry-Perot (i.e., the resonance occurs between flat parallel edges) or circular shapes, namely spheres, disks, rings, or tori, while a great variety of geometries (polygons, stadium, etc.) can be easily fabricated with nanometric etching quality, providing specific advantages, such as a higher directivity of emission [13,14], a better coupling to waveguides [15], or a high stability of modes versus perturbations [16]. The studies of these geometrical features remain to be improved—in particular when the polarization of modes is involved—and should lead to optimized devices for both fundamental and applied photonics. In particular, we will show hereafter that in-plane polarization is in general favored by gain and propagation, whereas out-of-plane polarization could be of crucial importance for applications, like sensing [17], for instance. We will then propose different ways to monitor the ratio of polarizations, making use either of the gain or of the resonator shape.

The experiments were carried out with solid-state organic lasers [18]. Their interest for this study is twofold. First, organic technology ensures a high etching quality from a relatively fast and easy fabrication, which enables one to investigate a great variety of resonator shapes. Secondly, the flexibility of organic chemistry allows one to explore various gain media in different pumping schemes in order to monitor the polarization states, as demonstrated in Secs. VI and VII. The analysis of the experimental results is then performed in the framework of "polarization spectroscopy," a domain

*igozhyk@lpqm.ens-cachan.fr

specific to organic materials, which matured in the late 1980s and has given birth to various applications in polymer physics or biology (see [19] and [20] for a review). This domain is based on the fluorescence anisotropy of dye molecules. A few theoretical articles [21–23] extend its range to the nonlinear regime of stimulated emission and lasers, as it was soon evidenced that unlike most other solid-state laser media, the output polarization of a solid-state dye laser does not only depend on the anisotropy of the gain medium or on the polarization-dependant losses due to the cavity, but also depends on the pump beam polarization [21,22]. The objective of this paper is to better understand the polarization characteristics of planar organic microresonators, in order to tailor the polarization output of these devices.

The paper is organized as follows. The experimental configurations are described in Sec. II. Basics on fluorescence anisotropy are then recalled in Sec. III, a more detailed analysis being postponed to the appendixes. The specific case of amplified spontaneous emission (ASE) is dealt with in Sec. IV. Then polarizations of laser modes are reported and discussed for various cavity shapes in Sec. V. These results evidence a strong influence of the polarization of the pump beam as expected, which prevents populating numerous families of modes, that would be otherwise available. In order to release this constraint and improve the accessibility of modes, we propose and demonstrate two different methods to tailor the polarization of the emission: on the one hand, a nonradiative energy transfer from an excited molecule to the dye laser (Sec. VI) and, on the other hand, the direct pumping to a higher excited state of the dye molecule (Sec. VII).

II. EXPERIMENTAL SETUPS

In this paper, we consider thin-film-based lasers in two different configurations represented in Fig. 1. The gain layer is made of a spin-coated poly(methylmethacrylate) (PMMA)

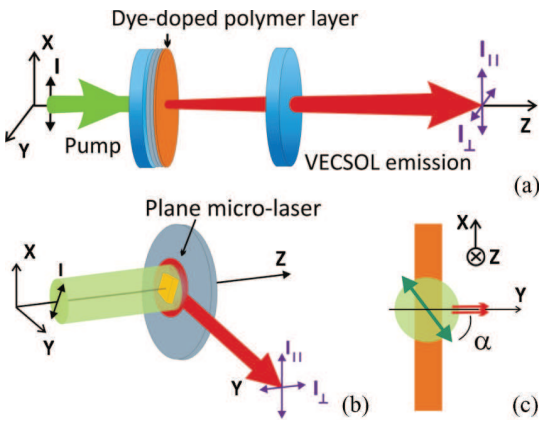

FIG. 1. (Color online) Experimental configurations of the solid-state organic lasers: (a) vertical emission (VECSOL) and (b) planar microlaser (oblique view); (c) planar microlaser geometry from a top view (xy plane), indicating the α angle between the polarization of the pump beam and the direction of observation (y), illustrated with the case of a Fabry-Perot cavity. For (a)–(c) the colors are green for pumping and red for emission.

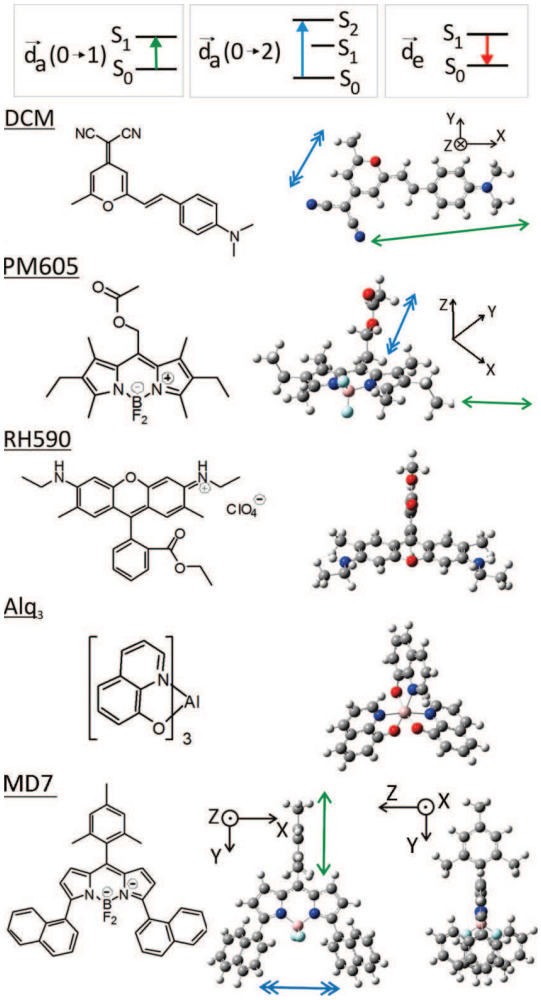

FIG. 2. (Color online) The molecular energy levels involved in the transitions are schematically shown on the top of the figure. Dye molecules involved in the study are as follows: DCM, PM605, RH590, Alq_3, and MD7. MD7 is a homemade modified pyrromethene. For DCM, PM605, and MD7 the calculated absorption transition dipoles are indicated with a single arrow for the $S_0 \rightarrow S_1$ transition and with a double arrow for the $S_0 \rightarrow S_2$ transition. For PM605, two transitions with similar oscillator strengths are involved when pumped at 355 nm. One of the absorption dipoles is parallel to the absorption dipole of the $S_0 \rightarrow S_1$ transition and is thus not represented.

film doped with laser dyes,[1] which are either commercial molecules, namely DCM, pyrromethene 605 (PM605), and rhodamine 590 (RH590), or noncommercial dye like MD7 [24]. Their molecular structures are presented in Fig. 2. To optimize the lasing efficiency, the concentration is typically 5% wt for in-plane microlasers and 1% wt for VECSOL, and the layer thickness is 0.6 μm and 20 μm, respectively. In case of VECSOL, the substrate is directly the back mirror of the cavity, while for in-plane microresonators it is a commercial silicon wafer with a 2-μm silica buffer layer.

[1]In this paper, each commercial dye was bought from Exciton, and PMMA from MicroChem, 6% wt in anisole 495 000 average chain length for in-plane microlasers and 15% wt 950 000 for VECSOL.

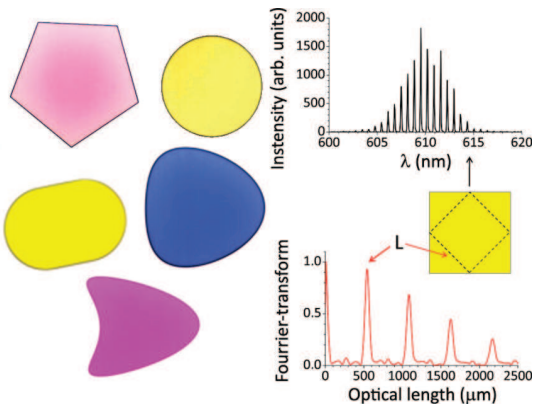

FIG. 3. (Color online) (a) Optical microscope photos of planar microlasers, which are investigated in this paper. Scales are 0.6 μm for the thickness and about 100 μm in-plane. Colors depend on the dye molecules. (b) Typical experimental spectrum of a square microlaser. (c) Fourier transform of the spectrum in (b). The position of the first peak indicates the optical length L of the periodic orbit (i.e., diamond) drawn in the inset, according to the data process described in [26]).

The specificities of each device are depicted in Fig. 1. In VECSOL [Fig. 1(a)], the cavity feedback is ensured by a curved dielectric mirror [9]. The pump beam radius is matched to the fundamental TEM00 cavity mode, which is much smaller than the diameter of the mirrors. So we assume a rotational symmetry of the setup, which is only broken by the polarization of the pump beam. In this sense, this geometry enables studying the sole influence of lasing gain medium on polarization, irrespective of any cavity-related effect. On the contrary, it is the geometries of the in-plane microlasers [Fig. 1(b)] which determines the types of modes which are lasing. Such cavities are fabricated from the single gain layer by electron-beam lithography, which ensures nanometric etching quality [25]. Arbitrary cavity contours can be designed [see Fig. 3(a)] to act as resonators. The emission of a single cavity is then collected in its plane.

Both types of devices are pumped with a pulsed linearly polarized frequency-doubled Nd:YAG laser (532 nm, 500 ps, 10 Hz). The emission is injected via a fiber to a spectrometer connected to a cooled CCD camera, allowing one to infer the lasing modes from their spectrum [see Figs. 3(b) and 3(c)] [26]. A polarizer is set between the device under study and the fiber to project the electric field of the far-field emitted beam onto two orthogonal directions, called $I_{||}$ and $I_{\perp}$ (see Fig. 1).

The VECSOL configuration is close to the usual geometry in fluorescence anisotropy measurements, since $I_{||}$ is registered in the direction parallel to the pump polarization and $I_{\perp}$ in the orthogonal direction. On the contrary, the case of in-plane microlasers is quite different. Actually the pump beam propagates perpendicularly to the cavity plane and its size is much larger than a single cavity, so that the pump intensity may be considered constant over one resonator. Thus although the polarization of the pump beam always lies within the cavity plane, the emission may be collected along any line within the cavity plane, which means that $I_{||}$ is not always parallel to the pump polarization. However, we uniformize the terminology for the two configurations by calling $I_{||}$ and $I_{\perp}$ as well, the components polarized within ($I_{||}$) and perpendicularly ($I_{\perp}$) to the film plane [Fig. 1(b)]. In order to describe the orientation of the pump polarization within the cavity plane, we also introduce the angle α defined as the angle between the pump polarization and the direction of observation [see Fig. 1(c)].

III. BASICS IN EMISSION ANISOTROPY

Before investigating stimulated emission in the following sections, we first review a few basic features in fluorescence anisotropy in connection with our specific solid-state systems.

An isotropic ensemble of dye molecules is known to emit light with a nontrivial polarization state. This phenomenon is known as fluorescence anisotropy and has generated a broad literature (see [19] and [20] for a review). If the pump laser is linearly polarized, then the fluorescence emission is not *a priori* equally polarized along the directions parallel $I_{||}$ and perpendicular $I_{\perp}$ to the polarization of the pump (see Fig. 1 for notations). This anisotropy can be quantified by the degree of polarization[2]:

$$P = \frac{I_{||} - I_{\perp}}{I_{||} + I_{\perp}},$$

which is zero for equal polarizations, and otherwise remains between -1 and 1 from a mathematical point of view. However its range is restricted due to physical limitations as discussed later in this section.

In experiments, the overall inaccuracy can be estimated to less than 0.05 unit for P. The P value can be inferred after integration over the whole spectrum for each polarization or by considering a specific mode, both methods leading to almost the same value if a single mode family is involved.

In a liquid solution, the dye molecules are free to rotate. The degree of polarization P is then zero, except at short delays after the excitation pulse. Once doped into a rigid polymer matrix, like PMMA, the fluorophores are not yet able to move, either by thermal or Weigert effects [27,28], and P could then be nonzero even under a stationary pumping. However if the dye concentration is high enough, Förster resonant energy transfer (RET) occurs between nearby molecules and tends to isotropize the emitted fluorescence under continuous excitation [29]. However, we noticed that RET is no longer a limitation to the emission anisotropy in the case of stimulated emission. This observation could be explained by the difference of time scales, which is of the order of the fluorescence lifetime (i.e., nanoseconds) for RET [19,20] and could be as short as a few picoseconds for stimulated emission [30,31]. In this paper, we consider various dye molecules doped in a rigid PMMA matrix in a stimulated emission regime. We then assume that the fluorophores are not rotating and moreover that RET does not occur between laser dye molecules under subnanosecond pumping conditions.

To deal with lasing, a full nonlinear approach should be derived. Some models were already developed [21–23], but as a robust theory is not yet mature, we prefer to resort here

[2]Sometimes, the anisotropy parameter $r = (I_{||} - I_{\perp})/(I_{||} + 2I_{\perp})$ is used. But in our experiments, no longitudinal component of the electric field is expected in the far field, so the normalized factor is $I_{||} + I_{\perp}$ and not $I_{||} + 2I_{\perp}$.

to a phenomenological approach. We assume that the dye molecules can be modeled as independent emitters, and only consider the influence of the geometry of the laser cavity. We will show hereafter that in general this simplified approach is able to capture the main physical features.

The sample is supposed to be exposed to a linearly polarized light. The probability that a dye molecule absorbs the pump light is proportional to $\cos^2(\chi)$, where χ is the angle between the pump polarization and the absorption transition dipole $\vec{d}_a$ of the molecule. Then the emission of the molecule is assumed to be that of an emitting transition dipole $\vec{d}_e$ in the far field. The dipoles $\vec{d}_a$ and $\vec{d}_e$ depend on the transitions which are involved in the absorption and subsequent emission processes. In this paper, we will consider the electronic transitions $S_0 \rightarrow S_1$ and $S_0 \rightarrow S_2$ for absorption, and $S_1 \rightarrow S_0$ for emission (see Fig. 2). Each electronic level S_i is broaden by vibrations, which allows one to consider dye molecules as an effective four-level laser system [32]. In general, there is an angle β between $\vec{d}_a$ and $\vec{d}_e$, which depends on the molecular structure. A more detailed account is given in Appendix A and some $\vec{d}_a$ were calculated with GAUSSIAN software and reported in Fig. 2.

The total electric field is then obtained from the integration over the orientations of the fluorophores. The distribution of these orientations is not *a priori* isotropic due to polymer stress [33] during spin coating, as it was reported for π conjugated polymers [34,35]. However, it was observed that PMMA does not present an alignment due to spin coating [36] and that the dye molecules embedded into PMMA remain isotropically distributed [37].[3] Hence we only consider an isotropic distribution of dye molecules. The case of an anisotropic distribution of dyes is theoretically addressed elsewhere [38], and checked experimentally in [31].

The analytical calculation of P in both configurations is detailed in Appendix B. For the VECSOL case, according to our model, P depends only on the angle β between the absorption and emission transition moments of the dye molecule:

$$P_{\mathrm{VECSOL}} = \frac{3\cos^2\beta - 1}{3 + \cos^2\beta}. \tag{1}$$

For the in-plane geometry, P depends also on the angle α of the pump polarization within the gain layer, and on the specific resonance which is excited. For the bulk case, we show in Appendix B that the expression of P is the following:

$$P_{\mathrm{in\,plane}} = \frac{(3\cos^2\beta - 1)(1 - \cos 2\alpha)}{7 - \cos^2\beta - \cos 2\alpha(3\cos^2\beta - 1)}. \tag{2}$$

It is plotted versus the angle β in Fig. 4 for various angles α. The degrees of polarization P in the in-plane and VECSOL configurations are then not equal, except for $\alpha = \pi/2$. However, the general meaning is similar and the calculations detailed in Appendix B lead to similar conclusions for both: $I_\perp$ does not depend on the orientation of the pump polarization α, and gets maximum (and P minimum) when $\beta \rightarrow \pi/2$. The practical case of stimulated emission in specific resonator geometries is developed in the following sections.

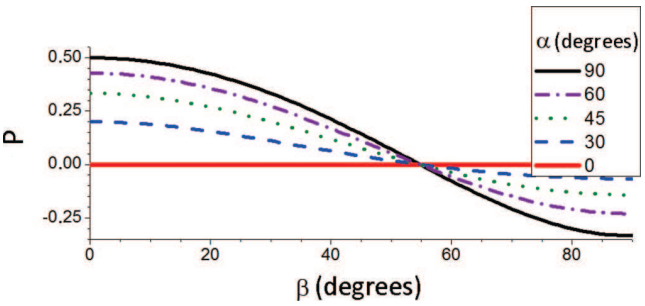

FIG. 4. (Color online) Degree of polarization $P_{\mathrm{in\,plane}}$ versus the angle β between the absorption and emission dipoles, following expression (2). For $\alpha = \pi/2$, $P_{\mathrm{in\,plane}} = P_{\mathrm{VESCOL}}$.

IV. AMPLIFIED SPONTANEOUS EMISSION (IN PLANAR CONFIGURATION)

The emission anisotropy is jointly determined by the molecular properties and the electromagnetic modes which sustain the generated light. This section deals with amplified spontaneous emission (ASE), which involves the nonlinear process of stimulated emission, but does not depend on the actual resonator shape. In ASE conditions, the emission is spontaneously generated within the excited gain medium and amplified by a single path propagation without any feedback.

ASE experiments were carried out in the in-plane configuration, but without any cavity shaping. A usual DCM-PMMA layer was pumped prior to any etching and the emission collected in-plane as described in Sec. II. Figure 5 (circles) shows, however, that P is always higher than the value expected from the fluorescence model ($P < 0.5$ for any angle β as seen in Fig. 4), and increases with the pump intensity [39].[4] Actually the anisotropy value defined from a fluorescence process in the previous section represents the anisotropy well below the ASE threshold, whenever spontaneous emission is dominant over stimulated emission. This fluorescence is mainly polarized in plane, since the pump polarization lies within the plane, and so the dyes oriented such as $\vec{d}_a$ lying in-plane are predominantly excited. And as β is small in general for an S_0-S_1 transition, they predominantly emit in-plane. As the ASE is fed by spontaneous photons that have a dominant polarization, the excited molecules are prone to mostly emit photons with this given polarization. Thus the avalanche effect amplifies the difference between the polarized components, $I_{||}$ is favored [8], and then P increases with the pump intensity.

The previous discussion summons up the properties of the dye molecules to explain the prevalence of $I_{||}$ over $I_\perp$. Furthermore, even in the absence of cavity, photons propagate within specific electromagnetic modes, which also tends to

[3]The molecular weight of the PMMA used in [36] is 15 000, while it is 495 000 in our experiments. It is not specified in [37]. This parameter could be relevant for the organization of the layer by spin-coating. The case of an anisotropic distribution of fluorophores was theoretically dealt with in [38].

[4]At low pump intensities, the ASE data are not shown on Fig. 5 due to low output intensity and thus high experimental uncertainties.

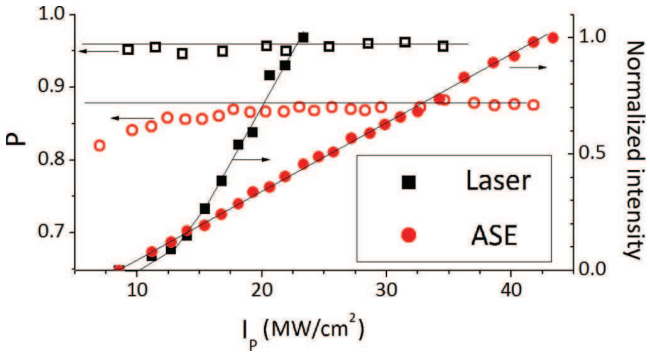

FIG. 5. (Color online) Degree of polarization P versus the pump intensity I_p (per pulse) for ASE and Fabry-Perot in planar microresonator configuration for a DCM-PMMA layer. The intensity of emission versus I_p is presented for comparison. Thin lines are drawn for guiding eyes.

enhance $I_{||}$. Therefore, in order to get a more comprehensive interpretation, an analysis of the modes must be performed.

In such in-plane configuration with infinite layers, the approximation of the effective refractive index applies. The electromagnetic field can then be split into two independent sets of modes with independent polarizations, traditionally labeled transverse electric (TE) [respectively, transverse magnetic (TM)] if there is no electric (respectively, magnetic) component along the z direction (see Fig. 6). It must be pointed out that, as the polarizer used for analysis is selective on the electric field, a measure of $I_\perp$ is sensitive only to TM modes (E_z component), while $I_{||}$ should *a priori* gather both TE and TM mode contributions (E_x component; see Fig. 6). In the case of ASE experiments with infinite layers, the electric field of the TM mode is measured in the far field and is thus purely polarized along the z direction (i.e., no E_x component). The strict equivalence TE-$I_{||}$ and TM-$I_\perp$ is then valid.

The parameters of our samples are gathered in Fig. 6. The bulk refractive index of PMMA is 1.49 at 600 nm and increased slightly with the addition of a dye, for instance, $n = 1.54$ for 5% wt DCM in PMMA. Assuming an infinite silica layer, then there exists a single mode for each polarization (one TE and one TM) propagating inside the doped PMMA layer, both with close effective refractive index, $n_{\text{eff}} \simeq 1.50$. However the tiny differences are enhanced by the nonlinearity of stimulated emission. First, the effective index of TE is slightly higher than that of TM ($\Delta n \simeq 5 \times 10^{-3}$), which means that the TE mode is more localized inside the gain layer [40] and thus

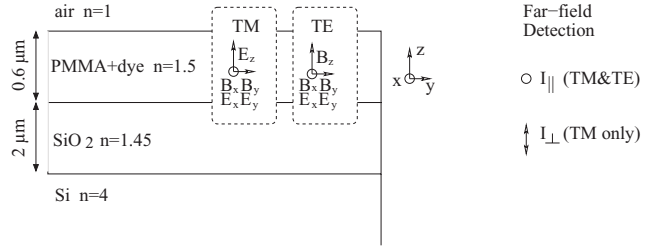

FIG. 6. Scheme of a sample slice in in-plane configuration (not at scale), with approximative values of bulk refractive indexes at 600 nm.

more amplified. Secondly, the silica layer is finite. Losses through the silicon layer are then altering mostly the TM mode, which is less confined into the PMMA propagating layer. These arguments show that mode considerations (without molecular influence) can explain the discrepancy between both components.

So even for ASE, which is the simplest case involving stimulated emission, both molecular properties and mode propagation combine to enhance $I_{||}$, whatever is the dye laser. At low pump intensity, $P_{\text{DCM}} = 0.8$ and $P_{\text{PM605}} = 0.65$. Both P are higher than 0.5, which is the maximal value expected for an ensemble of isotropically fluorescent dipoles, for any β. In the general case of an arbitrary shape of resonator, the effective index approximation fails at the boundary (since the layers are not infinite) [41], and the measure of P may provide an insight into the electromagnetic modes which coexist within the cavity as will be considered in the next section.

V. INFLUENCE OF THE CAVITY SHAPE

The resonator modifies the degree of polarization in two different ways. It creates a feedback which enhances further the dominant component (i.e., $I_{||}$). But at the same time, for in-plane microcavities, reflections at the boundary couple components of the electromagnetic field and lead to a partial redistribution of the energy.

The simplest case to consider is the Fabry-Perot cavity (i.e., the classical two-mirrors cavity), in which polarization states have been extensively studied with liquid dye lasers (see, for instance, [42–44]), but more rarely in the solid state [39,45].

1. VECSOLs

In VECSOL configuration with a RH640-PMMA layer, the degree of polarization P equals to unity for a linearly polarized pump beam, which means that the lasing emission is totally polarized, like the pump. Moreover when the pump beam is circularly polarized, the lasing emission is not polarized, which means that there is no noticeable difference between the $I_{||}$ and $I_\perp$ components, and a quarter wave plate added on the beam path does not allow to recover a preferential polarization direction. These results were recorded for a 1-cm-long cavity and above threshold. According to Refs. [39,44,46,47], cavity length and pump intensity should be relevant parameters, since they monitor the build-up time of the modes [48]. Work is in progress to get a more comprehensive understanding of the polarization states in this simple geometry which is rotational invariant [axis z; see Fig. 1(a)].

Another experiment was carried out with a (5% wt) DCM-PMMA layer, inserting a glass plate inside the cavity at Brewster angle to force the emission polarization, and then turning the polarization of the pump beam by a variable angle α' (see inset of Fig. 7 for notation). The laser threshold for $\alpha' = \pi/2$ was found twice higher than for $\alpha' = 0$. Then the pump intensity is fixed just above the higher threshold and the emitted intensity is recorded versus α'. The results are summarized with squares in Fig. 7 and show strong modulations. The curve in Fig. 7 was inferred from the calculations presented in Appendix B. Actually, the geometry of this system is similar to that of the in-plane configuration with $\alpha = \alpha'$. In the case of fluorescence, the emitted intensity

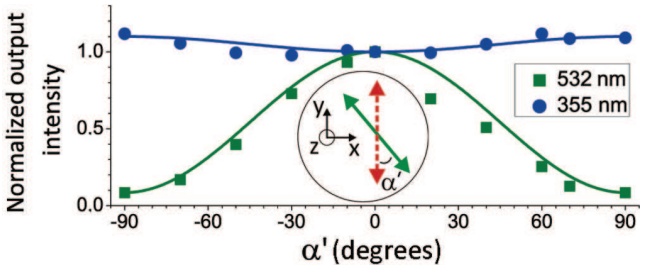

FIG. 7. (Color online) Normalized intensity emitted from a VECSOL with a PMMA-DCM gain material, versus the angle α' of the pump polarization. Comparison between a 532-nm pump (green, squares) and a 355-nm pump (blue, circles), after corrections from bleaching. The curves are fitted according to Eq. (3). (Inset) Scheme of a VECSOL section. The polarization of emission is fixed and represented as a dotted red arrow, while the linear pump polarization is shown as a green continuous arrow.

should then be predicted by Eq. (B3), which is a linear function of $\cos 2\alpha'$. So,

$$\frac{I(\alpha')}{I(\alpha'=0)} = A + B\cos 2\alpha', \tag{3}$$

where $\frac{A}{B} = \frac{3+\cos^2\beta}{1-3\cos^2\beta}$. Equation (3) is plotted in Fig. 7 up to a scale parameter and shows a good agreement with experiments, which indicates that the VECSOL is working not far from a linear regime, since Eq. (3) is inferred from fluorescence predictions.

2. *Planar microlasers*

In the case of the in-plane configuration, the symmetry is naturally broken between $I_{||}$ and $I_{\perp}$. Actually TE and TM polarizations experience slightly different losses during propagation, as mentioned in the previous section. Moreover, their reflection coefficients at the microresonator boundaries could be different, even at normal incidence, due to the thinness of the layer [49]. In any case, P is recorded at a higher level

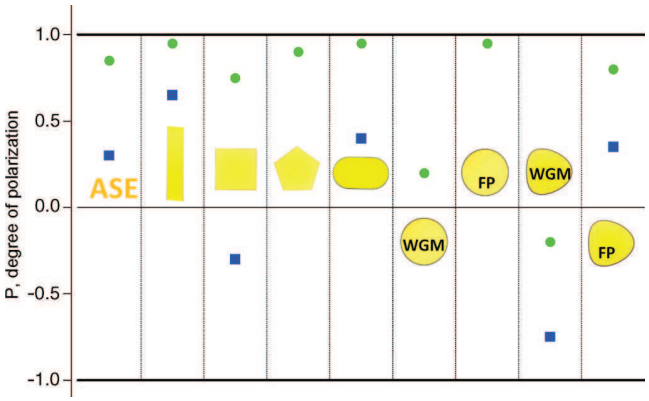

FIG. 8. (Color online) Degree of polarization P in connection with the resonator shape for a DCM-PMMA layer pumped at 532 nm (green disks) and a MD7-PMMA layer pumped at 355 nm (blue squares). (From left to right) ASE, Fabry-Perot, square (diamond modes), pentagon (inscribed pentagon), stadium (WGM), disk (WGM), disk (Fabry-Perot modes), kite (WGM), and kite (Fabry-Perot modes).

TABLE I. Comparison of P obtained from ASE and various shapes of microlasers in the in-plane configuration, depending on the dye laser and the wavelength of excitation. Some cavity shapes (e.g., disk and pentagon) were not available for each laser dye presented in this table. Moreover lasing under the UV pump was not achieved systematically for each shape.

	532 nm			355 nm		
P	DCM	PM605	MD7	DCM	DCM-Alq$_3$	MD7
ASE	0.85	0.65	0.6	0.1	0.05	0.3
Fabry-Perot	0.95	0.95	0.9	0.9	0.9	0.65
Square	0.75	0.85	0.7	0.7	0.55	−0.3
Pentagon	0.9	0.95	–	–	–	–
Stadium	0.95	0.85	0.1	0.5	0.4	0.4
Disk (FP modes)	0.95	0.87	–	0.5	–	–
Disk (WGM)	0.2	–	–	–	–	–
Kite (FP modes)	0.8	0.7	0.9	–	–	0.35
Kite (WGM)	−0.2	−0.85	−0.7	−0.54	−0.55	−0.75

than in ASE experiments, which indicates that laser feedback further enhances the prevalent polarization. P depends neither on the specific dye molecule used ($P_{\mathrm{DCM}} = P_{\mathrm{PM650}} = 0.95$), nor on the pump intensity (see Fig. 5), nor on the cavity length (checked from 100 to 200 μm). These observations could be accounted for by a short building time and short photon lifetime (∼1 ps), compared to the fluorescence lifetime (∼1 ns).

In the in-plane microlaser configuration, the degree of polarization P was measured for various cavity shapes and the results gathered in Fig. 8 and Table I. Generally, P depends neither on α, nor on the pump intensity, if recorded high enough above threshold (typically 20% higher). The results are quite reproducible, with error bars about 0.05, which means that the differences between shapes in Fig. 8 are relevant, and hence due to specific features of the lasing modes.

In square and pentagon, P is greater than zero, so $I_{||}$ component dominates. However P is significantly smaller than in a Fabry-Perot cavity, which evidences a redistribution of the light due to reflections at the borders. The difference between P_{square} and P_{pentagon} could arise from the periodic orbits sustaining the lasing modes, namely diamond orbit for square [see Figs. 3(b) and 3(c)] and pentagonal orbit for pentagon [26].

Eventually, the case of whispering gallery modes (WGM) should be considered. In stadium cavities [50], P is close to 1, as in Fabry-Perot lasers, whereas spectral analysis confirms that the lasing modes are indeed WGM [2]. Actually stadium shape leads to chaotic dynamical systems, which could result in a short photon lifetime (∼1 ps) [5] and then to a lasing behavior close to the Fabry-Perot cavity. With stadiums, we did not

[5]The photon lifetime of stadiums can be estimated from passive simulations. In [2] Fig. 23(a), the simulation corresponds to the same shape ratio than the experiments presented here. The imaginary part of the wave number [Im(kR)] of the most confined modes seems to be almost constant versus the real part of the wave number. The photon lifetime can then be estimated from formula $\tau \sim \frac{1}{c\,\mathrm{Im}(k)}$, with c as a speed of light in vacuum, Im(kR) ∼ 0.15 from simulations, and $R = 60\ \mu m$ in experiments, which leads to $\tau \sim 1$ ps.

notice any influence on P neither of the pump polarization α, nor of the cavity aspect ratio (ratio between length and radius; see [2], for instance).

Disk should be the archetypal shape for WGM. However, the presence of the substrate hinders their observation [51]. The P values reported here were then measured from disks lying on a pedestal. As reported in [51], these cavities present two kinds of lasing mode families: WGM and Fabry-Perot-like modes. The latter behave like real Fabry-Perot modes, in particular, regarding their P value. On the contrary, WGM are insensitive to the pump polarization α and their P value is close to zero, probably thanks to a long photon lifetime,[6] which allows for an efficient mixing of the polarized components at the boundary [3].

Finally we considered kite-shaped micro-lasers,[7] which are defined by a slight deformation from a disk [53] and present the crucial advantage to emit WGM without requiring a pedestal technology. In that case, P is negative. The structure of the electromagnetic modes is then allowing by itself to flip the ratio between the polarized components, which was forced by the gain properties in the other shapes.

In order to improve the understanding of the mode structure and the monitoring of the emitted polarization, it would be interesting to release the prevalence of TE polarization due to the gain material. As shown in Table I, the use of another laser dye does not significantly alter the TE prevalence. Actually theoretical curves in Fig. 4 indicate that the angle β between the absorption and emission dipoles should be greater than 55° to expect a negative P. As β is usually small for S_0-S_1 transitions, a drastic change cannot be expected that way. To significantly improve $I_\perp$ supplies, two different experimental schemes are considered and implemented in the following sections.

VI. USE OF RESONANT ENERGY TRANSFER

An obvious method to promote the $I_\perp$ component would be to use a dye with a molecular structure capable of isotropically redistributing the pump excitation. For this purpose, the small organo-metallic molecule Alq_3 is a good candidate, thanks to its symmetrical propeller shape. Unfortunately, Alq_3 cannot be used as a gain material alone, as in spite of being fluorescent, to our knowledge, no stimulated emission has been reported to date. But it is possible to add a laser dye, which will provide stimulated emission after a transfer of excitation via Alq_3 [54,55]. The scheme of the experiment is presented in Fig. 9(a). We expect an emission in both polarizations due to RET and the specific Alq_3 geometry.

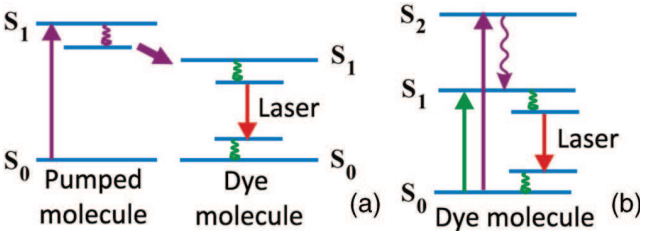

FIG. 9. (Color online) Pumping schemes are (a) via energy transfer from an excited molecule to the laser dye, (b) direct pumping to the S_2 state of the dye laser.

For this experiment, we used a pulsed frequency-tripled Nd:YAG laser (355 nm, 300 ps, 10 Hz) to excite the Alq_3 molecule in its $S_0 \rightarrow S_1$ absorption band. For the purity of the demonstration, the required laser dye should have negligible absorption at the pumping wavelength (355 nm) to ensure that the emission results from energy transfer. Besides, to provide an efficient energy transfer, the fluorescence spectrum of Alq_3 should significantly overlap with the absorption band of the laser dye. RH590 verifies both criteria as shown in Fig. 10.

3. *Planar microlasers*

Alq_3 and RH590 were taken in quantities necessary to satisfy a 1:1 stoichiometric ratio for 5% wt of RH590 in PMMA. The fluorescence emission of RH590-Alq_3 under 355-nm pumping was 10 times more intense than for RH590 alone [see Fig. 10(b)], which confirms the presence of an efficient energy transfer. In the case of ASE, the degree of polarization P for RH590 under 532-nm pumping is 0.5, while introducing Alq_3 molecules it decreases to −0.1 under 355-nm pumping. For RH590 alone under 355-nm pumping, there was even no measurable ASE signal. The transfer of excitation via Alq_3 is then an efficient method to increase the participation of $I_\perp$. However, the consequences on lasing could not be checked

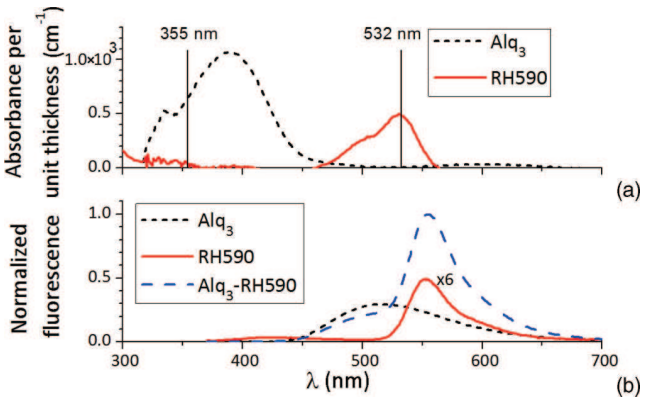

FIG. 10. (Color online) (a) Absorption spectra of Alq_3 and RH590. (b) Fluorescence spectra of Alq_3, RH590 and Alq_3-RH590 under the same pump intensity at 355 nm. They are normalized by the maximum of Alq_3-RH590 fluorescence spectrum and the variation of layer thickness is taken into account.

[6]For a perfect two-dimensional disk, the quality factor is huge for the parameter kR, which is used in our experiments ($kR \sim 1000$). It is then difficult to estimate it from numerical calculations. From simulations, it seems that the quality factor of the best confined modes is growing logarithmically versus $\mathrm{Re}(kR)$: $\log_{10} Q \sim 0.25\mathrm{Re}(kR)$. The extrapolation to $k = 2\pi/0.6\,\mu\mathrm{m}^{-1}$ and $R = 100\,\mu\mathrm{m}$ leads then to $Q \sim 10^{250}$, and so to a photon lifetime $\tau = Q/ck \sim 10^{235}$ s. Anyway, this photon lifetime is highly shortened by several processes, such as wall roughness or diffraction at the boundary, and the highest reported quality factors are about 10^{10} (see a review in [52]). In our experiments, we expect that the nanometric quality etching ensures a photon lifetime greater than 10–100 ps.

[7]The boundary is defined by the polar equation $\rho(t) = \rho_0\,(\cos t - 2d\,\sin^2 t)$, with $d = 0.165$ in this paper.

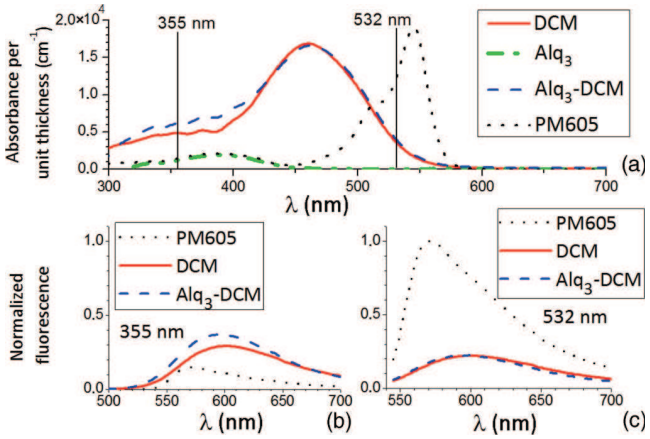

FIG. 11. (Color online) (a) Absorption spectra of PM605, DCM, Alq_3, and Alq_3-DCM. (b) and (c) Fluorescence spectra of PM605, DCM, and Alq_3-DCM under pumping at wavelengths of 355 nm (b) and 532 nm (c), normalized by the maximum of PM605 fluorescence spectrum under 532-nm pumping wavelength.

since no lasing from RH590-Alq_3 was observed, probably due to low gain values.

Similar experiments were then performed with DCM, since the transfer in Alq_3-DCM is known to be very efficient [56]. The perpendicular component of the electric field shows indeed higher intensities under lasing in various resonator shapes of in-plane microlasers. The P values are summarized in Table I. However, it is difficult to say if the decreasing of P can be only assigned to RET via Alq_3, since DCM absorbs significantly at 355 nm [see Fig. 11(a)]. Actually we show in the next section that absorption to higher excited states can be used to modify the P values.

VII. ABSORPTION IN HIGHER EXCITED STATES

To reach small or negative P values—which corresponds to the involvement of TM polarized modes—Fig. 4 shows that the angle β between the absorption and emission transition dipoles must be large. However, using the $S_0 \rightarrow S_1$ transition only, β is usually small. To release this constraint, a second method is based on pumping the dye laser to higher excited states. Actually the absorption dipole of a dye molecule is in general oriented in a very different manner for $S_0 \rightarrow S_n$ $(n > 1)$. For illustration, the absorption dipoles for $S_0 \rightarrow S_1$ and $S_0 \rightarrow S_2$ of DCM, PM605, and MD7 were calculated with GAUSSIAN software and reported in Fig. 2. After absorption, it is expected that the molecule relaxes from the S_2 state to the S_1 state, and then emits, as depicted in Fig. 9(b). For DCM, PM605, and MD7 some β angle between $\vec{d}_a(0 \rightarrow 2)$ and $\vec{d}_e(1 \rightarrow 0)$ are close to $\pi/2$, and negative P values are thus expected, as predicted in Fig. 4 and reported in [43]. Figure 11(b) confirms that DCM and PM605 can indeed be pumped within a higher excited state and then emit from the S_1 state. It is, however, difficult to single out which specific state of the dye lasers is being excited, since the absorption curves of the transitions partially overlap.

Contrary to the case of Sec. IV and in accordance with the expectations, ASE under 355-nm pumping switches to smaller or negative P values: $P_{\mathrm{DCM},355} = 0.1$ and $P_{\mathrm{PM605},355} = -0.50$ (planar configuration).

4. *VECSOLs*

In VECSOL configuration, the experiment of Sec. V was again carried out, inserting a glass plate inside the cavity at Brewster angle to force the emission polarization, and then turning the polarization of the pump beam by an angle α'. The results for a DCM-PMMA layer are plotted with circles in Fig. 7. Contrary to the case of 532-nm pumping, under a high 355-nm pumping, the laser emission is now almost insensitive to the pump polarization, which corresponds to $P = 0$. Besides, we performed time-resolved measurements of fluorescence anisotropy [57] and got $P \sim 0$ under a 355-nm pumping, even at very short delay after excitation. This effect could be assigned to different absorbing transitions, or maybe to RET occurring during the S_n to S_1 nonradiative transitions.

5. *Planar microlasers*

In microlaser configuration, pumping into higher excited states is also an efficient way to modify significantly the ratio between polarized components. Results for DCM and PM605 are summarized in Table I. However, the cavities suffered from a considerable bleaching, whereas it was not even an issue under the $S_0 \rightarrow S_1$ pumping. For reliable results, we then used a homemade laser dye, called MD7 [24], for which molecular structure and absorption dipole moments are presented in Fig. 2. The degree of polarization P was plotted in Fig. 8 for various cavity shapes and shows indeed considerably lower values than under 532-nm pumping. An important point is that P is still positive for ASE, while it is clearly negative for diamond modes in a square microlaser, and for WGM in a kite microlaser. So, although TE polarization is favored due to gain material and/or propagation, the coupling to TM modes within the resonator is strong enough to reverse the balance in favor of $I_\perp$.

To summarize, with a robust laser dye, pumping into high excited states is indeed an appropriate way to get a lasing polarization which is not strictly constrained by the pump polarization and pump geometry.

VIII. CONCLUSION

In this paper, we investigated the polarization states of organic solid-state lasers in two different configurations, VECSOL and in-plane microresonators. The framework of fluorescence anisotropy was used to interpret the data and showed that pump geometry favors a specific component of the electric field: parallel to the pump polarization for VECSOL and in-plane for microlasers. To release this constraint, we demonstrated that pumping into higher excited states of the laser dye can modify significantly the ratio between the polarized components of the emitted field. These experiments were used to explore the influence of the resonator shape on the polarization states. For Fabry-Perot cavities, thanks to the feedback, there is an enhancement of the dominant polarization compared to amplified spontaneous emission. On the contrary, for resonances with long photon lifetimes, like WGM, the polarization states can be strongly modified by coupling of

the electromagnetic components at the cavity boundary. This opens the way to a more systematic investigation of the relationship between mode structure and resonator shape, by combining experimental setup [58] and numerical simulations which should be both able to capture the three-dimensional nature of the electromagnetic field.

ACKNOWLEDGMENTS

The authors acknowledge J. Delaire, S. Brasselet, H. Benisty, and S. Bittner for fruitful discussions, A. Nosich and E. Smotrova for suggesting kite-shaped cavities, and I. Ledoux-Rak for financial support.

APPENDIX A: DIPOLAR MOMENTS

The absorption transition dipole from the fundamental state f to an excited state e is defined as the following vector (see p. 434 of Ref. [59]):

$$\vec{d}_a(f \rightarrow e) = < \psi_f \,|\, \hat{\vec{d}} \,|\, \psi_e > , \tag{A1}$$

where ψ_f and ψ_e are the stationary wave functions of the involved states, and $\hat{\vec{d}}$ is a vector operator that is the sum of the position vectors of all charged particles weighted with their charge. Absorption is a fast process; the positions of the nucleus are thus assumed to be fixed, and only the electronic part of the wave functions changes between ψ_f and ψ_e. Laser dyes are often plane aromatic molecules and the $S_0 \rightarrow S_1$ transition corresponds to the transfer of a single electron from a π to a $\pi^\star$ orbital. These orbitals are both symmetrical above and below the plane of the molecule, and so the integral (A1) along the direction perpendicular to this plane is zero, since the global function to integrate is odd. Hence $\vec{d}_a(0 \rightarrow 1)$ lies in the plane of the molecule. If the dye is pumped in its S_2 state, the excited wave function involves in general a $\pi^\star$ orbital as well, and $\vec{d}_a(0 \rightarrow 2)$ remains in the plane of the molecule. However, the profile of the $\pi^\star$ orbitals in the plane are different, and thus their corresponding $\vec{d}_a$ are not oriented similarly.

The definition of the emission transition dipole is similar to (A1), except the expression of ψ_e. Usually the molecule relaxes before emitting and the wave function of the excited state should then take into account the vibrations of the nucleus. Strictly speaking, the emission dipole is hence different from the absorption dipole of the same transition. However, the rearrangement in the S_1 state is in general not very huge and the angle β between the dipoles $\vec{d}_a$ and $\vec{d}_e$ remains close to zero.

Absorption dipoles were calculated with GAUSSIAN software and reported in Fig. 2. $S_0 \rightarrow S_1$ transition moments are calculated to be (4.04; 0.45; 0) for DCM, (0.3; −3.1; 0) for MD7 and (2.41; 1.35; 0.17) for PM605, while $S_0 \rightarrow S_2$ is (−0.8; −1.27; 0) for DCM, (−1.53; −0.02; −0) for MD7, and (−1.06; −0.6; −0.11) and (0.28; −0.54; 0.2) for PM605. The coordinates correspond to a frame, which is specific to each molecule and is indicated in Fig. 2.

APPENDIX B: DEGREE OF POLARIZATION

In this appendix, we derive formulas (1) and (2) in a similar way to those in [19] and [20], but adapted to the specific geometry of the devices in Fig. 1. Here we assume that the fluorophores are isotropically distributed in a bulk material and unable to rotate. The case of an anisotropic distribution is dealt with in [38].

The dye molecules are excited by a linearly polarized electric field defined by a unit vector $\mathbf{e} = \{\sin\alpha,\ \cos\alpha, 0\}$. A single molecule from the ensemble is located from its emission transition dipole $\vec{d}_e$ with the usual spherical coordinates $\Omega = (\theta,\varphi)$. The orientations of its transition dipoles are then characterized by the following unit vectors,

$$\begin{aligned}\mathbf{u_a} &= \frac{\vec{d}_a}{||\vec{d}_a||} \\ &= \{\sin\theta_a \cos(\varphi+\psi),\ \sin\theta_a \sin(\varphi+\psi),\ \cos\theta_a\},\end{aligned}$$

for absorption and

$$\mathbf{u_e} = \frac{\vec{d}_e}{||\vec{d}_e||} = \{\sin\theta\cos\varphi,\ \sin\theta\sin\varphi,\ \cos\theta\},$$

for emission. The notations are summarized in Fig. 12.

We are interested in the emission along axis z for a VECSOL configuration and along axis y for in-plane resonators. In the far-field approximation, the intensity emitted along a given axis j (z or y) can be presented as a three-dimensional integral of the following product: absorption probability $P_a \propto (\mathbf{e}\cdot\mathbf{u_a})^2$ and Poynting vector $\Pi_{e\,j}(\theta,\varphi) \propto (\mathbf{j}\times\mathbf{u_e})^2$ integrated over all possible orientations Ω of the emission dipoles and ψ of the absorption dipole around the emission dipole:

$$I_j = I_{j0}\int_\Omega P_a(\Omega)\Pi_{e\,j}(\Omega)d\Omega. \tag{B1}$$

The modulus squared of the Poynting vector can always be presented as a sum of two orthogonal polarizations:

$$\Pi_{e\,y}(\Omega) \propto \underbrace{\cos^2\theta}_{I_{||}} + \underbrace{\sin^2\theta\cos^2\varphi}_{I_\perp},$$

$$\Pi_{e\,z}(\Omega) \propto \underbrace{\sin^2\theta\sin^2(\varphi+\alpha)}_{I_{||}} + \underbrace{\sin^2\theta\cos^2(\varphi+\alpha)}_{I_\perp},$$

where $I_{||}$ and $I_\perp$ are defined in Fig. 1. After integration over all the possible orientations of the absorption moment around

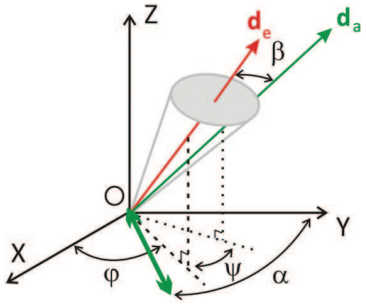

FIG. 12. (Color online) Notations are as follows: absorption ($\vec{d}_a$) and emission ($\vec{d}_e$) transition dipoles are oriented at the angles θ_a and θ_e with respect to the z axis, β, angle between the moments, ψ, between their projections on the xy plane, φ, angle between the x axis and projection of $\vec{d}_e$ on the xy plane, α, angle between the y axis and the pump beam polarization (thick green arrow).

the emission one, we get the following expression for the probability of absorption[8]:

$$P_a(\Omega) \propto 2 - 2\cos^2\beta - (1 - 3\cos^2\beta)\sin^2\theta \times [1 - \cos(2\varphi + 2\alpha)]. \quad \text{(B2)}$$

Then integration over Ω must be performed and leads to intensity components of interest:

$$I_{||\,\text{in plane}} \propto \frac{1}{30}[3 + \cos^2\beta + \cos 2\alpha(1 - 3\cos^2\beta)], \quad \text{(B3)}$$

$$\begin{aligned} I_{\perp\,\text{in plane}} &= I_{||\,\text{in plane}}(\alpha = 0), \\ I_{||\,\text{VECSOL}} &= I_{||\,\text{in plane}}(\alpha = \pi/2), \\ I_{\perp\,\text{VECSOL}} &= I_{\perp\,\text{in plane}}. \end{aligned} \quad \text{(B4)}$$

Therefore the expressions for the degrees of polarization P are

$$P_{\text{in plane}} = \frac{(3\cos^2\beta - 1)(1 - \cos 2\alpha)}{7 - \cos^2\beta - \cos 2\alpha(3\cos^2\beta - 1)}, \quad \text{(B5)}$$

$$P_{\text{VECSOL}} = \frac{3\cos^2\beta - 1}{3 + \cos^2\beta}. \quad \text{(B6)}$$

From these expressions, it follows that for a pump beam polarization characterized by $\alpha = \pi/2$ (orthogonal to the direction of observation), then $P_{\text{in plane}} = P_{\text{VECSOL}}$. The variation of $P_{\text{in plane}}$ with β angle is depicted on Fig. 4 for several orientations α of the linear pump polarization.

[8]Error in Eq. (6) of [38]. It should be read $\cos 2\varphi \cos 2\alpha$ instead of $\cos(2\varphi + 2\alpha)$

[1] H. E. Tureci, A. D. Stone, and L. Ge, Phys. Rev. A **76**, 013813 (2007).
[2] E. Bogomolny, N. Djellali, R. Dubertrand, I. Gozhyk, M. Lebental, C. Schmit, C. Ulysse, and J. Zyss, Phys. Rev. E **83**, 036208 (2011).
[3] N. Frateschi, A. Kanjamala, A. F. J. Levi, and T. Tanbun-Ek, Appl. Phys. Lett. **66**, 1859 (1995).
[4] D. K. Kim, S.-J. An, E. G. Lee, and O'Dae Kwon, J. Appl. Phys. **102**, 053104 (2007).
[5] N. Tsujimoto, T. Takashima, T. Nakao, K. Masuyama, A. Fujii, and M. Ozaki, J. Phys. D: Appl. Phys. **40**, 1669 (2007).
[6] S. V. Frolov, M. Shkunov, Z. V. Vardeny, and K. Yoshino, Phys. Rev. B **56**, 4363R (1997).
[7] J. Wang and K. Y. Wong, Appl. Phys. B **87**, 685 (2007).
[8] Chao Ye, Lei Shi, Jun Wang, Dennis Lo, and Xiao-lei Zhu, Appl. Phys. Lett. **83**, 4101 (2003).
[9] H. Rabbani-Haghighi, S. Forget, S. Chénais, and A. Siove, Opt. Lett. **35**, 1968 (2010).
[10] A. Matsko, editor, *Practical Applications of Micro-Resonators in Optics and Photonics* (CRC, Boca Raton, 2009).
[11] Lu Ding, C. Baker, P. Senellart, A. Lemaitre, S. Ducci, G. Leo, and I. Favero, Phys. Rev. Lett. **105**, 263903 (2010).
[12] P. Del'Haye, T. Herr, E. Gavartin, M. L. Gorodetsky, R. Holzwarth, and T. J. Kippenberg, Phys. Rev. Lett. **107**, 063901 (2011).
[13] N. Djellali, I. Gozhyk, D. Owens, S. Lozenko, M. Lebental, J. Lautru, C. Ulysse, B. Kippelen, and J. Zyss, Appl. Phys. Lett. **95**, 101108 (2009).
[14] Q. J. Wang, C. Yan, N. Yu, J. Unterhinninghofen, J. Wiersig, C. Pflügl, L. Diehl, T. Edamura, M. Yamanishi, H. Kan, and F. Capasso, PNAS **107**, 22407 (2010).
[15] C. Li and A. W. Poon, Opt. Lett. **30**, 546 (2005).
[16] See Sec. III. B.2 in [2].
[17] J. Topolancik and F. Vollmer, Biophys. J. **92**, 2223 (2007).
[18] S. Chénais and S. Forget, Polym. Int. **61**, 390 (2012).
[19] J. R. Lakowicz, *Principles of Fluorescence Spectroscopy*, 3rd ed. (Springer, New York, 2006).
[20] B. Valeur, *Molecular Fluorescence: Principles and Applications* (Wiley-VCH, New York, 2001).
[21] K. C. Reyzer and L. W. Casperson, J. Appl. Phys. **51**, 6075 (1980).
[22] K. C. Reyzer and L. W. Casperson, J. Appl. Phys. **51**, 6083 (1980).
[23] O. I. Yaroshenko, J. Opt. A: Pure Appl. Opt. **5**, 328 (2003).
[24] E. Y. Schmidt, N. V. Zorina, M. Y. Dvorko, N. I. Protsuk, K. V. Belyaeva, G. Clavier, R. Méallet-Renault, T. T. Vu, A. B. I. Mikhaleva, and B. A. Trofimov, Chem. Eur. J. **17**, 3069 (2011).
[25] M. Lebental, E. Bogomolny, and J. Zyss, Organic micro-lasers: a new avenue onto wave chaos physics, in [10].
[26] M. Lebental, N. Djellali, C. Arnaud, J.-S. Lauret, J. Zyss, R. Dubertrand, C. Schmit, and E. Bogomolny, Phys. Rev. A **76**, 023830 (2007).
[27] G. Dutier, V. de Beaucoudrey, A. C. Mitus, and S. Brasselet, Eur. Phys. Lett. **84**, 67005 (2008).
[28] G. Dutier, V. de Beaucoudrey, S. Brasselet, and J. Zyss (unpublished).
[29] V. Le Floc'h, S. Brasselet, J.-F. Roch, and J. Zyss, J. Phys. Chem. B **107**, 12403 (2003).
[30] V. Bulović, V. G. Kozlov, V. B. Khalfin, and S. R. Forrest, Science **279**, 553 (1998).
[31] I. Gozhyk *et al.* (in preparation).
[32] O. Svelto, *Principles of Lasers* (Plenum Press, New York, 1998).
[33] E. W. Thulstrup and J. Michl, J. Am. Chem. Soc. **104**, 5594 (1982).
[34] M. Tammer and A. P. Monkman, Adv. Mat. **14**, 210 (2002); C. M. Ramsdale and N. C. Greenham, *ibid.* **14**, 212 (2002).
[35] J. Sturm, S. Tasch, A. Niko, G. Leising, E. Toussaere, J. Zyss, T. C. Kowalczyk, K. D. Singer, U. Scherf, and J. Huber, Thin Solid Films **298**, 138 (1997).
[36] S. Agan, F. Ay, A. Kocabas, and A. Aydinli, Appl. Phys. A **80**, 341 (2005).
[37] L. Novotny, M. R. Beversluis, K. S. Youngworth, and T. G. Brown, Phys. Rev. Lett. **86**, 5251 (2001).
[38] I. Gozhyk, S. Forget, S. Chénais, C. Ulysse, A. Brosseau, R. Méallet-Renault, G. Clavier, R. Pansu, J. Zyss, and M. Lebental, Proceedings of SPIE **8258**, 82580K (2012).
[39] S. Y. Lam and M. J. Damzen, Appl. Phys. B **77**, 577 (2003).
[40] T. D. Visser, B. Demeulenaere, J. Haes, D. Lenstra, R. Baets, and H. Blok, J. Lightwave Technol. **14**, 885 (1996).

[41] S. Bittner, B. Dietz, M. Miski-Oglu, P. O. Iriarte, A. Richter, and F. Schafer, Phys. Rev. A **80**, 023825 (2009).
[42] B. B. McFarland, Appl. Phys. Lett. **10**, 208 (1967).
[43] I. Nagata and T. Nakaya, J. Phys. D: Appl. Phys. **6**, 1870 (1973).
[44] X. Wang, R. A. Linke, G. Devlin, and H. Yokoyama, Phys. Rev. A **47**, 2488R (1993).
[45] L. Persano, P. del Carro, E. Mele, R. Cingolani, D. Pisignano, M. Zavelani-Rossi, S. Longhi, and G. Lanzani, Appl. Phys. Lett. **88**, 121110 (2006).
[46] S. A. van den Berg, V. A. Sautenkov, G. W. 't Hooft, and E. R. Eliel, Phys. Rev. A **65**, 053821 (2002).
[47] A. Aiello, F. de Martini, and P. Mataloni, Opt. Lett. **21**, 149 (1996).
[48] H. Rabbani-Haghighi, S. Forget, A. Siove, and S. Chénais, Eur. Phys. J. Appl. Phys. **56**, 34108 (2011).
[49] T. Ikegami, IEEE J. Quantum Electron. **8**, 470 (1972).
[50] M. Lebental, J.-S. Lauret, J. Zyss, C. Schmit, and E. Bogomolny, Phys. Rev. A **75**, 033806 (2007).
[51] S. Lozenko, N. Djellali, I. Gozhyk, C. Delezoide, J. Lautru, C. Ulysse, J. Zyss, and M. Lebental, J. Appl. Phys. **111**, 103116 (2012).
[52] K. J. Vahala, Nature (London) **424**, 839 (2003).
[53] M. V. Balaban, E. I. Smotrova, O. V. Shapoval, V. S. Bulygin, A. I. Nosich, Int. J. Numerical Modeling: Electronic Networks, Devices and Fields **25**, 490 (2012).
[54] M. Berggren, A. Dodabalapur, R. E. Slusher, and Z. Bao, Nature (London) **389**, 466 (1997).
[55] V. G. Kozlov, V. Bulović, P. E. Burrows, and S. R. Forrest, Nature (London) **389**, 362 (1997).
[56] V. G. Kozlov, V. Bulović, P. E. Burrows, M. Baldo, V. B. Khalfin, G. Parthasarathy, S. R. Forrest, Y. You, and M. E. Thompson, J. Appl. Phys. **84**, 4096 (1998).
[57] J.-A. Spitz, R. Yasukuni, N. Sandeau, M. Takano, J.-J. Vachon, R. Méallet-Renault, and R. B. Pansu, J. Microscopy-Oxford **229**, 104 (2008).
[58] D. K. Kim, S.-J. An, E. G. Lee, and O'Dae Kwon, J. Appl. Phys. **102**, 053104 (2007).
[59] E. Braslavsky, Pure Appl. Chem **79**, 293 (2007).